

VOLUME 34

AUGUST 1956

NUMBER 8

# Canadian Journal of Physics

**Editor:** G. M. VOLKOFF

**Associate Editors:**

- L. G. ELLIOTT, *Atomic Energy of Canada, Ltd., Chalk River*  
J. S. FOSTER, *McGill University*  
G. HERZBERG, *National Research Council of Canada*  
L. LEPRINCE-RINGUET, *Ecole Polytechnique, Paris*  
R. W. PRINGLE, *University of Manitoba*  
B. W. SARGENT, *Queen's University*  
Sir FRANCIS SIMON, *Clarendon Laboratory, University of Oxford*  
W. H. WATSON, *University of Toronto*

*Published by THE NATIONAL RESEARCH COUNCIL  
OTTAWA CANADA*

## CANADIAN JOURNAL OF PHYSICS

*(Formerly Section A, Canadian Journal of Research)*

Under the authority of the Chairman of the Committee of the Privy Council on Scientific and Industrial Research, the National Research Council issues THE CANADIAN JOURNAL OF PHYSICS and six other journals devoted to the publication, in English or French, of the results of original scientific research. Matters of general policy concerning these journals are the responsibility of a joint Editorial Board consisting of: members representing the National Research Council of Canada; the Editors of the Journals; and members representing the Royal Society of Canada and four other scientific societies.

### EDITORIAL BOARD

#### Representatives of the National Research Council

A. N. Campbell, <i>University of Manitoba</i>	H. G. Thode, <i>McMaster University</i>
G. E. Hall, <i>University of Western Ontario</i>	D. L. Thomson, <i>McGill University</i>
	W. H. Watson (Chairman), <i>University of Toronto</i>

#### Editors of the Journals

D. L. Bailey, <i>University of Toronto</i>	G. A. Ledingham, <i>National Research Council</i>
T. W. M. Cameron, <i>Macdonald College</i>	Léo Marion, <i>National Research Council</i>
J. B. Collip, <i>University of Western Ontario</i>	R. G. E. Murray, <i>University of Western Ontario</i>
G. M. Volkoff, <i>University of British Columbia</i>	

#### Representatives of Societies

D. L. Bailey, <i>University of Toronto</i> Royal Society of Canada	R. G. E. Murray, <i>University of Western Ontario</i> Canadian Society of Microbiologists
T. W. M. Cameron, <i>Macdonald College</i> Royal Society of Canada	H. G. Thode, <i>McMaster University</i> Chemical Institute of Canada
J. B. Collip, <i>University of Western Ontario</i> Canadian Physiological Society	T. Thorvaldson, <i>University of Saskatchewan</i> Royal Society of Canada
G. M. Volkoff, <i>University of British Columbia</i> Royal Society of Canada; Canadian Association of Physicists	

#### Ex officio

Léo Marion (Editor-in-Chief), *National Research Council*  
F. T. Rosser, Director, Division of Administration, *National Research Council*

---

*Manuscripts* for publication should be submitted to Dr. Léo Marion, Editor-in-Chief, Canadian Journal of Physics, National Research Council, Ottawa 2, Canada.  
(For instructions on preparation of copy, see **Notes to Contributors** (inside back cover).)

*Proof, correspondence concerning proof, and orders for reprints* should be sent to the Manager, Editorial Office (Research Journals), Division of Administration, National Research Council, Ottawa 2, Canada.

*Subscriptions, renewals, requests for single or back numbers, and all remittances* should be sent to Division of Administration, National Research Council, Ottawa 2, Canada. Remittances should be made payable to the Receiver General of Canada, credit National Research Council.

The journals published, frequency of publication, and prices are:

Canadian Journal of Biochemistry and Physiology	Bimonthly	\$3.00 a year
Canadian Journal of Botany	Bimonthly	\$4.00 a year
Canadian Journal of Chemistry	Monthly	\$5.00 a year
Canadian Journal of Microbiology	Bimonthly	\$3.00 a year
Canadian Journal of Physics	Monthly	\$4.00 a year
Canadian Journal of Technology	Bimonthly	\$3.00 a year
Canadian Journal of Zoology	Bimonthly	\$3.00 a year

The price of single numbers of all journals is 75 cents.





# Canadian Journal of Physics

*Issued by THE NATIONAL RESEARCH COUNCIL OF CANADA*

VOLUME 34

AUGUST 1956

NUMBER 8

## THE EFFECT OF INCIDENT ATOMIC VELOCITY ON THE STRUCTURE OF EVAPORATED SILVER FILMS<sup>1</sup>

BY R. A. AZIZ AND G. D. SCOTT

### ABSTRACT

The influence of the incident atomic velocity on the structure of evaporated films has been studied for silver films in the thickness range from 50 to 500 Å. The thermal velocities of the evaporated atoms were reduced (i) by "reflection" from a teflon surface at room temperature, and (ii) by "diffusion" through nitrogen gas at 3.0  $\mu$ . Films formed by these two methods are compared with "normal" high vacuum films for the same rates of deposition, which were relatively slow (0.4 to 4 Å of thickness per second). The results of both resistivity measurements and electron microscopy show that "diffusion" films are less aggregated, i.e. more continuous, than "normal" high vacuum films. "Reflected" films have a structure intermediate between the other two. A qualitative explanation of the observed effects is given in terms of the formation of nuclei and the growth of aggregates.

### INTRODUCTION

Controversy exists in the literature as to whether the velocity of incident atoms has a decided influence on the structure of evaporated films. In contrast the important effect of the rate of deposition has been well established (Sennett and Scott 1950). An increase in atomic velocity can be produced by raising the temperature of the source. However, accompanying this increase of velocity is an increase of beam intensity and therefore rate of deposition. On this account, Holland (1951) suggests that a number of workers have been mistakenly led to believe that velocity does have an effect on structure. Levinstein (1949) studied the possible effect of atomic velocity on both aggregation and crystal structure. His experiments were carried out with a rotating velocity selector. In the case of gold, which was shown to be monatomic in the vapor phase, no difference was observed between deposits in the high and in the low velocity regions. Differences were observed in the case of antimony but this was attributed to the presence of polyatomic particles in the vapor phase in the low velocity region. The polyatomic particles result in fewer but larger nuclei for condensation and thus in larger patches or aggregates in the deposit.

In the experiments to be described two methods were used to alter the velocity of the incident atoms. In the first, the metallic vapor was passed by diffusion through an inert gas at low pressure. In the second, the metallic

<sup>1</sup>Manuscript received March 13, 1956.

Contribution from the Department of Physics, University of Toronto, Toronto, Ontario.

vapor was "reflected" from a solid surface and then collected on the substrate. The latter process was carried out under high vacuum conditions.

Silver was selected as the metal for evaporation. It is readily available in a pure state, is easily evaporated, is resistant to oxidation, and is monatomic in the vapor phase. Because silver forms films which are more aggregated, i.e., of a coarser structure than gold, the effect under investigation is likely to be more marked than in the case of gold, for which Levinstein (1949) was unable to observe differences.

Two characteristics of the films were used to detect differences resulting from the method of formation: (1) their electrical resistivity and (2) their appearance by transmission electron microscopy.

#### EXPERIMENTAL

The apparatus and procedure were essentially the same as those employed in previous work in this laboratory (Aziz 1951). Microscope slides served as the substrate and a glow discharge in the evaporation chamber was used for the final cleaning. The vacuum obtained was better than  $10^{-2} \mu$  of Hg. The silver was evaporated from a tungsten ribbon enclosed in a shield so that little radiation reached the substrate, and consequently for all the experiments the substrate temperature remained close to that of the room.

The time of deposition was chosen as 100 sec. and was controlled by a photographic shutter. For evaporating films, 100 to 500 Å thick, such a time is considered long. Shorter times might have been used, but in these experiments it was important not to overshadow the effect of beam velocity with a high rate of deposition.

The thickness of the films was measured by a multiple interference technique (Scott *et al.* 1950). Though readings can be made within a few angstroms, there is evidence that a constant error of 20 to 30 Å may arise in this method. Such an error would not affect the main results of these experiments since it would involve merely a shift of the thickness scale. Because the error has not been studied adequately, no correction was made and the thicknesses given are the values as measured by multiple interference.

##### (a) Diffusion Experiments

The problem of selecting a gas to act as moderator to reduce the speed of the silver atoms during the travel from source to substrate involves several factors. Clearly the gas must not react chemically with the silver and must not adsorb too readily on the glass substrate or on the silver film. The molecules of the gas must be massive enough to reduce appreciably the speed of the silver atoms on each collision and yet preferably not so massive as to destroy completely the forward momentum of the beam. Nitrogen gas at a pressure of about  $3.0 \mu$  was chosen as a suitable compromise.

An analysis of the slowing down of atomic particles by diffusion through a gas has been carried out by Cravath (1930). It can be shown that the average energy of evaporated silver atoms passing through low pressure nitrogen will reach almost that of the nitrogen molecules in six or seven collisions. A calcu-

lation was made of the mean free path in nitrogen gas of silver atoms with different energies. The energies selected corresponded to the average value of the silver atoms initially (i.e. at 1300°K.), and then in turn the value attained after each of seven successive collisions. The results showed that the source to substrate distance for seven collisions should be about 15 cm. in nitrogen at 3.0  $\mu$  pressure.

Nitrogen gas from a cylinder was introduced into the evaporating chamber through a needle valve. After an initial pump down to  $10^{-2} \mu$ , the needle valve was adjusted to maintain a steady pressure of 3.0  $\mu$  while the pumps were in continuous operation.

The microscope slides used as a substrate for the films were provided with thick evaporated silver electrodes for making electrical contact to the film. Electron microscope mounts were placed along the edge of the slide. As in previous work the slide was set at about 45 degrees to the direction of the beam to give a range of thickness with each evaporation.

After an evaporation the film was kept in the chamber for one hour and then in room air for 30 min. before resistance measurements were attempted. This procedure allowed time for irreversible aging to occur and hence for the resistance of the films to reach a stable value (Aziz 1955). For individual resistance measurements the films were cut in strips about 3 mm. wide. From the resistance and the length, width, and thickness of the strip the resistivity of the film was calculated.

#### (b) *Reflection Experiments*

When a molecule or atom impinges on a solid surface it may return to the gas phase instantaneously or it may condense on the surface. In the latter case, where the collision is inelastic, the atom may remain permanently on the surface or after a small finite time it may re-evaporate. These effects have been studied for example by Estermann and Stern (1930). Atoms with energies higher than that corresponding to the temperature of the solid surface will in general suffer energy loss upon reflection or scattering at the surface.

A number of tests were carried out to determine a suitable scattering surface. The main requirement is for a high scattering power. The surfaces tested included glass, glass coated with vacuum grease, glass coated with silicone oil, polythene, and teflon. Teflon was chosen as having a high scattering power, though not as high as the grease coating. However the latter would preclude the use of the glow discharge for cleaning the substrate. It can be assumed that after a single encounter with a teflon surface at room temperature a silver atom will lose a large fraction of its initial energy.

A sheet of teflon was set above the silver source at an angle of about 45 degrees to the beam so as to scatter silver atoms onto a nearby microscope slide. The slide is in such a position that it would not receive atoms directly from the source but only by reflection or scattering from the teflon. The slide was prepared with electrodes for resistance measurements and with electron microscope grids as described above. The evaporations were made at a pressure of  $10^{-2} \mu$ .

## RESULTS

The observations on electrical resistivity are shown in Fig. 1. The logarithm of the resistivity is plotted against thickness for the three types of silver films: A—direct deposition in high vacuum, B—deposition in high vacuum after

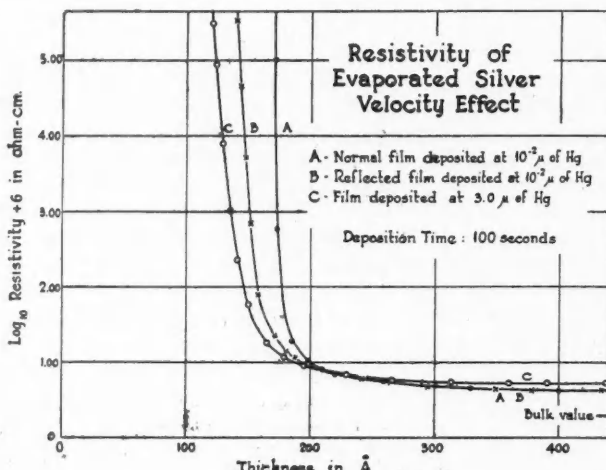


FIG. 1. Electrical resistivity against thickness for three types of evaporated silver films.

reflection from a solid surface at room temperature, C—deposition after diffusion through nitrogen gas at  $3.0\mu$  pressure. It is to be noted that the deposition time is in all cases 100 sec. As this is a relatively slow rate of deposition ( $0.4\text{--}4\text{ \AA}$  of thickness per second), the resulting resistivities are much higher than can be produced with shorter deposition times.

Electron micrographs of films at different thicknesses and for the three methods of preparation are reproduced in Fig. 2. These show how the aggregates of the thinner films gradually change with increasing thickness to form a more continuous structure. The micrographs also show a distinct difference in the film structure for the three methods of formation.

From Fig. 1 it can be seen that the resistivity of a normal high vacuum silver film (curve A) when deposited in 100 sec. is infinite up to a thickness of  $160\text{ \AA}$ . This thickness is called the "critical" thickness for these conditions. As the film thickness increases the resistivity drops sharply and then more slowly until by about  $220\text{ \AA}$  it levels off and further increase in thickness makes little change. The lowest value reached is nearly three times the resistivity of bulk silver. In curve B it is seen that the "critical" thickness of the "reflected" film occurs at about  $135\text{--}140\text{ \AA}$ , indicating that the aggregates have joined to provide electrical continuity at an earlier stage in the formation of the film than in the case of the normal film. This effect can be verified in the micrographs of Fig. 2. The normal film shows the aggregates joining at about

## PLATE I

## EVAPORATED SILVER FILMS

## VELOCITY EFFECTS

Time of deposition—100 sec.

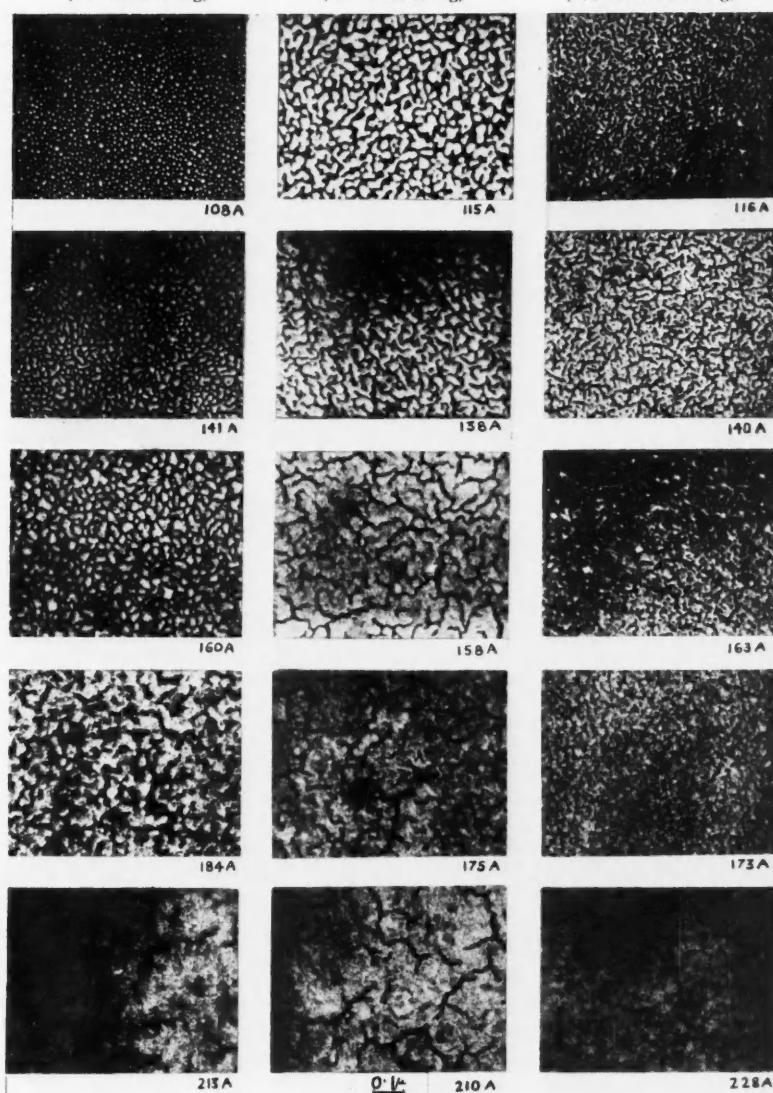
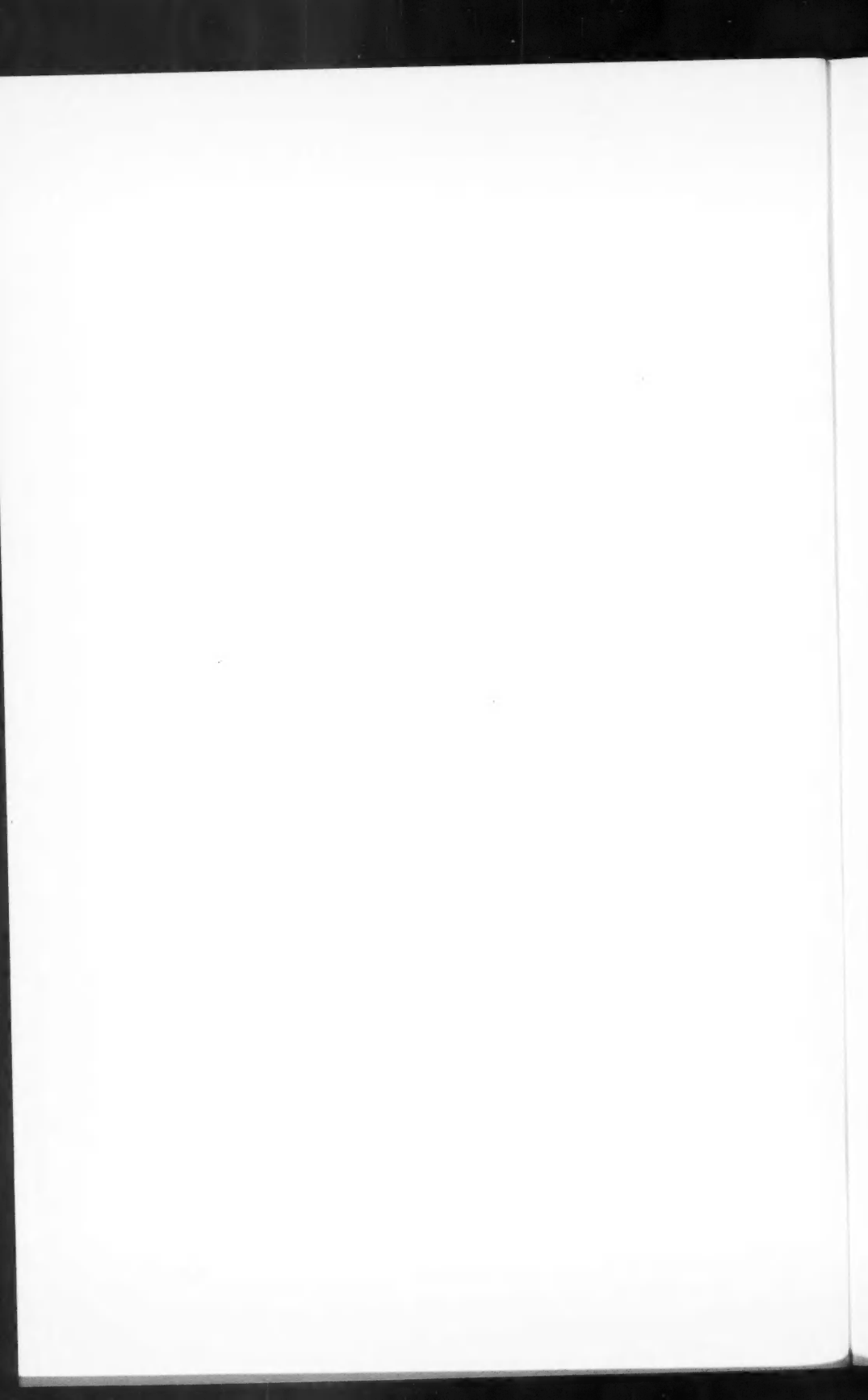
Normal in vacuum  
( $10^{-5}$  mm. of Hg)Reflected in vacuum  
( $10^{-5}$  mm. of Hg)Nitrogen atmosphere  
( $3 \times 10^{-3}$  mm. of Hg)

FIG. 2. Electron micrographs of three kinds of evaporated silver films. A series of five thicknesses is given for each case. (Magnification 50,000X.)



160 Å, whereas in the reflected film the aggregates are beginning to join at 138 Å. For deposits thicker than 200 Å there is no significant difference between the normal and reflected films in either resistivity or appearance. Curve C of Fig. 1 shows that films deposited by diffusion through nitrogen have a still smaller critical thickness—about 110 Å. The micrographs again confirm this observation: the aggregates in the “diffusion” film are beginning to join at a thickness of 116 Å. For films thicker than 220 Å the resistivity remains above that of the vacuum film. The micrographs of the “diffusion” films show a more gradual change in structure with thickness as we would expect from the shape of the resistivity curve.

It is interesting to note the similarity in appearance of the “diffusion” silver films and sputtered silver film (Ells and Scott 1952). Since the gas pressure used in producing “diffusion” films is about the same as for sputtered metal films, the velocity of the atoms as they approach the substrate should correspond approximately to room temperature thermal energies for both cases and lead to similar film structure.

#### DISCUSSION

The microscopic structure of thin evaporated films depends chiefly on two factors: first, on the number of nuclei per unit area which are formed initially on the substrate and second, on the way in which the resulting aggregates grow. The differences between the structures of the three types of films studied in these experiments can be explained at least qualitatively in terms of these factors.

An evaporated silver atom impinging on the substrate will in general remain mobile on the surface until through loss of energy it is rendered non-mobile either by binding with another silver atom to form Frenkel doublets or by binding with atoms of the substrate. The non-mobile singlets or doublets provide nuclei on which subsequent atoms will collect. Higher energy atoms would presumably be more mobile after reaching the substrate and produce fewer nuclei per unit area since there would be a greater tendency for more mobile atoms to “find” existing nuclei than to produce new ones. Hence films formed from higher energy atoms will exhibit a coarser, more aggregated, structure.

During the growth of an aggregate, atoms will migrate over the surface of the particle until favorable sites are reached. Thus aggregates formed from higher energy atoms will tend to be more compact in shape than those from lower energy atoms, which will tend to spread out in irregular flat platelets. It is also clear that this effect will be enhanced by the higher local temperatures in aggregates produced from atoms with greater incident energy.

The observation of resistivity and of structure for the three types of films studied confirms the above ideas. The vacuum films are formed from atoms of the highest energy—the average energy corresponds to about 1300°K., while for the “diffusion” films the atoms have an average energy of about 320°K. For the “reflection films” the atoms must have an intermediate energy. As both the micrographs and the resistivity curves show, the “vacuum”

films are the most aggregated in the thinner ranges, the "diffusion" films are the least aggregated, and the "reflection" films are intermediate. For the thicker films, which are continuous in appearance, the resistivity of the "diffusion" films is higher than for the other two types presumably because there is more gas occluded in the film as it forms.

It may be noted that the angles of incidence of atoms have a greater variation at a point on the substrate for the "diffusion" and "reflection" films than for the vacuum films. Since it is known that in general angles of incidence up to 45 degrees have little influence on the film structure, this effect should certainly be small. Finally it is pointed out that in the diffusion experiments the gas might conceivably affect the condition of the substrate. However, as the adsorption of nitrogen on glass at room temperature is very small, the difference between the condition at  $3\text{ }\mu$  and  $10^{-2}\text{ }\mu$  would be expected to have a negligible influence on the structure of the films.

#### REFERENCES

- AZIZ, R. A. 1951. M.A. Thesis, University of Toronto, Toronto, Ont.  
AZIZ, R. A. 1955. Unpublished.  
CRAVATH, A. M. 1930. Phys. Rev. **36**: 248.  
ELLS, C. E. and SCOTT, G. D. 1952. J. Appl. Phys. **23**: 31.  
ESTERMANN, I. and STERN, O. 1930. Z. Physik, **61**: 95.  
HOLLAND, L. 1951. Vacuum, **1**: 23.  
LEVINSTEIN, H. 1949. J. Appl. Phys. **20**: 306.  
SCOTT, G. D., McLAUCHLAN, T. A., and SENNETT, R. S. 1950. J. Appl. Phys. **21**: 843.  
SENNETT, R. S. and SCOTT, G. D. 1950. J. Opt. Soc. Amer. **40**: 203.

# THE RAMAN SPECTRUM OF ETHYLENE<sup>1</sup>

BY T. FELDMAN,<sup>2</sup> J. ROMANKO,<sup>3</sup> AND H. L. WELSH

## ABSTRACT

The vibrational Raman spectrum of ethylene was photographed at gas pressures of 1-3 atm. with a reciprocal linear dispersion of  $10.5 \text{ cm}^{-1}$  per mm. The rotational structures of the totally symmetric bands,  $\nu_1$  and  $\nu_3$ , were analyzed using an approximate asymmetric top model; only the  $Q$  branch of  $\nu_2$  was observed. In the complicated structure of the non-totally symmetric  $\nu_5$  band a series of  $o, s Q_K$  branches was identified and the band origin determined as  $3102.5 \text{ cm}^{-1}$ . A satisfactory interpretation of a broad maximum at  $1662 \text{ cm}^{-1}$  could not be given.

## INTRODUCTION

The ethylene molecule (point group  $V_h$ ) is a slightly asymmetric top and has 12 fundamental modes of vibration. The six vibrational forms which are symmetrical with respect to the center of symmetry are active in the Raman effect (Table III); since the rule of mutual exclusion applies, these vibrations are inactive in infrared absorption. The extensive work on the Raman and infrared spectra of ethylene prior to 1945 has been summarized and discussed by Herzberg (1945).

In the early studies on the Raman spectrum of gaseous ethylene at low dispersion by Dickinson, Dillon, and Rasetti (1929) and Bhagavantam (1936), the  $Q$  branches of the three totally symmetric bands,  $\nu_1$ ,  $\nu_2$ , and  $\nu_3$ , were recorded. In a recent study by Stoicheff (1953), also at low dispersion but with improved techniques, a broad band centered near  $3108 \text{ cm}^{-1}$  was photographed and assigned to  $\nu_5(b_{1g})$ . A weak band at about  $950 \text{ cm}^{-1}$  was assigned by Stoicheff to  $\nu_6(b_{2g})$ . The fundamental  $\nu_6(b_{1g})$  has not been observed in the gas; however, a line was recorded in the liquid by Rank, Shull, and Axford (1950) at  $1236 \text{ cm}^{-1}$ , corresponding to the position for  $\nu_6$  calculated by Arnett and Crawford (1950) from infrared data.

## EXPERIMENTAL

The rotation-vibrational bands of ethylene were photographed with the Raman source and spectrograph which have been previously described (Welsh, Stansbury, Romanko, and Feldman 1955). The spectrograph has a reciprocal linear dispersion of  $10.5 \text{ cm}^{-1}$  per mm. at  $4358 \text{ \AA}$ . Ethylene gas of research purity was used in the pressure range 1-3 atm. The spectra were recorded on Kodak 103a-O spectroscopic plates with a spectral slit width of  $0.7 \text{ cm}^{-1}$ . The frequency shifts of the Raman lines were measured with iron arc lines as standards and the values  $22,938.04$  and  $24,705.30 \text{ cm}^{-1}$  for the frequencies

<sup>1</sup>Manuscript received May 3, 1956.

Contribution from the McLennan Laboratory, University of Toronto, Toronto, Ontario. This research was supported by Grant No. 1001-01, Project D46-10-01-01, of the Defence Research Board of Canada.

<sup>2</sup>Holder of the E. F. Burton Fellowship in Physics, School of Graduate Studies, University of Toronto, 1954-55.

<sup>3</sup>Holder of a Garnet W. McKee - Lachlan Gilchrist Scholarship, School of Graduate Studies, University of Toronto, 1952-54. Present address: Convair Corporation, Fort Worth, Texas.

of Hg4358 and Hg4047, respectively. The measurements were made on density traces obtained with a Leeds and Northrup microphotometer.

#### RESULTS AND DISCUSSION

The  $\nu_1$ ,  $\nu_3$ , and  $\nu_5$  bands with extensive rotational structure and the  $Q$  branch of  $\nu_2$  were recorded. Although prolonged exposures were made in the 800–1300 cm.<sup>-1</sup> region, the remaining Raman active fundamentals,  $\nu_6$  and  $\nu_8$ , were not observed.

#### The 1200–1700 cm.<sup>-1</sup> Region

With a sodium nitrite filter to remove Hg4047 radiation from the exciting light and a gas pressure of 3 atm., the spectrum excited by Hg4358 showed in

TABLE I  
RAMAN FREQUENCIES OF C<sub>2</sub>H<sub>4</sub> IN THE 1200–1700 CM.<sup>-1</sup> REGION

$\Delta\nu$ (cm. <sup>-1</sup> )	Assignment*	$\Delta\nu$ (cm. <sup>-1</sup> )	Assignment*
1251.4	O(25)	1357.4	R(7)
1255.0	O(24)	1359.1	S(3); R(8)
1258.1	O(23)	1361.1	R(9)
1262.2	O(22)	1362.4	S(4); R(10)
1265.7	O(21)	1364.8	R(11)
1269.5	O(20)	1366.4	S(5); R(12)
1271.9	O'(21)	1368.1	R(13)
1272.1	O(19)	1370.8	S(6)
1275.6	O'(20)	1371.4	S'(7)
1276.5	O(18)	1373.6	S(7)
1278.9	O'(19)	1375.0	S'(8)
1282.0	O(17)	1377.7	S(8)
1282.5	O'(18)	1381.0	S(9)
1342.2†	$\nu_3(Q_{\max})$	1385.3	S(10)
1289.1	O(15)	1388.3	S'(12)
1292.4	O(14)	1388.9	S(11)
1296.0	O(13)	1391.9	S'(13)
1299.3	O(12)	1392.5	S(12)
1302.1	O'(12)	1395.9	S'(14)
1303.3	O(11)	1396.2	S(13)
1305.6	O'(11)	1399.0	S'(15)
1307.0	O(10)	1400.3	S(14)
1308.7	O'(10)	1402.0	S'(16)
1311.1	O(9)	1403.2	S(15)
1313.0	O'(9)	1405.4	S'(17)
1314.4	O(8)	1407.5	S(16)
1316.2	P(14)	1408.7	S'(18)
1317.9	O(7); P(13)	1411.7	S(17)
1320.2	P(12)	1412.8	S'(19)
1321.7	O(6); P(11)	1415.7	S(18)
1323.7	P(10)	1419.2	S(19)
1325.2	O(5); P(9)	1422.3	S(20)
1326.9	P(8)	1426.3	S(21)
1328.9	O(4); P(7)	1428.9	S(22)
1330.9	P(6)	1432.7	S(23)
1333.7	O(3); P(5)	1436.2	S(24)
1335.7	$\nu_3(H_2C^{12}=C^{12}H_2)$	1440.1	S(25)
1342.3	$\nu_3(Q_{\max})$	1605.8	$2\nu_{10}$
1349.2	R(3)	1613.9	$\nu_2(H_2C^{12}=C^{12}H_2)$
1351.0	S(1); R(4)	1622.6	$\nu_2(Q_{\max})$
1353.2	R(5)	1662	?
1354.9	S(2); R(6)		

\*The rotational assignments refer to the  $\nu_3$  band.

†Excited by Hg4347.

a four hour exposure two strong lines at Raman displacements of 1622.6 and 1342.4  $\text{cm}^{-1}$ , the *Q* branches of the totally symmetric  $\nu_2$  and  $\nu_3$  bands, respectively. In a 56 hr. exposure more structure was photographed, especially in the neighborhood of the *Q* branch of  $\nu_3$ , as shown in Fig. 1(*b*) and (*c*). The frequencies listed in Table I are averages from three plates at various gas pressures.

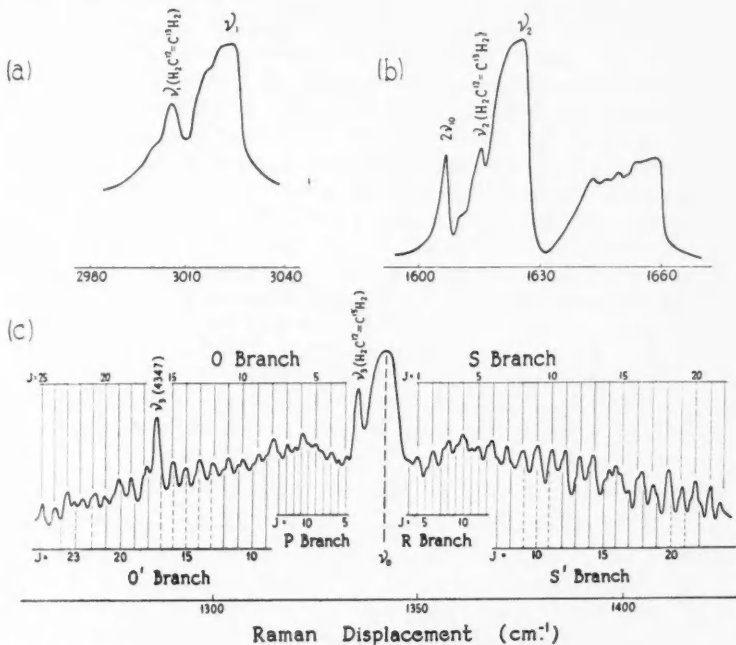


FIG. 1. Microphotometer traces of the totally symmetric Raman bands of ethylene: (a)  $\nu_1$  (lightly exposed spectrogram), (b)  $\nu_2$ , (c)  $\nu_3$ .

Two lines at 1613.9 and 1335.7  $\text{cm}^{-1}$  are interpreted as the *Q* branches of the  $\nu_2$  and  $\nu_3$  bands of the isotopic molecule  $\text{H}_2\text{C}^{12}=\text{C}^{13}\text{H}_2$ . These assignments rest on a visual estimation of the intensities and on a calculation using the system of five force constants derived by Wu (1939) for  $\text{C}_2\text{H}_4$ . The frequencies of  $\text{H}_2\text{C}^{12}=\text{C}^{13}\text{H}_2$  were determined from the force constants, and one-half of the deviations of these frequencies from those of the normal molecule were used as an approximation for the deviations of  $\text{H}_2\text{C}^{12}=\text{C}^{13}\text{H}_2$ . The agreement of the calculated frequencies, 1613.1 and 1333.7  $\text{cm}^{-1}$ , with those observed was considered satisfactory.

The weak maximum at 1605.8  $\text{cm}^{-1}$  is assigned to the overtone,  $2\nu_{10}$ , in Fermi resonance with  $\nu_2$ . This designation is indicated by the value 810.3  $\text{cm}^{-1}$  for  $\nu_{10}$ , as determined from the infrared spectrum by Arnett and Crawford (1950). The line at 1605.8  $\text{cm}^{-1}$  apparently corresponds to the line at

1602 cm.<sup>-1</sup> observed in the liquid and designated by Herzberg (1945) as an isotopic component.

On the high frequency side of  $\nu_2$  a peculiar band was observed with a maximum at 1662 cm.<sup>-1</sup> and an intensity degradation towards lower Raman shifts (Fig. 1(b)). A line corresponding to this frequency has been observed in the liquid and interpreted by Herzberg as  $2\nu_4$ ; however, this assignment must be incorrect if the value, 1027 cm.<sup>-1</sup>, proposed by Arnett and Crawford (1950) for  $\nu_4$  is accepted. The explanation of this band, which has an intensity at least one-quarter of the  $Q$  branch of  $\nu_2$ , appears to be an outstanding problem in the vibrational assignments in ethylene. Some of the spectrograms of the band showed traces of structure, and it is possible that with improved resolution more detail would be observed which would aid in identifying its origin.

The remaining, fainter lines in this region can be assigned to the rotational branches of the totally symmetric  $\nu_3$  band. The  $O$ ,  $P$ ,  $R$ , and  $S$  branches of the symmetric top approximation are readily identified (Fig. 1(c)). The Raman displacements of the  $O$  and  $S$  lines, plotted against the rotational angular momentum quantum number,  $J$ , yield a straight line of no noticeable curvature, so that centrifugal stretching terms can be neglected. An additional series, the  $O'$  and  $S'$  branches, is alternately in and out of step with the  $O$  and  $S$  series as the value of  $J$  increases; this gives the spectrum a characteristic appearance similar to that observed for the rotational spectrum (Romanko, Feldman, Stansbury, and McKellar 1954). The assignment of the lines and the analysis of the two series, in terms of the energy levels of the slightly asymmetric rotor, were carried out as for the rotational spectrum.

For a symmetric top, the rotational energy levels have the form

$$(1) \quad F(J, K) = BJ(J+1) + (A - B)K^2, \quad J, K = 0, 1, 2, \dots ; J \geq K$$

where each level for which  $K \neq 0$  is doubly degenerate. This degeneracy is removed in the asymmetric top, and for each value of  $J$  there are  $2J+1$  rotational sublevels,  $F(J_\tau)$ , where  $\tau = J, J-1, \dots, -J+1, -J$ , and  $\tau = -J$  is assigned to the lowest level. For a slight departure from the symmetric top the  $\tau$  levels can be identified with the  $K$  levels of the equivalent symmetric top and can be represented by (1) if  $B$  is replaced by  $\tilde{B} = (1/2)(B+C)$ .\* The  $O$ ,  $P$ ,  $Q$ ,  $R$ , and  $S$  branches indicated in Fig. 1(c) correspond to the transitions,  $\Delta J = 0, \pm 1, \pm 2$ ,  $\Delta K = 0$ , involving the higher  $\tau$  levels in the symmetric top approximation. As shown by Romanko *et al.* (1954), the  $O'$  and  $S'$  lines have their origin in the transitions,  $\Delta J = \pm 2$ , involving the two lowest  $\tau$  levels for each  $J$  value. For example, the  $S'(12)$  line arises from the superposition of two lines corresponding to the transitions  $14_{-14}-12_{-12}$  and  $14_{-13}-12_{-11}$ . The average energy of the lowest  $\tau$  levels can be adequately represented by

$$(2) \quad \frac{1}{2}[F(J_{-J}) + F(J_{-J+1})] = CJ^2 + \frac{1}{2}(A+B)J - \frac{1}{2}(A-B)J\{(2J-1)/(J-1)\}b^*\{1 + \frac{1}{4}b^{*2}\},$$

where  $b^* = (B-A)/2[C - \frac{1}{2}(A+B)]$  ( $= 0.910$  for  $C_2H_4$ ). This formula, given by Mecke (1933), can be derived from the series expansions of the eigenvalues of the asymmetric top calculated by Witmer (1926, 1927).

\*The nomenclature follows that of Herzberg (1945) and Romanko *et al.* (1954).

If calculated rotational terms for the ground state,  $F_0(J)$ , for which the molecular constants are known with a fair degree of accuracy, are combined with the observed frequency shifts,  $S(J)$ , etc., relations of the following type are obtained:

$$(3) \quad S(J) + F_0(J) = \nu_0 + \tilde{B}_1(J+2)(J+3),$$

$$(4) \quad S'(J) + \frac{1}{2}[F_0(J-J) + F_0(J-J+1)] = \nu_0 + C_1(J+2)^2 \\ + [\frac{1}{2}(A_1+B_1) - \frac{1}{4}(A_1-B_1)b_1^*(1+\frac{1}{4}b_1^{*2})](J+2) \\ - \frac{1}{8}(A_1-B_1)b_1^*(1+\frac{1}{4}b_1^{*2}),$$

where, in the latter expression,  $J/(J-1)$  has been taken to be equal to unity. For the ground vibrational state, the following values of the rotational constants were used:  $A_0 = 4.867$  (Gallaway and Barker 1942),  $B_0 = 1.008_5$ ,  $C_0 = 0.828_9$ , and  $\tilde{B}_0 = 0.9187 \text{ cm.}^{-1}$  (Romanko *et al.* 1954). A regression solution performed on 22  $O$  and  $S$  lines and on 19  $O'$  and  $S'$  lines yielded the values:  $\nu_0 = 1342.2$ ,  $\tilde{B}_1 = 0.920_5$ , and  $C_1 = 0.836_2 \text{ cm.}^{-1}$ . From these and the relation  $1/A = 1/C - 1/B$ , for planar molecules, the values  $A_1 = 4.51$  and  $B_1 = 1.004_8 \text{ cm.}^{-1}$  were obtained for the  $\nu_3$  band. However, since  $B_1$  and  $C_1$  are not very different, the calculated value of  $A_1$  cannot be considered accurate.

#### The 2800–3300 $\text{cm.}^{-1}$ Region

The  $Q$  branch of the  $\nu_1$  band at  $3020.5 \text{ cm.}^{-1}$  and the corresponding  $Q$  branch of the isotopic molecule,  $\text{H}_2\text{C}^{12} = \text{C}^{13}\text{H}_2$ , at  $3006.4 \text{ cm.}^{-1}$  were photographed with exposure times of a few hours (Fig. 1(a)). The calculated position of the

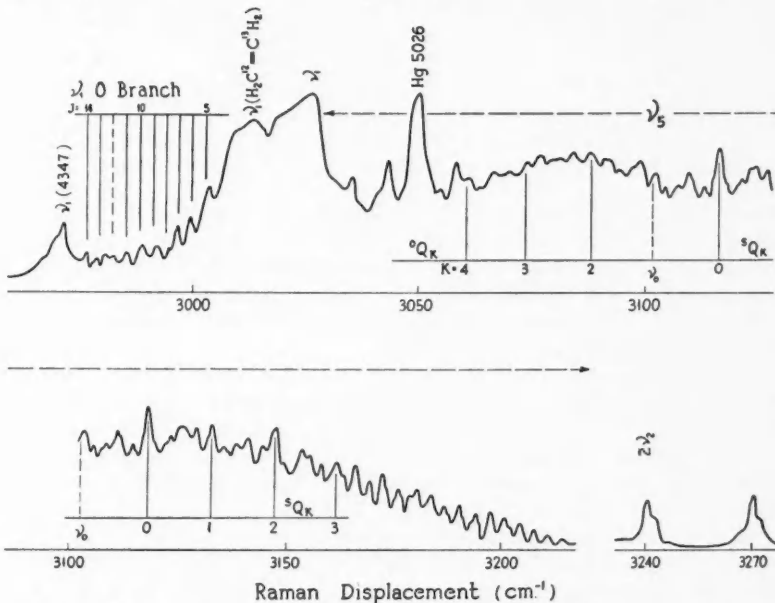


FIG. 2. Microphotometer trace of the  $2950$ – $3280 \text{ cm.}^{-1}$  region of the Raman spectrum of ethylene, showing the rotational structure of the  $\nu_1$  and  $\nu_5$  bands.

TABLE II  
RAMAN FREQUENCIES OF  $C_2H_4$  IN THE 2800-3300 CM.<sup>-1</sup> REGION

$\Delta\nu$ (cm. <sup>-1</sup> )	Assignment	$\Delta\nu$ (cm. <sup>-1</sup> )	Assignment
2880.8	$2\nu_{12}$	3113.2	
3020.7*	$\nu_1(Q_{\max})$	3118.3	$sQ_0$ ( $\nu_8$ band)
2972.8	$O(14)$ ( $\nu_1$ band)	3123.0	
2976.3	$O(13)$ ("")	3126.4	
2979.7	?	3129.8	
2982.8	$O(11)$ ("")	3133.3	$sQ_1$ ("")
2986.0	$O(10)$ ("")	3136.6	
2989.1	$O(9)$ ("")	3139.9	
2992.6	$O(8)$ ("")	3142.7	
2996.2	$O(7)$ ("")	3145.8	
2999.5	$O(6)$ ("")	3148.7	$sQ_2$ ("")
3002.8	$O(5)$ ("")	3150.8	
3006.4	$\nu_1(H_2C^{12}=C^{13}H_2)$	3155.3	
3020.3	$\nu_1(Q_{\max})$	3158.7	
3025.5		3160.1	
3029.9		3163.5	$sQ_3$ ("")
3035.3		3165.6	
3039.2		3168.1	
3050.8		3170.5	
3055.1	${}^oQ_4$ ( $\nu_8$ band)	3173.6	
3058.6		3177.8	
3065.3		3181.8	
3062.7		3185.8	
3070.3	${}^oQ_3$ ("")	3188.3	
3074.1		3190.6	
3078.9		3193.3	
3084.1		3197.7	
3086.4	${}^oQ_2$ ("")	3201.1	
3089.7		3204.7	
3094.3		3208.3	
3097.7		3211.7	
3102.3		3214.8	
3105.7		3219.2	
3109.1		3240.5	$2\nu_2$
3110.5		3271.9	?

\*Excited by Hg4347.

isotopic band was 3008.5 cm.<sup>-1</sup>. With exposure times approaching 100 hr. considerable structure was observed throughout the region (Fig. 2, Table II). Previous assignments of the lines at 3240.5 and 2880.8 cm.<sup>-1</sup> as  $2\nu_8$  and  $2\nu_{12}$ , respectively, in Fermi resonance with  $\nu_1$ , are undoubtedly correct. The line at 3271.9 cm.<sup>-1</sup> can perhaps be identified as the combination tone of  $\nu_2$  and the unexplained frequency at 1662 cm.<sup>-1</sup>.

The remaining lines constitute the rotational structures of the  $\nu_1$  and  $\nu_8$  bands. Although these structures overlap to some extent, the lines in the 2970-3000 cm.<sup>-1</sup> region, with an average spacing of 3.4 cm.<sup>-1</sup>, can be identified as members of the  $O$  branch of the  $\nu_1$  band. From the slope of the straight line, which results when the Raman shifts are plotted against consecutive integers, the value  $\bar{B}_1 = 0.839$  cm.<sup>-1</sup> is obtained. The comparatively large value of  $\bar{B}_1 - \bar{B}_0 (= -0.080$  cm.<sup>-1</sup>) explains the marked intensity degradation of the  $Q$  branch towards lower frequency shifts (Fig. 1(a)), and can perhaps be interpreted in terms of a Coriolis interaction of  $\nu_1$  with  $\nu_8$ . To obtain the absolute numbering of the  $O$  lines, and hence the band origin  $\nu_0$ , the the-

oretical intensity contour of the  $Q$  branch was calculated and compared with the experimental contour. This procedure established with fair certainty the assignments of the  $O$  lines given in Table II and gave  $\nu_0 = 3026.4 \text{ cm}^{-1}$ .

The  $\nu_6(b_{1g})$  vibration follows the selection rule  $\Delta K = \pm 2$ . In the symmetric top approximation the band consists of a number of subbands, each corresponding to a given  $K$  and consisting of  $O_K(J)$ ,  $P_K(J)$ ,  $Q_K(J)$ ,  $R_K(J)$ , and  $S_K(J)$  branches. If  $B_1 - B_0$  is sufficiently small the  ${}^0{}^S Q_K$  branches form a series of lines at the origins of the subbands, whose frequencies are given by

$$(5) \quad \nu_0^{\text{sub}} = \nu_0 + 4(A_1 - B_1) \pm 4(A_1 - B_1)K + [(A_1 - B_1) - (A_0 - B_0)]K^2.$$

Since, for  $\Delta K = -2$ , the smallest value of  $K$  is 2, there is a missing line,  ${}^0{}^S Q_1$ , at the band origin  $\nu_0$ . The relative intensities of the  $Q_K$  branches were calculated in the symmetric top approximation using the matrix elements derived by Placzek and Teller (1933) and the statistical weights of Wilson (1935). A careful comparison of these intensities with the lines observed on four spectrograms of different exposure strengths yielded the  $K$ -numbering of the  $Q$  branches given in Table II. Assuming the values of the molecular constants in their ground state, the observed frequencies of seven  ${}^0{}^S Q_K$  branches were fitted to equation (5) and the constants  $\nu_0 = 3102.5$ ,  $(A_1 - B_1) = 3.87 \text{ cm}^{-1}$  were obtained.

On the high frequency wing of the band a fairly well defined series of lines with a spacing  $\sim 4.0 \text{ cm}^{-1}$  was observed (Fig. 2). This series can probably be explained as an accidental superposition of  $S_K(J)$  lines from different subbands, since the spacing of the origins of the subbands,  $4(A_1 - B_1) = 15.6 \text{ cm}^{-1}$ , is approximately four times the spacing of the  $S_K(J)$  lines,  $5B_1 - B_0$ . The lines cannot be given specific designations, nor can they be used to determine molecular constants. In this interpretation  $5B_1 - B_0$  is approximately equal to  $3.7 \text{ cm}^{-1}$ , and it follows that  $B_1 - B_0$  is positive as would be expected from the Coriolis interaction between  $\nu_1$  and  $\nu_6$ , which was postulated above.

The frequencies of the Raman active vibrations of ethylene are summarized in Table III.

TABLE III  
THE RAMAN ACTIVE FUNDAMENTALS OF  $C_2H_4$

Designation	Species	Selection rule	Frequency ( $\text{cm}^{-1}$ )
$\nu_1$	$a_{1g}$	$\Delta K = 0$	3026.4 ( $\nu_0$ )
$\nu_2$	$a_{1g}$	$\Delta K = 0$	1622.6 ( $Q_{\text{max}}$ )
$\nu_3$	$a_{1g}$	$\Delta K = 0$	1342.2 ( $\nu_0$ )
$\nu_5$	$b_{1g}$	$\Delta K = \pm 2$	3102.5 ( $\nu_0$ )
$\nu_6$	$b_{1g}$	$\Delta K = \pm 2$	1236 (liquid)*
$\nu_6$	$b_{3g}$	$\Delta K = \pm 1$	950†

\*Rank, Shull, and Axford (1950).

†Stoicheff (1953).

#### REFERENCES

- ARNETT, R. L. and CRAWFORD, B. L., JR. 1950. J. Chem. Phys. 18: 118.  
 BHAGAVANTAM, S. 1936. Nature, 138: 1096.  
 DICKINSON, R. G., DILLON, R. T., and RASETTI, F. 1929. Phys. Rev. 34: 582.

- GALLAWAY, W. S. and BARKER, E. F. 1942. *J. Chem. Phys.* **10**: 88.  
HERZBERG, G. 1945. Molecular spectra and molecular structure. Vol. II. Infrared and Raman spectra of polyatomic molecules. D. Van Nostrand Company, Inc., N.Y.  
MECKE, R. 1933. *Z. Physik*, **81**: 313.  
PLACZEK, G. and TELLER, E. 1933. *Z. Physik*, **81**: 209.  
RANK, D. H., SHULL, E. R., and ALEXANDER, D. W. E. 1950. *J. Chem. Phys.* **18**: 116.  
ROMANKO, J., FELDMAN, T., STANSBURY, E. J., and MCKELLAR, A. 1954. *Can. J. Phys.* **32**: 735.  
STOICHEFF, B. P. 1953. *J. Chem. Phys.* **21**: 755.  
WELSH, H. L., STANSBURY, E. J., ROMANKO, J., and FELDMAN, T. 1955. *J. Opt. Soc. Amer.* **45**: 338.  
WILSON, E. B., JR. 1935. *J. Chem. Phys.* **3**: 276.  
WITMER, E. E. 1926. *Proc. Natl. Acad. Sci. U.S.* **12**: 602.  
——— 1927. *Proc. Natl. Acad. Sci. U.S.* **13**: 60.  
WU, T. Y. 1939. Vibrational spectra and structure of polyatomic molecules. University Press, Kunming, China.

# CROSS SECTIONS OF $(p, xn)$ REACTIONS IN THE ISOTOPES OF LEAD AND BISMUTH<sup>1</sup>

BY R. E. BELL<sup>2</sup> AND H. M. SKARSGARD<sup>3</sup>

## ABSTRACT

Measurements have been made by the activation method of cross sections of  $(p, xn)$  reactions in  $\text{Bi}^{209}$ ,  $\text{Pb}^{206}$ ,  $\text{Pb}^{207}$ , and  $\text{Pb}^{208}$ . The present results cover  $x = 3$  to 7 in  $\text{Bi}^{209}$ , 2 to 6 in  $\text{Pb}^{206}$ , 2 to 4 in  $\text{Pb}^{207}$ , and 3 and 4 in  $\text{Pb}^{208}$ , over a total proton energy range from 12 to 85 Mev. The absolute accuracy is about 15%. Each cross section plotted as a function of proton energy rises above its threshold to a peak whose height is of the order of one barn, and then falls again to a low and fairly constant value. The results from  $x = 3$  to 7 are consistent with a compound nucleus plus prompt nucleon-nucleon cascade model using reasonable nuclear parameters, but the experimental  $(p, 2n)$  cross section appears to be almost double the value so predicted. Since  $(p, xn)$  reactions are dominant in the energy range 10 to 40 Mev., their sum approximates the total reaction cross section; the experimental sum fluctuates around the smooth curve computed for the compound nucleus model with  $r_0 = 1.3 \times 10^{-13}$  cm. The fluctuations are similar to, but more marked than, those in the total neutron cross section of heavy elements in the same energy range. A more detailed theoretical discussion of these results is given by Jackson in the paper immediately following.

## INTRODUCTION

This paper reports the results of measurements of cross sections of  $(p, xn)$  reactions in  $\text{Bi}^{209}$  and  $\text{Pb}^{206}$ , and with less detail in  $\text{Pb}^{207}$  and  $\text{Pb}^{208}$ . The proton bombardments were made in the circulating beam of the McGill synchrocyclotron, the beam intensity being monitored through known cross sections in  $\text{Cl}^{12}$  and  $\text{Cu}^{63}$ . Measurements were made over the proton energy range 12 to 85 Mev. The values of the  $(p, xn)$  cross sections were obtained by absolute counting of the electron capture activities produced in the various reactions. The object of the work was to collect a body of data as a test of nuclear models. The energy range covered is an interesting one, because it is here that the compound nucleus formation characteristic of low energy reactions begins to be replaced by the direct nucleon-nucleon cascade processes characteristic of high energy reactions. The present results have also proved useful in this laboratory in identifying reactions in other heavy nuclei by comparing their yield curves with those found here. Some of the results on  $\text{Bi}^{209}$  and  $\text{Pb}^{206}$  have already been reported in brief (Bell 1954; Bell and Skarsgard 1955).

Previous measurements of  $(p, xn)$  cross sections in heavy elements have been confined to proton bombardment energies below 32 Mev. or above about 70 Mev., and few absolute values are given. Kelly (1950) measured the  $(p, 2n)$  cross section in  $\text{Bi}^{209}$  over the energy range 9 to 32 Mev., and also measured the shape (but not the absolute magnitude) of the  $(p, n)$  and  $(p, 3n)$  cross section curves as a function of energy. Qualitatively, the cross sections appear characteristic of the shapes expected from compound nucleus theory. As the proton

<sup>1</sup>Manuscript received May 3, 1956.

Contribution from the Radiation Laboratory, Physics Department, McGill University, Montreal, Quebec.

<sup>2</sup>Staff Member, Atomic Energy of Canada Limited, Chalk River, Ontario.

<sup>3</sup>Now at Reactor Research Division, Atomic Energy Research Establishment, Harwell, England.

bombardment energy is raised above the threshold for a particular ( $p, xn$ ) reaction, the cross section rises rapidly to a peak and then falls almost equally rapidly above the threshold for the next higher reaction ( $p, (x+1)n$ ). The magnitude of Kelly's result for ( $p, 2n$ ) was interpreted to indicate a nuclear radius corresponding to  $r_0 = 1.43 \times 10^{-13}$  cm. Andre *et al.* (1954, 1956) have also measured the ( $p, n$ ) and ( $p, 2n$ ) cross sections in Bi<sup>209</sup> for energies ranging up to 10.6 Mev., deducing a nuclear radius parameter  $r_0 = 1.5 \times 10^{-13}$  cm. Their paper includes data showing that Kelly's assumed normalization for the ( $p, n$ ) cross section is essentially correct. Karraker (1951) measured the shapes of ( $p, xn$ ) cross section curves in Bi<sup>209</sup> for  $x = 2, 4, 6$ , and 8 at high energies (70 to 345 Mev.). Again the absolute cross section was measured only for ( $p, 2n$ ), and the energies used were too high to display the main cross section peaks for any except the ( $p, 8n$ ) cross section. The ( $p, n$ ) and ( $p, 3n$ ) cross sections have been measured for Th<sup>232</sup> and U<sup>238</sup> at various energies up to 32 Mev. by Tewes (1955) and McCormick and Cohen (1954). In these cases the interpretation is complicated by the presence of large amounts of proton-induced fission.

Kelly (1950) (see also Kelly and Segre 1949) has also measured the ( $\alpha, 2n$ ) and ( $\alpha, 3n$ ) cross sections in Bi<sup>209</sup> at energies up to 30 Mev., and the ( $d, p$ ), ( $d, n$ ), ( $d, 2n$ ), and ( $d, 3n$ ) cross sections up to 19 Mev. John (1955) has measured some ( $\alpha, xn$ ) cross sections in the isotopes of lead at energies up to 48 Mev.

Measurements made on medium- and light-weight elements are more extensive but of less interest here, except where they provide comparison cross sections for monitoring. Of these the most important is the C<sup>12</sup>( $p, pn$ )C<sup>11</sup> cross section, whose value from threshold at 19 Mev. up to 340 Mev. was reported by Aamodt *et al.* (1952); this work represents the combined efforts of a number of experimenters. A revision of the values of Aamodt *et al.* (1952) has been published by Crandall *et al.* (1956), in which improved foil stack techniques and the use of  $4\pi$  counting of activities enabled these workers to quote a standard error for the C<sup>12</sup>( $p, pn$ ) cross section of about 5%. These results have been used throughout the present work for beam monitoring. Ghoshal (1950) measured ( $p, n$ ), ( $p, 2n$ ), and ( $p, pn$ ) cross sections in Cu<sup>63</sup>, as well as ( $\alpha, n$ ), ( $\alpha, 2n$ ), and ( $\alpha, pn$ ) cross sections in Ni<sup>60</sup>. Ghoshal's work was intended as a test of the compound nucleus model rather than as an accurate absolute cross section measurement, and we believe that his values for the Cu<sup>63</sup>( $p, n$ ) and ( $p, pn$ ) reactions are about 40% high. The same cross sections have been measured in Cu<sup>63</sup> by Meadows (1953) with results agreeing with this conclusion. These copper cross sections were used as secondary standard monitors in some of the present measurements.

Some workers have pointed out that in light elements the ( $p, pn$ ) cross section is comparable with or higher than the ( $p, 2n$ ) cross section, in spite of the inhibition on proton emission due to the potential barrier (Ghoshal 1950; Cohen and Newman 1955). This tendency is expected to disappear rapidly as the  $Z$  of the target nucleus is raised; experimentally the ratio of ( $p, pn$ ) to ( $p, 2n$ ) cross sections averaged over  $Z = 22$  to 29 has dropped by nearly a factor of 10 by the time we reach the range  $Z = 30$  to 33 (Cohen and Newman

1955). Throughout the present work we assume that near the peak of any  $(p, xn)$  cross section the  $(p, p(x-1)n)$  cross section is small in comparison. At several points in our work this conclusion is checked by measurement, though no accurate measure of the smaller cross section was obtained.

#### IRRADIATION PROCEDURE

The targets consisted of thin metallic foils or electroplated metallic deposits up to 80 mgm./cm.<sup>2</sup> in thickness, cut in strips  $\frac{1}{4}$  in. wide. Each target was irradiated together with a monitor foil (usually 25 mgm./cm.<sup>2</sup> teflon) cut to the same shape so that the same proton beam passed through both. The pair of foils was attached to the end of the main radial probe of the cyclotron so as to intercept the circulating proton beam at any desired radius. The small attenuation of the proton beam in passing through the foils was neglected, but allowance was made for the degradation in proton energy (order of 1 Mev.). Tests showed that placing the teflon monitor foil in front of or behind the target foil gave the same result to within 5%. In most cases the foils were backed by a copper block thick enough to stop the proton beam, but no appreciable change was found when this block was omitted.

The isotopic compositions of the target materials employed are shown in Table I. In this table the column headed Lead 206 refers to a radiogenic lead originally supplied by Eldorado Mining and Refining (1944) Limited, which was available in gram quantities. Most of the measurements were made using natural Bi<sup>209</sup> and this lead. The columns headed Lead 207 and Lead 208 refer

TABLE I  
ISOTOPIC COMPOSITION (IN ATOMIC PERCENT) OF THE TARGET MATERIALS

Mass No.	Bismuth	Natural lead	Lead 206	Lead 207	Lead 208
204	—	1.48	—	0.119	0.069
206	—	23.6	88.2	7.73	1.99
207	—	22.6	8.7	61.06	9.97
208	—	52.3	3.04	31.09	87.97
209	100	—	—	—	—

to electromagnetically enriched lead samples of 40 mgm. each (as PbO) supplied by Oak Ridge. Four targets of each of Lead 207 and Lead 208 were prepared by electroplating metallic lead onto 1 mil copper foils. The Pb<sup>207</sup> and Pb<sup>208</sup> cross sections were measured in these foils by repeatedly using the same targets, allowing the induced activities to decay each time. On account of the lower enrichment of these targets and the extra time necessary for measurement, the results for Pb<sup>207</sup> and Pb<sup>208</sup> are less extensive and possibly somewhat less accurate than those in Bi<sup>209</sup> and Pb<sup>206</sup>. Some measurements were also made on the Pb<sup>207</sup>( $p, 2n$ ) cross section using targets of natural lead in a narrow energy range near 20 Mev. where the other lead isotopes did not interfere.

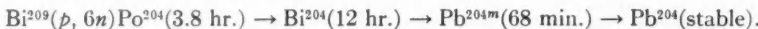
A summary of the method of depositing the electroplated targets and of calibrating them for thickness is given in Appendix I.

The targets were bombarded at a proton beam of about 0.1  $\mu\text{a}$ . (reduced from the normal cyclotron beam of 1 to 2  $\mu\text{a}$ . to avoid overheating) for periods of from one to five minutes. The proton energy incident on the target was varied by bombarding at different radii. The basic data for computing the effective proton energy as a function of radius, and the spread in energy, were drawn from a McGill internal report by Kirkaldy (1953). Some small modifications to the energy values so obtained were made on the basis of monitor measurements described later.

#### MEASUREMENT OF ABSOLUTE ELECTRON CAPTURE RATES

All the products of  $(p, xn)$  reactions in the isotopes of lead decay by electron capture; in the case of  $\text{Bi}^{209}$ , the products for  $x > 2$  sometimes show an  $\alpha$  branching that is either known or small. The lifetimes and many of the radiation characteristics of these products are well known (Hollander *et al.* 1953). The half lives range from a few minutes to a few days. It was therefore possible to identify the various activities by pulse analysis and decay analysis alone, without recourse to chemical separations. The decay analysis was aided by the use of computed growth and decay curves. Chemical separation would have been out of the question in any case for the  $\text{Pb}^{207}$  and  $\text{Pb}^{208}$  samples, where only 40 mgm. of material was available.

The absolute yield of any particular  $(p, xn)$  product activity was usually based upon the initial activity of  $K$  X-rays following  $K$ -capture. In some cases, however, it was necessary to work on daughters and granddaughters of the activities produced in the original  $(p, xn)$  reactions, and this introduces the following slight complication, illustrated by an example. The  $(p, 6n)$  reaction in  $\text{Bi}^{209}$  produces the following decay chain:



If measurements are made on the  $\text{Bi}^{204}$  daughter, it must be kept in mind that  $\text{Bi}^{204}$  can be produced directly by the  $(p, p5n)$  reaction (which has approximately the same energetic threshold as the  $(p, 6n)$  reaction), as well as by decay from the  $(p, 6n)$  reaction product. The cross section indicated by the yield of  $\text{Bi}^{204}$  is therefore that of  $(p, 6n) + (p, p5n)$ . If measurements are made on the  $\text{Pb}^{204}$  granddaughter, the cross section is that of  $(p, 6n) + (p, p5n) + (p, 2p4n)$ . The evidence of our measurements is that these added cross sections are small, at least near the peak of a particular  $(p, xn)$  cross section.

The activities of the target foils were examined with sodium iodide scintillation counters in conjunction with single-channel pulse analyzers (in the earlier part of the work) or a 28-channel analyzer (in the later stages). The scintillation counter used in most of the work was a 1½ in. diameter  $\times$  1 in. high sodium iodide crystal, with a resolution width of 9% for the  $\text{Cs}^{137}$  662 kev. photopeak. The efficiency of this counter for counting full energy pulses for gamma rays of different energies was measured as a function of distance from source to crystal, using sources of known strength.\* (In counting  $K$  X-rays

\*We are indebted to Dr. L. Yaffe and his group for supplying us with sources calibrated by  $4\pi$  counting.

the pulses in the iodine X-ray escape peak are reckoned as full energy pulses.) The Oak Ridge group (McGowan 1954a, 1954b; Bell 1955) has given curves of efficiency for a similar counter, both measured and computed; for energies below 0.1 Mev. their results were used for the present counter. Many of the results on  $\text{Bi}^{209}$  were obtained by counting  $K$  X-rays with a 1/16 in. thick crystal whose efficiency for X-rays was determined by solid angle calculations and shown to be in good agreement with the data of McGowan for a 1 in. thick crystal. This result is expected, since at this low energy the X-rays are absorbed in a thin surface layer of the crystal, and the efficiency of the counter is equal to the fractional solid angle that it subtends at the source.

Since there were usually two or three reaction products present in an active sample, it was difficult at some bombarding energies to analyze the gross X-ray decay curve into its several components. In such cases a suitably chosen gamma ray could be used as an indicator of the relative yield of a reaction product; the results so found were normalized to the absolute value measured by the  $K$  X-rays at some bombardment energy where the decay situation was clearer. In several cases the absolute intensity of some gamma ray in a decay scheme was known; in these cases a separate absolute cross section could be computed as a check on the one measured through the X-rays. In most cases a single bombardment yielded cross sections for two or three reactions.

The measured counting rate of  $K$  X-rays from a sample, together with the  $K$  X-ray efficiency of the counter, yields the total rate of emission of  $K$  X-rays from that sample, whereas what is desired is the total electron capture rate in the sample. To arrive at the latter figure from the former involves the following corrections:

(i)  *$K$  fluorescent yield.*—A compilation by Bergstrom (1955) gives a value  $\omega_K = 0.95$  for the  $K$  fluorescent yield of lead and bismuth. The measured counting rates are divided by this factor.

(ii) *Self-absorption in the sample.*—The greatest sample thickness used was 80 mgm./cm.<sup>2</sup> The measured attenuation of lead (bismuth)  $K$  X-rays by a lead (bismuth) foil of this thickness was 14%; assuming that the effective attenuation thickness for a source distributed within the foil is one half the total thickness, the correction to be applied is 7%. This figure agrees well with that computed from tabulated X-ray absorption coefficients. The correction for thinner samples is proportionately smaller.

(iii) *Ratio of  $K$  to total electron capture.*—In order to compute accurately the fraction of the total electron captures that proceed *via* the  $K$  shell, it is necessary to know the disintegration energy of the electron capture process and its order of forbiddenss. Fortunately the variation of the  $K$  to total ratio with these factors is slow except near the energetic threshold for electron capture. We have assumed that all our electron capture processes are first forbidden, and have taken the energy difference  $W_0$  between the disintegrating nucleus and its daughter nucleus as  $mc^2$  (a disintegration energy just equal to the threshold energy for positron emission). With these assumptions the  $K$  to total capture ratio is found from the computations of Brysk and Rose (1955)

to be 1: 1.33. With a typical  $\log ft$  value of 7.0, our assumptions correspond to a half life of six days. Since most of the half lives encountered in this work were less than six days, most of the disintegration energies are likely to be higher than that assumed here. To show how insensitive the  $K$  to total capture ratio is to the energy assumption, we may take a trial energy difference  $W_0$  of  $5mc^2$  (instead of just  $mc^2$  as above); the  $K$  to total capture ratio then is found to be 1: 1.275, differing from the adopted value by only 4%. The non-observation of positrons in these activities means that the energy cannot be much higher than  $5mc^2$ . If in fact some of the electron capture processes are allowed rather than first forbidden, we must assume a somewhat lower disintegration energy in order to fit with a  $\log ft$  value of, say, 5.5; the  $K$  to total capture ratio is then almost identical with that assumed above. Further assurance that this factor cannot cause a large error lies in the fact that in several cases cross sections calculated from X-rays agreed within 5 or 10% with those calculated from gamma rays of known intensity in the same activity. In addition, Wapstra *et al.* (1954) have measured the  $K$  to total electron capture ratio in one of the activities involved in the present work,  $Pb^{203}$ ; their value of 1:  $1.34 \pm 0.1$  is in excellent agreement with the value adopted here. A measurement has also been made in the present work of the intensity of  $L$  X-rays emitted by 14.5 day  $Bi^{205}$ , the activity that seems *a priori* most likely to have a low disintegration energy and hence a large capture rate from the  $L$  shell. This method is of very low accuracy, since a large intensity of  $L$  X-rays is expected in any case, and the results showed only that the assumed  $K$  to total ratio of 1.33 is not grossly wrong for this activity.

(iv) *Internal conversion X-rays.*—An error in any of the measured ( $p, xn$ ) cross sections might have been caused by ignoring the possible presence in the radioactivity being measured of abundant gamma rays highly converted in the  $K$  shell, and hence of excess  $K$  X-rays. This error is expected to be small on the average but could be large in particular cases. The most likely kind of offender would be a low energy  $M1$  gamma ray of high abundance. The occurrence of this effect would be shown by the presence of suitable gamma rays in the source, and in particular by the emission from the source of  $K$  X-rays in coincidence with the  $K$  X-rays from  $K$ -capture. Indeed, the latter fact enables a correction factor to be measured, for if such a source is brought close to a sodium iodide counter there is an appreciable chance of detecting two  $K$  X-rays simultaneously. In such a single-counter coincidence experiment, a measurement of the intensity of the sum peak relative to that of the single  $K$  X-ray peak in the pulse height spectrum, together with a knowledge of the counter efficiency, gives at once the required correction factor. These sum peak measurements have been made for nearly all the activities involved in this study. The "summing corrections" found are usually fairly small, ranging from 3 to 15%; in one case, however, the result was 27%, and in another questionable case 35%. The activity giving the 27% result was  $Bi^{204}$  (12 hr.) produced in the reactions  $Bi^{209}(p, 6n)Po^{204}$  (3.8 hr.)  $\rightarrow Bi^{204}$ ,  $Pb^{206}(p, 3n)Bi^{204}$ ,  $Pb^{207}(p, 4n)Bi^{204}$ , and  $Pb^{208}(p, 5n)Bi^{204}$ . The well-known abundant 217 kev. gamma ray is probably responsible. In two other cases, gamma ray

intensities and  $K$  conversion coefficients are known and the measured summing correction could be checked. The agreement was within 2% in both cases.

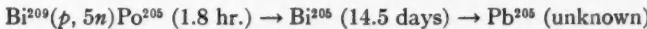
The following paragraphs give details of the absolute counting procedures involved in the determination of each cross section.



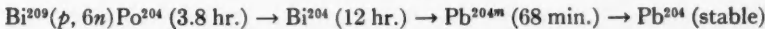
This was the reaction with the lowest  $x$  value observed in bismuth, because  $(p, n)$  and  $(p, 2n)$  both produce  $\alpha$  emitters. The  $K$  X-ray decay curve showed a clean 5.7 hr. half life at all bombarding energies where this activity was the main short-lived one (20–40 Mev.). The cross section was calculated from the  $K$  X-ray rate with a measured summing correction of 9%. At two points above 40 Mev. a gamma ray was used for relative yields. The  $\alpha$  branching here is only about 10<sup>-2</sup>%.



The nine-day decay and six-day growth of the  $K$  X-ray peak gives a total activity curve that stays almost constant for several days and then tails off into a nine-day decay. In order to identify this activity properly it was necessary to wait for shorter lived activities to die, so that effectively this cross section was measured mainly through the radiations of the 6.2 day  $\text{Bi}^{206}$  daughter. This radioactivity is very rich in gamma rays and also contains a 145  $\mu$ sec. metastable state. Fortunately it has been studied in detail by Alburger and Pryce (1954), who give the number of  $K$  X-rays emitted per disintegration as 1.45. There is also a group of gamma rays of between 800 and 900 kev. energy that appears as a single peak in the sodium iodide spectrum, and whose total intensity is given as 1.75 per disintegration. Both features of the decay were used in computing cross sections, with agreement within 5%. Since this cross section is estimated largely from a daughter activity, it includes most of the  $(p, p3n)$  cross section as well as the  $(p, 4n)$ . The 9 day parent has a 10%  $\alpha$  branching to an undetected lead isotope; the cross section must be corrected upwards 10% on this account.

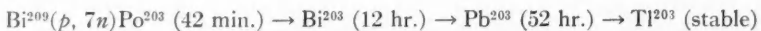


The published value of the half life of  $\text{Po}^{205}$  is 1.5 hr., but our decay curves consistently show a value between 1.7 and 1.9 hr., averaging 1.8 hr. The cross section was computed from the  $K$  X-ray rate only, using a measured summing correction of 8%. The  $\alpha$  branching is only 0.074%.

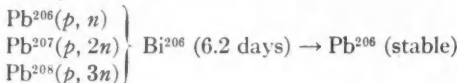


The  $K$  X-ray activity for this chain straightens out after a few hours into the 12 hr. daughter half life with which the 68 min.  $\text{Pb}^{204m}$  granddaughter is in equilibrium. The cross section can be computed from the  $K$  X-ray counting rate using a measured summing correction of 27% (mentioned earlier) plus a 10% correction for  $K$  X-rays arising from internal conversion in  $\text{Pb}^{204m}$ . The  $\text{Pb}^{204m}$  isomer is now well understood (Bergstrom and Wapstra 1955; Krohn and Raboy 1954), and it is agreed that its radiations consist of a cascade of the following three gamma rays in order: 913 kev. ( $E5$ ), 374 kev. ( $E2$ ), and

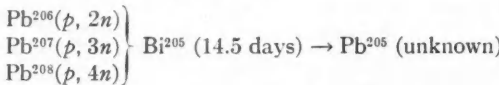
899 kev. (*E*2). The computed *K* conversion coefficients corresponding to these three gamma rays are respectively 5.85, 4.1, and 0.71% (Rose 1955), yielding the 10% correction mentioned above. The 374 kev. gamma ray was used in following the shape of the cross section above its peak; the 12 hr. *K* X-rays cannot be used here because of interference from another 12 hr. period, Bi<sup>203</sup>, produced by (*p*, 7*n*). The *K* X-ray yield measures (*p*, 6*n*) + (*p*, *p*5*n*) while the gamma ray yield measures (*p*, 6*n*) + (*p*, *p*5*n*) + (*p*, 2*p*4*n*). In the later work on the lead isotopes, the 374 kev. gamma ray was used to evaluate absolute cross sections (see below).



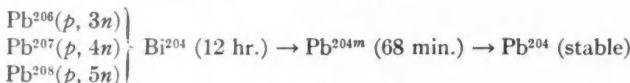
The published value for the half life of Po<sup>203</sup> is 47 min., but our decay curves indicate a value close to 42 min. Below the threshold of the (*p*, 8*n*) reaction the cross section was evaluated from the *K* X-ray rate. No summing correction has been measured for this activity. Above the threshold of the (*p*, 8*n*) reaction a 52 min. activity, Po<sup>202</sup>, enters the decay curves, and the shape of the (*p*, 7*n*) cross section curve had to be followed through the 279 kev. gamma ray in the 52 hr. Pb<sup>203</sup> granddaughter, the values being normalized to the X-ray results at lower energies. Here the X-ray results measure (*p*, 7*n*) while the gamma ray results measure (*p*, 7*n*) + (*p*, *p*6*n*) + (*p*, 2*p*5*n*).



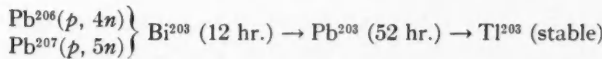
The cross sections were evaluated from the *K* X-rays and gamma rays of Bi<sup>206</sup> as discussed above under Bi<sup>209</sup>(*p*, 4*n*). In this case there is of course no correction for  $\alpha$  branching.



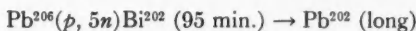
The *K* X-ray activity was used exclusively for evaluating these cross sections. Since the 14.5 day half life was the longest encountered in this work with appreciable intensity, it was only necessary to wait until other activities had decayed to get a very clean decay curve. This fact was used to measure the Pb<sup>206</sup>(*p*, 2*n*) cross section over a wide range of energies above its peak. The measured summing correction was 5%.



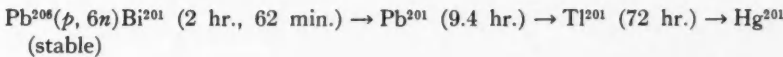
The situation here is the same as that listed under Bi<sup>209</sup>(*p*, 6*n*) except that there is no 3.8 hr. parent preceding the 12 hr. Bi<sup>204</sup> in this case. Cross sections were evaluated both from *K* X-rays and from the 374 kev. gamma ray of Pb<sup>204m</sup>, with agreement within 5%. In Pb<sup>208</sup> the X-rays measure (*p*, 3*n*) and the gamma rays measure (*p*, 3*n*) + (*p*, *p*2*n*); the agreement shows that (*p*, *p*2*n*) is small compared with (*p*, 3*n*). Similar remarks apply for Pb<sup>207</sup> and Pb<sup>208</sup>.



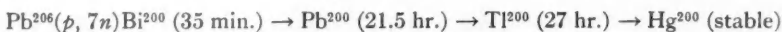
Owing to the presence of 12 hr. Bi<sup>204</sup> from the next lower reaction, it was impossible to determine these cross sections directly from the 12 hr. decay of Bi<sup>203</sup> K X-rays. The cross section was therefore evaluated from the K X-rays of the 52 hr. daughter activity remaining after the decay of the 12 hr. activities. The well-known 279 kev. gamma ray accompanying the disintegration of Pb<sup>203</sup> is the same as that observed in the disintegration of Hg<sup>203</sup>, the gamma transition occurring in Tl<sup>203</sup>. The earlier published conversion coefficients for this gamma ray ranged around the values  $\alpha_K = 0.23$ ,  $\alpha_T = 0.30$ , which would give a computed summing correction of 18%. The measured summing correction was 12%, and it was only through the use of the latter figure that reasonable agreement was secured between absolute cross sections computed from K X-rays and those computed from the 279 kev. gamma rays. This check is more effective than it appears from these figures, because internal conversion effectively takes counts out of the gamma ray peak and adds them to the K X-ray peak, thus doubling any discrepancy. The measured 12% summing correction would correspond to  $\alpha_K = 0.14$  instead of 0.23 given above. For some time the difference was considered serious enough to cast doubt on the identity of the gamma rays from Pb<sup>203</sup> and Hg<sup>203</sup>. Now, however, Wapstra *et al.* (1954) have remeasured the conversion coefficient as  $\alpha_K = 0.14$  in satisfactory agreement with the value deduced from the summing measurement. The gamma ray evidence gave cross sections about 10% higher than the K X-rays. The X-ray results have been used for the quoted cross sections.



Absolute yields were computed from the 95 min. K X-ray activity. A gamma ray peak at about 0.43 Mev. helped to determine relative yields at energies above the (p, 6n) cross section where periods similar to 95 min. are produced. The summing correction measured for this activity is relatively large, 35%, and uncertain owing to the short half life of the activity and especially to what appears to be a gamma ray near the sum peak (0.17 Mev.). This gamma ray and one at 0.23 Mev. are undoubtedly responsible for the apparently large value obtained for the summing correction. On this account the Pb<sup>206</sup>(p, 5n) cross sections have relatively low accuracy.



The value of this cross section was determined from the 72 hr. K X-ray decay of the granddaughter Tl<sup>201</sup>. The summing correction was measured as 15% with low accuracy because of the presence of other long lived activities in the source. Fortunately the result can be verified from the measurements of Bergkvist *et al.* (1955) on the relative K conversion intensities of the 0.135 and 0.167 Mev. M1 gamma rays; their result gives a summing correction of 17%. Since a granddaughter activity is being measured, the cross section is actually that of (p, 6n)+(p, 5n)+(p, 2p4n).



A single determination of this cross section was made at 64 Mev., using the 35 min. K X-ray activity. No summing correction was applied.

#### PROTON BEAM MONITORING

The energy of the proton beam of the McGill synchrocyclotron has been studied as a function of radius by Kirkaldy (1953). The nominal or synchronous energy of a proton at a given radius is easily calculated from the value of the magnetic field, but in fact the existence of radial oscillations in the proton orbits makes it possible for a proton in an orbit of smaller radius of curvature to reach a given cyclotron radius. The mean amount of this effect, according to Kirkaldy's measurements, is the equivalent of about one inch in radius. The energy spread of the proton beam is given by Kirkaldy as the equivalent of about 1.5 in. in radius (corresponding to about 4 Mev. at 20 Mev. mean energy and about 5.5 Mev. at 50 Mev.). These results were used to give a basic energy scale. In the energy region 15 to 30 Mev., some auxiliary measurements described later in this section seemed to show that the energies computed in the way just described are slightly low, i.e. that the effect of the radial oscillations has been slightly overestimated. Accordingly, the energy values adopted in this region are between 1 and 2 Mev. higher than Kirkaldy's values. It is also easy to show experimentally that the cyclotron operating conditions can affect the energy at a given radius by 1 or 2 Mev.; perhaps the energy spread is similarly affected. All the absolute proton energies above 30 Mev. given here should therefore be looked upon as uncertain by about 2 Mev. Exact energy values are not important of themselves in this study, because the  $(p, xn)$  cross section peaks are always wide compared with the uncertainty in proton energy, but errors in energy can cause errors in the proton beam intensity monitoring in energy regions where the monitor cross sections are changing rapidly, i.e. in the region 15-30 Mev. Owing to the auxiliary energy measurements to be described below, the energies in this region are probably uncertain by only about 1 Mev. The spread in proton energy does not greatly affect the  $(p, xn)$  results, because its square is small compared with the square of the width of the individual  $(p, xn)$  peaks.

The monitor reactions used were the following:

- (a)  $\text{Cl}^{32}(p, pn)\text{C}^{11}$  (20.5 min.)  $\rightarrow \text{B}^{11}$  (stable),
- (b)  $\text{Cu}^{63}(p, n)\text{Zn}^{63}$  (38.3 min.)  $\rightarrow \text{Cu}^{63}$  (stable),
- (c)  $\text{Cu}^{63}(p, pn)\text{Cu}^{62}$  (10 min.)  $\rightarrow \text{Ni}^{62}$  (stable).

The cross section for reaction (a) has been given by Aamodt *et al.* (1952) and modified by Crandall *et al.* (1956). The only effect of the modification for the energy region of interest is an over-all reduction of the older cross section by 13%. The cross sections for reactions (b) and (c) were measured by Ghoshal (1950) and Meadows (1953). These workers differ by a factor of about 1.4 in their values for the cross sections, and to a smaller extent in the shapes of the cross section curves. We have adopted the shapes of the curves given by Ghoshal, on the grounds that he was using the proton beam of the Berkeley

linear accelerator with its excellent energy definition. On the other hand, check measurements made by bombarding carbon and copper simultaneously seemed to show that Ghoshal's absolute values were 39% high compared with the carbon cross section, in agreement with Meadows' conclusion. The copper cross sections adopted are Ghoshal's curves reduced by the factor 1.39, and these should be regarded only as secondary standards connecting the low energy region with the carbon cross section. The copper monitors were used essentially only for the  $(p, 2n)$  cross sections which peak near 20 Mev. To anticipate, the results for the  $(p, 2n)$  cross sections were surprisingly high; if Ghoshal's values for the copper cross sections had been accepted, these results would have been even higher.

Each of the three monitor cross section curves was adjusted for the energy spread of the cyclotron by folding this energy spread into the original curves by a numerical procedure. The effect of this adjustment is small. The monitor cross section curves finally used are shown in Fig. 1.

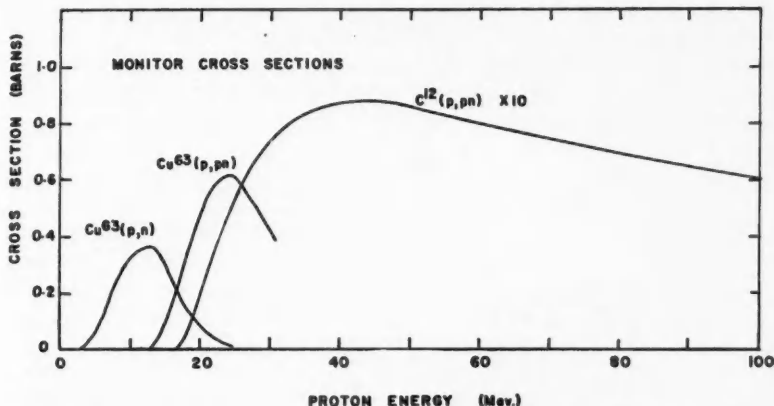


FIG. 1. Cross section curves adopted for proton flux monitoring. The curves are not exactly those given by the original authors; see the text.

The radioactive products of the monitor reactions are positron emitters,  $Zn^{65}$  having a 7% electron capture branch. The activities were counted by surrounding the monitor foils with sufficient material to stop the positrons, and counting the full energy peak of the resulting annihilation radiation in the calibrated sodium iodide scintillation counter. This determination should be accurate because one of the calibration points for the scintillation counter was provided by annihilation radiation from  $Na^{22}$ . The monitor foils were 5 mil teflon for the carbon monitor, chosen for its chemical and thermal stability, and 1 mil natural metallic copper for the copper monitors. In the case of teflon ( $(CF_2)_n$ ), the 112 min.  $F^{18}$  was also produced, but its half life differs so much from that of  $C^{11}$  that no problem was introduced. The copper monitors also produce two easily separated half lives.

It is clear from Fig. 1 that a bombardment of a copper foil at some energy between 14 and 24 Mev. will yield a ratio of the two copper monitor activities that is a rapid function of energy. A measurement of this kind at a particular cyclotron radius gives a check measurement on the mean proton energy at that radius. The same technique can be applied with less certainty between 19 and 24 Mev., using copper versus carbon. These are the measurements, referred to above, that caused a slight revision of the energies computed from Kirkaldy's results in this energy region. In the case of the  $Pb^{207}$  and  $Pb^{208}$  samples that were electroplated onto 1 mil copper foil, the copper monitor was always present. It was frequently accompanied by a teflon monitor foil, so that a large number of check measurements were made in this way. Above 30 Mev. the carbon cross section is slowly varying and was used alone.

#### ESTIMATION OF ERRORS

The standard error of the measurements is difficult to assess, both because of the large number of factors entering the measurements, and because the error certainly varies from one cross section to another as well as within the same cross section. We attempt only to estimate an average standard error for points on any  $(p, xn)$  cross section curve not too far from the peak of that curve. Table II shows the factors entering the cross section measurements, with their estimated individual standard errors.

TABLE II  
ESTIMATED STANDARD ERRORS OF THE INDIVIDUAL FACTORS ENTERING  
THE MEASUREMENT OF  $(p, xn)$  CROSS SECTIONS

Entry number	Factor	Standard error, %
1	Sample thickness	7
2	Analysis of $K$ X-ray decay curves	5
3	Errors in monitoring not including the absolute value of the monitor cross section	5
4	Scintillation counter efficiency	7
5	Monitor cross sections	7
6	$K$ X-ray fluorescent yield	1
7	Absorption of $K$ X-rays in sample	1
8	$K$ to total capture ratio	5
9	Summing correction for internal conversion	2

From Table II we may compute three kinds of standard errors for the measurement, compounding the errors in the usual way.

(a) Relative errors among the measured points in a single  $(p, xn)$  curve, i.e. the shapes of the cross section curves. Here we need only include entries number 1, 2, 3, and 4, with 4 arbitrarily reduced to 5% because only a ratio of efficiencies at different energies in the same counter is involved. Result: 11%.

(b) Relative heights of different  $(p, xn)$  peaks in a given target isotope. Here we include all the factors except 5. Result: 12.5%.

(c) Absolute values of  $(p, xn)$  cross sections in barns. Here we include all factors. Result: 15%.

Individual ( $p, xn$ ) cross sections may depart from these error estimates in either direction. For example, those cross sections whose values have been checked by gamma ray measurements should be slightly more reliable than the above estimates indicate. On the other hand, a cross section such as  $\text{Bi}^{209}(p, 7n)$  which lacks the summing correction for internal conversion must be regarded as less reliable.

In addition to the above, all the  $\text{Pb}^{207}$  cross sections suffer from a different type of error arising in the following way. The final result of a measurement on one activity in a target bombarded at one energy is the cross section for production of that activity by the mixture of isotopes contained in that target. To convert from this result to the corresponding cross section for the single isotope most abundant in the sample, we must subtract the effect of the other isotopes present. The problem is non-existent for the  $\text{Bi}^{209}$  targets, and is almost trivial for the  $\text{Pb}^{206}$  and  $\text{Pb}^{208}$  targets where the proportion of the desired isotope approaches 90%. In the  $\text{Pb}^{207}$  targets, however, the amount of  $\text{Pb}^{208}$  present is about half the amount of  $\text{Pb}^{207}$ , and this correction represents a serious limit on the accuracy obtained. Consider, for example, the measurement of the ( $p, 2n$ ) cross section in  $\text{Pb}^{207}$ , producing 6.2 day  $\text{Bi}^{206}$ . As the energy is raised from the apparent threshold for this reaction near 10 Mev., the cross section increases and reaches a peak near 20 Mev., thereafter falling. At about 20 Mev., however,  $\text{Bi}^{206}$  starts to be produced by  $\text{Pb}^{208}(p, 3n)$ , this production rising as the  $\text{Pb}^{207}(p, 2n)$  cross section falls. With  $\text{Pb}^{208}$  half as abundant as  $\text{Pb}^{207}$  in the sample, at around 30 Mev. the production of  $\text{Bi}^{206}$  is still large and is now perhaps two-thirds due to  $\text{Pb}^{208}$ . Assuming that the  $\text{Pb}^{208}$  cross section has been measured separately, a subtraction gives the production by  $\text{Pb}^{207}$ , but with errors of about 10% in the two quantities to be subtracted the error in the result is large. The measured  $\text{Pb}^{207}$  cross sections are therefore increasingly inaccurate above their respective peaks.

#### RESULTS AND DISCUSSION

The cross section results are given in Table III and in Figs. 2, 3, 4, and 5 for  $\text{Bi}^{209}$ ,  $\text{Pb}^{206}$ ,  $\text{Pb}^{207}$ , and  $\text{Pb}^{208}$  respectively. In the case of  $\text{Bi}^{209}$ , the ( $p, 2n$ ) cross section was not measured in the present work, and the measured curve of Kelly (1950) has been adapted for use in Fig. 2. Kelly's results were measured with good proton energy resolution, and his original curve has been smeared with our proton energy spread in order to present a fair comparison with the present work. The effect on Kelly's curve was small, the curve being lowered at its peak by about 5% and widened correspondingly.

The individual cross section curves all show the peaked shape expected from compound nucleus formation followed by neutron evaporation, successive ( $p, xn$ ) cross sections being shifted up the energy scale by a little over 10 Mev. per neutron emitted. Since the binding energy of a neutron in this region is about 7 Mev., the mean kinetic energy of the evaporation neutrons must be a little over 3 Mev., implying an effective nuclear temperature between 1.5 and 2 Mev. The curves also show a long tail extending towards higher energies; this is seen very well on the  $\text{Pb}^{206}(p, 2n)$  curve in Fig. 3, and can also be inferred

from some of the other curves. This tail can only occur as a result of one or more neutrons being ejected with a kinetic energy much higher than that characteristic of neutron evaporation, presumably in a direct nucleon cascade process.

TABLE III

MEASURED  $(p, xn)$  CROSS SECTIONS IN  $\text{Bi}^{209}$ ,  $\text{Pb}^{206}$ ,  $\text{Pb}^{207}$ , AND  $\text{Pb}^{208}$ . THE PROTON BOMBARDING ENERGY (LABORATORY SYSTEM) IN MEV. APPEARS IN THE FIRST COLUMN HEADED  $E$ . THE MANY DIFFERENT  $E$  VALUES REFLECT SMALL CORRECTIONS MADE IN THE PROTON ENERGIES AT DIFFERENT TIMES. ALL CROSS SECTIONS ARE QUOTED IN BARNS. IN SOME CASES A CROSS SECTION LABELLED, FOR EXAMPLE,  $(p, 6n)$ , IS REALLY  $(p, 6n) + (p, p5n)$  AND SO ON; SEE THE TEXT FOR DETAILS IN EACH CASE

(a) $\text{Bi}^{209}(p, xn)$ cross sections					
$E$	$(p, 3n)$	$(p, 4n)$	$(p, 5n)$	$(p, 6n)$	$(p, 7n)$
21.9	0.37				
24.8	0.57				
27.7	0.79				
29.6		0.12			
30.7	0.82				
33.7	0.56				
35.5		0.89			
36.6	0.34				
38.8		1.22			
39.8	0.22		0.10		
42.0		0.96			
43.0			0.51		
45.2		0.71			
46.4	0.11		0.63	0.06	
50.4	0.08		0.80	0.21	
55.0			0.68	0.40	
59.7			0.45	0.49	0.09
66.3				0.47	0.39
74.9				0.45	0.49
79.9					0.39
83.7				0.28	0.36

(b) $\text{Pb}^{208}(p, xn)$ cross sections						
$E$	$(p, n)$	$(p, 2n)$	$(p, 3n)$	$(p, 4n)$	$(p, 5n)$	$(p, 6n)$
12.7	0.23	0.06				
16.3	0.06	0.53				
20.7		1.05	0.02			
24.6		0.98	0.52			
25.0		0.76	0.54			
27.8		0.53	0.88			
27.9			0.73			
28.0		0.54				
30.0		0.36	0.89			
31.0			0.77	0.06		
34.0			0.73	0.37		
35.9		0.15	0.57	0.49		
36.6			0.40	0.62		
39.2		0.12			0.02	
39.8				0.91		
41.2			0.15	1.11		
42.4		0.13	0.18		0.14	
45.4		0.16	0.19	1.03	0.37	
45.8				0.97	0.36	
49.0		0.13	0.14	0.52	0.57	0.05
52.5		0.15		0.47	0.59	0.26
56.3		0.11		0.30	0.38	0.40
63.8		0.09		0.21	0.21	0.55
						0.18

TABLE III (*Concluded*)

(c) $\text{Pb}^{207}(p, xn)$ cross sections				
<i>E</i>	( <i>p</i> , 2 <i>n</i> )	( <i>p</i> , 3 <i>n</i> )	( <i>p</i> , 4 <i>n</i> )	( <i>p</i> , 5 <i>n</i> )
13.0	0.08			
15.2	0.36			
17.5	0.58			
17.8	0.62			
18.4	0.70			
19.3	0.89			
20.1	0.82			
20.9	0.96			
24.5	0.56	0.46		
26.9	0.34	0.70		
30.7	0.09	0.94		
33.9	0.02	0.79	0.17	
37.1			0.60	
39.9			0.81	
43.2			0.84	0.08
46.4			0.69	0.39

(d) $\text{Pb}^{208}(p, xn)$ cross sections			
<i>E</i>	( <i>p</i> , 3 <i>n</i> )	( <i>p</i> , 4 <i>n</i> )	( <i>p</i> , 5 <i>n</i> )
24.5	0.48		
26.9	0.74		
30.8	0.98		
33.8	0.73	0.28	
37.1	0.52	0.72	
39.9	0.27	0.93	
43.2	0.22	0.84	0.20
46.4	0.14	0.56	0.45

In the diagrams for  $\text{Bi}^{209}$  (Fig. 2) and  $\text{Pb}^{208}$  (Fig. 3) we also show the computed value of the total "compound nucleus" reaction cross section,  $\sigma_c$ , as a function of energy, taken from the compilation of Shapiro (1953), for nuclear radius parameters  $r_0 = 1.3 \times 10^{-13}$  and  $1.5 \times 10^{-13}$  cm. It is clear from a glance at these diagrams that the (*p*, 2*n*) cross section is unexpectedly large compared with the succeeding cross sections. An experimenter measuring only the (*p*, 2*n*) cross section would conclude that  $r_0$  should be taken as nearly  $1.5 \times 10^{-13}$  cm., while one measuring the (*p*, 3*n*) or (*p*, 4*n*) cross sections would deduce a value of  $r_0$  less than  $1.3 \times 10^{-13}$  cm. The  $\sigma_c$  curves would lead one to expect the peak of the (*p*, 2*n*) cross section curve to have a value just over half the peak of the (*p*, 3*n*) curve.

A theoretical discussion of these cross section results has been given in brief by Jackson (1954), and is reported in full in the paper immediately following this one (Jackson 1956).

The sum of the (*p*, *xn*) cross sections should be nearly equal to  $\sigma_c$  at energies where (*p*, *xn*) reactions are predominant over all other reactions, say from 10 to 40 Mev. The experimental sum curve is shown for  $\text{Bi}^{209}$  (Fig. 2) and  $\text{Pb}^{208}$  (Fig. 3) as a row of open circles labelled "sum". These curves were obtained by adding together the smooth curves drawn through the measured points for the various (*p*, *xn*) cross sections. The small ripples in this sum

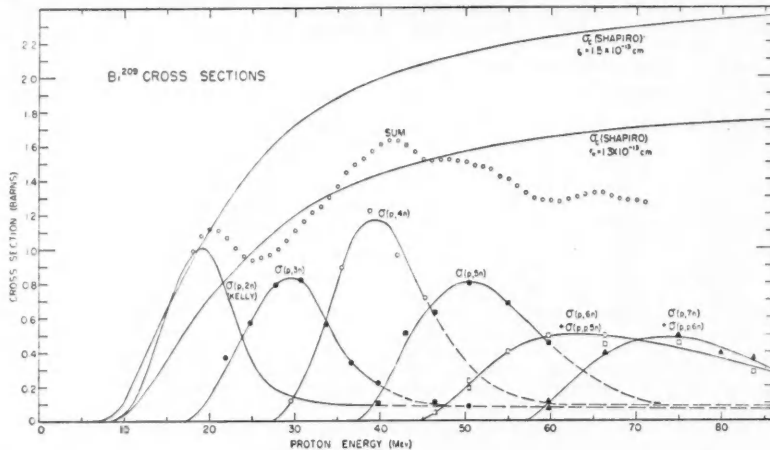


FIG. 2. Measured  $(p, xn)$  cross sections of  $\text{Bi}^{209}$  as a function of proton energy. The  $(p, 2n)$  curve is from the work of Kelly (1950), slightly modified for comparison with the other curves; see the text. The solid lines outlining the various cross sections do not represent any theory, but are simply drawn freehand among the measured points. Three points shown double on the  $(p, 6n)$  and  $(p, 7n)$  curves represent separate determinations; these have been averaged in Table III(a).

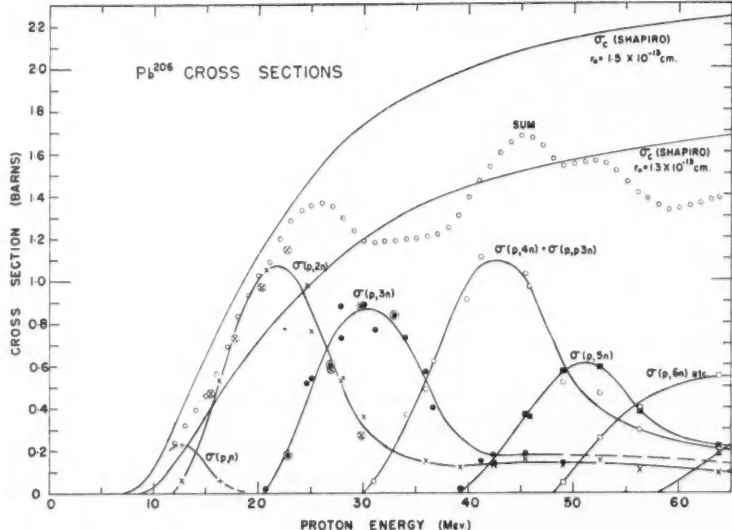


FIG. 3. Measured  $(p, xn)$  cross sections of  $\text{Pb}^{206}$  as a function of proton energy. The en-circled points on the  $(p, 2n)$  and  $(p, 3n)$  curves represent measurements made with electroplated lead 206 targets as a method of calibrating this type of target for thickness. These points are omitted from Table III(b). The solid lines outlining the various cross sections are simply drawn freehand among the measured points.

curve should not be taken seriously, and the curve is increasingly uncertain at higher energies, but it is impossible to ignore a peak in it at 20 to 25 Mev., followed by a dip at around 30 Mev., a further rise to a maximum around 40 to 45 Mev., and then a slow falling off. The falling off at higher energies is expected both because  $\sigma_c$  itself will begin to fall off owing to nuclear transparency effects, and because of the increasing importance of reactions other than  $(p, xn)$ . If a smooth curve is sketched in connecting the part of the sum curve below 20 Mev. with that above 40 Mev., it passes about 0.5 barn above the bottom of the dip near 30 Mev. The estimated errors in the measured cross section are of course incapable of explaining this discrepancy. Any correction for the energy spread of the cyclotron could only increase these fluctuations.

A possible explanation for the dip at 30 Mev. would be the existence of some undetected reaction (or reactions) with a cross section amounting to about 0.5 barn at 30 Mev., and varying with energy in the correct way to fill the dip. Since  $(p, pxn)$  reactions have been shown to be too small, the next most likely possibility seems to be a  $(p, \alpha)$  reaction. In the targets used,  $(p, \alpha)$  reactions produce either  $\beta^-$  emitters or stable elements, either of which would have escaped detection in the previous experiments. Accordingly an experiment was performed to try to detect  $Pb^{207}(p, \alpha)Tl^{204}$  (2.7 yr.), the product being a well-known beta emitter having an end point energy of 0.76 Mev. A target of "specpure" natural lead 8 Mev. thick was given a three hour bombardment at a mean proton energy of 32 Mev. The total proton flux passing through the target was estimated from the production of  $Bi^{204}$ , using the  $Pb^{206}(p, 3n)$  cross section already measured. Three weeks later the target was dissolved and thallium was chemically separated and counted in a  $4\pi$  counter.\* The counting yield corresponded to a cross section for  $Pb^{207}(p, \alpha)$  of about 2 millibarns. This figure is a rough upper limit, because no extreme precautions were taken to hold back impurity activities in the separated thallium. Although this experiment was conceived as a  $(p, \alpha)$  test, it is clear that  $Tl^{204}$  could also have been produced by the reactions  $Pb^{206}(p, 2pn)$  and  $Pb^{208}(p, \alpha n)$ . Since  $Pb^{208}$  is roughly twice as abundant as  $Pb^{206}$  or  $Pb^{207}$  in natural lead, we have the following limits on reactions other than  $(p, xn)$  at 32 Mev.:

$$\begin{aligned}\sigma(p, \alpha) &< 2 \text{ mb.,} \\ \sigma(p, 2pn) &< 2 \text{ mb.,} \\ \sigma(p, \alpha n) &< 1 \text{ mb.}\end{aligned}$$

None of the above cross sections is within a factor of 100 of filling the dip at 30 Mev., and we can conclude that other similar reactions are equally inadequate.

The dip at 30 Mev. could also be removed by assuming that the  $(p, 2n)$  cross sections had been overestimated by a factor approaching 2 in  $Bi^{209}$ ,  $Pb^{206}$ , and  $Pb^{207}$ . Apart from the objection that this involves Kelly's work as well as our own, there is an internal check on such a possibility. Such a large

\*We thank Dr. L. Yaffe and his group for the chemical separation and  $4\pi$  counting.

error could presumably arise only through some unrecognized peculiarity in the radioactivity through which the cross section is measured. In the case of  $\text{Pb}^{206}(p, 2n)$ , the radioactivity is  $\text{Bi}^{206}$ , but the same activity serves as indicator of  $(p, 3n)$  in  $\text{Pb}^{207}$  and of  $(p, 4n)$  in  $\text{Pb}^{208}$ , where the same error, if it existed, would be repeated. The cross section curves for these targets (Figs. 4 and 5) show no sign of an error of the required magnitude.

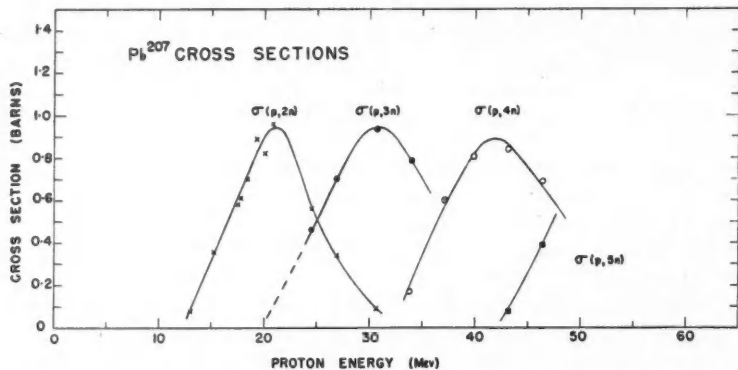


FIG. 4. Measured  $(p, xn)$  cross sections of  $\text{Pb}^{207}$  as a function of proton energy. Each of these curves is to be regarded as increasingly unreliable at energies above its peak, for reasons discussed in the text. In particular, the  $(p, 2n)$  curve appears to drop too steeply above its peak.

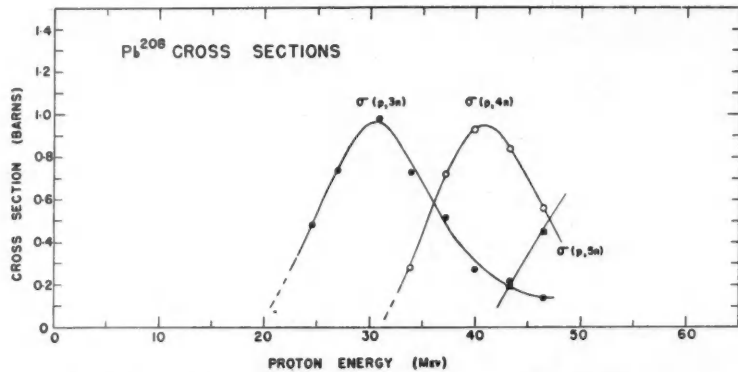


FIG. 5. Measured  $(p, xn)$  cross sections of  $\text{Pb}^{208}$  as a function of proton energy.

We are therefore led to believe that the dip at 30 Mev. is real, or even, with the maximum allowance for error, that the sum curve levels off above 20 Mev. and does not start to rise again until above 30 Mev. This dip or levelling off seems to dispose of the argument that what we are observing is an excessive  $(p, 2n)$  cross section (and possibly also  $(p, 4n)$  cross section) owing to varying level densities in the product nuclei, for in that case one would expect the  $(p, 2n)$  cross section to be high at the expense of adjacent cross sections with-

out affecting the total ( $p, xn$ ) cross section. The argument also does not seem plausible because the effect is common to  $\text{Bi}^{209}$  and  $\text{Pb}^{206}$  targets, which have different odd-even characteristics.

Turning to the results on  $\text{Pb}^{207}$  (Fig. 4) and  $\text{Pb}^{208}$  (Fig. 5), less can be said because of the less complete measurements performed. In particular, the  $\text{Pb}^{208}(p, 2n)$  cross section has not yet been measured, because it leads to the 8 yr.  $\text{Bi}^{207}$  activity. This cross section should be obtainable using natural lead targets, the only other reactions producing  $\text{Bi}^{207}$  being  $\text{Pb}^{207}(p, n)$  and  $\text{Pb}^{206}(p, \gamma)$ , both with small cross sections. In  $\text{Pb}^{207}$  (Fig. 4), the ( $p, 2n$ ) cross section again appears high, though not quite to the same extent as in  $\text{Bi}^{209}$  and  $\text{Pb}^{206}$ . Drawing a sum curve for  $\text{Pb}^{207}$  is hardly justifiable, and it has not been done in Fig. 4; nevertheless if the attempt is made, the curve found is generally similar to those for  $\text{Bi}^{209}$  and  $\text{Pb}^{206}$ .

We conclude that the cross section for the formation of the compound nucleus,  $\sigma_c$ , is not a smooth function of energy, but fluctuates around the smooth curve of  $\sigma_c$  computed for  $r_0 = 1.3 \times 10^{-13}$  cm. Fluctuations of a roughly similar kind are seen in the total neutron cross sections of heavy elements. Fig. 6 shows this effect in a curve of the total neutron cross section of natural lead as a function of neutron energy. The data for this curve were taken from the compilations of Jackson *et al.* (1953) and Hughes and Harvey (1955), with additional points from the work of Bonner *et al.* (1955) and Mazari *et al.* (1955). Below 14 Mev. the measured points are numerous and are not shown indi-

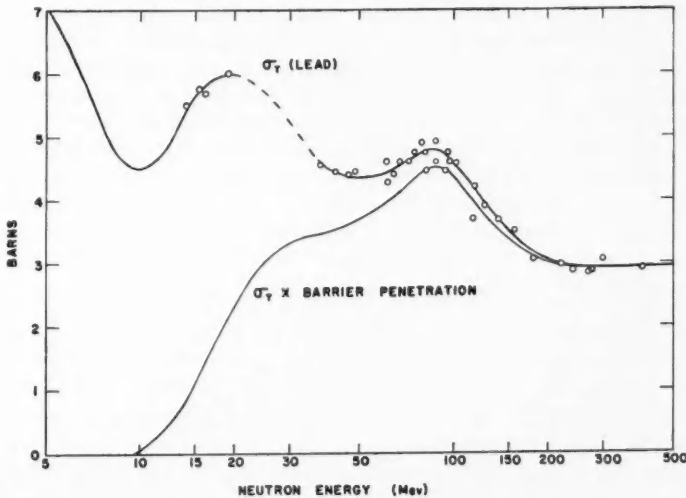


FIG. 6. Upper curve, total neutron cross section of lead as a function of neutron energy, using data collected from various sources. Below 14 Mev. the measured points are numerous and are not shown individually; between 20 and 35 Mev. there are no measurements, and a broken line shows the probable shape of the curve. Lower curve, total neutron cross section multiplied by a barrier penetration function for a rough comparison with the "sum" curves of Figs. 2 and 3.

vidually, and between 20 and 35 Mev. measurements are lacking. For the sake of making a rough comparison with the proton case, the curve of  $\sigma_T$  in Fig. 6 has been multiplied by a barrier penetration factor, giving the lower curve. The fluctuations in the lower curve are less marked than the experimental fluctuations in the proton  $\sigma_c$  (Figs. 2 and 3), but have similar features. The fluctuations in the neutron case are incompletely understood, but it is widely felt (e.g. Lawson 1953) that they are nuclear size effects similar to those observed at lower neutron energies (Hughes and Harvey 1955) and interpreted on this basis by Feshbach, Porter, and Weisskopf (1954). It may be objected that the comparison of the proton *reaction* cross section with the neutron *total* cross section is not valid, because most of the fluctuations in the neutron total cross section are expected to arise from the elastic scattering part and not from the reaction part; the experimental evidence on this point is incomplete (Hughes and Harvey 1955). Nevertheless there is reason to hope that a model not too different from the current ones can be found that will explain both the neutron results and the proton results found here. Owing to the Coulomb effect in the proton case, the calculations needed may be very laborious.

We wish to thank Dr. J. S. Foster for encouragement and valuable suggestions. A number of colleagues, particularly Dr. J. D. Jackson, have contributed very useful discussions. One of us (H.M.S.) was supported during this work by National Research Council Scholarships.

#### APPENDIX: PREPARATION OF TARGET FOILS

##### *Bismuth Foils*

Metallic foils were made by allowing drops of molten bismuth to fall a distance of about two feet onto a clean sheet of plate glass. Each drop made a frozen splash about one inch in diameter having a remarkably uniform central area about 0.003 in. thick, with a thicker rim around the edge. The foils so formed were quite flexible when first made, but seemed to become embrittled after a few days. Target strips  $\frac{1}{4}$  in. wide were cut from the central area and were checked for thickness both by weight and by micrometer.

##### *Lead 206 Foils*

The lead 206 sample material was received as coarse metal turnings. Foils were made by beating out the turnings between thin iron sheets until their thickness was about 0.003 in., and then cutting  $\frac{1}{4}$  in. strips. The uniformity of thickness was perhaps not so good as in the case of bismuth, but sufficient material was available to enable a selection to be made.

##### *Lead 207 and Lead 208 Samples*

The original sample material consisted of 43 mgm. of lead oxide containing 40 mgm. of lead, for each of lead 207 and lead 208. The targets were made by electroplating metallic lead onto one face of a 1 mil copper foil, using the following procedure.

The lead oxide ( $PbO$ ) was dissolved in  $NH_4Cl$ , and sufficient  $Na_2CO_3$  was added to precipitate all the lead as the basic carbonate ( $Pb(OH)_2 \cdot 2PbCO_3$ ). The precipitate was washed several times in distilled water and then dissolved

in a minimum amount of fluoboric acid (42% solution of  $\text{HBF}_4$ ). At this stage polyethylene containers and paraffin-coated stirring rods and pipettes were used. This solution was used for the plating, but in agreement with commercial lead plating practice, it was found that the adhesion and uniformity of the lead deposit were improved by the addition to the plating solution of about one part per thousand of household molasses.

The plating solution, having a volume of about 0.2 ml., was transferred to a lucite plastic cell having a rectangular cross section of dimensions  $\frac{1}{4}$  in. by  $\frac{1}{2}$  in. with the copper foil forming the bottom. This foil was the cathode for the plating, so that the result was an area of deposited lead  $\frac{1}{4}$  in. by  $\frac{1}{2}$  in. The anode was a carbon rod whose tip was wrapped in filter paper to catch any loose particles of carbon released during the plating. A current of about 15 ma. was passed through the solution from a storage cell and rheostat, the plating being continued for 10 to 15 min. until the current began to fall rapidly. At this stage about 65% of the lead had been deposited, and tests with natural lead had shown that forcing the current up by increasing the applied voltage at this point produced an inferior deposit. The 65% yield was therefore accepted. The deposit was smooth and non-porous as far as the eye could judge, but tests showed that it was thicker by almost a factor of two in the center than at the edges. The total amount of lead deposited was determined by weight, with results agreeing within 5% with that calculated from the total charge passed in plating. The latter fact demonstrates that little else besides lead was deposited. The copper foil on which the lead was plated was cut into four strips each  $\frac{1}{4}$  in. wide and having its tip covered with lead for a distance of  $\frac{1}{2}$  in. back from the end. The average superficial density of the lead in these targets was about 20 mgm./cm.<sup>2</sup>.

A target foil held radially in the circulating beam of the cyclotron receives most of its bombardment near its extreme tip. The activity of the target falls off as we move back from the tip in an approximately exponential manner with a "half distance" of about 1.25 mm., at least for the conditions of the present experiments. For the lead targets extending back  $\frac{1}{2}$  in. ( $\sim 3$  mm.) from the tip, over 90% of the total bombardment was received by the lead. If the lead deposit is non-uniform, as in the present case, an effective lead thickness can be found by integrating the product of the distribution of proton flux (given above) and the distribution of lead as a function of distance from the tip. The latter distribution was measured by the following method.

A lead slit about 0.5 mm. wide and just less than  $\frac{1}{4}$  in. long was placed cross-ways over the  $\frac{1}{4}$  in. wide target foil. The slit defined a narrow beam of mixed cerium-lanthanum *K* X-rays from a strong  $\text{Ce}^{137}$  source made in the cyclotron. The energy of these *K* X-rays lies around 34 kev., where the absorption coefficient of lead is about  $25 \text{ cm.}^2/\text{gm.}$ , corresponding to a mean transmission thickness of 40 mgm./cm.<sup>2</sup>. At the same energy the absorption coefficient of the copper backing is less than one-third of that of the lead. The transmission of the target foils was measured using a sodium iodide counter and 28-channel analyzer as the detector of the X-rays. The measured transmission was then easily converted to a measured thickness of lead on the copper foil. Points were taken at intervals of 0.5 mm. over the part of the foil where the lead was de-

posited. In fact, of course, the lead thicknesses found in this way were regarded only as relative values, owing to the various uncertainties involved. The plotted curve of relative lead thickness as a function of the distance from the tip of each target was numerically integrated with the proton flux distribution given above, to give the effective relative target thickness. The final normalization to an absolute thickness was performed by carrying two samples of  $Pb^{206}$  through this whole procedure and using them as targets to measure cross sections in the 20–40 Mev. region. The thicknesses of the electroplated targets were then adjusted to make these results agree with the cross sections previously measured with solid  $Pb^{206}$  foils. The amount of this normalization was 15%, and the points used in its establishment are shown encircled in Fig. 3. The same normalization was then used for the  $Pb^{207}$  and  $Pb^{208}$  electroplated targets for which no solid foils were available.

## REFERENCES

- AAMODT, R. L., PETERSON, V., and PHILLIPS, R. 1952. Phys. Rev. **88**: 739.  
 ALBURGER, D. E. and PRYCE, M. H. L. 1954. Phys. Rev. **95**: 1482.  
 ANDRE, C. G., HUIZENGA, J. R., MECH, J. F., RAMLER, W. J., RAUH, E. G., and ROCKLIN, S. R. 1956. Phys. Rev. **101**: 645.  
 ANDRE, C. G., RAMLER, W. J., RAUH, E. G., THORN, R. J., and HUIZENGA, J. R. 1954. Phys. Rev. **93**: 925.  
 BELL, P. R. 1955. *In Beta- and gamma-ray spectroscopy*. Edited by K. Siegbahn. North-Holland Pub. Co., Amsterdam.  
 BELL, R. E. 1954. Phys. Rev. **95**: 651A.  
 BELL, R. E. and SKARSØRD, H. M. 1955. Presented at the Annual Meeting of the Royal Society of Canada. Unpublished.  
 BERGKVIST, K. E., BERGSTROM, I., HERRLANDER, C. J., HULTBERG, S., SLATIS, H., SOKOLOWSKI, E., WAPSTRA, A. H., and WIEDLING, T. 1955. Phil. Mag. **46**: 65.  
 BERGSTROM, I. 1955. *In Beta- and gamma-ray spectroscopy*. Edited by K. Siegbahn. North-Holland Pub. Co., Amsterdam.  
 BERGSTROM, I. and WAPSTRA, A. H. 1955. Phil. Mag. **46**: 61.  
 BONNER, T. W., ALBA, F., FERNANDEZ, A., and MAZARI, M. 1955. Phys. Rev. **97**: 985.  
 BRYSK, H. and ROSE, M. E. 1955. ORNL-1830. Unpublished.  
 COHEN, B. L. and NEWMAN, E. 1955. Phys. Rev. **99**: 718.  
 CRANDALL, W. E., MILLBURN, G. P., PYLE, R. V., and BIRNBAUM, W. 1956. Phys. Rev. **101**: 329.  
 FESHBACH, H., PORTER, C. E., and WEISSKOPF, V. F. 1954. Phys. Rev. **96**: 448.  
 GHOSHAL, S. N. 1950. Phys. Rev. **80**: 939.  
 HOLLANDER, J. M., PERLMAN, I., and SEABORG, G. T. 1953. Revs. Mod. Phys. **25**: 469.  
 HUGHES, D. J. and HARVEY, J. A. 1955. Neutron cross sections, BNL-325. U.S. Government Printing Office, Washington.  
 JACKSON, J. D. 1954. Phys. Rev. **95**: 651A.  
 ——— 1956. Can. J. Phys. **34**: 767.  
 JACKSON, J. D., McMANUS, H., SHARP, W. T., and NEWTON, T. D. 1953. Chalk River Rept. TPI-71. Unpublished.  
 JOHN, W., Jr. 1955. UCRL-3093. Unpublished.  
 KARRAKER, D. G. 1951. UCRL-1202. Unpublished.  
 KELLY, E. L. 1950. UCRL-1044. Unpublished.  
 KELLY, E. L. and SEGRE, E. 1949. Phys. Rev. **75**: 999.  
 KIRKALDY, J. S. 1953. McGill Radiation Laboratory internal report. Unpublished.  
 KROHN, V. E. and RABOY, S. 1954. Phys. Rev. **95**: 1354.  
 LAWSON, J. D. 1953. Phil. Mag. **44**: 102.  
 MCCORMICK, G. H. and COHEN, B. L. 1954. Phys. Rev. **96**: 722.  
 McGOWAN, F. K. 1954a. Phys. Rev. **93**: 163.  
 ——— 1954b. Unpublished.  
 MAZARI, M., ALBA, F., and SERMENT, V. 1955. Phys. Rev. **100**: 972.  
 MEADOWS, J. W. 1953. Phys. Rev. **91**: 885.  
 ROSE, M. E. 1955. *In Beta- and gamma-ray spectroscopy*. Edited by K. Siegbahn. North-Holland Pub. Co., Amsterdam.  
 SHAPIRO, M. 1953. Phys. Rev. **90**: 171.  
 TEWES, H. A. 1955. Phys. Rev. **98**: 25.  
 WAPSTRA, A. H., MAEDER, D., NIJGH, G. J., and ORNSTEIN, L. Th.M. 1954. Physica, **20**: 169.

# A SCHEMATIC MODEL FOR ( $p$ , $xn$ ) CROSS SECTIONS IN HEAVY ELEMENTS<sup>1</sup>

BY J. D. JACKSON

## ABSTRACT

A schematic model for the description of ( $p$ ,  $xn$ ) reactions in heavy elements is presented. Reactions are divided into two steps, a prompt multiple collision process, followed by an evaporation stage. The various prompt processes are given by the results of Monte Carlo calculations, while the evaporation processes are described by a simplified model assuming constant nuclear temperatures and only neutron evaporation. The resulting ( $p$ ,  $xn$ ), and to a minor degree ( $p$ ,  $pxn$ ), cross sections are compared with the experimental data of Bell and Skarsgard (1956) in the energy range up to 100 Mev. With an average neutron binding energy of around 7.3 Mev., a nuclear temperature of about 1.8 Mev., and a nuclear radius of  $8.0 \times 10^{-13}$  cm., a reasonable over-all fit can be made to the data for  $Pb^{206}$ ,  $Pb^{207}$ ,  $Pb^{208}$ , and  $Bi^{209}$ . Characteristic fluctuations in the experimental results for the ( $p$ ,  $2n$ ), ( $p$ ,  $3n$ ), and ( $p$ ,  $4n$ ) reactions for all targets seem to be attributable to variations in the total reaction cross section, and are not reproduced by the present model.

## 1. INTRODUCTION

At bombarding energies below 20 or 30 Mev. per incident nucleon, nuclear reactions proceed predominantly through the amalgamation of the incident and target nuclei into a compound nucleus with all the available energy as excitation energy. This excitation energy is subsequently dissipated, commonly by the emission ("evaporation") of one or more nucleons or groups of nucleons, each taking away on the average a relatively small amount of kinetic energy. The general features of reactions in this energy range are well known (Blatt and Weisskopf 1952). The rapid rise of the cross section for the emission of a given selection of particles as the bombarding energy goes above the corresponding threshold, and the subsequent rapid decrease due to the competition from other reactions at higher energies, is characteristic.

When the incident particle has energy of 100 Mev. or more a different mechanism appears in the reaction processes (Serber 1947). The target nucleus appears partially transparent to the incident particle, and the primary interactions of the incoming particle with the nucleus are a series of quasi-free, two-body collisions. Only rarely is a compound nucleus formed. Commonly, the incident particle either passes through the nucleus without any interaction, or makes a few collisions with nucleons in the nucleus, knocking some of them out and perhaps emerging itself. In this way, the first step of a reaction involves the emission of a few prompt particles. These particles, somewhat random in number and in kinetic energy, may be expected to carry away varying amounts of kinetic energy and leave the residual nucleus with a wide range of different excitations. The second step of the reaction is the evaporation of further particles from the excited residual nucleus. In this energy range, the cross section for the emission of a given selection of particles will be a slowly varying function of bombarding energy on account of averaging over the

<sup>1</sup>Manuscript received May 3, 1956.

Contribution from the Radiation Laboratory, McGill University, Montreal, Quebec.

distribution of residual excitations. At any given energy there will be a large number of different reactions competing, contrary to the behavior at low energies. This general behavior above 100 Mev. has been confirmed by numerous experiments on excitation functions for light and medium weight elements (see, for example, Fink and Wiig 1954; Wagner and Wiig 1954).

In the energy range between 20 and 100 Mev. there is a gradual transition from purely compound nucleus formation to the initial internal cascade or multiple collision process. Study of reactions in this energy region may be expected to give information on how the transition between the different mechanisms takes place. Considerable experimental data have already been obtained for light and medium weight elements in this energy range by various workers at Harvard, the most recent being those of Sharp, Diamond, and Wilkinson (1956) for cobalt.

The present work is concerned with calculations of cross sections for the emission of an arbitrary selection of nucleons (the sum of prompt and evaporated particles) from heavy nuclei bombarded by protons with energies up to 100 Mev. Particular attention is paid to  $(p, xn)$  and, to a much lesser extent,  $(p, pxn)$  reactions. Detailed comparison will be made with the experimental data on  $(p, xn)$  cross sections for  $Pb^{206}$ ,  $Pb^{207}$ ,  $Pb^{208}$ , and  $Bi^{209}$  presented in the preceding paper (Bell and Skarsgard 1956). The model used is a schematic one in which detailed properties of individual nuclei are suppressed. The reaction is divided into two distinct phases as described in the second paragraph of this section. A description of the different prompt processes and their relative probabilities is given in Section 2. The evaporation phase is discussed in Section 3, while the combining of the prompt and evaporation results to yield the cross section for specific reactions is presented in Section 4. Comparison with experiment appears in Section 5, and the summary and conclusions in Section 6.

A preliminary report of these calculations was presented at the Washington meeting of the American Physical Society, May, 1954 (Jackson 1954).

Related calculations have been made for stars in photographic emulsions bombarded by high energy deuterons (Hornig and Baumhoff 1949), for 100 Mev. protons on targets of mass near 64 (Meadows 1955), for proton-induced reactions on iron and tin up to 30 Mev. (Hayakawa, Kawai, and Kikuchi 1955), and for the  $(n, 2n)$  reaction on copper up to 30 Mev. (Nakasima and Kikuchi 1955).

## 2. RELATIVE PROBABILITIES FOR THE PROMPT PROCESSES

The first step in calculating a specific reaction cross section is the determination of the relative probabilities of the prompt (cascade) processes. No satisfactory analytic method has yet been devised to handle the complicated multiple collisions that occur as the incident particle traverses the nucleus. Instead, it has been necessary to rely on numerical procedures such as the Monte Carlo method to evaluate the relative frequencies of the various kinds of prompt processes (Goldberger 1948; Bernardini, Booth, and Lindenbaum 1952; McManus, Sharp, and Gellmann 1954). In the present work, the Chalk

River Monte Carlo calculations (McManus, Sharp, and Gellmann 1954; McManus and Sharp unpublished) for proton bombardment of uranium at 60 and 90 Mev. have been used. On the basis of the model employed for the calculations and on general physical grounds it can be assumed that the relative probabilities for the prompt events vary slowly from one nucleus to another, and that they should be very nearly the same for all heavy elements. All Monte Carlo calculations made so far are based on a model of successive, essentially free, two-body collisions within the target nucleus. The neglect of binding effects during the collisions can be justified at high energies, but is a poorer and poorer approximation as the energy decreases. The use of the Monte Carlo model at energies of the order of 50 or 60 Mev. is consequently recognized as being of borderline validity (Peaslee 1952).

The numerical results of the Monte Carlo calculations may be sorted out into categories corresponding to the ejection of  $i$  prompt neutrons and  $j$  prompt protons, denoted by  $(i, j)$ , with a distribution of residual excitation energies appropriate to each. With the assumption that below 20 Mev. complete compound nucleus formation occurs in heavy elements, the various relative probabilities  $q(i, j)$  at 60 and 90 Mev. may be linked with smooth, although somewhat arbitrary, curves to obtain the results shown in Fig. 1. It may be

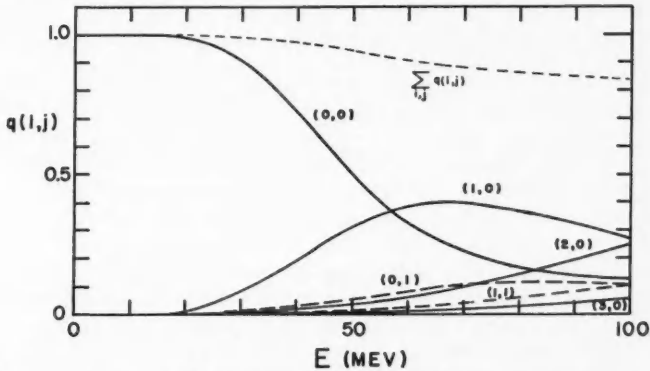


FIG. 1. The relative probabilities  $q(i, j)$  for the ejection of  $i$  prompt neutrons and  $j$  prompt protons from a heavy nucleus bombarded by protons as a function of the incident proton energy  $E_0$  in Mev. Compound nucleus formation corresponds to the process  $(0, 0)$ . The abscissa scale in this figure, and in Figs. 3, 4, 5, 6, and 7, should be labelled  $E_0$  rather than  $E$ .

noted that above 60 Mev. the theoretical probability for compound nucleus formation  $(0, 0)$  is smaller than the probability for the ejection of one prompt neutron  $(1, 0)$  and is of just the same order as the probabilities for the emission of two prompt neutrons  $(2, 0)$  or one proton  $(0, 1)$ . The effect of nuclear transparency at the higher energies is indicated by the sum curve shown in Fig. 1. The computed effect of about 15% at 90 Mev. is in agreement with experiment (DeJuren and Knable 1950).

Each of the relative probabilities shown in Fig. 1 has an associated distribution of residual excitation energy. The statistical accuracy of the present

Monte Carlo calculations is poor for these excitation distributions, especially for the less likely processes. For computational purposes, the Monte Carlo histograms have been approximated by simple analytic forms. For the (1, 0) events at incident energies below 100 Mev. the probability of a residual excitation  $E$  is roughly proportional to  $E$ . For the (1, 0) and (0, 1) events in nuclei of mass around 64, Meadows' (1955) Monte Carlo calculation gave an excitation distribution peaking at low energies, contrary to the present Monte Carlo results for heavy nuclei. The difference is apparently due to the mass of the target. McManus and Sharp's calculations (unpublished) give results similar to Meadows' for light element targets. For the (0, 1) and (2, 0) events the Monte Carlo histograms at 60 and 90 Mev. are consistent with a rectangular distribution of excitation. The final results for specific reaction cross sections are not sensitive to the exact details of these excitation distributions.

To convert the relative probabilities of Fig. 1 into absolute cross sections it is necessary to multiply them by the effective "geometrical" cross section of the target nucleus. It is assumed here that this cross section is the same as the compound nucleus formation cross section defined at lower energies (Blatt and Weisskopf 1952; Shapiro 1953), the effects of nuclear transparency being included in the  $q(i, j)$ . The possibility that this assumption needs modification is discussed in Section 5.

### 3. RELATIVE PROBABILITIES FOR NEUTRON EVAPORATION

After the emission of the prompt nucleons as a result of the multiple collisions within the target nucleus, the residual nucleus loses energy by the evaporation of one or more nucleons or groups of nucleons. The detailed calculation of the relative probabilities of evaporation is in general very complicated. In heavy nuclei, however, a simplifying assumption can be made. Because of the high Coulomb barriers the emission probabilities for charged particles are very small compared to the emission probability for neutrons. While there is indeed a relative favoring of proton emission after the emission of a large number of neutrons, due to decreased proton binding energies, for excitations of the order of 100 Mev. or less this effect is negligible. Consequently the evaporation process is here assumed to consist entirely of the emission of successive neutrons.

At excitations of the order of 15 Mev. or higher the probability of emission of a neutron with energy  $\epsilon$  is approximately proportional to  $\epsilon \exp(-\epsilon/T)$  where  $T$  is the nuclear temperature appropriate to the maximum energy available to the neutron. Reasonable theoretical models lead to the expression  $T = (aE_{\max})^{\frac{1}{3}}$  where  $a$  is a constant related to the level density of the nucleus in question. For heavy nuclei  $a$  is empirically found to be of the order of 0.1 Mev. (Blatt and Weisskopf 1952). This gives nuclear temperatures in the range 1.4 Mev. to 2.8 Mev. for a heavy nucleus with excitation between 20 and 80 Mev. Experimental evidence on the variation of nuclear temperature with excitation is not clear cut; what evidence there is does not support the square root of energy dependence. In fact, data on the energy spectra of inelastically scattered protons seem to imply a constant temperature or even one

decreasing with increasing excitation (Gugelot 1954). In the present calculations, therefore, the simplifying assumption of a constant nuclear temperature, independent of the type of nucleus or its state of excitation, will be made. It is considered unlikely that significant errors are thereby introduced.

The neutron evaporation probabilities have been evaluated in an approximate manner by assuming that the neutron energy spectrum is  $\epsilon \exp(-\epsilon/T)$  and that neutron emission occurs whenever it is energetically possible. If the  $i^{\text{th}}$  neutron has a binding energy  $B_i$ , and the nuclear temperature is  $T$ , the probability that a nucleus with initial excitation  $E$  will emit exactly  $x$  neutrons is found to be:

$$(1) \quad P(E, x) = I(\Delta_x, 2x-3) - I(\Delta_{x+1}, 2x-1)$$

where  $I(z, n)$  is Pearson's incomplete gamma function

$$I(z, n) = (1/n!) \int_0^z x^n e^{-x} dx,$$

and  $\Delta_x = \left( E - \sum_1^x B_i \right) / T$  is the energy (in units of  $T$ ) above threshold for

the emission of  $x$  neutrons. This expression for  $P(E, x)$  is in error by terms of order  $\exp(-B/T)$  where  $B$  is a typical neutron binding energy. For  $x = 1, 2$  it agrees with the results of Weisskopf (Blatt and Weisskopf 1952).

Fig. 2 shows typical curves of  $P(E, x)$  for  $x = 1, 2, \dots, 8$  versus excitation energy  $E$ . For simplicity, the successive neutron binding energies were taken to be the same. It is expected that  $B/T$  should lie in the range from 3 to 5. The curves are drawn for  $B/T = 4.0$ . This happens to be the value finally chosen for the fitting to experiment. For  $x = 1, 2, 3, 4, 5$  the dotted curves show the effect of the alternations in successive neutron binding energies

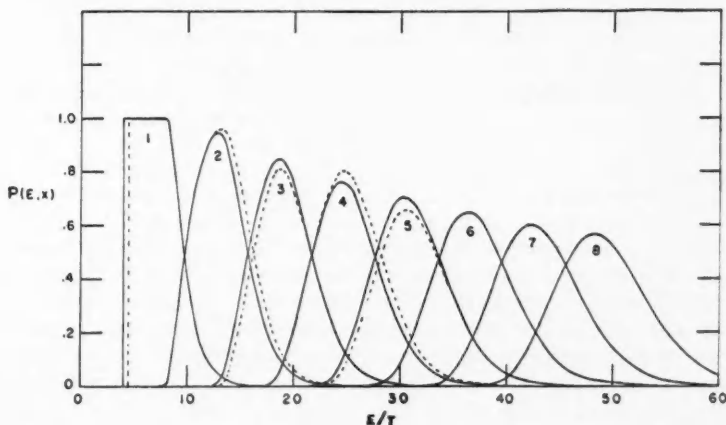


FIG. 2. The probabilities  $P(E, x)$  that a nucleus with excitation energy  $E$  will evaporate exactly  $x$  neutrons as a function of  $E/T$ , where  $T$  is the nuclear temperature. The curves are for  $B/T = 4.0$ ,  $B$  being the average neutron binding energy. The effect of alternation of the successive neutron binding energies is shown by the dotted curves (appropriate for even neutron number targets).

appropriate for even neutron number targets such as  $\text{Pb}^{206}$ ,  $\text{Pb}^{208}$ , and  $\text{Bi}^{209}$ . For odd neutron number targets the alternations go the opposite way. The alternations shown correspond typically to about  $\pm 0.7$  Mev. in neutron binding energy, an amount rather larger than that observed. Similar curves for neutron evaporation have been presented recently by Leachman (1956) in connection with the emission of neutrons in fission.

The successive neutron binding energies  $B_i$  are known in the region above lead and bismuth from the systematics of the natural radioactive chains. Apart from the alternations between successive pairs of neutrons the individual binding energies show a slow increase with increasing numbers of neutrons emitted. For bismuth and polonium there is less experimental information, but the average binding energy is close to 7.3 Mev., at least for the first four or five neutrons. In the attempts to fit the experimental yields of  $(p, xn)$  reactions for Pb and Bi it is assumed that the binding energy, averaged over successive pairs of neutrons, is constant and equal to 7.3 Mev.

#### 4. $(p, xn)$ AND $(p, pxn)$ CROSS SECTIONS

On the basis of our schematic model the cross section for a specific reaction involving the emission of  $x$  neutrons, either as prompt knock-on particles or as evaporation particles, is obtained by averaging the neutron evaporation probabilities over the various excitation distributions appropriate to each of the prompt processes. Then the averaged probabilities are combined in the following way:

$$(2) \quad \sigma(p, xn) = \sigma_c(E_0) \sum_{i=0}^x q(i, 0) \langle P(E, x-i) \rangle$$

where  $\sigma_c(E_0)$  is the reaction cross section for an incident proton of energy  $E_0$  taken from Shapiro (1953),  $q(i, 0)$  is the relative probability of the emission of  $i$  prompt neutrons and no prompt protons, and  $\langle P(E, x-i) \rangle$  is the averaged neutron evaporation probability.

For the  $(p, pxn)$  reactions the simplifying assumption of no charged particle evaporation implies that the emitted proton is always a prompt proton. Therefore the cross section for this process can be written:

$$(3) \quad \sigma(p, pxn) = \sigma_c(E_0) \sum_{i=0}^x q(i, 1) \langle P(E, x-i) \rangle.$$

Because of the smallness of  $q(i, 1)$  this cross section will be small compared to the  $(p, xn)$  cross sections; consequently the neglect of proton evaporation is not so well justified. Rough estimates indicate that where the  $(p, pxn)$  cross section given by Eq. 3 is less than about 30 millibarns appreciable errors are introduced by this neglect. In the present paper, however, only minor interest centers on  $(p, pxn)$  reactions, and no attempt has been made to include proton evaporation.

In the comparison with experiment there is one parameter, the nuclear temperature, that can be varied considerably to obtain agreement. To a lesser extent the nuclear radius and the neutron binding energies can be adjusted as well. For energies less than 50 Mev. the various  $(p, xn)$  cross sections show

well-defined peaks. The energy separation between peaks corresponds closely to the average energy (kinetic and binding) carried off by successive neutrons. This average energy is approximately  $(\bar{B} + 2T)$ . With  $\bar{B}$  sufficiently well known, the experimental spacing allows the determination of an average nuclear temperature  $T$ . Once  $T$  is specified, agreement in absolute magnitude can be sought by adjustment of the nuclear radius.

In Fig. 3 the  $(p, xn)$  cross sections are plotted as a function of incident proton energy for  $x = 1, 2, \dots, 8$  with the constants appropriate for  $\text{Bi}^{209}$ .

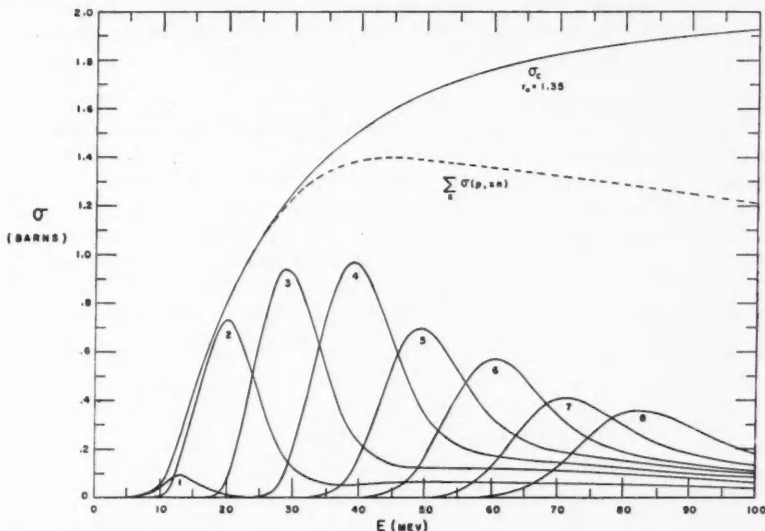


FIG. 3. Calculated  $(p, xn)$  cross sections in barns for heavy elements as a function of incident proton energy in Mev. The curves are drawn for  $\text{Bi}^{209}$  as target with  $R = 8.0 \times 10^{-13} \text{ cm.}$ ,  $\bar{B} = 7.3 \text{ Mev.}$ ,  $T = 1.8 \text{ Mev.}$  Also shown are the sum of the  $(p, xn)$  cross sections and the "geometrical" cross section  $\sigma_e$ .

The binding of the incident proton is 5.0 Mev., the average neutron binding energy is 7.3 Mev., and the nuclear temperature is approximately 1.8 Mev. The nuclear radius was taken to be  $8.0 \times 10^{-13} \text{ cm.}$ , corresponding to  $r_0 = 1.35 \times 10^{-13} \text{ cm.}$  in the formula  $R = r_0 A^{\frac{1}{3}}$ . At low energies, the conventional compound nucleus behavior is evident. As the energy increases, the effects of the internal multiple collision cascade become apparent. A given cross section has the usual compound nucleus peak but has a tail extending to higher energies. The magnitude of the tail increases as the peak energy goes up, while the peak height goes down. Correspondingly, at any given energy there are more and more different cross sections contributing. At energies much above 100 Mev. the internal cascade will dominate; there will be no marked peaks in the cross sections and all cross sections will be the same order of magnitude. Also shown in Fig. 3 are the "geometrical" cross section  $\sigma_e$  and the sum curve of the  $(p, xn)$  cross sections. The sum curve falls off at high energies—

reflecting the increased importance of prompt proton emission and nuclear transparency.

While the cross sections plotted in Fig. 3 are for  $\text{Bi}^{209}$  as target, the same general behavior is expected for other nearby nuclei. Differences of a few Mev. in the positions of the peaks will occur because of differences in proton binding energy and perhaps variations in neutron binding energies and nuclear temperatures. Absolute values of the cross sections, especially at energies below 30 Mev. where the Coulomb barrier is important, will depend on the choice of nuclear radius. For elements much heavier than Bi, fission will contribute appreciably to the reaction cross section at the expense of the  $(p, xn)$  processes.

### 5. COMPARISON WITH EXPERIMENT

The experimental data of Bell and Skarsgard (1956) on  $(p, xn)$  cross sections for  $\text{Pb}^{206}$  and  $\text{Pb}^{208}$ , and of Bell and Skarsgard (1956) and Kelly (unpublished) for  $\text{Bi}^{209}$ , are compared with the calculated cross sections in Figs. 4, 5, 6, and 7. The data for  $\text{Pb}^{207}$  are not shown. Within experimental error, they are the same as  $\text{Bi}^{209}$  for the  $(p, 2n)$  reaction and the same as  $\text{Pb}^{208}$  for the  $(p, 3n)$  and  $(p, 4n)$  reactions, except for slight shifts in the positions of the peaks. The calculated curves in the figures are basically those shown in Fig. 3, except that the incident proton binding energies for  $\text{Pb}^{206}$  and  $\text{Pb}^{208}$  are 3.3 Mev. and 3.8 Mev. respectively, as compared to 5.0 Mev. for  $\text{Bi}^{209}$ . This has the effect

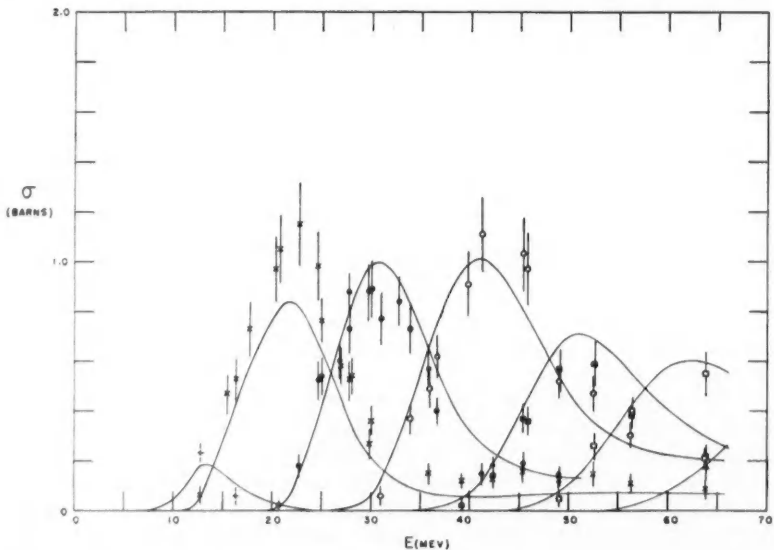


FIG. 4. Comparison of the calculated cross sections with the experimental data for  $\text{Pb}^{206}$ . The binding energy of the incident proton is 3.3 Mev. The quoted experimental uncertainty of 15% is shown on all the points. The code used for the experimental points is the same as for Fig. 3 of Bell and Skarsgard (1956). For the  $(p, 4n)$  and  $(p, 6n)$  cross sections the small added contributions of  $(p, p3n)$  and  $(p, p5n)$  are included.

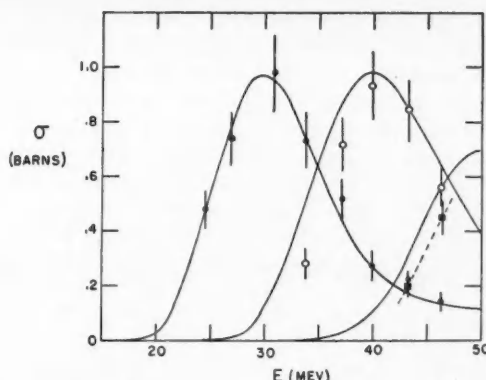


FIG. 5. Comparison of the calculated cross sections with the experimental data for  $\text{Pb}^{208}$ . The binding energy of the incident proton is 3.8 Mev.

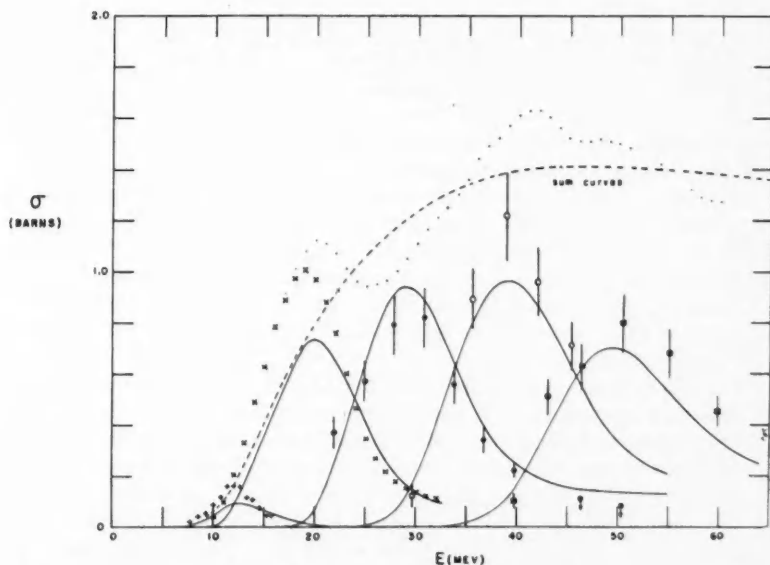


FIG. 6. Comparison of the calculated cross sections with the experimental data for  $(p, n)$ ,  $(p, 2n)$ ,  $(p, 3n)$ ,  $(p, 4n)$ , and  $(p, 5n)$  reactions on  $\text{Bi}^{209}$ . The binding energy of the incident proton is 5.0 Mev. The  $(p, n)$  and  $(p, 2n)$  data are those of Kelly (unpublished). The code used for the other experimental points is the same as for Fig. 2 of Bell and Skarsgard (1956). The experimental and calculated sum curves are also shown.

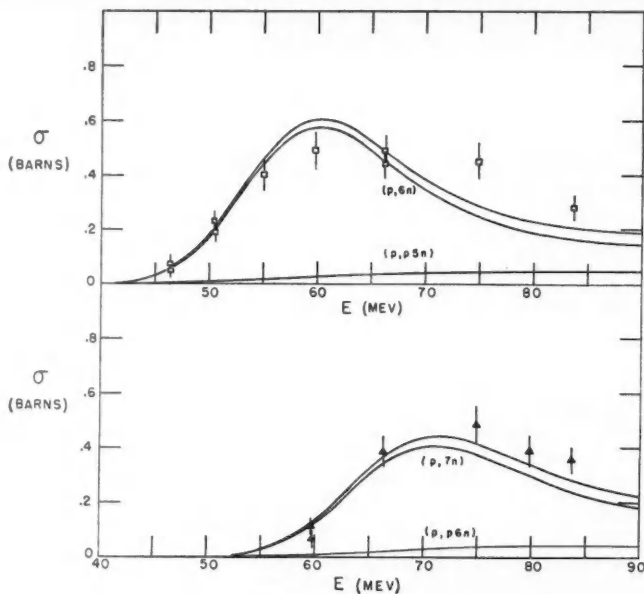


FIG. 7. Comparison of the calculated cross sections with the experimental data for the  $(p, 6n) + (p, p5n)$  and  $(p, 7n) + (p, p6n)$  reactions in  $\text{Bi}^{209}$ . The calculated  $(p, xn)$  and  $(p, p(x-1)n)$  cross sections are shown separately as well as summed together.

of shifting the Pb curves to higher energies, as is found experimentally. In Fig. 4 the calculated curves for  $(p, 4n)$  and  $(p, 6n)$  in  $\text{Pb}^{206}$  contain  $(p, p3n)$  and  $(p, p5n)$  contributions respectively for comparison with actual observations. Similarly in Fig. 7 the  $(p, 6n)$  and  $(p, 7n)$  curves for  $\text{Bi}^{209}$  have the effect of the  $(p, p5n)$  and  $(p, p6n)$  reactions added in. The smallness of the  $(p, pxn)$  cross sections as shown in Fig. 7 is typical of the theoretical results for these reactions. As mentioned in Section 4, the neglect of proton evaporation may cause these cross sections to be appreciably in error, although probably not by as much as a factor of two.

A glance at these four figures shows that the calculated cross sections are in agreement with the gross behavior of the experimental data. The evidence for the onset of the prompt multiple collision process is apparent in the fall-off and smearing out of the individual cross sections as the energy increases and in the presence of low, flat, high energy tails on such cross sections as the  $(p, 2n)$  and  $(p, 3n)$  in  $\text{Pb}^{206}$ . If compound nucleus formation were dominant at 50 Mev. the peak of the  $(p, 5n)$  cross section would be nearly twice as high as is observed. The general trend of the probabilities for the prompt processes as shown in Fig. 1 seems to be borne out by the data, although 15 to 20% variations are not excluded.

In addition to the general agreement as to over-all trend with energy, certain detailed discrepancies are apparent. In  $\text{Pb}^{206}$ ,  $\text{Pb}^{207}$ , and  $\text{Bi}^{209}$  the

observed ( $p, 2n$ ) cross section is about 50% higher than the calculated curve. The most accurately measured of the ( $p, 4n$ ) cross sections (in  $\text{Pb}^{206}$  and  $\text{Bi}^{209}$ ) are similarly larger than the calculated cross section, although by a lesser amount. On the other hand, the ( $p, 3n$ ) cross sections are somewhat smaller than the calculated one. The first explanation that comes to mind is alternations in neutron binding energies and/or in level densities (an effect found to be important in lighter elements by Meadows (1953, 1955)). The binding energy alternation has already been more than taken into account in the calculations for  $\text{Pb}^{206}$ ,  $\text{Pb}^{208}$ , and  $\text{Bi}^{209}$  and produces only a small effect in the right direction. For  $\text{Pb}^{207}$  it is in the wrong direction. The level density effect is in the wrong direction for  $\text{Pb}^{206}$ ,  $\text{Pb}^{208}$ , and  $\text{Bi}^{209}$ . That the behavior of the cross sections is not attributable to either of these effects is emphasized by the fact that the sum of all the ( $p, xn$ ) cross sections for a given target is not a smoothly increasing function of energy, but shows fluctuations around the calculated sum curve. Such a sum curve is shown for  $\text{Bi}^{209}$  in Fig. 6, and for  $\text{Pb}^{206}$  in Fig. 3 of the preceding paper (Bell and Skarsgard 1956). If the alternations from one cross section to the next were due to binding energy differences or other similar causes, one reaction would be augmented at the expense of another and the sum of all the cross sections would still be smoothly varying with energy.

The fluctuations in the sum curve are strikingly similar to the behavior found in total neutron cross sections at similar and lower energies. Comparison with the variation of these total neutron cross sections has been made by Bell and Skarsgard (1956)—see their Fig. 6. The fluctuations found in their ( $p, xn$ ) data seem even larger than those observed in the total neutron cross sections. They point out that below 20 Mev. the data would imply a radius constant  $r_0 = 1.5 \times 10^{-13}$  cm. or greater as also found by Andre *et al.* (1956) for ( $p, n$ ) and ( $p, 2n$ ) reactions in bismuth up to 10.6 Mev., and by McCormick and Cohen (1954) in heavier elements; while around 30 Mev. a radius constant  $r_0 = 1.3 \times 10^{-13}$  cm. is indicated. It is well known that the gross behavior of the neutron cross sections has been interpreted in terms of a complex potential well (Feshbach, Porter, and Weisskopf 1954; Weisskopf 1956), and that the angular distributions of elastically scattered neutrons at 14 Mev. and protons at 17 and 31 Mev. have been described by essentially the same model (Culler, Fernbach, and Sherman 1956; Melkanoff, Nodvik, and Saxon 1955). It is not clear at present whether the present fluctuations observed in the proton reaction cross sections in the energy interval up to 40 Mev. can be successfully interpreted with this model, or whether some other explanation is necessary.\*

\**Note added in proof.*—Since this paper was submitted, Drs. Melkanoff, Moszkowski, Nodvik, and Saxon of the University of California at Los Angeles have kindly evaluated the reaction cross section for a typical heavy element in the energy range from 15 to 40 Mev. for the complex potential well model which fits the angular distributions of elastically scattered protons at 5, 17, and 31 Mev. (see Melkanoff, M. A., Moszkowski, S. A., Nodvik, J., and Saxon, D. S. 1956. Phys. Rev. **101**: 507). The well parameters were assumed to vary smoothly with energy in this energy range. For convenience the target nucleus was assumed to be gold. The computed cross section increases monotonically with energy between 15 and 40 Mev. having a magnitude somewhat larger than, but an energy dependence similar to, the reaction cross section of Shapiro (1953) with  $r_0 = 1.5$ . It therefore appears that the observed fluctua-

In the framework of the calculations presented here, variations of the type obtained with a complex potential well would be grafted on by modification of the reaction cross section  $\sigma_e$ . This procedure would, of course, have only approximate validity.

#### 6. SUMMARY AND CONCLUSIONS

Calculations have been performed to obtain  $(p, xn)$  cross sections for heavy elements in the energy range up to 100 Mev. Particular emphasis has been placed on numerical results for lead and bismuth. The relative probabilities for various prompt processes have been taken from the Chalk River Monte Carlo calculations. The evaporation of neutrons has been handled in a simplified manner assuming a constant nuclear temperature. Comparison with the experimental data shows that theory and experiment can be brought into general agreement by taking  $R = 8.0 \times 10^{-13}$  cm.,  $B = 7.3$  Mev., and  $T = 1.8$  Mev. The main unexplained feature of the data is the fluctuations found in the  $(p, xn)$  cross sections for  $Pb^{206}$ ,  $Pb^{207}$ , and  $Bi^{209}$ , the observed  $(p, 3n)$  cross section being somewhat lower than theory and the  $(p, 2n)$  and  $(p, 4n)$  cross sections abnormally high. The fluctuations seem to be due to gross variations in the total reaction cross section with energy.

The over-all agreement between theory and experiment implies that the general picture of high energy reactions proceeding by an internal nucleon cascade followed by evaporation of particles from the residual nucleus is qualitatively correct, and can yield semiquantitative results for  $(p, xn)$  reactions with a reasonable choice of parameters. Presumably the cross sections shown in Fig. 3 can be utilized to give approximate excitation functions to aid in the identification of neutron deficient activities in heavy elements.

#### ACKNOWLEDGMENTS

The author wishes to acknowledge the kindness and assistance of Dr. H. McManus and Mr. W. T. Sharp in making available their unpublished Monte Carlo calculations and for tailoring their computing program to fit the needs of this work. He also wishes to thank Dr. R. E. Bell for countless stimulating discussions on both the experiments and the theory, and Dr. J. S. Foster for

---

tions do not find an easy explanation in terms of the complex potential well model. The author wishes to thank Drs. Melkanoff, Moszkowski, Nodvik, and Saxon for their generous cooperation in performing these computations.

As to other explanations, Dr. H. McManus has pointed out to the author that Eisberg and Igo (Eisberg, R. M. and Igo, G. 1954. Phys. Rev. **93**: 1039) have found cross sections for the inelastic scattering of protons (the sum of  $(p, p', \gamma)$ ,  $(p, pn)$ ,  $2(p, 2p)$ ,  $(p, p2n)$ , etc.) which seem to be of the order of 0.25 barn at 31 Mev. for tantalum and lead. They interpret this large cross section as due to prompt quasi-free, two-body collisions in the diffuse edge of the nucleus. Eisberg and Igo's results imply that the prompt emission probabilities for protons shown in Fig. 1 are an order of magnitude too small, at least at low energies. If the inelastic proton cross section is negligible at 20 Mev., rises rapidly to about 0.25 barn at 30 Mev., and then levels off at a roughly constant value above that energy, it will add to the  $(p, xn)$  sum curve to give a reaction cross section which is fairly smoothly varying with energy, and probably consistent with a Shapiro-type curve with  $r_0 \approx 1.5 \times 10^{-13}$  cm. This conclusion, when combined with the computations of Melkanoff *et al.*, leads to the interesting possibility that the large radius inferred by McCormick and Cohen (1954) using Shapiro's curves and implied here can be reconciled with a smaller radius plus a diffuse boundary. The author is grateful to Dr. McManus for reminding him of the work of Eisberg and Igo and for emphasizing its significance.

his continued interest and encouragement. Financial assistance by Atomic Energy of Canada, Limited, during a major portion of this research is gratefully acknowledged.

## REFERENCES

- ANDRE, G. C., HUIZENGA, J. R., MECH, J. F., RAMLER, W. J., RAUH, E. G., and ROCKLIN, S. R. 1956. Phys. Rev. **101**: 645.  
BELL, R. E. and SKARSGARD, H. M. 1956. Can. J. Phys. **34**: 745.  
BERNARDINI, G., BOOTH, E. T., and LINDENBAUM, S. J. 1952. Phys. Rev. **88**: 1017.  
BLATT, J. M. and WEISSKOPF, V. F. 1952. Theoretical nuclear physics. John Wiley and Sons, Inc., New York. Chap. VIII and IX.  
CULLER, G., FERNBACH, S., and SHERMAN, N. 1956. Phys. Rev. **101**: 1047.  
DEJUREN, J. and KNABLE, N. 1950. Phys. Rev. **77**: 606.  
FESHBACH, H., PORTER, C. E., and WEISSKOPF, V. F. 1954. Phys. Rev. **96**: 448.  
FINK, R. W. and WIIG, E. O. 1954. Phys. Rev. **96**: 185.  
GOLDBERGER, M. L. 1948. Phys. Rev. **74**: 1269.  
GUGELOT, P. R. 1954. Phys. Rev. **93**: 425.  
HAYAKAWA, S., KAWAI, M., and KIKUCHI, K. 1955. Progr. Theoret. Phys. (Japan), **13**: 415.  
HORNING, W. and BAUMHOFF, L. 1949. Phys. Rev. **75**: 370.  
JACKSON, J. D. 1954. Phys. Rev. **95**: 651A.  
KELLY, E. L. Unpublished.  
LEACHMAN, R. B. 1956. Phys. Rev. **101**: 1005.  
McCORMICK, G. H. and COHEN, B. L. 1954. Phys. Rev. **96**: 722.  
MCMANUS, H., SHARP, W. T., and GELLMANN, H. 1954. Phys. Rev. **93**: 924A.  
MCMANUS, H. and SHARP, W. T. Unpublished.  
MEADOWS, J. W. 1953. Phys. Rev. **91**: 885.  
——— 1955. Phys. Rev. **98**: 744.  
MELKANOFF, M. A., NODVIK, J., and SAXON, D. 1955. Phys. Rev. **100**: 1805A.  
NAKASIMA, R. and KIKUCHI, K. 1955. Progr. Theoret. Phys. (Japan), **14**: 126.  
PEASLEE, D. C. 1952. Phys. Rev. **86**: 269.  
SERBER, R. 1947. Phys. Rev. **72**: 1114.  
SHAPIRO, M. M. 1953. Phys. Rev. **90**: 171.  
SHARP, R. A., DIAMOND, R. M., and WILKINSON, G. 1956. Phys. Rev. **101**: 1493.  
WAGNER, G. D. and WIIG, E. O. 1954. Phys. Rev. **96**: 1100.  
WEISSKOPF, V. F. 1956. Proceedings of the International Conference on the Peaceful Uses of Atomic Energy. Vol. 2. United Nations, New York, N.Y. p. 23.

## EMISSION BAND SPECTRA OF NITROGEN THE LYMAN-BIRGE-HOPFIELD SYSTEM<sup>1</sup>

BY ALF LOFTHUS<sup>2</sup>

### ABSTRACT

The near ultraviolet part of the emission spectrum of nitrogen has been photographed under high resolution. Thirteen bands of the  $a^1\Pi_g - X^1\Sigma_g^+$  system (Lyman-Birge-Hopfield) have been analyzed and new vibrational and rotational constants obtained. Combining the observed data with those obtained by Stoicheff from the Raman spectrum of nitrogen, refined equilibrium constants for the ground state were obtained. The predissociation in the  $a^1\Pi_g$  state was observed.

### INTRODUCTION

The  $a^1\Pi_g - X^1\Sigma_g^+$  band system has previously been observed in both emission and absorption by several workers, but owing to low dispersion and resolution of the spectrographs used, the accuracy of the rotational and vibrational constants obtained seems to be somewhat limited. Stoicheff (1954), however, has measured the rotational and vibrational Raman spectra under high resolution, giving some accurate data for the ground state. Recently, Wilkinson and Houk (1956)<sup>3</sup> have remeasured the  $b' - X$  and  $a - X$  systems under high resolution with a 21-ft. vacuum grating spectrograph, thus giving extensive and more reliable rotational and vibrational constants for the states involved. The present author obtained some of the  $a - X$  bands in the near ultraviolet region under very high resolution, giving refined rotational and vibrational constants for the  $a$  and  $X$  states. The predissociation in the  $a^1\Pi_g$  state was also observed and studied.

### EXPERIMENTAL

The bands were excited in an ordinary  $\Pi$ -shaped water-cooled discharge tube (length of capillary 30 cm.; bore 5 mm.), viewed end-on. A slow flow of pure tank nitrogen at a pressure of about 0.1 mm. was maintained through the tube. Ordinary alternating current was used with a current of 0.2 amp. at about 1000 volts across the electrodes.

The photographs were taken in the third order of a 30,000 line per inch grating on a 21-ft. spectrograph, giving a dispersion of 0.43 Å/mm., and a resolving power up to 350,000. Eastman Kodak "Experimental SWR" photographic plates were used. Under these conditions the exposure time was about four hours. From 2050 to 1940 Å however, the exposure time was 12 hr. Second-order iron standard lines were used as comparison spectrum.

<sup>1</sup>Manuscript received April 19, 1956.

Contribution from Laboratory of Molecular Structure and Spectra, Department of Physics, The University of Chicago, Chicago 37, Illinois. This work was assisted in part by the Geophysics Research Directorate of the Air Force Cambridge Research Center, Air Research and Development Command, under Contract No. AF19(604)-1019 with the University of Chicago.

<sup>2</sup>Royal Norwegian Council for Scientific and Industrial Research Fellow at the University of Chicago. Permanent address: Department of Physics, The University of Oslo, Blindern, Norway.

<sup>3</sup>For a review of earlier works, the reader is referred to the paper by Wilkinson and Houk (1956).

TABLE I  
WAVE NUMBERS OF THE LINES IN THE  $a^1\Pi_g - X^1\Sigma_g^+$  N<sub>2</sub> BANDS

J	2-10 band, $\nu_0 = 50251.55$			3-11 band, $\nu_0 = 49820.91$		
	Q(J)	R(J)	P(J)	Q(J)	R(J)	P(J)
0	—	b	—	—	b	—
1	w	b	—	w	b	—
2	50250.12	b	b	w	b	w
3	248.63	b	b	w	b	w
4	246.71	b	b	49819.08	b	w
5	244.31	b	b	813.62	b	w
6	241.41	50263.28b	50222.54b	810.77	49832.39	w
7	237.08	—	215.93b	807.37	—	w
8	234.17b	262.45	208.94b	803.55	831.54	49778.66
9	229.80	261.21	201.33b	799.18	830.30	w
10	225.03	259.54	193.55b	794.35	828.54	763.23
11	219.71	257.34	185.03	788.99	826.28	w
12	213.89	254.69	176.17	783.22	823.57	745.97
13	207.61	251.56	166.78	776.95	820.27	w
14	200.85b	247.90	156.89	770.16	816.70	726.73
15	193.55b	243.78	146.50	762.95	812.56	w
16	185.89	239.19	135.67	755.20	807.89	705.54
17	177.65	234.17b	124.36	746.96	802.78	w
18	168.99	228.51b	112.50	738.28	797.13	682.45
19	159.83	222.54b	100.20	729.13	—	w
20	150.12	215.93b	87.45	719.43	—	657.46
21	139.99	—	70.18	w	—	—
22	129.36	—	60.42	698.65	—	—
23	118.28	—	046.57b	w	—	—
24	106.65	—	031.52	675.94	—	—
25	094.60	—	—	w	—	—
26	082.01	—	—	651.30	—	—
27	069.00	—	—	—	—	—
28	055.46	—	—	—	—	—
29	041.53b	—	—	—	—	—
J	4-11 band, $\nu_0 = 51404.11$			4-12 band, $\nu_0 = 49391.85$		
	Q(J)	R(J)	P(J)	Q(J)	R(J)	P(J)
0	—	b	—	—	b	—
1	b	b	—	w	b	w
2	51402.54	b	b	b	b	w
3	401.01	b	b	w	b	w
4	398.92	b	b	49387.03	b	w
5	396.31	b	b	384.57	b	w
6	393.19	b	b	381.69	49403.06	49363.24
7	389.55	b	b	378.25	b	b
8	385.40b	51413.04	b	374.45	402.14	349.86
9	380.73	411.37	b	370.04	400.77	342.39
10	375.50	409.28	b	365.26	399.01	334.55
11	369.80	406.61	b	359.93	396.86	b
12	363.55	403.47	b	354.13	394.01	317.32
13	356.80	399.72	b	347.84	390.69	b
14	—	395.52	b	341.07	387.03	298.14
15	—	—	—	333.82	w	287.82
16	—	—	—	326.11	378.25	277.03
17	—	—	—	317.88	373.01	w
18	—	—	—	309.01	367.33	254.00
19	—	—	—	299.94	w	—
20	—	—	—	290.32	354.49	—
21	—	—	—	280.14	—	—
22	—	—	—	269.53	—	—
23	—	—	—	258.39	—	—
24	—	—	—	246.82	—	—
J	5-12 band, $\nu_0 = 50947.27$			5-13 band, $\nu_0 = 48964.34$		
	Q(J)	R(J)	P(J)	Q(J)	R(J)	P(J)
0	—	—	—	—	b	—
1	w	—	—	b	b	—
2	50945.81	—	—	48962.87	b	w
3	944.10	—	—	961.45	b	w
4	942.12	—	—	959.51	48974.74	48947.24
5	939.48	—	—	957.09	b	w
6	936.36	—	—	954.19	975.36	936.01
7	932.71	—	—	950.79	b	w
8	928.50	—	—	946.98b	974.26	922.67
9	923.89	—	—	942.60	972.92	915.26
10	918.67	—	—	937.73	971.12	907.41
11	912.95	—	—	932.44	968.81	898.94b
12	906.73	—	—	926.60b	966.06	890.29b

TABLE I (Concluded)

J	5-12 band, $\nu_0 = 50947.27$			5-13 band, $\nu_0 = 48964.34$		
	Q(J)	R(J)	P(J)	Q(J)	R(J)	P(J)
13	50899.94			48920.33	48962.876	48881.028
14	892.68			913.58	959.06	871.15
15	884.99			906.31	954.698	860.918
16	876.55			898.61	950.05	850.12
17	867.73			890.296	944.82	838.93
18	858.41			881.66	939.15	827.12
19	848.53			872.46	932.94	w
20	838.14			862.82	926.43	802.25
21	829.26			852.65	w	w
22	815.77			844.00	911.48	775.49
23	803.87			830.89	w	
24	791.28			819.28		
25	778.28			807.11	894.73	
26	764.80			794.60		
27	750.76					
28	736.21					
29	721.02					
30	705.49					

J	5-14 band, $\nu_0 = 47010.84$			6-13 band, $\nu_0 = 50492.18$		
	Q(J)	R(J)	P(J)	Q(J)	R(J)	P(J)
0	—	b	—	—	—	—
1	w	b	—	w	w	—
2	w	b	w	w	w	—
3	47008.23	b	w	50489.04		
4	006.35	47021.54	w	486.95		
5	004.12	b	w	w		
6	001.47	022.628	46983.23	481.29		
7	46998.33	022.628	w	477.62		
8	994.76	022.05	970.43	473.47		
9	990.71	021.05	963.48	468.78		
10	986.28	019.59	955.90	463.56		
11	981.33	w	948.00	457.85		
12	975.97	015.37	939.59	451.62		
13	970.17	w	930.69	444.82		
14	963.90	009.388	921.46	437.57		
15	957.20		911.73	429.79		
16	950.05		901.61	421.45		
17	942.43		891.03	412.63		
18	934.39		879.95			
19	925.89	w				
20	916.97		856.47			
21	907.57		w			
22	887.80		831.21			
23	887.51					
24	876.79					
25	865.63					
26	853.97					

J	6-14 band, $\nu_0 = 48538.63$			6-15 band, $\nu_0 = 46614.53$		
	Q(J)	R(J)	P(J)	Q(J)	R(J)	P(J)
0	—	b	—	—	b	—
1	w	b	—	w	b	—
2	48537.19	b	w	46613.18	b	b
3	535.75	b	w	611.88	b	b
4	533.86	b	w	610.07	b	b
5	531.37	b	w	607.84	b	b
6	528.52	48549.37	48510.46	605.16	46026.058	46587.16
7	525.10	b	504.11	602.01	626.058	b
8	521.24	548.19	497.26	598.45	625.42	574.47
9	516.89	546.85	489.90	594.41	624.42	b
10	512.06	545.01	482.12	589.96	622.94	569.01
11	506.74	542.68	473.73	585.96	620.98	552.10
12	500.90	539.85	464.98	579.70	618.61	543.78
13	494.68	536.53	455.76	573.89	615.77	534.96
14	487.90	532.78	445.97	567.64	612.51	525.72
15	480.73		435.79	560.96		516.04
16	472.93		425.02	553.81		505.90
17	464.69			546.20		

— indicates absent lines.  
w indicates weak lines.  
b indicates blended lines.

## RESULTS

Complete rotational analyses were carried out for the 2-10, 3-11, 4-11, 4-12, 5-13, 5-14, 6-14, and 6-15 bands. Only the *Q* branches were measured for the 5-12 and 6-13 bands, and only the heads for the 1-9, 2-11, and 5-15 bands. The wave numbers<sup>4</sup> of the lines of the bands and the band origins determined from the rotational structure are given in Table I. Band origins calculated from band head measurements are given in Table II.

TABLE II  
BAND ORIGINS FOR THE *a-X* TRANSITION OF  
NITROGEN CALCULATED FROM BAND HEAD  
MEASUREMENTS

$v' - v''$	$\nu_0, \text{cm}^{-1}$
1-9	50683.29
2-11	48210.20
5-15	45086.87

The measured bands were relatively free from overlapping structure, and it was therefore quite easy to separate the branch lines except close to the band heads, which were formed by the *R* branch. The branch lines showed alternating intensities, even *J* giving strong lines, and odd *J* giving weak lines in all branches. The *P* and *R* branches had about the same over-all intensities, but were considerably weaker than the *Q* branches. Since all branches were rather short, the  $\lambda$ -type splitting of the rotational levels in the  $a^1\Pi_g$  state could not be detected with certainty. The  $v' = 6$  progression showed a clear, but not sharp, breaking-off of the rotational structure due to a well-known predissociation; this will be discussed more fully in a later section.

The analyses were carried out using both the least squares method and graphical methods as outlined by Herzberg (1950). The *D* values could not be determined very accurately from these short bands; therefore calculated *D* values (Herzberg 1950, p. 103) were used throughout the further calculations.

### The $X^1\Sigma^+$ State

The observed  $B_v$  values are listed in Table III, and plotted versus  $v$  in Fig. 1. Although it can immediately be seen that these points fit a slightly curved line very nicely, the interval from  $v = 10$  to  $v = -\frac{1}{2}$  is too large for determination of  $B_e$  by extrapolation. If however we use Stoicheff's (1954) precise value ( $B_0 = 1.9897 \pm 0.0003 \text{ cm}^{-1}$ ), we can determine a curve of the form  $B_v = B_e - \alpha_e(v + \frac{1}{2}) + \gamma_e(v + \frac{1}{2})^2$  which goes through  $B_0 = 1.9897$  and fits the observed points as well as possible, thus giving  $B_e = 1.9983 \pm 0.0003 \text{ cm}^{-1}$ ,  $\alpha_e = 0.01709 \text{ cm}^{-1}$ , and  $\gamma_e = -4.60 \times 10^{-5} \text{ cm}^{-1}$ . This curve is drawn in Fig. 1, and the calculated  $B_v$  values are given in Table III for comparison with the experimental ones. The observed  $B_v$  values by Wilkinson and Houk (1956), Spinks (1942), Watson and Koontz (1934), and Tschulanowsky (1935) are also given.

<sup>4</sup>The wavelength corrections from air to vacuum were taken from Edlén's tables (1951).

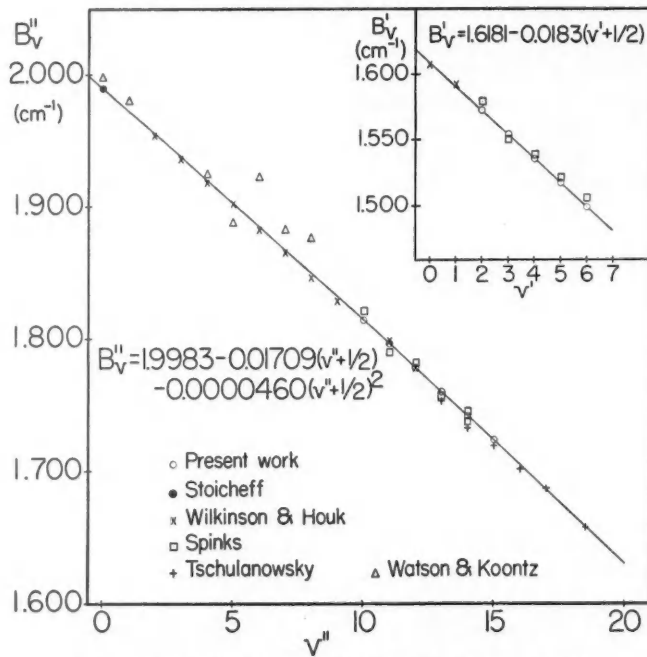
FIG. 1.  $B_v$  graphs for the ground state and the  $a^1\Pi_g$  state of  $N_2$ .

TABLE III  
OBSERVED AND CALCULATED ROTATIONAL CONSTANTS FOR THE GROUND STATE OF  
NITROGEN ( $\text{CM}^{-1}$ )

$v$	$B_v$					
	Calculated*	Present work	Wilkinson and Houk	Spinks	Watson and Koontz	Tschulanowsky
0	1.9897				1.998	
1	1.9726				1.980	
2	1.9553		1.954			
3	1.9379		1.936			
4	1.9205		1.918		1.924	
5	1.9029		1.902		1.888	
6	1.8853		1.882		1.912	
7	1.8675		1.865		1.882	
8	1.8497		1.845		1.876	
9	1.8318		1.828			
10	1.8138	1.8137		1.821		
11	1.7957	1.7957	1.798	1.790		
12	1.7775	1.7775	1.778	1.780		
13	1.7592	1.7594		1.758		1.7550
14	1.7409	1.7406			1.744(737)	1.7327
15	1.7224	1.7224				1.7190
16	1.7038					1.7010
17	1.6851					1.6867
18	1.6664					1.6571
19	1.6476					1.6475
20	1.6286					1.6274
21	1.6096					1.6089

\*  $B_v = 1.9983 - 0.01709(v + \frac{1}{2}) - 4.60 \times 10^{-8}(v + \frac{1}{2})^2$ .

In order to show the deviations of the  $B_v$  values from the calculated ones on a large scale, Fig. 2 shows  $B_e$  values calculated from the expression  $B_e = B_e^{\text{obs}} + 0.01709(v + \frac{1}{2}) + 4.60 \times 10^{-5}(v + \frac{1}{2})^2$  plotted versus  $v$ . It can be seen that there is good agreement between calculated and observed  $B_v$  values from this work. Most of the values given by Wilkinson and Houk (1956) show a small but apparently systematic deviation from the same curve. The values given by the other workers deviate more arbitrarily.

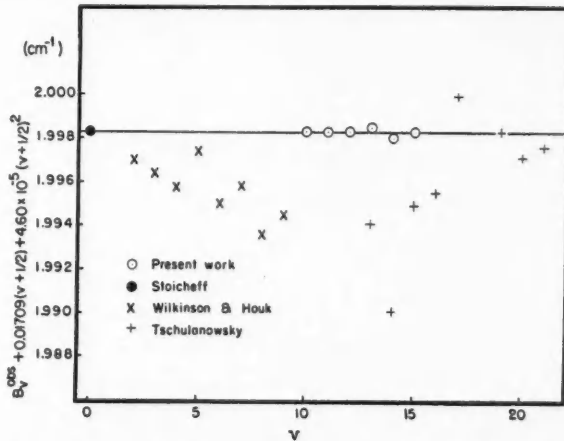


FIG. 2. Graphical determination of  $B_e$  for the ground state of  $N_2$ .

The vibrational constants were found by a similar method. Stoicheff's value  $\Delta G_{\frac{1}{2}} = 2329.66 \pm 0.2 \text{ cm}^{-1}$  was employed, and the equation for the term values,  $G(v)$ , was determined such as to reproduce  $\Delta G_{\frac{1}{2}}$  exactly and the observed  $\Delta G$  values from this work as well as possible. The coefficients of the third-order equation are

$$\omega_e = 2358.07 \pm 0.2 \text{ cm}^{-1}, \quad \omega_e x_e = 14.188 \text{ cm}^{-1}, \quad \omega_e y_e = -0.0124 \text{ cm}^{-1}.$$

The calculated  $\Delta G$  values are given in Table IV, together with the observed values, and those given by Wilkinson and Houk (1956) and by Tschulanowsky (1935). The deviations of the observed  $\Delta G$  values from the calculated ones are shown in Fig. 3 by plotting

$$\Delta G^{\text{obs}} + 28.376(v+1) + 0.0372(v+1)^2$$

versus  $v$ , and it can be seen that there is good agreement between computed and observed values from this work.

#### *The $a^1\Pi_g$ State*

Because of the predissociation in this state, no bands with  $v' > 6$  were present. The observed  $B_v$  values are listed in Table V, and plotted versus  $v$  in Fig. 1. In this case a linear extrapolation to  $v = -\frac{1}{2}$  was done, thus giving  $B_e = 1.6181 \pm 0.0003 \text{ cm}^{-1}$  and  $\alpha_e = 0.0183 \text{ cm}^{-1}$ . The curve  $B_v = 1.6181 - 0.0183(v + \frac{1}{2})$  is drawn in Fig. 1. Table V and Fig. 1 give also  $B_v$  values

TABLE IV  
OBSERVED AND CALCULATED VIBRATIONAL QUANTA FOR THE GROUND STATE OF NITROGEN (CM<sup>-1</sup>)

v	$\Delta G$			
	Calculated*	Present work	Wilkinson and Houk	Tschulanowsky
0	2329.66			
1	2301.17			
2	2272.61			
3	2243.97			
4	2215.26			
5	2186.47		2187.7	
6	2157.62		2157.0	
7	2128.88		2128.8	
8	2099.67		2099.4	
9	2070.59		2070.2	
10	2041.43	2041.4	2040.6 (2042.6)	
11	2012.20	2012.3	2011.5	
12	1982.90	1982.9		
13	1953.51	1953.5		1953.8
14	1924.06	1924.1		1923.6
15	1894.53			1892.5
16	1864.93			1870.5
17	1835.25			1829.5
18	1805.50			1805.0
19	1775.67			1775.3
20	1745.77			1745.7

$$* \Delta G = 2358.07 - 28.376(v+1) - 0.0372(v+1)^2.$$

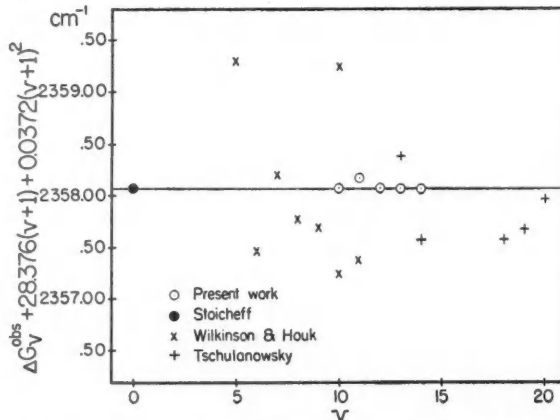


FIG. 3. Graphical determination of  $\omega_e$  for the ground state of N<sub>2</sub>.

observed by Wilkinson and Houk (1956) and by Spinks (1942). The deviations of the observed  $B_v$  values from the computed ones can be seen from Fig. 4, where  $B_v^{\text{obs}} + 0.0183(v+\frac{1}{2})$  is plotted versus  $v$ . There is also in this case good agreement between computed and observed  $B_v$  values from this work. The coefficients of a second-order equation for the term values  $G(v)$  were determined to be  $\omega_e = 1693.70 \pm 0.2$  cm<sup>-1</sup>,  $\omega_e x_e = 13.825$  cm<sup>-1</sup>, and according to Table VI there is good agreement between calculated and observed values.

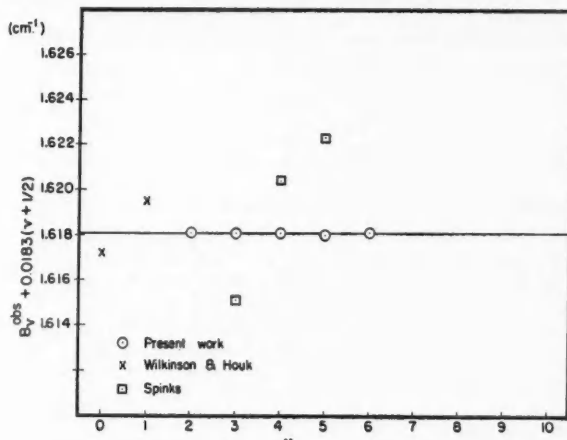
FIG. 4. Graphical determination of  $B_v$  for the  $a^1\Pi_g$  state of  $N_2$ .

TABLE V

OBSERVED AND CALCULATED ROTATIONAL CONSTANTS FOR THE  $a^1\Pi_g$  STATE OF NITROGEN (CM<sup>-1</sup>)

$v$	$B_v$				
	Calculated*	Present work	Wilkinson and Houk	Spinks	Watson and Koontz
0	1.6090		1.608		1.635
1	1.5907		1.592		1.613
2	1.5724	1.5724		1.579	1.590
3	1.5541	1.5541		1.551	
4	1.5358	1.5358		1.538	
5	1.5175	1.5174		1.521	
6	1.4992	1.4992		1.507	

\* $B_v = 1.6181 - 0.0183(v + \frac{1}{2})$ .

TABLE VI

OBSERVED AND CALCULATED VIBRATIONAL QUANTA FOR THE  $a^1\Pi_g$  STATE OF NITROGEN (CM<sup>-1</sup>)

$v$	Calculated*	Observed
0	1666.05	
1	1638.40	
2	1610.75	1610.7
3	1583.10	1583.2
4	1555.45	1555.4
5	1527.80	1527.8

\* $\Delta G = 1693.70 - 27.65(v + 1)$ .

## SUMMARY AND DISCUSSION

The molecular constants derived for the  $a$  and  $X$  states of nitrogen are summarized in Table VII.

TABLE VII

SUMMARY OF THE MOLECULAR CONSTANTS FOR THE  $a^1\Pi_g$  AND THE  $X^1\Sigma_g^+$  STATES OF NITROGEN  
( $\text{CM}^{-1}$ )

State	$\omega_e$	$\omega_e x_e$	$\omega_e y_e$	$B_e$	$\alpha_e$	$\gamma_e$	$D_e$	$r_e (\text{\AA})$	$T_e$	$\nu_{00} (a-X)$
$a^1\Pi_g$	1693.70 <sup>a</sup>	13.825		1.6181 <sup>b</sup>	0.0183		$6 \times 10^{-6}$	1.21970 <sup>c</sup>	69285.10	68953.00
$X^1\Sigma_g^+$	2358.07 <sup>a</sup>	14.188	-0.0124	1.9983 <sup>b</sup>	0.01709	-4.60 $\times$ 10 <sup>-5</sup>	$6 \times 10^{-6}$	1.09755 <sup>c</sup>		

<sup>a</sup> ± 0.2 cm<sup>-1</sup>.

<sup>b</sup> ± 0.0003 cm<sup>-1</sup>.

<sup>c</sup> ± 0.0001 Å.

Wilkinson and Houk— $\omega_e' = 1693.90$ ,  $\omega_e' x_e' = 13.97$ ,  $B_e' = 1.617$ ,  $\alpha_e' = 0.0173$ ,  $r_e' = 1.2202$ ;  $\omega_e'' = 2357.78$ ,  $\omega_e'' x_e'' = 14.08$ ,  $\omega_e'' y_e'' = -0.02$ ,  $B_e'' = 1.999$ ,  $\alpha_e'' = 0.01802$ ,  $r_e'' = 1.0971$ ,  $\nu_{00} = 68948.3$ .

Stoicheff— $B_e'' = 1.99874 \pm 0.00035$ ,  $r_e'' = 1.09758 \pm 0.0001$  Å,  $\omega_e'' = 2357.84$ ,  $\omega_e'' x_e'' = 14.062$ ,  $\omega_e'' y_e'' = -0.0175$ .

As can be seen from preceding tables and figures, there are certain disagreements between observed data from this work and those from other works. Most of these latter were carried out under low resolution, except that by Wilkinson and Houk (1956). In the latter case, the disagreement between results obtained and those obtained from this work is smallest, but since the resolution and dispersion were three times better than obtained by Wilkinson and Houk, it is believed that the present results are the most reliable. In order to check the present results a few more  $B_v$  values between  $v = 0$  and 10 attained from vacuum region measurements under the same high resolution would be desirable. The well-known predissociation in the  $v = 6$  level of the  $a^1\Pi_g$  state was also observed. The branches could be followed up to  $R(14)$ ,  $P(16)$ , and  $Q(17)$ , but the intensity started decreasing a few  $J$  numbers before the breaking-off. Douglas and Herzberg (1951), however, observed a sharp breaking-off of all branches above  $J' = 13$ . Since the gas pressure was lower in this case (0.001 mm. against 0.1 mm. for the present work) it can be concluded that the predissociation is sensitive to the pressure, a fact which also was observed by Herman (1943, 1945). It can be expected that the predissociation limit found by Douglas and Herzberg is the lowest, since at the low pressure used by them the kinetic collision time ( $\sim 2 \times 10^{-4}$  sec. at 0.001 mm.) is longer than the radiation time.<sup>5</sup> However, a more extensive investigation on the pressure dependence of the predissociation in this case seems desirable.

Following Douglas and Herzberg's (1951) reasoning, and using vibrational and rotational constants from this work, the predissociation limit is found to be  $78828 \pm 50$  cm<sup>-1</sup>.

<sup>a</sup>Private communication from A. E. Douglas.

## ACKNOWLEDGMENTS

The author is indebted to Dr. P. G. Wilkinson for valuable discussions and advice during the work, to Dr. A. E. Douglas for correspondence regarding the observed predissociation, and to Professor R. S. Mulliken for reading the manuscript.

## REFERENCES

- DOUGLAS, A. E. and HERZBERG, G. 1951. Can. J. Phys. **29**: 294.  
EDLÉN, B. 1951. Vacuum corrections to three decimal places for 2000–13900 Å. University of Lund, Sweden.  
HERMAN, R. 1943. Compt. rend. **217**: 141.  
— 1945. Ann. phys. **11**: 20, 241.  
HERZBERG, G. 1950. Molecular spectra and molecular structure. I. Spectra of diatomic molecules. 2nd ed. D. Van Nostrand Company, Inc., New York.  
SPINKS, J. W. T. 1942. Can. J. Research, A, **20**: 1.  
STOICHEFF, B. P. 1954. Can. J. Phys. **32**: 630.  
TSCHULANOWSKY, W. M. 1935. Bull. acad. sci. U.R.S.S. **1**: 1313.  
WATSON, W. W. and KOONTZ, P. G. 1934. Phys. Rev. **46**: 32.  
WILKINSON, P. G. and HOUK, N. B. 1956. J. Chem. Phys. **24**: 528.

## A HOMOGENEOUS DIELECTRIC SPHERE AS A MICROWAVE LENS<sup>1</sup>

By G. BEKEFI AND G. W. FARRELL

### ABSTRACT

A homogeneous dielectric sphere illuminated by a small external source of electromagnetic radiation will be free, because of its special symmetry, from all off-axis aberrations such as coma and astigmatism. If the only monochromatic aberration, namely spherical aberration, is not too excessive or if it is partially corrected by a suitably designed source, a sphere could be used for purposes of rapid scanning of a microwave beam through an angle of 360° of arc without moving the lens. This possibility was investigated by computations based on geometrical optics and on the diffraction theory of optical aberrations. The results suggest that a sphere of fairly small refractive index and less than about 30 wavelengths in diameter will produce a good diffraction image of a point source. Methods are also discussed of designing appropriate sources for use with larger spheres.

### INTRODUCTION

In recent years considerable attention has been given to the design and construction of microwave antennas that would prove amenable to high speed, wide angle scanning of a beam of electromagnetic radiation (Microwave Optics Symposium 1953; Brown 1953). Although scanning can be achieved by rotating the antenna as a whole, very high speeds cannot be attained because of the weight and size of the antennas generally encountered in practice. However, a beam can be swung in space by displacing the primary source transversely to the principal axis of the collimating reflector or lens, without the necessity of moving the whole antenna. This property of optical systems is clearly of great advantage if high speed scanning is desired, since the primary source forms only a small fraction of the total weight of the antenna. It is well known that this method of scanning has serious limitations governed by the off-axis aberrations such as coma and astigmatism which cause a progressively greater deterioration of the shape of the image with source displacement (Cheston and Shinn 1952; Bachynski and Bekefi 1955, 1956). Hence one finds that in most conventional collimating devices, such as metal reflectors and simple lenses, there is a maximum angle through which the beam can be rotated in space, beyond which the image has deteriorated to such an extent that it becomes unusable for practical applications. This angle depends upon the degree to which the aberrations can be reduced in a given optical system.

Microwave aplanats, that is lenses free from coma and spherical aberration, have been designed and are relatively easy to construct (Martin 1944; Friedlander 1946; Ruze 1950; Sternberg 1956). However, a rotationally symmetric lens of this type designed to give a sharp pencil beam of radiation will still suffer from astigmatism which sets an upper limit upon the performance of

<sup>1</sup>Manuscript received May 15, 1956.

Contribution from the Eaton Electronics Research Laboratory, Department of Physics, McGill University, Montreal, Canada.

This work forms part of a project on microwave optics that is supported at McGill University by the United States Air Force, Air Force Cambridge Research Center, on Contract AF 19(122)-81. The paper was presented at the Annual Congress of the Canadian Association of Physicists, June 1956, Montreal, Canada.

the lens and upon the degree of scanning that can be achieved (Cloutier 1956). The latter aberration cannot be eliminated from a single thin lens, and anastigmatic systems, consisting of two or more lenses separated in space, are for a number of reasons impractical for use at microwave frequencies.

If very wide scanning angles are required, thin lenses and metal reflectors must be abandoned and other means sought of scanning pencil beams. The Maxwell Fish-eye (Brown 1953) and the Luneburg scanner (Luneburg 1944; Peeler, Kelleher, and Coleman 1953) are two devices that offer attractive possibilities. The latter lens, for instance, permits scanning through  $360^\circ$  of arc without image deterioration. Unfortunately, the refractive index of the material of both lenses must vary continuously as a function of position within the lens; this and other problems that arise make construction and attainment of the necessary tolerances very difficult.

A homogeneous dielectric sphere illuminated by an external source of radiation (see Fig. 1) is a simple optical system which is free from all off-axis aberrations, since any straight line drawn from the center of the sphere and extended to intersect the source is a principal axis of the lens. If the only monochromatic aberration present in the system, namely spherical aberration, is not too large or if it is partially or wholly corrected by a suitably designed source, a sphere could be used for rapid scanning through  $360^\circ$  by moving the primary source along a circular arc whose center coincides with that of the sphere. In this paper, the feasibility of using such a sphere as a microwave antenna is investigated. The computations, some of which were made with the aid of an analogue computer built by one of us (Farnell 1956), suggest that this lens, if not of too high a dielectric constant, will produce a good diffraction image of a point source, provided that the diameter of the sphere does not exceed about 30 wavelengths. Spheres much larger than this are beset by excessive amounts of spherical aberration and special sources are needed to reduce this lens error. Methods of designing such sources are discussed briefly at the end of this paper.

#### THE IMAGING PROPERTIES OF THE DIELECTRIC SPHERE

The optical system under consideration is shown in Fig. 1. A lossless dielectric sphere of radius  $a$  and refractive index  $\mu$  is illuminated by a source of electromagnetic radiation (for instance a dipole oriented with its axis perpendicular to the line  $OF$ ) situated at a distance  $s$  from the center of the sphere. It is required to calculate the radiation pattern of this antenna, or in the language of physical optics, the distribution of energy in the diffraction image.

A boundary-value solution of this problem based on Maxwell's electromagnetic equations is possible. Calculations of a similar type such as occur in the theory of the rainbow (Van der Pol and Bremmer 1937) and in the theory of terrestrial radio propagation (Bremmer 1949) indicate however that, because of the large size of the sphere with which we are concerned (15 wavelengths in diameter or greater), the work is quite prohibitive. The method described here, though approximate, is believed to yield sufficiently accurate results to enable one to make a fairly critical evaluation of the properties of this antenna.

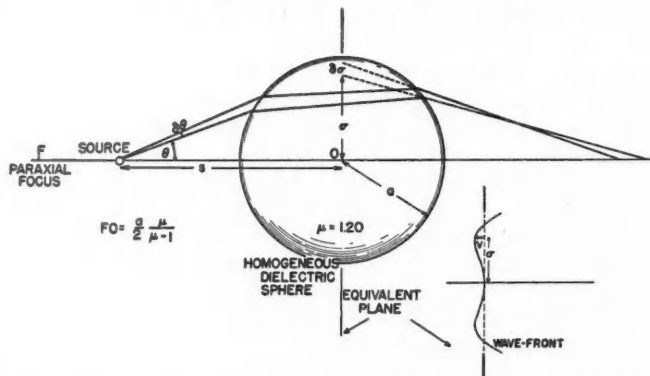


FIG. 1. Schematic diagram of the optical system showing a meridional section of the dielectric sphere.

The method of deducing the antenna radiation pattern rests upon the use of geometrical optics and analytic ray tracing on the one hand, and classical diffraction theory of optical aberrations on the other hand. With the assumption of an isotropic point source irradiating the sphere, geometrical optics is used in calculating the optical path lengths and density of the emergent rays. From this, the shape of the wave-front and the amplitude distribution across it are obtained; the phase and amplitude variations over a plane (referred to as the equivalent plane) lying perpendicular to the axis  $FO$  are then found. The scattering effects produced by the sphere are simulated to our degree of approximation by diffraction due to a hole in the equivalent plane.

The discussion will be subdivided into two sections. The first deals with calculations of the phase and amplitude over the equivalent plane, while the second concerns itself with the evaluation of the diffraction image.

### 1. Phase and Amplitude Distributions over the Equivalent Plane

In all subsequent work a sphere made from a material of refractive index  $\mu = 1.20$  is assumed. A simple calculation shows that with this value of  $\mu$ , the paraxial focus is at a distance  $FO = 3a$  from the center of the sphere and the  $f$ -number (ratio of focal length to lens diameter) is equal to 1.5. A refractive index much smaller than the one chosen results in an excessively large  $f$ -number which should be kept reasonably small for antenna applications; a large refractive index on the other hand tends to make the focal length too short with a subsequent increase in spherical aberration.

The calculation of the shape of the emergent wave-front is a straightforward procedure and no mathematical details will be given. With Snell's law applied at each refracting surface, the optical path length and the actual path traced out by an arbitrary ray are found and the shape of the wave-front obtained at any desired place in the image space. The quantity that is of interest in the present work is the path length difference between the actual wave-front and the ideal plane wave that would be obtained from an aberrationless system.

This quantity is known as the aberration function  $V(\sigma)$ ; it specifies the amount of spherical aberration present in the system over a given plane perpendicular to the axis  $FO$ , as a function of distance  $\sigma$  from this axis.\*

The choice as to location of the plane over which the aberration function  $V$  is to be computed is somewhat arbitrary. Since this plane is the one over which the diffraction integral will eventually be evaluated in computing the diffraction image, it is important to keep the plane as close as possible to the optical system; otherwise, the assumptions made in the diffraction theory will not be applicable and erroneous results will be obtained. However near the plane may be to the sphere (even touching it on its image side), it will cut the caustic surface; the phase and amplitude will then show troublesome singularities whenever two rays happen to intersect at some point of the chosen plane. For this and other reasons, the calculations of  $V$  and of the amplitude are referred back to a plane, from now on called the "equivalent plane", that passes through the center of the sphere  $O$  (see Fig. 1).

The phase error  $kV$ , that is the aberration function multiplied by the wave-number  $k$  ( $k = 2\pi/\text{wavelength}$ ), is shown graphically in Fig. 2 for the special case when the source is situated at the paraxial focus ( $s = FO = 3a$ ); here  $kV$ , expressed in units of  $ka$ , is plotted against the distance  $\sigma$  (in units of  $a$ ) from

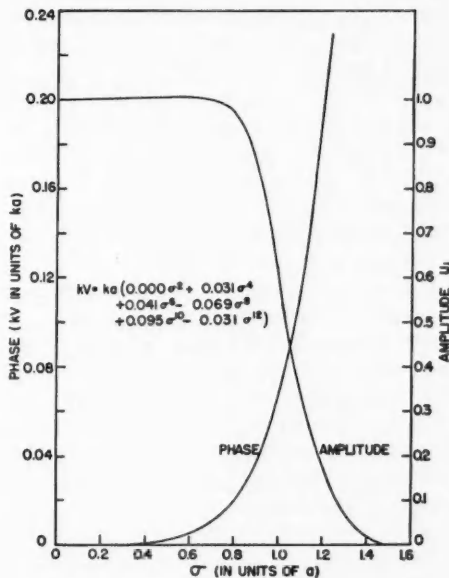


FIG. 2. The relative phase ( $kV$ ) and amplitude ( $u_i$ ) over the equivalent plane with the source situated at the paraxial focus  $F$  at a distance  $s = 3a$ .

\*This restricted definition of  $V$  applies only to our special case. A general definition applicable to any optical system is given by Wolf (1951).

the axis  $FO$ . It should be noted that  $\sigma$  can exceed the sphere's radius. This is due to the fact that some marginal rays leaving the lens, when projected back onto the equivalent plane, appear to originate at points outside the volume of the sphere.

The magnitude of the spherical aberration is seen to rise very rapidly with distance from the axis. When  $\sigma$  is about  $1.2a$ ,  $kV \sim 0.2ka$ . At this point, the departure of the wave-front from a plane wave is 20 radians for a sphere 32 wavelengths in diameter ( $ka \sim 100$ ). In order to obtain some idea about the magnitudes of the various orders of spherical aberration present in the system, one can write the following general expression for  $kV$  (Nijboer 1943, 1947; Nienhuis and Nijboer 1949):

$$kV = ka[A\sigma^2 + B\sigma^4 + C\sigma^6 + \dots]$$

where  $A, B, C, \dots$  are coefficients which determine the magnitudes of the various orders. The first term in the series does not strictly speaking represent an aberration; it is known as the defocusing error and is a function of the displacement of the source from the paraxial focus. The second term is the well-known von Seidel, third-order spherical aberration, the next term is the fifth-order aberration, and so on. By fitting the first six terms of the above power series to the curve shown in Fig. 2, the coefficients were evaluated and are given in the same figure. The coefficient of the first term is zero as expected because the source is at the focus and no defocusing error exists.

The higher order aberrations are of appreciable magnitude. The fact that they alternate in sign is helpful insofar that their individual effects tend to cancel. In fact, if for a given magnitude of the highest order aberration some control were had over the lower orders, much could be done to minimize the total effect; this process is referred to as balancing of aberrations. In our case we have control only over the first coefficient which can be adjusted by displacing the source. Even this restricted way of balancing will be seen to help considerably in obtaining a good image at infinity.

We shall now turn to a discussion of the amplitude distribution over the equivalent plane as shown in Fig. 2. For convenience, the amplitude was normalized to unity at  $\sigma = 0$ . The rapid decrease of the amplitude with distance from the axis is of considerable importance; it is one of the major factors that explains why, despite the large phase errors, the diffraction image shows relatively little deterioration. The region of the wave-front which deviates most from a plane wave contributes little to the process of image formation and only the central portion of the wave-front, over which the amplitude is high, is of significance.

The reduction of the amplitude over the wave-front with increasing distance from the axis is due to a combination of two effects. First, the density of rays decreases with increasing  $\sigma$ ; secondly, the amount of energy reflected at the air-dielectric boundaries increases with the angle of incidence of the ray. The theoretical expression used in calculating the amplitude curve of Fig. 2 will now be derived. On the basis of geometrical optics, the power radiated by the source into the region of space enclosed by two concentric cones (see Fig. 1),

one of semiangle  $\theta$  and the other of semiangle  $(\theta + \delta\theta)$ , appears over the equivalent plane in an annular ring of radius  $\sigma$  and width  $\delta\sigma$ . From conservation of energy, it can then be shown that if  $P(\theta)$  is the power radiated per unit solid angle and  $P(\sigma)$  the power received per unit area of the equivalent plane, then (Silver 1949)

$$P(\sigma) = P(\theta) \frac{\sin \theta}{\sigma} \frac{d\theta}{d\sigma}.$$

In the case of an isotropic point radiator assumed here,  $P(\theta)$  is constant.

The above equation must be modified to take account of reflections at the refracting surfaces. This can only be done approximately. The transmission coefficient  $T$ , that is the fraction of the total incident energy transmitted at an air-dielectric boundary when a plane wave impinges on the surface, is a function of the angle of incidence, the refractive index, and the direction of polarization of the wave relative to the boundary (Stratton 1941). Parallel and perpendicular planes of polarization are the two principal cases generally considered; the respective transmission coefficients are denoted by  $T_{||}$  and  $T_{\perp}$ . When bundles of rays are incident on a section of the sphere, the polarization can assume any direction that lies between the two principal cases. Since our work deals with scalar waves only and since  $T_{||}$  and  $T_{\perp}$  do not differ greatly, we define an effective transmission coefficient as

$$T_E = \frac{1}{2}(T_{||} + T_{\perp}).$$

The amplitude distribution  $u_i$  over the equivalent plane was then evaluated from the relation

$$u_i(\sigma) = \alpha \left| P(\theta) T_{E_1} T_{E_2} \frac{\sin \theta}{\sigma} \frac{d\theta}{d\sigma} \right|^{\frac{1}{2}}$$

where  $T_{E_1}$  and  $T_{E_2}$  are the effective transmission coefficients at the two refracting boundaries of the sphere and  $\alpha$  is a normalization constant adjusted so that  $u_i = 1$  when  $\sigma = 0$ .

The results discussed so far refer to the case of a source situated at the paraxial focus of the lens. This position is not to be chosen if a good image is desired at infinity. The amount of displacement necessary, that is the correct choice of the coefficient  $A$ , in the power series for  $kV$  given previously, falls under the general study of "balancing of aberrations". This problem has received considerable attention at the hands of Richter (1925), Nijboer (1943, 1947), Zernike (1954), and others. For example, suppose that an optical system suffers from third-order spherical aberration only, whose magnitude is fixed but small ( $C = D = E = \dots = 0$ ;  $B$  small) and the illumination  $\mu_i$  is constant. It is then found that the intensity at the center of the image will be greatest if the source is positioned so as to make  $A\sigma_m^2 = -B\sigma_m^4$  where  $\sigma_m$  is the maximum value of  $\sigma$ . Physically, this corresponds to a source placed midway between the paraxial and marginal foci of the optical system. If the higher aberrations are also present and if the illumination is not constant, appropriate relations between the coefficients can be found (Bachynski, Bekefi, and Farnell 1956), provided that the magnitude of the aberrations is

not large. Since the sphere is known to suffer heavily from spherical aberration, calculations of the source displacement can only be done approximately. In our case, in which only the first coefficient ( $A$ ) is at our disposal, a rough estimate shows that the source should be moved towards the lens by a distance equal to  $0.8a$  for best performance of the system. With this new value of the source-position ( $s = 2.2a$ ) the aberration function  $kV$  and the amplitude distribution  $u_i$  over the equivalent plane were derived in a manner analogous to that described previously. The computed results are shown graphically in Fig. 3. It will be noted that defocusing caused the aberration function to take

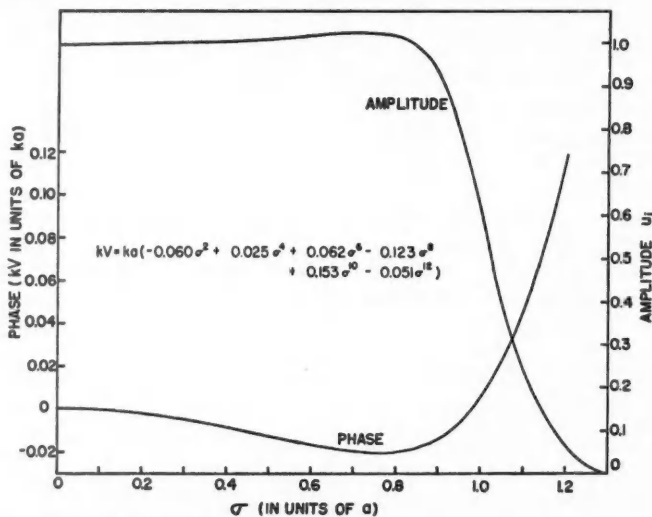


FIG. 3. The relative phase and amplitude distributions over the equivalent plane when the source is situated at a distance  $s = 2.2a$ , showing the effects of refocusing.

on negative values over the central portion of the wave-front (the rays diverge) and that the maximum value of  $kV$  has been reduced by a factor of about two as compared to what it was with the source at the focus. Furthermore, the defocusing coefficient  $A$  has become quite large and the remaining coefficients have changed significantly from their previous values.

Using the results for the phase and amplitude distributions shown in Fig. 3, the task of calculating the energy distribution in the diffraction image was undertaken. This is described in the next section.

## 2. The Diffraction Image

The scattering of energy due to the dielectric sphere is taken into account approximately by replacing the sphere with a circular hole imagined to be cut in the equivalent plane. The size of the hole is such as to include the complete wave-front whose properties are shown in Fig. 3. Outside this maximum value of  $\sigma$  (called  $\sigma_m$ ) the amplitude  $u_i$  is assumed to be zero, that is no energy is

allowed to reach the image space by paths other than through the dielectric sphere.\* The problem therefore reduces to calculating the field at some point  $(\rho, \psi, z)$  of the image space (see Fig. 4) behind a circular aperture of radius  $\sigma_m$  over which the amplitude  $u_i(\sigma)$  and phase  $kV(\sigma)$  are known.

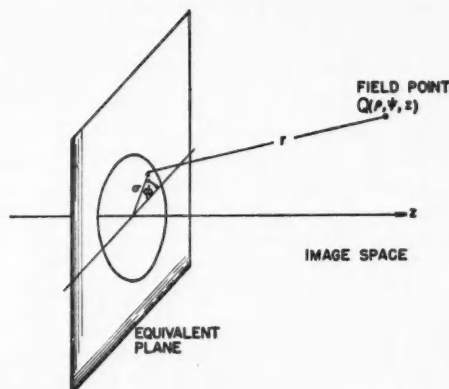


FIG. 4. Schematic diagram of the coordinate system used in calculating the intensity in the diffraction image.

The classical scalar, Kirchhoff-Fresnel diffraction theory will be used. Despite its well-known limitations, previous work on diffraction (Bekefi and Woonton 1952; Bekefi 1953) and on lens aberrations (Bachynski and Bekefi 1955, 1956) has shown that the theory agrees well with measurements, provided that these are not made too near the diffracting hole. Subject to the usual assumptions, the field  $u_Q$  at some point  $Q$  is given by

$$u_Q = \frac{1}{2\pi} \int_S u_0 \frac{\partial}{\partial n} \left( \frac{\exp(-ikr)}{r} \right) dS$$

where  $S$  denotes an integration over our circular aperture and  $r$  is the distance from an element  $dS$  of the aperture to the field point  $Q$ ;  $n$  is a normal to the equivalent plane directed into the image space and  $u_0$  is the field distribution (in amplitude and phase) over the diffracting hole. In the present case  $u_0$  is given by

$$u_0 = u_i(\sigma) e^{-jkV(\sigma)}$$

with  $u_i$  and  $V$  as depicted in Fig. 3. In an aberrationless optical system with uniform amplitude distribution and a source placed at the paraxial focus,  $u_0$  would be constant.

With the aid of a cylindrical coordinate system and under the assumptions  $kr \gg 1$ ,  $\sigma \ll r$ ,  $\rho \ll r$ , one finds from the above equations that:

\*With this assumption the effects of "spill-over" of energy past the collimating device are avoided. In the laboratory, spill-over can be eliminated by mounting the sphere in a metal screen. In practice, a sufficiently directive primary source would be used to minimize this troublesome effect.

$$u_Q(q, p) = \frac{ika^2}{2\pi} \frac{\exp(-ikR)}{R} \int_0^{\sigma_m} \int_0^{2\pi} u_i(\sigma) \exp[ip\sigma^2 + iq\sigma \cos \phi - ikV(\sigma)] \sigma d\sigma d\phi.$$

Here  $a$  is the radius of the sphere,  $R = \sqrt{(z^2 + p^2)}$ , and  $\sigma_m$  and  $\sigma$  are the aperture radius and radial coordinate of integration respectively, both expressed in units of  $a$ . The parameters  $p$  and  $q$  are functions of the coordinates of the field point and are defined as:

$$p = -ka^2/2z, \quad q = kap/R.$$

Henceforth  $p$  instead of  $z$  will be used to represent the position of the image plane relative to the lens and  $q$  rather than  $\rho$  will express the radial distance of the field point from the axis  $z$ . When the plane of observation lies at infinity,  $p = 0$  and the ratio  $\rho/R$  is then generally written as  $\sin \gamma$  where  $\gamma$  is known as the angle of diffraction. In view of the fact that  $V(\sigma)$  is independent of the azimuthal angle  $\phi$ , the field distribution  $u_Q$  is circularly symmetrical and independent of  $\psi$ .

An evaluation of the above integral using the results for  $u_i$  and  $V$  shown in Fig. 3 was performed with the aid of an analogue computer. A direct numerical solution would be a nearly impossible undertaking.

Before proceeding with a description of the computed results, the idea of refocusing will be re-examined in the light of the diffraction integral given above. It is seen that the term  $p\sigma^2$  can be included in the aberration function  $V$ , which for purposes of the present discussion can be written as  $(p-A)\sigma^2 + O(\sigma^4)$  where  $A$  is once again the first term of the series expansion of  $V$  and  $O(\sigma^4)$  denotes the higher order aberrations. Therefore, as far as calculations of the diffraction image are concerned, refocusing can be effected either by moving the source (changing  $A$ ) or by shifting the plane of observation (varying  $p$ ) or by a combination of both these methods. Hence, it would appear that the coefficient of  $\sigma^2$  can be found by keeping the source at the focus ( $A = 0$ ) and varying  $p$  alone until the best image is found. In any experimental arrangement this image could be shifted to infinity by an appropriate source displacement. This procedure, generally followed, is only valid if the source displacement is so small that the higher order aberrations do not change significantly in the process (i.e.  $O(\sigma^4)$  remains constant). In our case of large aberrations, the source must be moved through a fairly large distance (approximately  $0.8a$ ) with the result that the higher order coefficients undergo an appreciable change (compare Figs. 2 and 3). With this new position of the source found by a crude estimate, the effect of any further refocusing that may be necessary, if not excessive, can be calculated by varying  $p$  in the vicinity of  $p = 0$ . It should be remarked that only zero or negative values of  $p$  have physical significance in terms of distances  $z$  measured in the image space; a positive  $p$  signifies that the source must be moved closer to the paraxial focus in order to bring the plane of observation into some real region of the image space.

The best image is generally considered to be in the region where the intensity at the center of the diffraction image ( $q = 0$ ) is highest. In the language of optical designers, this is the region of maximum "Strehl definition"; in the words of antenna engineers, this is the region of maximum "relative gain".

The analogue computer was therefore used first in calculating the intensity distribution along the axis  $z$  ( $q = 0$ ) as function of  $p$  over a limited region in the neighborhood of  $p = 0$ . The results are shown in Fig. 5. Here the intensity

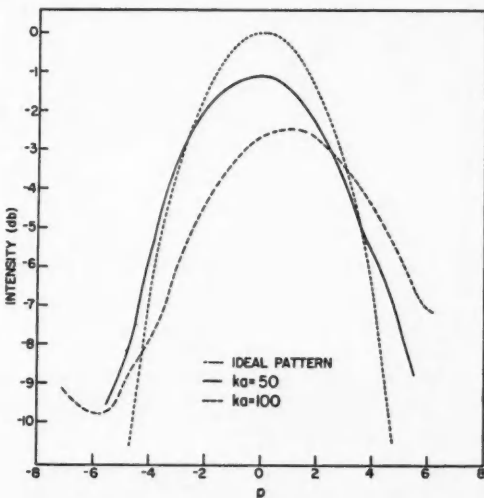


FIG. 5. The axial field distribution in the image space of two spheres of size  $ka = 50$  and  $ka = 100$ . Comparison is made with the ideal distribution given by  $|\sin(p/2)/(p/2)|^2$  obtained from an aberrationless optical system of equivalent size.

$|u_0(p)|^2$  is plotted on a decibel scale for two sizes of sphere  $ka = 50$  and  $ka = 100$  as a function of  $p$ . The quantity  $(ka^2/R)^2$  appearing outside the diffraction integral was excluded from the graphs. In calculating the actual intensity distribution along the axis of a given optical system this quantity must be inserted as a multiplying factor. For the sake of comparison, Fig. 5 also shows the axial field distribution that would be obtained in an ideal, aberration-free system ( $kV = 0$ ) having a uniform distribution ( $u_i = \text{constant}$ ) and of a size equivalent to that of the sphere ( $\sigma_m = 1$ ). The gain of our antenna relative to the "ideal" system is down by about 1.1 db. when  $ka = 50$  and by about 2.4 db. when  $ka = 100$ . This decrease in gain is due primarily to the presence of spherical aberration and to a lesser extent to the non-uniform illumination over the equivalent plane.

The intensity distribution in the diffraction image situated in the maximum gain planes ( $p = 0$  when  $ka = 50$ ;  $p = 1.24$  when  $ka = 100$ ) for the two sizes of sphere is shown in Fig. 6. Comparison is made with the ideal Airy-ring distribution. A deterioration of the patterns relative to the ideal pattern is seen; the larger the sphere (and hence  $kV$ ) the lower the intensity at the center of the pattern and the higher are the side lobe levels relative to the central maximum. The minima tend to fill in and the width of the main lobe has increased slightly. Nevertheless, the patterns are still well defined and the

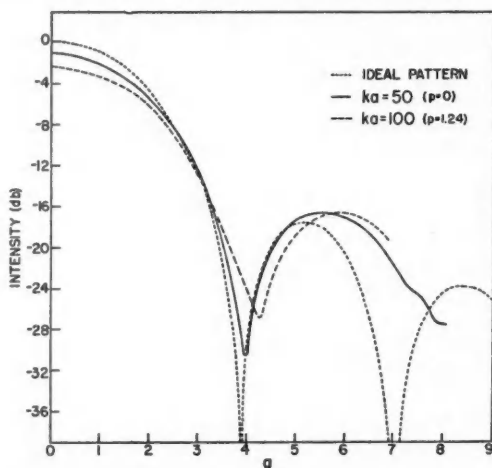


FIG. 6. The intensity distribution (i.e. the radiation pattern) in the maximum gain plane for two spheres  $ka = 50$ ,  $ka = 100$ . Comparison is made with the ideal distribution given by  $|J_1(q)/q|^2$  obtained from an aberrationless optical system of equivalent size. ( $J_1$  is a Bessel function of the first kind and first order.)

deterioration not excessive. Although the intensity at the center of the patterns is a maximum in the plane for which the above calculations were made, it does not necessarily follow that lower relative side lobes could not be obtained in different regions of space (Bachynski, Bekefi, and Farnell 1956). It is in fact found that, if a slight loss in gain can be tolerated, lower side lobes can be obtained in planes displaced with respect to the maximum gain planes. These patterns are shown in Fig. 7. In these planes the main lobe has become slightly

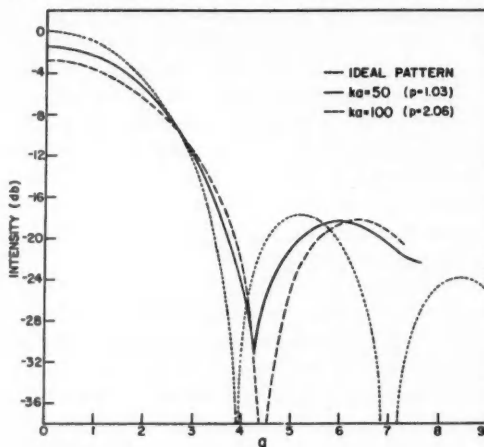


FIG. 7. The intensity distribution over planes containing patterns with low relative side lobe levels, for two spheres  $ka = 50$  and  $ka = 100$ . Comparison is made with the ideal distribution  $|J_1(q)/q|^2$ .

broader and the relative side lobe levels lowered by 20 to 30%. The characteristics of these and the previous patterns are summarized in Table I.

TABLE I

Ideal system	Maximum gain plane		Plane of low relative side-lobe level	
	$ka = 50$	$ka = 100$	$ka = 50$	$ka = 100$
Position of image plane	$p = 0$	$p = 0$	$p = 1.03$	$p = 2.06$
Gain relative to ideal system, db.	—	— 1.1	— 2.4	— 1.5 — 2.7
Depth of first side lobe relative to central maximum, db.	-17.6	-15.5	-14.2	-16.8 -15.4
Beam width* at 10 db. points in units of $q$	5.3	5.7	5.9	5.9 6.3
Total beam width† in units of $q$	7.7	8.0	8.5	8.5 8.9

\*Width of the main lobe as measured at points 10 db. below the intensity at the center of the pattern.

†Width of main lobe measured across the first minima in the pattern.

From the above results one can conclude that as far as the calculations are able to show, a dielectric sphere illuminated by a small source acts as a fairly good collimating lens. The diffraction image produced by a sphere less than about 15 wavelengths in diameter is good and could be used for many applications; the loss in gain is not excessive and the side lobe levels not much higher than what is obtainable from a system free of aberrations. The side lobes could of course be greatly reduced by using a directive source in place of the isotropic radiator and thus taper the illumination over the equivalent plane still further. This is a practice generally followed in antenna systems (Silver 1949). Spheres of the order of 30 wavelengths in diameter show a considerably greater loss in gain, although the patterns themselves are still satisfactory. Spheres much larger than 30 wavelengths suffer too heavily from spherical aberration and could not be used with a simple source of the type discussed so far. In these cases (and even for smaller spheres if an improvement in patterns is sought), special sources could be employed to reduce the amount of aberration present. The design of such sources is discussed briefly in the next chapter.

#### REDUCTION OF SPHERICAL ABERRATION BY PROPER SOURCE DESIGN

The question arises whether or not it is possible to replace the simple source used in the preceding chapter by a reasonably compact system of sources, which, when used to irradiate the sphere, would by proper adjustment of their relative phase compensate for the spherical aberration of the lens. The sources could be arranged spatially in a variety of ways; we shall concern ourselves only in an axial distribution, that is in a discrete or continuous distribution of sources (say dipoles) arranged along the axis  $FO$  of the optical system. A rather detailed discussion of this problem as applied to spherical reflectors was given by Spencer and co-workers (Spencer, Sletten, and Walsh 1951). To analyze this situation we shall reverse the path of the rays and assume a plane wave incident on the sphere from the right (see Fig. 8) and calculate the phase and amplitude distributions of the emergent rays along the axis  $FO$ .

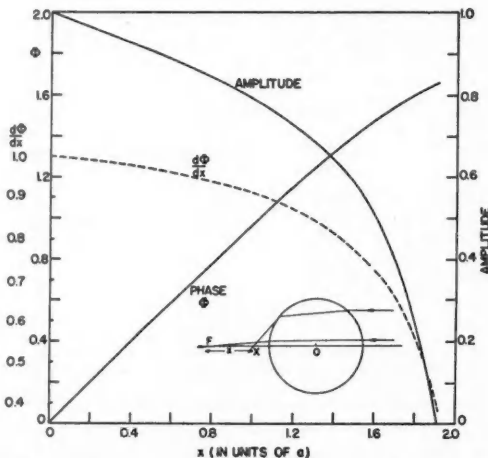


FIG. 8. Phase and amplitude distributions of rays crossing the optical axis when a sphere is irradiated by plane waves;  $\Phi$  denotes the path-length difference (in units of  $a$ ) between a paraxial ray and some arbitrary ray crossing the axis at some point  $X$  at a distance  $x$  from the focus  $F$ . The amplitude curve refers to the (energy) $^{\frac{1}{2}}$  per unit axial distance contained in a bundle of rays crossing the axis at a distance  $x$  from the focus.

A set of receivers of the energy can then be pictured to be situated along the axis. If the receivers are properly phased, then by the principle of reciprocity these receivers when acting as sources would combine to give a plane wave after collimation by the sphere.

Under the assumption of a plane incident wave, the path length difference between a paraxial ray proceeding to the focus  $F$  and some arbitrary ray crossing the axis at  $X$  (distant  $x$  from  $F$ ) was calculated. This quantity is denoted as the phase  $\Phi$  in Fig. 8; it is plotted along the ordinate in units of  $a$  versus the distance  $x$  from the focus. The amplitude associated with a bundle of rays cutting the axis between  $x$  and  $x+\delta x$  was computed in a similar manner to the one described in the previous section. It will again be noted that the amplitude of the marginal rays is very small and they will play but a small part in the formation of the image.

Hence to eliminate the effects of spherical aberration it would be necessary to have an axial distribution of sources such as an array of dipoles or slot radiators in a waveguide, phased relative to each other in a manner conforming to the variation of  $\Phi$  with  $x$  shown in Fig. 8. Their characteristics, as far as the radiated power is concerned, would have to conform to the amplitude curve. There are many disadvantages to such an extended source; it is difficult to construct, it may be quite frequency sensitive, and owing to its length (nearly equal to the diameter of the sphere) it may be rather bulky. However, the realization that the phase is nearly linear with distance  $x$  over a good portion of the axis may lead to considerable simplification. The departure from linearity is best seen by reference to the curve showing the gradient of  $\Phi$  (i.e.  $d\Phi/dx$ ) versus  $x$ . Over more than half the distance separating the marginal

from the paraxial focus, the phase does not depart from linearity by more than 10%. Over the remaining portion ( $1.05a < x < 1.92a$ ) the intensity associated with the rays is down by a factor of two or more from the maximum intensity. Hence it is reasonable to assume that a linear or nearly linear source distribution extending from  $x = 0$  to about  $x = a$  could give a good correction for spherical aberration. A relatively simple source of this type is the dielectric rod antenna (Kiely 1953) consisting of a dielectric bar of circular or rectangular cross section, tapered towards one end and excited by a dipole at the other. Such a rod can be thought of, at least approximately, as a continuous linear distribution of sources.

Experimental work on a spherical lens similar to the one discussed on these pages is under way. The investigations are made on a sphere 18 in. in diameter and at wavelengths ranging between about 1 and 3 cm. The results are very satisfactory and will be reported at a later date.

#### ACKNOWLEDGMENTS

The authors are greatly indebted to Miss M. E. Dougherty who performed most of the calculations, and to Professor G. A. Woonton for his interest in this work.

#### REFERENCES

- BACHYNSKI, M. P., and BEKEFI, G. 1955. Eaton Electronics Research Laboratory Rept. No. 35. McGill University, Montreal, Que.
- 1956. Professional Group on Antennas and Propagation, Institute of Radio Engineers. In press.
- BACHYNSKI, M. P., BEKEFI, G., and FARNELL, G. W. 1956. Volume II of the Final Report from the Eaton Electronics Research Laboratory, McGill University, Montreal, Que., to the United States Air Force, Cambridge Research Center, Cambridge, Mass. In press.
- BEKEFI, G. 1953. Symposium on Microwave Optics. Vol. II. Paper No. 53. McGill University, Montreal, Que.
- BEKEFI, G., and WOONTON, G. A. 1952. Eaton Electronics Research Laboratory Rept. No. 24. McGill University, Montreal, Que.
- BREMMER, H. 1949. Terrestrial radio waves. Elsevier Press Inc., New York.
- BROWN, J. 1953. Microwave lenses. Methuen & Co. Ltd., London.
- CHESTON, T. C. and SHINN, D. H. 1952. Marconi Rev. 15: 174.
- CLOUTIER, G. G. 1956. M.Sc. Thesis, McGill University, Montreal, Que.
- FARNELL, G. W. 1956. Paper presented at the Spring Meeting of the Optical Society of America. Paper No. FB 32.
- FRIEDLANDER, F. G. 1946. J. Inst. Elect. Engrs., Pt. IIIA, 93: 658.
- KIELY, D. G. 1953. Dielectric aerials. Methuen & Co. Ltd., London.
- LUNEBURG, R. K. 1944. The mathematical theory of optics. Brown University Press, Providence, R.I.
- MARTIN, L. C. 1944. Proc. Phys. Soc. 56: 104.
- MICROWAVE OPTICS SYMPOSIUM. 1953. McGill University, Montreal, Que.
- NIENHUIS, K. and NIJBOER, B. R. A. 1949. Physica, 14: 590.
- NIJBOER, B. R. A. 1943. Physica, 10: 679.
- 1947. Physica, 13: 605.
- PEELER, G. D. M., KELLEHER, K. S., and COLEMAN, H. P. 1953. Microwave Optics Symposium. Vol. II. Paper No. 37. McGill University, Montreal, Que.
- RICHTER, R. 1925. Z. Instrumentenk. 45: 1.
- RUZE, J. 1950. Proc. I.R.E. 38: 53.
- SILVER, S. Editor. 1949. Microwave antenna theory and design. McGraw-Hill Book Company, Inc., New York.
- SPENCER, R. C., SLETTEN, C. J., and WALSH, J. E. 1951. Air Force Cambridge Research Center. Rept. E. 5069.
- STERNBERG, R. L. 1956. J. Math. and Phys. 34: 209.
- STRATTON, J. A. 1941. Electromagnetic theory. Chap. IX. McGraw-Hill Book Company, Inc., New York.
- VAN DER POL, B. AND BREMMER, H. 1937. Phil. Mag. (7), 24: 857.
- WOLF, E. 1951. Repts. Progr. in Phys. 14: 95.
- ZERNIKE, F. 1954. Optical image evaluation. Natl. Bur. Standards (U.S.), Circ. 526.

# SHELL EFFECTS ON THE SPACING OF NUCLEAR LEVELS<sup>1</sup>

BY T. D. NEWTON

## ABSTRACT

Recent measurements of resonances in slow neutron total cross sections yield good estimates of the average level spacing,  $D$ , in medium and heavy nuclei. These spacings show large variations, by factors of  $10^4$  to  $10^6$ , in the region of magic numbers of nucleons. There are also variations by smaller factors between nuclei with even and odd numbers of protons or neutrons. The even-odd effect is a co-operative phenomenon; it can be approximately treated by redefining the ground state to be used for a Fermi gas model. After this correction the gas model should predict  $D$  with reasonable accuracy since it is required only to define the density of a complete set of states. The magic number variations are shown to be fitted by an improved approximation to the single-nucleon level density. This is obtained from the observed sequence of single-particle spins and the assumption that the energy interval between spin subshells is constant. Fifty-two observed spacings are fitted by a two-parameter formula with an average uncertainty factor 3. Many of the larger remaining differences between observation and the predictions of the model are qualitatively explicable as expected departures from this uniform spacing hypothesis.

## 1. THE EXPERIMENTAL DATA

The thermal neutron resonances in separate isotopes obtained by the fast chopper technique (Harvey, Hughes, Carter, and Pilcher 1955; Hughes and Harvey 1955)\* give much the most reliable measurements of the average nuclear level spacings presently available. It is shown by these authors that very nearly all levels of the one or two possible spins which can be excited by neutrons of energy up to about a kilovolt are observed. The method has the drawback that it measures the level spacing in a given nucleus at one energy only, so that we must seek indirect confirmation of the energy variation of the spacing from other work.

In order to obtain a more extended set of data some spacings have also been evaluated from neutron resonances observed by other than fast chopper techniques. The observed average spacing has been recomputed from the levels listed by Harvey *et al.* (1955) and computed from the excitation curves of BNL 325 (Hughes and Harvey 1955) by fitting the first  $N$  observed levels, by least squares, to the formula

$$(1) \quad E_n = E_0 + nD, \quad n = 1, \dots, N.$$

In (1)  $E_n$  is the position of the  $n$ th level observed;  $E_0$  and  $D$  are parameters to be determined. In cases where only a few resonances have been observed and a well-defined region  $E_i < E_n < E_f$  has been searched, we have added to the equations of condition (1) one or both of the equations

$$(1a) \quad \begin{aligned} \frac{1}{2}(2E_f - E_1) &= \frac{1}{2}E_0, \\ \frac{1}{2}(2E_f - E_N) &= \frac{1}{2}E_0 + \frac{1}{2}(N+1)D. \end{aligned}$$

<sup>1</sup>Manuscript received April 23, 1956.

Contribution from Atomic Energy of Canada Limited, Chalk River, Ontario. Issued as A.E.C.L. No. 335.

\*The writer is very grateful to these gentlemen for the receipt of this paper before its publication, and particularly to Dr. Harvey for his unpublished summary of level spacing data available in the summer of 1955.

These, weighted by the factor  $\frac{1}{2}$ , contain the assumption that the lower and upper limits,  $E_i$  and  $E_f$ , of the searched interval occur, on the average, midway between levels. This incorporates in the least squares procedure the same postulate used by Harvey *et al.* (1955), that  $D = N^{-1}(E_f - E_i)$ .

Our procedure does not significantly alter the value of  $D$  obtained. It was adopted in order to provide a consistent definition of the variation to be expected in  $D$ . On the assumption that no levels have been missed, or wrongly attributed to the nucleus being studied, the expected error in the average value  $D$  of the spacing between levels (see, for example, Rose 1953) is given by the estimated variance,

$$(2) \quad \sigma_D^2 = \beta_{DD}(N-2)^{-1} \sum_n (E_n - E_0 - nD)^2.$$

$\beta_{DD}$  is the appropriate diagonal element of the inverse of the matrix of the normal equations. If equations (1a) are included, (2) must be modified to contain the appropriately weighted sum of the squares of the deviations of the equations of condition. The quoted limits on  $D$  are  $\pm\sigma_D$  defined by (2). This is much smaller than the root mean square of  $(E_n - E_{n-1} - D)^2$ , since  $\sigma_D^2$  is the estimated variance of the average spacing, not the variance of the observed intervals between levels. It should probably be remarked that the chief value of (2) is to give a reproducible definition of the variation to be expected in  $D$ . It is an underestimate, because it takes no account of the possibility of missed or wrongly included levels, and in any case there is here very little justification for the use of least squares procedures.

There are few light nuclei for which the average level spacing may be estimated in this way. There exists a large body of data on levels of light nuclei obtained from charged particle reactions. This is not very useful as a means of testing the level spacing formula, because many spin states are formed at the relatively high bombarding energies necessary with charged particles. In many cases spin assignments have been made, but this is usually possible only for the lower lying levels. The formulae which will be discussed here apply either to states of assigned spin, or to all states of every spin, in an energy interval sufficiently above the ground state. The charged particle reactions do not supply data which certainly satisfy these conditions, so we have limited this discussion to the data derived from slow neutron resonances.

The observed level spacings are recorded in Table I, as  $D_{obs}$ , and displayed in Fig. 1, which is similar to one in the paper of Harvey, Hughes, Carter, and Pilcher (1955). For target spin  $I = 0$ , the observed level spacing is shown; for  $I \neq 0$ , twice the observed spacing is plotted. This follows the practice of the experimentalists; it is a recognition of the fact that levels with spins  $I \pm \frac{1}{2}$  are formed. The most prominent feature of this figure is the sparseness of levels in the nuclei with magic numbers of neutrons. It is the purpose of this note to show how these irregularities can be related to the shell structure of nuclei by means of the statistical formula for the level density in the Fermi gas model of a nucleus.

This model (e.g. Bethe 1937; Fermi 1950; Blatt and Weisskopf 1952) has often been used to estimate the density of nuclear levels, but generally not

TABLE I  
INITIAL DATA

- References: (a) Hughes and Harvey 1955.  
 (b) Harvey, Hughes, Carter, and Pilcher 1955.  
 (c) ( $d\beta$ ) and ( $n\gamma$ ) reactions, van Patter and Whaling 1954.  
 (d) Harvey 1955.  
 (e) Huizenaga 1955.  
 (f) Computed from reaction,  $\beta$ -decay, and mass-spectroscopic data, King 1954; van Patter and Whaling 1954; Duckworth, Hogg, and Pennington 1954.

Compound nucleus		Observed $D$ (ev.)	Number of resonances used to fix $D$	Target spin	$D_0$ (ev.)	Neutron binding (Mev.)	Pairing corrections (Mev.)
Z	N						
9	11	$0.854 \pm 0.016 \times 10^6$	8 (a)	1/2	$3.416 \times 10^6$	$6.60 \pm 0.01$ (c)	0
11	13	$0.729 \pm 0.027 \times 10^6$	14 (a)	3/2	$5.832 \times 10^6$	$6.95 \pm 0.01$ (c)	0
13	15	$0.488 \pm 0.015 \times 10^6$	17 (a)	5/2	$5.856 \times 10^6$	$7.72 \pm 0.01$ (c)	0
15	17	$2.105 \pm 0.049 \times 10^4$	18 (a)	1/2	$8.42 \times 10^4$	$7.93 \pm 0.01$ (c)	0
21	25	$1.89 \pm .14 \times 10^3$	5 (a)	7/2	$30.24 \times 10^3$	$8.85 \pm 0.08$ (c)	0
23	29	$2.18 \pm .21 \times 10^3$	4 (a)	7/2	$34.88 \times 10^3$	$7.30 \pm 0.01$ (c)	0
25	31	$2.58 \pm .90 \times 10^3$	4 (a)	5/2	$30.96 \times 10^3$	$7.26 \pm 0.01$ (c)	0
27	33	$3.73 \pm .54 \times 10^3$	3 (a)	7/2	$59.68 \times 10^3$	$7.68 \pm 0.20$ (c)	0
33	43	$108.3 \pm 3.6$	9 (a)	3/2	866.4	$7.30 \pm 0.04$ (c)	0
41	53	$37.5 \pm 3.7$	7 (a)	9/2	750.0	$7.19 \pm 0.03$ (c)	0
42	54	$209.5 \pm 33.0$	4 (b)	5/2	2514	$9.15 \pm 0.05$ (c)	2.49
42	56	$175.5 \pm 18.0$	4 (b)	5/2	2106	$8.29 \pm 0.10$ (c)	2.48
43	57	$13.81 \pm 1.60$	5 (a)	9/2	276.2	$7.10 \pm 0.40$ (d)	0
47	61	$19.4 \pm 7.5$	4 (a)	1/2	77.6	$7.27 \pm 0.02$ (c)	0
47	63	$16.13 \pm 0.85$	6 (a)	1/2	64.52	$6.15 \pm 0.33$ (f)	0
49	65	$7.15 \pm 0.60$	7 (b)	9/2	143	$7.19 \pm 0.70$ (f)	0
49	67	$7.5 \pm 0.7$	8 (b)	9/2	150	$6.59 \pm 0.20$ (c)	0
50	63	$153 \pm 43$	2 (b)	0	153	$8.0 \pm 1$ (d)	1.18
50	67	$137 \pm 71$	2 (b)	0	137	$7.24 \pm 0.27$ (f)	1.16
50	68	$54.0 \pm 5$	5 (b)	1/2	216	$9.24 \pm 2$ (c)	2.31
50	69	$240 \pm 120$	2 (b)	0	240	$6.54 \pm 0.12$ (c)	1.15
50	70	$140 \pm 47$	2 (b)	1/2	560	$8.98 \pm 0.25$ (f)	2.30
51	71	$14.25 \pm 3.39$	7 (a)	5/2	171	$6.80 \pm 0.04$ (c)	0
51	73	$31.29 \pm 9.6$	3 (a)	7/2	500.6	$6.15 \pm 0.37$ (f)	0
53	75	$11.68 \pm 0.73$	7 (a)	5/2	140.2	$6.58 \pm 0.05$ (c)	0
55	79	$21.45 \pm 0.55$	12 (b)	7/2	343.2	$6.73 \pm 0.10$ (c)	0
56	80	$35.4 \pm 11.4$	3 (a)	3/2	283.2	$9.1 \pm 0.5$ (d)	2.16
57	83	$1000 \pm 700$	1 (a)	7/2	16000	$5.1 \pm 1$ (c)	0
59	83	$112.8 \pm 4.6$	9 (a)	5/2	1353.6	$5.83 \pm 0.03$ (c)	0
65	95	$5.052 \pm 1.15$	16 (b)	3/2	40.42	$5.8 \pm 5$ (f)	0
67	99	$5.754 \pm 1.42$	15 (b)	7/2	92.06	$5.7 \pm 5$ (d)	0
69	101	$6.81 \pm 2.5$	10 (b)	1/2	27.24	$5.9 \pm 5$ (d)	0
71	105	$2.65 \pm 0.11$	14 (b)	7/2	42.4	$6.0 \pm 0.5$ (d)	0
71	106	$1.05 \pm 0.55$	2 (a)	5/2	12.6	$7.3 \pm 5$ (d)	0.91
72	106	$2.946 \pm 1.36$	12 (b)	5/2	35.35	$7.6 \pm 5$ (d)	1.82
72	108	$3.595 \pm 1.25$	26 (b)	3/2	28.76	$7.4 \pm 5$ (d)	1.80
73	109	$3.921 \pm 0.203$	10 (b)	7/2	62.74	$6.07 \pm 0.03$ (c)	0
74	110	$19.6 \pm 9$	3 (a)	3/2	156.8	$7.42 \pm 0.02$ (c)	1.77
78	118	$24.7 \pm 7.4$	3 (a)	1/2	98.8	$7.92 \pm 0.01$ (c)	1.67
79	119	$33.9 \pm 8.2$	3 (a)	3/2	271.2	$6.49 \pm 0.01$ (c)	0
81	123	$5.0 \pm 3.78 \times 10^3$	1 (a)	1/2	$20 \times 10^3$	$6.54 \pm 0.03$ (c)	0
82	125	$4.73 \pm 1.30 \times 10^4$	5 (a)	0	$4.73 \times 10^4$	$6.73 \pm 0.02$ (e)	0.79
82	127	$18.3 \pm 6 \times 10^4$	3 (a)	0	$18.3 \times 10^4$	$3.87 \pm 0.05$ (e)	0.78
83	127	$3.42 \pm 2.73 \times 10^4$	3 (a)	9/2	$68.4 \times 10^4$	$4.17 \pm 0.02$ (c)	0
90	143	$15.1 \pm 2.3$	6 (a)	0	15.1	$5.08 \pm 0.22$ (e)	0.68
92	142	$0.973 \pm 0.027$	9 (a)	5/2	11.68	$6.81 \pm 0.20$ (e)	1.36
92	143	$15.1 \pm 1.3$	7 (a)	0	15.1	$5.18 \pm 0.22$ (e)	0.68
92	144	$0.871 \pm 0.026$	15 (a)	5/2	10.45	$6.42 \pm 0.22$ (e)	1.34
92	145	$15.7 \pm 1.6$	6 (a)	0	15.7	$5.42 \pm 0.23$ (e)	0.66
92	147	$17.71 \pm 0.62$	11 (a)	0	17.71	$4.70 \pm 0.24$ (e)	0.66
94	146	$2.49 \pm 0.41$	7 (a)	1/2	9.96	$6.41 \pm 0.23$ (e)	1.31
95	147	$0.4275 \pm 0.0406$	7 (a)	7/2	6.84	$5.52 \pm 0.24$ (e)	0

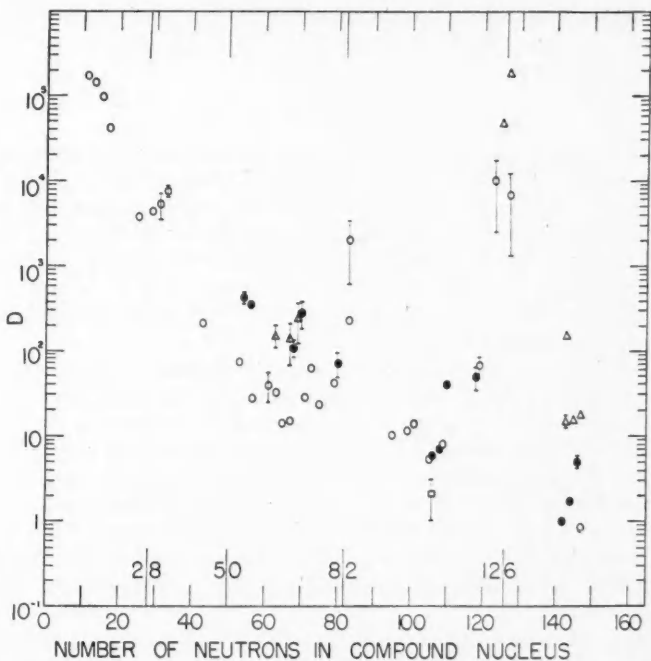


FIG. 1. Experimental level spacings. The plotted values of  $D$  are the observed average energy intervals between slow neutron resonances (calculated as stated in the text) if the target has zero spin; twice the observed average interval if the target has non-zero spin. Open circles  $\circ$  represent odd  $Z$  odd  $N$ , the square  $\square$  odd  $Z$  even  $N$ , triangles  $\Delta$  even  $Z$  odd  $N$ , and closed circles  $\bullet$  even  $Z$  even  $N$  compound nuclei.

with precision, because it was regarded as so poor a representation of the nucleus that its detailed predictions would not be valuable. It is, indeed, an inadequate representation, but for the particular purpose of estimating the density of levels the model may be capable of greater accuracy than is contained in the formulation most commonly used.

Some justification of this statement is to be found in the success of the shell model and its more recent development into "nuclear spectroscopy". In these calculations a potential is used to represent the average effect of all nucleons. Single-particle states in this potential are assumed for nucleons outside closed shells, and residual effects of internucleon forces accounted for by configuration mixing. This technique has had reasonable success (e.g. Elliott and Flowers 1955; Levinson and Ford 1955) in predicting the properties of low lying states of several nuclei. The point important for our present purpose is that this mixing does not change the number of states and, moreover, does not cause any marked uniform shift of energy. Consequently the average level density remains that of the basic combinations of the single-particle states, i.e. of a Fermi gas. The same argument is applicable in any energy region, and, pro-

vided the residual interactions do not cause a general shift of all levels in one direction, the level density calculated on the simple model should remain reasonably accurate.

## 2. THE PAIRING ENERGY

All the observations shown in Fig. 1 are made at an excitation equal to the binding energy of a neutron in the compound nucleus studied. Consequently odd neutron compound systems are at a lower excitation than even neutron systems, while there is little difference between the excitations of odd and even proton systems. On the other hand, Fig. 1 shows no general increase of the level spacings in odd neutron systems over those in even neutron systems, while the level spacings in odd proton systems are appreciably smaller than in even proton systems.

These observations are consistent with the frequently made remark that the pairing energy which depresses the ground states of nuclei containing even numbers of neutrons or protons is a co-operative phenomenon which cannot be contained in the model of a Fermi gas of non-interacting particles. Consequently one should redefine, for the purposes of calculation with this model, the ground state of the nucleus to have some smoothly varying value, say that of the ground states of odd-odd nuclei. It is certainly possible that there is a better procedure than this for accounting for the odd-even variation, but this simple device which seems almost directly implied by the experimental results will be used here.

It then becomes necessary to define the pairing energy for each nucleus. As used in the semiempirical mass formula, for instance, the pairing energy is a very simple concept. Yet, as Green and Edwards (1953) have shown, it is extremely difficult to separate from other effects and when one has done so, according to one of many possible schemes, it remains a very irregular function of the nucleus. The shell-theoretical prediction that the pairing energy varies as  $(2j+1)$  does not seem to fit the data with enough consistency to warrant the introduction of such a complication.

After several trials of various other devices, which were not satisfactory, an approximation to the pairing energy was obtained from experimental mass values (Wapstra 1955; Huizenga 1955) in the following way. The quantity (Green and Engler 1953)

$$(3) \quad \Delta = \{(A - 100)^2 10^{-6} - (M - A)\} \text{ A.M.U.}$$

has a total variation over the range of known masses of about 20 m.M.U. By plotting  $\Delta$  of the set of nuclei with a given even value of  $N-Z$  the mass difference,  $\delta$ , between even-even and odd-odd nuclei with that value of  $N-Z$  becomes very evident.  $\delta$ , averaged over  $A \pm 5$  for  $A < 60$ , and over all nuclei having a given even value of  $N-Z$  for  $A > 60$ , is plotted in Fig. 2. Even after the smoothing it remains an irregular function.

Plots of  $\Delta$  for odd values of  $N-Z$  provide the mass difference between even-odd and odd-even nuclei. These vary in sign and have a magnitude of the same order as the variations in the even-even to odd-odd differences. For

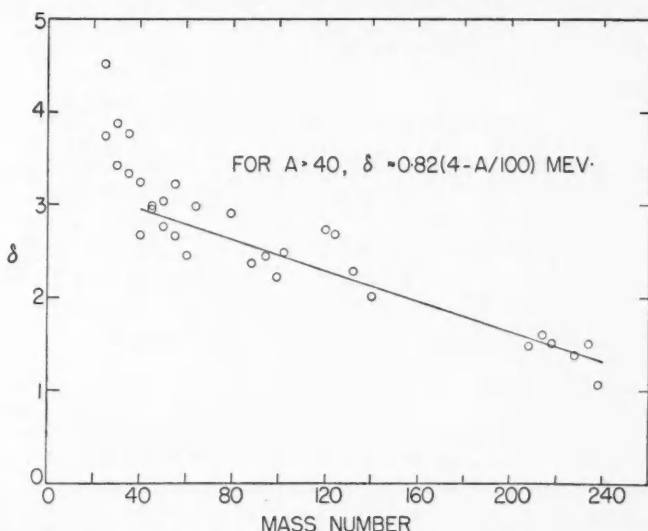


FIG. 2. The doubled pairing energy. The plotted values of  $\delta$  are the mass differences between even-even and odd-odd nuclei at the same values of  $N-Z$ .  $\delta$  has been averaged over a varying range of values of  $A$  as described in the text.

simplicity we have decided to neglect the even-odd to odd-even difference; we take  $\frac{1}{2}\delta$  to be the pairing energy of either two neutrons or two protons at the mass number shown.

To represent the value of  $\delta$  for  $A > 40$  a straight line seems as accurate as any simple curve; the line

$$(4) \quad \text{for } A > 40, \quad \delta = 0.82(4 - A/100) \text{ Mev.}$$

has been obtained. For lower values of  $A$ ,  $\delta$  can be obtained by inspection of Fig. 2, or from the formula  $\delta \approx 22A^{-\frac{1}{2}}$  Mev. recommended by Green and Edwards (1953) which agrees reasonably well with the points on Fig. 2.

Fig. 3, which is described in the next section, has been drawn using excitation energies adjusted for pairing effect as we have just described. A comparison of Fig. 1 with Fig. 3 shows that our rough adjustment has removed most of the separation between even and odd proton systems.

### 3. LEVEL SPACING DEFINED BY MASS NUMBER ONLY

In the appendix the spacing between energy levels having total momentum  $J\hbar$  at an excitation energy  $U$  of a Fermi gas model of a nucleus containing  $Z$  protons and  $N$  neutrons is obtained by standard methods (Bethe 1937; Lang and LeCouteur 1954). It is found that this spacing depends only on the defining variables  $J$ ,  $U$ ,  $Z$ ,  $N$  and the densities  $g_1$  and  $g_2$  of individual neutron and proton levels evaluated at their respective Fermi energies (see (A32) and (A33)):

$$D(UNZJ) = P^{-1}(UNZJ)$$

$$(5) \quad = 12G^{-1}(G_1G_2\bar{m}^2G)^{1/2}(2U+3t)^{3/2}F(J) \exp\{-2(\frac{1}{6}\pi^2GU)^{1/2}\}.$$

In this formula

$$(6) \quad F^{-1}(J) = [1+(\bar{m}^2G)^{-1}(2U+3t)^{-1}J^2]^{-3/2} \exp\{-(2\bar{m}^2Gt)^{-1}J^2\}$$

$$- [1+(\bar{m}^2G)^{-1}(2U+3t)^{-1}(J+1)^2]^{-3/2} \exp\{-(2\bar{m}^2Gt)^{-1}(J+1)^2\},$$

$$(7) \quad \bar{m}^2G = \sum_m m^2 g_1(m\lambda_1) + \sum_\mu \mu^2 g_2(\mu\lambda_2),$$

$$(8) \quad G_1 = \sum_m g_1(m\lambda_1), \quad G_2 = \sum_\mu g_2(\mu\lambda_2),$$

$$(9) \quad G = G_1 + G_2,$$

$$(10) \quad t = (\frac{1}{3}\pi^2G)^{-1/2}(2U+3t)^{1/2} \approx (6\pi^{-2}G^{-1}U)^{1/2}.$$

$g_1(m\lambda_1)$  is the number of individual neutron levels per unit energy at the neutron Fermi energy  $\lambda_1$  which have the magnetic quantum number  $m$ ,  $g_2(\mu\lambda_2)$  is the similar level density for protons, and  $t$  is the "nuclear temperature".

The expression is somewhat complicated. As a first practical step for present calculations we can simplify  $F(J)$ . For the low values of the excitation  $U$  and the values of  $\bar{m}^2G$  which occur in the experimental data we use here,  $J^2(2\bar{m}^2Gt)^{-1}$  ranges from about  $10^{-1}$  to  $10^{-3}$ . If in  $F(J)$  we neglect the terms  $(\bar{m}^2G)^{-1} \times (2U+3t)^{-1}J^2$  and replace the exponentials by two terms of their series expansions,

$$(6a) \quad F(J) \approx (2J+1)^{-1}2\bar{m}^2Gt.$$

Since  $F^{-1}(J)$  is a difference, the approximation (6a) is not as accurate as the smallness of  $J^2(2\bar{m}^2Gt)^{-1}$  might lead one to expect. However for the cases listed in Table I it has been found that (6a) differs from (6) by at most 20%, and this is smaller than errors due to other approximations in this computation. The simplification (6a) would not be justified at high excitations or in light nuclei, but it will serve for our present purposes.

Using (6a) the level spacing becomes

$$(5a) \quad D(UNZJ) = (2J+1)^{-1}D_0(UNZ),$$

$$(5b) \quad D_0(UNZ) = \pi^{-1}(12\bar{m}^2)^{3/2}(G_1G_2)^{1/2}(2U+3t)^2 \exp\{-2(\frac{1}{6}\pi^2GU)^{1/2}\}.$$

Bethe (1937, equation 299) evaluated  $\bar{m}^2G$  by means of statistical theory and a WKB approximation to be

$$(11) \quad \bar{m}^2G = \frac{2}{3}\hbar^{-2}M_N R^2 A,$$

where  $M_N$  is the mass of a nucleon. Lang and LeCouteur (1954) point out that the entire nucleus may not participate in the angular momentum so that an undetermined fraction of the classical moment of inertia (11) should be used in (5b). We will use in this section only the assertion that  $\bar{m}^2G$  is proportional to  $A^{5/3}$ .

The standard theory (e.g. Fermi 1950) of many particles of spin  $\frac{1}{2}$  in a box leads to

$$(12) \quad \frac{1}{6}\pi^2 G = 2^{-2/3} f^{-1} A^{2/3} (Z^{1/3} + N^{1/3}) \approx f^{-1} A.$$

When one uses (12) and  $\bar{m}^2 G$  proportional to  $A^{5/3}$  in (5b), and puts  $4G_1 G_2 \approx G^2$ , one obtains a function which depends only on the mass number of the nucleus, as indicated by the superscript ( $A$ ):

$$(13) \quad D_0^{(A)} = \beta A^2 (2U + 3t)^2 \exp -2(f^{-1} A U)^{1/2}$$

(cf. Lang and LeCouteur 1954) in which  $\beta$  and  $f$  are parameters to be adjusted to fit experiment.

This formula clearly cannot represent the irregularities of  $D$  which appear in Fig. 1. The best that can be done is to try to obtain a smooth curve to fit the local average level densities in non-magic nuclei. Such a fit has been made, and the results can be seen in Fig. 3 in which  $\log[A^{-2}(2U + 3t)^{-2} D_0]$  is plotted

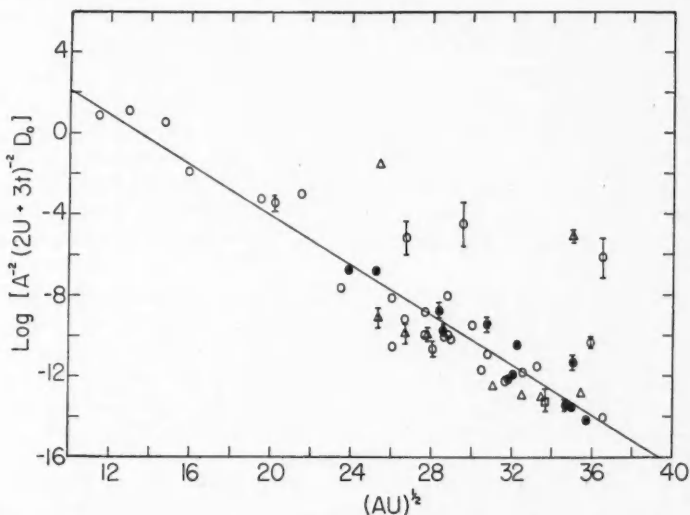


FIG. 3. Level spacings as a function of  $A$  only; the straight line is given by equation (15).

against  $(AU)^{1/2}$ .  $U$  is the equivalent excitation of the Fermi gas, obtained by subtracting the pairing correction defined in the last section from the neutron binding energy (see Table I). The resonances found by the slow neutron absorption experiments correspond to states of spin  $I \pm \frac{1}{2}$ , where  $I$  is the spin of the target nucleus. Thus the observed level density is the sum of the densities of states having these values of spin, and the spacing  $D_0$  is, using (5a),

$$(14) \quad D_0 = 2(2I+1)D_{\text{obs}} \quad \text{if } I \neq 0,$$

$$= D_{\text{obs}} \quad \text{if } I = 0.$$

The straight line drawn on Fig. 3 corresponds to the relation

$$(15) \quad D_0 = A^2 (2U + 3t)^2 \exp(8.30 - 0.62 \sqrt{AU}),$$

provided that  $D_0$  is expressed in ev.,  $U$  and  $t$  in Mev. The constants 8.30 and 0.62 are found by making a best fit to all spacings in Table I except those in Tl<sup>204</sup>, Pb<sup>207</sup>, Pb<sup>209</sup>, Bi<sup>210</sup>. The fit is not greatly disturbed by small changes of the value  $0.62 = 2\sqrt{f^{-1}}$  provided compensatory changes are made in the constant exponent 8.30. Hence it is not very meaningful to make comparison with other authors at this stage.

Since the experimental quantities  $D_0$  and  $U$  are subject to error, and the best formula we have to present is far from complete accuracy, we require some statistical criterion of goodness of fit. For this we define (cf. (5b))

$$(16) \quad \gamma = \log \{ \pi D_0 (12\bar{m}^2)^{-3/2} (G_1 G_2)^{-1/2} (2U + 3t)^{-2} \} + 2(\frac{1}{6}\pi^2 GU)^{1/2}.$$

For application to Fig. 3 and formula (15) this becomes

$$(17) \quad \gamma^{(A)} = \log \{ D_0 A^{-2} (2U + 3t)^{-2} \} + 0.62(AU)^{1/2} - 8.30.$$

The criterion is provided by

$$(18) \quad s^2 = (n-1)^{-1} \sum_k \gamma_k^2$$

in which  $n$  is the number of nuclei for which  $\gamma$  is determined.

For formula (13), we find, using all 52 cases in Table I,  $s^2 = 5.4$ , or if we omit the four nuclei Tl<sup>204</sup>, Pb<sup>207</sup>, Pb<sup>209</sup>, Bi<sup>210</sup>, then  $s^2 = 1.5$ . Thus for most medium and heavy weight nuclei (not close to Pb<sup>208</sup>) this simple formula, essentially one of those considered by Lang and LeCouteur (1954), provides an estimate of the level spacing which has an "expected error" of a factor  $\exp(1.5)^{1/2} \approx 3.4$ .

It has been pointed out by Harvey, Hughes, Carter, and Pilcher (1955) that the observed level spacings do not give definite evidence in favor of the factor  $(2I+1)$  which occurs in the relation (14) between observed spacings and  $D_0$ . A possible explanation for this is discussed in the next section, but here we may mention that if one omits that factor  $(2I+1)$  and supposes with the experimenters that  $D_0$  is twice the observed spacing if  $I \neq 0$ , and equal to the observed spacing if  $I = 0$ , one obtains almost exactly the same value for  $s^2$  from a formula of the form (13). The two constants are of course different. All one can say, therefore, is that this formula cannot distinguish between the two definitions of  $D_0$ . Since this factor is required by our simple treatment of the theory, we have used it throughout this paper.

#### 4. EFFECTS OF SHELL STRUCTURE

Efforts to refine the level density formula should clearly be directed at improving the fit in the regions of magic numbers. Having in mind the clearly indicated device for reducing the effect of pairs of nucleons one is first attracted to the concept that magic effects are similar in nature, i.e. are caused by some co-operative action of many particles. One would then try to determine special depressions of the magic ground state levels, and use these to reduce the effective excitation energy of the gas model in the neighborhood of magic numbers.

However this is contrary to the elementary concept of shell structure which supposes that the single-particle levels are defined by an average nuclear

potential, including spin-orbit coupling, and that these levels exhibit the main features of the shells without inclusion of two-particle effects. Moreover, if one found such a set of energy decrements as would decrease the irregularities in a given energy region, say that of the neutron binding, the effects of the correction would decrease rapidly with increasing excitation energy. Lang and LeCouteur (1954, Fig. 4) show that, on the contrary, these effects persist to a very marked degree in the spectrum of neutrons emitted after bombardment with 14 Mev. neutrons (Graves and Rosen 1953). This corresponds to an excitation of  $(14 - K)$  Mev. where  $K \sim 1$  Mev. is the kinetic energy of the first neutron emitted. This is almost twice the binding energy in the (residual) nucleus whose excitation is being measured.

The quantity which shows these magic effects at  $(14 - K)$  Mev. is  $t^{-2}U$  which is proportional to  $G$ , the individual particle level density. It may be seen from the derivation of the level spacing formula in the Appendix that the only way one can introduce the effects of the finite size of the nucleus, the finite number of particles in it, and of the effective nuclear potential, is through the individual neutron and proton level densities,  $g_1$  and  $g_2$ , evaluated at their respective Fermi energies. Hence we turn our attention to these functions.

Given the shell model of the nucleus there is no need to evaluate the individual level densities by use of the model of a Fermi gas in a box. One can proceed in a semiempirical fashion. The basic postulate of the model is that the spin-orbit coupling force is sufficiently strong that  $j = l \pm \frac{1}{2}$  is a much better quantum number than the orbital angular momentum number  $l$ . In a spherical nucleus the  $(2j+1)$  levels which have the same total angular momentum  $j\hbar$  would coincide. Klinkenberg (1952) has determined from experiment a sequence of  $j$ -values which can be used in such a spherical model. Later it will appear that we use these values explicitly only in the neighborhood of magic numbers, where they are most probably valid (cf. Nilsson 1955).

However the Klinkenberg order provides us with a tentative level scheme for single nucleons in which groups of  $(2j+1)$  coincident or closely spaced levels occur with wider intervening spaces. If one such group is separated from its neighbors above and below by an average interval  $d$ , then over that interval the single-particle levels have an average density

$$(19) \quad g = d^{-1}(2j+1).$$

If one adopts a spherical well for the average nuclear potential then the energy levels occur at

$$2m\hbar^{-2}R^2E_{nl} = x_{nl}^2 + b_{nj}, \quad l = j \pm \frac{1}{2},$$

where  $R$  is the radius of the well,  $x_{nl}$  is the  $n$ th root of the spherical Bessel function  $j_l(x)$ , and  $b_{nj}$  is the shift caused by the spin-orbit forces. We do not intend to use this relation except to point out that it implies that the spacing  $d \sim R^{-2} \sim A^{-2/3}$ . This relation will not be greatly modified if the well be changed. Thus we postulate

$$(20) \quad g_i = \alpha A^{2/3}(2j_i+1), \quad i = 1, 2,$$

for the individual neutron and proton level densities. Since  $g$  is to be evaluated

at the Fermi energy, the  $j$  to be used in (20) is, in the first approximation, that of the top occupied level in the ground state; i.e. Klinkenberg's (1952) value  $j$  for the given  $N$  or  $Z$ .  $\alpha A^{2/3}$  represents the reciprocal of the average interval between the sets of  $(2j+1)$  levels of individual nucleons; this interval is assumed to be the same for both neutrons and protons, so that we have for the sum of the neutron and proton densities

$$(21) \quad G = 2\alpha(j_1+j_2+1)A^{2/3}.$$

Fig. 4 shows the value of  $A^{-2/3}G^{(A)}$  as determined from the  $A$ -dependent formula (15) of the last section, and dotted on the same graph is  $2\alpha(j_1+j_2+1)$ ,

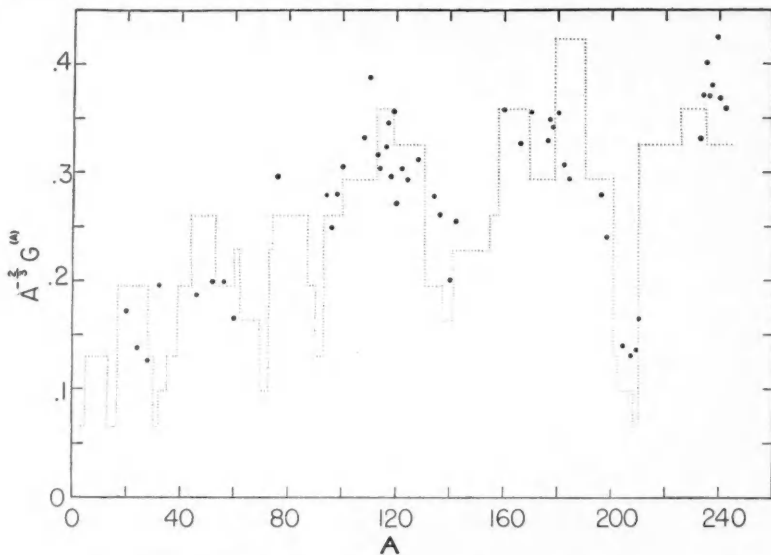


FIG. 4. The single-particle level spacing  $G^{(A)}$ , derived from equation (15).  $A^{-2/3}G^{(A)}$  is compared with  $0.0326(j_z+j_n+1)$ , the  $j$  values being those of Klinkenberg's (1952) table.

the value of  $A^{-2/3}G$  from (21). Since this is not a function of  $A$ , but of  $N$  and  $Z$ , we have evaluated it for one nucleus at each value of  $N$ , choosing approximately the most stable nucleus having that number of neutrons.

If  $G$  is to be given by a relation like (21), it is incorrect to compare it with  $G^{(A)}$  derived from equation (15) since (20) should also be used in the non-exponential factors. Also the nuclei whose average level spacing is known are not the most stable ones. Hence we do not expect the points of Fig. 4 to fall on the dotted line. However making allowance for this, and for the scatter of the "experimental" values, it appears that the value (21) for  $G$  does show large decreases near the magic numbers similar to those exhibited by the "experimental" values.

It also appears that the "measured" values do not show as much structure as does equation (21). This indeed is to be expected, for (20) assumes that the

nuclei are spherical, whereas it is now well known that most nuclei, except those that contain "magic numbers" of nucleons, are distorted. Nilsson (1955) has calculated the effects of distortion. His results show that between the larger magic numbers the spherical quantum number  $j$  has lost all validity, and the states of different  $j$  are completely intermingled. The simplest way to modify (20) to take account of this is to assume equal spacing between all states occupied by protons between  $Z = 58$  (close of  $h_{7/2}$  shell) and  $Z = 76$  (close of  $h_{11/2}$  shell), between  $Z = 92$  (close of  $h_{9/2}$  shell) and  $Z = 120$  (close of  $i_{13/2}$  shell); and similarly for states occupied by neutrons between  $N = 56$  (close of  $g_{5/2}$  shell) and  $N = 76$  (close of  $h_{11/2}$  shell), between  $N = 90$  (close of  $h_{7/2}$  shell) and  $N = 120$  (close of  $i_{13/2}$  shell). This assumption can be incorporated in (20) without modifying the constant  $\alpha$  if we define effective values  $\bar{j}_Z$  and  $\bar{j}_N$ , which take the spherical value in shells immediately preceding and following magic numbers, and a constant value in the intermediate regions defined above. The calculations of Nilsson (1955) do not indicate so much intermingling of states for  $N$ , or  $Z$ , less than 50, and our data at  $A < 100$  are meager, so we have used Klinkenberg's (1952) values for  $j_N$  and  $j_Z$  in that region.

We have however applied one more smoothing operation to define the effective value of  $j$ . Let us first recall why the single-nucleon level density occurs in the nuclear level spacing function. When a small amount of energy is given to a Fermi gas in the ground state only a few of the fermions in the higher occupied levels can be excited to a few of the lower unoccupied states. Consequently it is the single-particle level density in the immediate neighborhood of the top occupied level of the degenerate system which determines the number of states of the gas. As more energy is added to the gas, deeper lying levels of the degenerate system may be emptied and higher levels become occupied. The range over which levels may be emptied or filled becomes larger while remaining roughly centered on the Fermi energy; i.e. the number of states of the gas can be expressed in terms of the single-particle density averaged over a larger energy interval centered on the Fermi energy. Mathematically these concepts arise from the evaluation, as integrals, of the sums over levels which occur in the partition function (see Appendix). A typical integral of this kind is that which defines the contribution of excited neutrons to the total energy (equation (A24); we here ignore the sum over  $m$  which is extraneous to our present purpose):

$$(22) \quad U_1 \approx t \int_{-\infty}^{\infty} g_1(\epsilon) d\epsilon \log \{1 + \exp(-t^{-1}|\lambda_1 - \epsilon|)\}.$$

Here  $t$  is the nuclear temperature,  $g_1(\epsilon)$  the single neutron level density, and  $\lambda_1$  the neutron Fermi energy. The integral (22) is evaluated by observing that the logarithm possesses a sharp maximum at  $\epsilon = \lambda_1$ , and we write

$$(23) \quad \begin{aligned} U_1 &\approx t g_1(\lambda_1) \int_{-\infty}^{\infty} d\epsilon \log \{1 + \exp(-t^{-1}|\lambda_1 - \epsilon|)\} \\ &= \frac{1}{6} \pi^2 g_1(\lambda_1) t^2. \end{aligned}$$

This treatment assumes that  $g(\epsilon)$  is a continuous slowly varying function. When we replace it by a discontinuous function like (20), and yet seek to use the form (23) as a value of the integral, it is necessary to replace  $g_1(\lambda_1)$  by a value locally averaged over a range of  $\epsilon$  defined by the width of the maximum of the logarithmic kernel of (22).

The full width at half maximum of this logarithm, an interval which contains 55% of the area  $\frac{1}{6}\pi^2 t$ , is given by

$$(24) \quad w = -2t \log(\sqrt{2}-1).$$

We wish to determine over how many neutron levels this width extends. From the fitting of the  $A$ -dependent formula (13) we have found

$$4\left(\frac{1}{6}\pi^2\right)(g_1+g_2) = (0.62)^2 A \text{ (Mev.)}^{-1},$$

so that from (10)

$$t \approx 3.2A^{-1/2}U^{1/2}$$

and the interval between neutron levels, if  $g_1 = g_2$ , is

$$(25) \quad \Delta\epsilon = g_1^{-1} = 34A^{-1} \text{ Mev.}$$

Thus, putting  $A = 2N$ , the width  $w$  corresponds to a range  $\Delta N$  of neutron number given by

$$(26) \quad \Delta N = (\Delta\epsilon)^{-1}w = 0.23N^{1/2}U^{1/2}.$$

The average excitation of the nuclei we study is, after correction for pairing effects,  $U = 6$  Mev., so that we should use

$$\Delta N = 0.56N^{1/2}.$$

If we find the width at one-quarter maximum instead of at one-half maximum

TABLE II  
SINGLE-PARTICLE  $j$

$Z$	Klinkenberg (1952) ( $2j_z+1$ )	Effective ( $2j_z+1$ )	$Z$	Klinkenberg (1952) ( $2j_z+1$ )	Effective ( $2j_z+1$ )
1	2	2	42-48	10	10
2	2	2	49	10	9.6
3	4	3 $\frac{1}{3}$	50	10	9.2
4-5	4	4	51	8	8.8
6	4	3 $\frac{1}{3}$	52	8	8.4
7	2	2 $\frac{2}{3}$	53-56	8	8
8	2	3 $\frac{1}{3}$	57	8	8.2
9	6	4 $\frac{1}{3}$	58	8	8.4
10-13	6	6	59	6	8.6
14	6	4 $\frac{2}{3}$	60	6	8.8
15	2	3 $\frac{1}{3}$	61-64	6	9
16	2	2 $\frac{2}{3}$	65-74	12	9
17	4	3 $\frac{1}{3}$	75	12	8
18-19	4	4	76	12	7
20	4	5 $\frac{1}{3}$	77	4	6
21	8	6 $\frac{1}{3}$	78	4	5
22-27	8	8	79	4	3.6
28	8	6 $\frac{1}{3}$	80	4	3.2
29	4	5 $\frac{1}{3}$	81	2	4.4
30-31	4	4 $\frac{2}{3}$	82	2	5.6
32	4	4 $\frac{1}{3}$	83	10	6.8
33	6	5 $\frac{1}{3}$	84	10	8.4
34-37	6	6	85-90	10	10
38	6	4 $\frac{2}{3}$	91	10	9.867
39	2	3 $\frac{1}{3}$	92	10	9.733
40	2	4 $\frac{1}{3}$	93	8	9.6
41	10	7	94	8	9.467
			95-98	8	9 $\frac{1}{3}$

TABLE II (Concluded)

<i>N</i>	Klinkenberg (1952) ( $2j_N+1$ )	Effective ( $2j_N+1$ )	<i>N</i>	Klinkenberg (1952) ( $2j_N+1$ )	Effective ( $2j_N+1$ )
1	2	2	59-64	8	10
2	2	2	65-74	12	10
3	4	3	75	12	8.8
4-5	4	4	76	12	7.6
6	4	3	77	4	6.4
7	2	2	78	4	5.2
8	2	3	79	4	3.6
9	6	4	80	4	3.2
10-13	6	6	81	2	4
14	6	4	82	2	4.8
15	2	3	83	8	5.6
16	2	2	84	8	6.8
17	4	3	85-88	8	8
18-19	4	4	89	8	8.4
20	4	5	90	8	8.8
21	8	6	91	10	9.2
22-27	8	8	92	10	9.6
28	8	6	93-100	10	10
29	4	5	101-106	6	10
30-31	4	4	107-118	14	10
32	4	4	119	14	8.8
33	6	5	120	14	7.6
34-37	6	6	121	4	6.4
38	6	4	122	4	5.2
39	2	3	123	4	3.6
40	2	2	124	4	3.2
41	10	7	125	2	4.4
42-48	10	10	126	2	5.6
49	10	9.2	127	10	6.8
50	10	8.4	128	10	8.4
51	6	7.6	129-134	10	10
52	6	6.8	135	10	10.4
53-54	6	6	136	10	10.8
55	6	6.8	137	12	11.2
56	6	7.6	138	12	11.6
57	8	8.4	139-148	12	12.0
58	8	9.2			

the value of  $\Delta N$  is almost doubled. We have averaged over  $\Delta N = 3$  for  $N < 50$  and over  $\Delta N = 5$  for  $N > 50$ . The effective values of  $j$  resulting from the mixing due to distortion and from the local averaging are displayed in Table II, and the resulting form of  $G$  for the most stable nuclei is plotted in Fig. 5.

One other observation may be made from the preceding analysis. It makes explicit the fact that more levels are involved at higher excitations; the range  $\Delta N$  over which  $g_1$  must be averaged increases in proportion to  $U^{1/2}$ . However the effect is not very rapid; at 100 Mev., for example, the value of  $A^{-2/3}G$  at  $A \sim 208$  is still only about 80% of that of  $A^{-2/3}G$  for  $A \sim 180$ . We return to this question later.

There remains in the expression (5b) for the spacing  $D_0$  the factor  $(\bar{m}^2)^{3/2}$  which we have not yet discussed in connection with the value (20) for the single-nucleon level density. It will be recalled that

$$(7) \quad \bar{m}^2 G = \sum_m m^2 g_1(m\lambda_1) + \sum_\mu \mu^2 g_2(\mu\lambda_2),$$

i.e. the sum of the squares of the single neutron and proton magnetic quantum numbers. For spherical nuclei, away from the subshell edges, one obtains, using (20),

$$(27) \quad \bar{m}^2 G = \frac{1}{2} \alpha A^{1/2} \{ j_1(j_1+1)(2j_1+1) + j_2(j_2+1)(2j_2+1) \} .$$

However distortion has a greater effect on this quantity than on the average level spacing, especially on the states of high spin. The effect on  $\bar{m}^2$  of the mixing of states is very difficult to estimate. We have adopted the easier course of postulating simply

$$(28) \quad \bar{m}^2 = bA^{2/3}.$$

That  $\bar{m}^2$  is proportional to  $A^{2/3}$  follows from Bethe's (1937) relation (11), using the approximation that  $G$  is proportional to  $A$ . It may be verified that  $\{\bar{m}^2\}^{3/2}$  evaluated from (27) and (20), using Klinkenberg's  $j$ -values, and smoothed by local averaging, increases approximately linearly with  $A$ .

Since  $\bar{m}^2$  occurs in the non-exponential factor of  $D_0$  its accuracy need not be so great, but nevertheless it may be that an appreciable part of the difference between experimental and calculated average level spacings is caused by this factor, i.e. by the spin dependent factor  $F(J)$  (equation (6)). It has been mentioned that the variation of observed level spacing with target spin is not obviously consistent with equation (5a). One explanation for this would be that  $\bar{m}^2$  varies considerably and is, for many nuclei, too small to permit the approximation (6a) for the exponential factors in  $F(J)$ . To compute these quantities with more precision requires, however, a much more detailed theoretical model than we use here.

#### SUMMARY AND DISCUSSION

As a result of the arguments of the last section we write

$$(29) \quad D_0 = cAG_1^{1/2}G_2^{1/2}(2U+3t)^2 \exp\{-2(\frac{1}{6}\pi^2GU)^{1/2}\},$$

with

$$(30) \quad G_1 = \alpha(2\bar{j}_N+1)A^{2/3}, \quad G_2 = \alpha(2\bar{j}_Z+1)A^{2/3},$$

$$(31) \quad G = G_1+G_2 = 2\alpha(\bar{j}_N+\bar{j}_Z+1)A^{2/3}.$$

Here  $\bar{j}_N$  and  $\bar{j}_Z$  are the effective values of  $j$  discussed in the last section and listed in Table II. The temperature  $t$  is given by (10):

$$(10) \quad t = (6\pi^{-2}G^{-1}U)^{1/2}.$$

The constants of (29) have been determined by fitting the 52 observed spacings of Table I, using for  $U$  the neutron binding energy less the correction for pairing effect shown in that table. One obtains

$$(32) \quad D_0 = A^{5/3}(2\bar{j}_N+1)^{1/2}(2\bar{j}_Z+1)^{1/2}(2U+3t)^2 \\ \times \exp\{8.75 - 0.4982(\bar{j}_N+\bar{j}_Z+1)^{1/2}A^{1/3}U^{1/2}\}$$

in which  $D_0$  is expressed in ev.,  $U$  and  $t$  in Mev.

As a test of the statistical improvement of (32) over (15) we compute the quantity  $\gamma$ , equation (16), for each measured spacing;  $\gamma$  is the logarithm of the ratio of the observed  $D_0$  to the value of the right side of (32). We compute also  $s^2$ , equation (18), which gives a measure of the expected deviation of this difference of logarithms; for equation (32)

$$s^2 = 1.21.$$

This includes, of course, the four measured spacings near  $Pb^{208}$  and is to be compared with the value 5.4 obtained for the  $A$ -dependent formula (15). The ratio of observed values of  $D_0$  to values calculated from (32) is listed in Table III, together with the uncertainties due to imprecise knowledge of the

TABLE III  
RELATIVE ACCURACY OF EQUATION (32)

$Z$	$N$	$\log \frac{D_0(\text{calc})}{D_0(\text{obs})}$	$\frac{D_0(\text{calc})}{D_0(\text{obs})}$	$Z$	$N$	$\log \frac{D_0(\text{calc})}{D_0(\text{obs})}$	$\frac{D_0(\text{calc})}{D_0(\text{obs})}$
9	11	+.03 0.46-.38 +.04	1.6	56	80	2.55±.87	12.9
11	13	-0.88-.70 +.04	0.4	57	83	-1.12±.68	0.3
13	15	-0.50-.51 +.03	0.6	59	83	0.27±.08	1.3
15	17	2.43-.28 +.14	11.4	65	95	0.87±.86	2.4
21	25	-1.44-.15 +.11	0.2	67	99	0.01±.88	1.0
23	29	-0.43-.17 +.31	0.7	69	101	0.81±.88	2.3
25	31	0.07-.38 +.32	1.1	71	105	0.04±.89	1.0
27	33	-1.63-.40	0.2	71	106	0.66±1.24	1.9
33	43	1.13±.08	3.1	72	106	0.48±.92	1.6
41	53	1.60±.13	5.0	72	108	0.89±.92	2.4
42	54	-0.56±.22	0.6	73	109	-0.64±.10	0.5
42	56	-0.27±.24	0.8	74	110	-0.99±.08	0.4
43	57	-0.06±.63	0.9	78	118	0.44±.28	1.6
47	61	-0.08±.36	0.9	79	119	0.71±.26	2.0
47	63	1.33±.55	3.8	81	123	-0.39±.60 +.06	0.7
49	65	-0.70±1.06	0.5	82	125	-2.28-.42 +.14	0.1
49	67	-0.13±.39	0.9	82	127	-1.51-1.65 +.63	0.2
50	63	-0.11±1.65	0.9	83	127	-2.72-.64	0.1
50	67	0.72±.83	2.0	90	143	-0.81±.61	2.2
50	68	-0.80±.38	0.5	92	142	-0.84±.44	0.4
50	69	0.95±.60	2.6	92	143	0.68±.59	2.0
50	70	-1.54±.70	0.2	92	144	-0.09±.50	0.9
51	71	-0.39±.08	0.7	92	145	0.09±.61	1.1
51	73	-0.76±.59	0.5	92	147	1.36±.61	3.8
53	75	0.82±.13	2.3	94	146	-0.06±.66	0.9
55	79	2.39±.15	10.9	95	147	-0.44±.59	0.6

observed spacing, of the neutron binding energy, and in some light and magic nuclei, of the range of excitation over which  $D$  was determined. These show that equation (32) reproduces these 52 measured spacings with an expected error of a factor  $\exp\sqrt{1.21} = 3$ . In view of the approximations used in the treatment of the spin dependence, of the pairing energy, and of the evaluation of the sums over states, this is not a surprisingly large factor.

From the fitted constants of (32) one may determine  $c$  and  $\alpha$ ; then using (30) only in the non-exponential factors, one can solve (29) for the single-nucleon level density,  $G$ , for each measured spacing. These quantities, plotted as  $A^{-2/3}G$ , with the variation due to uncertainties in  $U$  and  $D_0$ , are the points shown in

Fig. 5, which is useful for discussion of the validity of our results. The lines shown on Fig. 5 are: (1) the value  $A^{-2/3}G = 0.07 A^{1/3}$  Mev.<sup>-1</sup> which is derived by the methods discussed in Section 3 for the spacing of nucleon levels in a spherical box of radius\*  $R = 1.5 A^{1/3}$  f. (Fermi 1950); (2)  $A^{-2/3}G = 0.076 A^{1/3}$  Mev.<sup>-1</sup> derived by Lang and LeCouteur (1954), from application of statistical theory to high energy processes, using the assumption that  $t = \text{const} \sqrt{(A^{-1} U)}$  which follows from the nucleons in a box hypothesis; (3)  $A^{-2/3}G = 0.058 A^{1/3}$  Mev.<sup>-1</sup> which is derived from our fitting of Section 3 and corresponds to

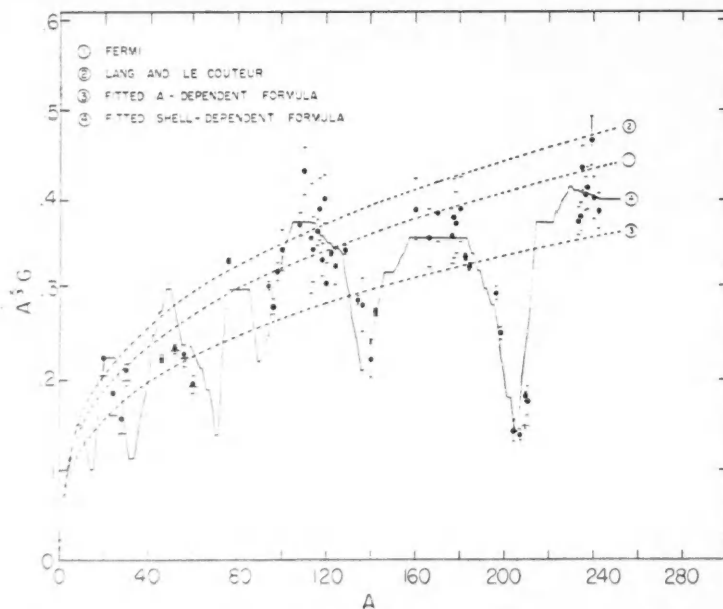


FIG. 5. The single-particle level spacing  $G$ , derived from equation (32).  $A^{-2/3}G$  is compared with  
 (1)  $0.07 A^{1/3}$  deduced for neutrons and protons in a box of radius  $1.5 A^{1/3}$  fermis.  
 (2)  $0.076 A^{1/3}$ , deduced by Lang and LeCouteur (1954) from statistical theory of high-energy processes.  
 (3)  $0.058 A^{1/3}$ , which was obtained in equation (15).  
 (4)  $0.03772 (j_N + j_Z + 1)$ , from fitting equation (29).

$R = 1.37 A^{1/3}$  f.; and (4)  $A^{-2/3}G = 0.03772(j_N + j_Z + 1)$  which follows from the definitions (30) and the constant of (32). Since this last is a function of  $N$  and  $Z$ , it has been evaluated for the most stable nucleus of each value of  $N$  in order to obtain a unique value as a function of  $A$ .

The figure demonstrates clearly that the shell effects on the single-nucleon level density  $G$  should be taken into account. It also indicates that the simple assumption of this paper, that between  $j$ -subshells the interval in  $R^2 E$  is

\*f. is an abbreviation for fermi, a unit of length equal to  $10^{-13}$  cm.

constant, is not completely adequate. At small values of  $A$ , with the conspicuous exception of  $P^{22}$ , the measured level spacings are somewhat larger than those predicted by our formula; this indicates that the lowest single-nucleon levels should be more widely spaced. Fig. 5 also suggests that the large dips in line 4 near  $A = 136$  and  $208$  due to the  $s$  and  $p$  subshells preceding  $N = 82$ , and  $Z = 82$ ,  $N = 126$  should be shifted to higher  $A$ . This would occur if one assumed that the single-nucleon levels just preceding a magic number are closer together and those just succeeding one are farther apart than the average. Such variations are to be expected according to the usual view of shell theory, but here their effects seem to be small compared to the main changes of  $G$ , and to be meaningful these variations should be determined by other evidence than that provided by these data.

On the whole Fig. 5 indicates that the spacing formula (32) has a satisfactory dependence on  $N$  and  $Z$ . It has been pointed out in the first section that the data from thermal neutron resonances do not provide a good test of the energy variation of the formula. Here we must rely on indirect evidence.

Lang and LeCouteur (1954) show in an appendix that a formula essentially identical with the one we have used predicts very accurately the energy variation of the level spacing of a system of fermions with a known (uniform) single-particle spacing. Our investigation indicates that the cases we have considered can be treated as the spacings of a system of fermions provided the proper single-particle spacings be used. This gives us some confidence that the energy variation is reasonable; i.e. the exponential variation with  $U^{1/2}$  is probably correct. However the constant  $\alpha$  also affects this variation. Its value is not very well fixed by the "best fit" to the thermal neutron data; a change of 10% in  $\alpha$  with compensatory changes in  $c$  increases  $s^2$  from 1.21 to 1.36, the mean factor of error from 3 to 3.2. Thus the best we can say from this discussion is that the constants of (32) should provide a reasonable description of the energy variation for a small range of energy, say up to a few times the neutron binding; a 10% change in the value of  $\alpha$ , with the compensating change in  $c$ , would give at four times the neutron binding a change of  $D$  by a factor less than 10.

Further indirect evidence on the validity of the energy dependence can be obtained from the single-particle level density deduced by Lang and LeCouteur (1954) by application of statistical theory to processes at energies from 10 to 200 Mev. They assumed the form  $G = A/f$  and determined  $f$  from data at  $A = 27, 103, 200$ . Their value of  $G$  agrees reasonably with ours (line (2) in Fig. 5) at the two lighter masses. The data they use at  $A = 200$  come from W, Pt, Hg, and Pb; the value of  $G$  seems to show no shell effect, and to be much larger than ours. This evidence should be compared, however, with their discussion of the  $A$ -dependence of  $G$ , which shows a strong magic effect near  $Pb^{208}$ , obtained by a statistical treatment of the 14-Mev. data of Graves and Rosen (1953). Thus the discrepancy in  $G$  at  $A = 200$  may not be so great as appears, but it does seem to indicate that our formula would give a poor account of the high energy value of  $D$  at large  $A$ . This may be another indication that the uniform spacing between  $j$ -subshells is inadequate; that the

single-nucleon spacing should be smaller at the higher levels. This is consistent with the previous observation that it should be larger in the low lying levels, and is not contradicted by the apparent fit of our points because of the double adjustment of constants described above.

Fig. 6 illustrates the large scale energy dependence of nuclear level spacing predicted by formula (32). Over small energy intervals the energy dependence is explicitly shown in the formula, but over large ranges of energy it is necessary to consider the variation of the effective values of  $G_1(\bar{j}_N)$  and  $G_2(\bar{j}_Z)$  due to the changing interval over which these are averaged (equation (26)).

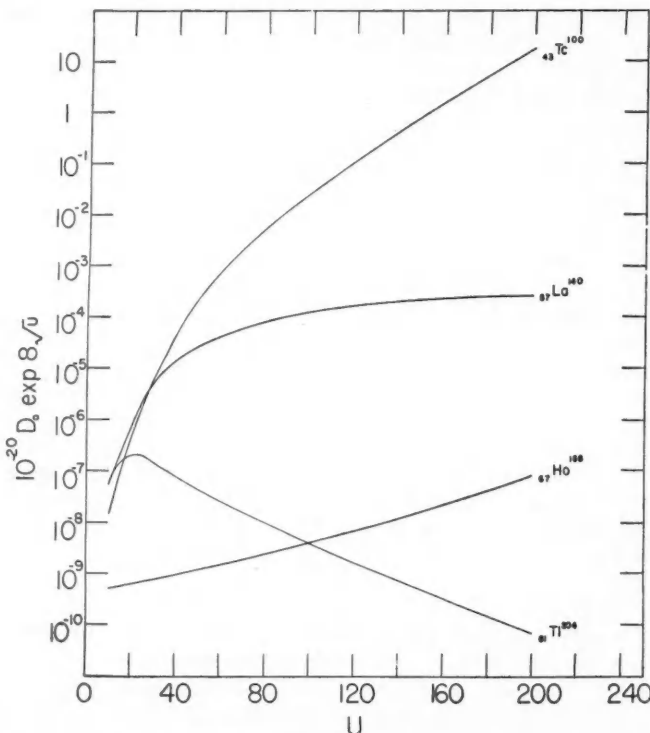


FIG. 6. The predicted variation with energy of the level spacings in two non-magic and two magic nuclei. The factors  $10^{-20} \exp 8\sqrt{U}$  have been used in the ordinate to reduce its range.

The figure shows the predicted variation of  $D$  for four typical nuclei,  $^{43}\text{Tc}^{100}$  and  $^{67}\text{Ho}^{166}$  whose neutron and proton numbers are not magic,  $^{57}\text{La}^{140}$  and  $^{81}\text{Ti}^{204}$  whose behaviors show magic effects. The actual quantity plotted,  $10^{-20}D_0 \exp 8\sqrt{U}$ , has been chosen to reduce the range of ordinate required. At low energies the spacing in magic nuclei behaves like that in light nuclei; it decreases more slowly with energy than the spacing in neighboring non-

magic nuclei. At higher energies when the  $G_i$  have to be averaged over a wide range of single-particle levels, the nuclear level spacing returns to a smooth dependence on  $A$ .

I wish to acknowledge gratefully the painstaking work of Miss I. W. Hay in carrying out much of the extensive exploratory and final computation required for the preparation of this paper.

#### APPENDIX

This appendix contains the development of the formula for the level spacing of a Fermi gas model of a nucleus. It is but slightly varied from that given by other writers (Bethe 1937; Lang and LeCouteur 1954).

We consider a gas of  $N$  neutrons and  $Z$  protons. The individual neutron levels have energy  $a_s$ , and magnetic quantum number  $m_s$ ; proton levels are designated by  $\alpha_s$  and  $\mu_s$ . The number of neutrons (either 0 or 1) occupying level  $s$  is denoted by  $n_s$ ; the similar number of protons by  $z_s$ . We shall assume that a single state of the whole system is defined by the four constants of the motion

$$(A1) \quad \begin{aligned} N &= \sum n_s, & Z &= \sum z_s, \\ E &= \sum n_s a_s + \sum z_s \alpha_s, & M &= \sum n_s m_s + \sum z_s \mu_s. \end{aligned}$$

The total angular momentum  $J\hbar$  should also be included as a constant of the motion. We have not done so principally because of the great mathematical difficulty such a non-linear relation entails; if the nucleus is not spherical, as appears to be the case for most nuclei, one cannot even form  $J$  as the vector sum of the single-particle total angular momenta  $j_s$  since these latter are not good quantum numbers. Bethe (1937) has used a method of deriving the number of levels of specified  $J$  from those of specified  $M$  which we shall adopt here.

The grand partition function from which we start (Schroedinger 1948) depends upon four parameters  $\beta, \lambda_1, \lambda_2, \lambda_3$ , one for each constant  $E, N, Z, M$  of the motion. It becomes

$$(A2) \quad \begin{aligned} \exp[-\beta\Phi(\beta, \lambda_1, \lambda_2, \lambda_3)] &= \sum \exp[\beta(\lambda_1 N' + \lambda_2 Z' + \lambda_3 M' - E')] \\ &= \sum_{N'Z'M'} \int dE' P(E'N'Z'M') \exp[\beta(\lambda_1 N' + \lambda_2 Z' + \lambda_3 M' - E')]. \end{aligned}$$

The sum is carried out over all possible states  $(N'Z'M'E')$ , and the function  $P(E'N'Z'M')$  which occurs in the integral representation of the  $E'$  sum is the density of levels with the specified values of the constants. It is this function we seek to determine. The sum over all possible states is equivalent to the sum over all occupation numbers of all single-particle states. Hence, using (A1),

$$(A3) \quad \begin{aligned} \exp[-\beta\Phi] &= \sum_{n_s z_s} \exp\left[\beta\left\{\sum_s n_s (\lambda_1 + \lambda_3 m_s - a_s) + \sum_s z_s (\lambda_2 + \lambda_3 \mu_s - \alpha_s)\right\}\right], \\ -\beta\Phi &= \sum_s \log\{1 + \exp[\beta(\lambda_1 + \lambda_3 m_s - a_s)]\} \\ &\quad + \sum_s \log\{1 + \exp[\beta(\lambda_2 + \lambda_3 \mu_s - \alpha_s)]\}. \end{aligned}$$

We now invert the sum (A2) and from it obtain an expression for the level density (Bethe 1937; Lang and LeCouteur 1954),

$$\begin{aligned} \sum_{Z'M'} \int dE' P(E'NZ'M') \exp[\beta(\lambda_2 Z' + \lambda_3 M' - E')] \\ = \frac{1}{2\pi i} \int_{-\gamma-i_\infty}^{\gamma+i_\infty} d(\beta\lambda_1) \exp[-(\beta\lambda_1)N - \beta\Phi] \\ = (2\pi f_1)^{-1/2} \exp[-\beta(\Phi + \lambda_1 N)]. \end{aligned}$$

The integral has been approximated by the method of steepest descents. The saddle point, at which the exponent is to be evaluated, is defined by

$$(A4) \quad N = -\partial\Phi/\partial\lambda_1$$

and

$$(A5) \quad f_1 = -\beta^{-1} \frac{\partial^2}{\partial\lambda_1^2} (\Phi + \lambda_1 N).$$

The values (A4) and (A5) are to be used for  $N$  and  $f_1$  in the final integrated form.

In similar ways we invert the sum with respect to the variables  $Z, M$ . It is also convenient to introduce, in place of the total energy  $E$ , the excitation energy  $U$  above the energy  $E_0$  of the completely degenerate state

$$(A6) \quad U = E - E_0.$$

Thus we obtain

$$(A7) \quad \begin{aligned} \int dU' P(U'NZM) \exp[-\beta U'] \\ = (2\pi)^{-3/2} (f_1 f_2 f_3)^{-1/2} \exp[-\beta(\Phi + \lambda_1 N + \lambda_2 Z + \lambda_3 M - E_0)] \end{aligned}$$

in which the exponent has been evaluated at the saddle points

$$(A8) \quad Z = -\frac{\partial}{\partial\lambda_2} \left( \Phi + \lambda_1 N + \frac{1}{2\beta} \log f_1 \right),$$

$$(A9) \quad M = -\frac{\partial}{\partial\lambda_3} \left( \Phi + \lambda_1 N + \lambda_2 Z + \frac{1}{2\beta} \log f_1 f_2 \right),$$

and the second derivatives are

$$(A10) \quad f_2 = -\beta^{-1} \frac{\partial^2}{\partial\lambda_2^2} \left( \Phi + \lambda_1 N + \lambda_2 Z + \frac{1}{2\beta} \log f_1 \right),$$

$$(A11) \quad f_3 = -\beta^{-1} \frac{\partial^2}{\partial\lambda_3^2} \left( \Phi + \lambda_1 N + \lambda_2 Z + \lambda_3 M + \frac{1}{2\beta} \log f_1 f_2 \right).$$

The final inversion with respect to the variable  $U$  yields

$$(A12) \quad P(UZNM) = (2\pi)^{-2} (f_1 f_2 f_3 f_4)^{-1/2} \exp[-\beta(\Phi + \lambda_1 N + \lambda_2 Z + \lambda_3 M - E_0 - U)]$$

in which the exponent is evaluated at the saddle point

$$(A13) \quad U = \frac{\partial}{\partial\beta} \left\{ \beta \left( \Phi + \lambda_1 N + \lambda_2 Z + \lambda_3 M - E_0 + \frac{1}{2\beta} \log f_1 f_2 f_3 \right) \right\}$$

and

$$(A14) \quad f_4 = -\frac{\partial^2}{\partial \beta^2} \left\{ \beta \left( \Phi + \lambda_1 N + \lambda_2 Z + \lambda_3 M - E_0 - U + \frac{1}{2\beta} \log f_1 f_2 f_3 \right) \right\}.$$

At this stage the only approximations used are those inherent in the method of steepest descents. We have now to fix the parameters  $\lambda_1$ ,  $\lambda_2$ ,  $\lambda_3$ , and  $\beta$  and to express the final form (A12) in terms of the constants  $N$ ,  $Z$ ,  $M$ , and  $U$  of the motion. To do so we shall make use of the standard integral representations of the sums of (A3) which define  $\Phi$ . For the Fermi gas model of a nucleus these representations are much less accurate than for, say, the electron gas in metals. However the integrals are used only to express the various sums in terms of one function, the individual particle level density, which is to be adjusted to fit experimental results. Thus, even though the integral representation of the sums leads to inaccurate absolute results, it provides a reasonable framework on which to fit the measurements.

As a preliminary to the evaluation of the parameters we rewrite (A3). Noting that the single-particle states  $(a_s, m_s)$  and  $(a_s, -m_s)$  are always degenerate in the absence of an external field, we write (A3) as

$$(A15) \quad -\beta\Phi = \sum_{a_s < \lambda_1} \beta(\lambda_1 - a_s) + \sum_{a_s < \lambda_1} \log \{1 + \exp[-\beta(\lambda_1 + \lambda_3 m_s - a_s)]\} \\ + \sum_{a_s > \lambda_1} \log \{1 + \exp[+\beta(\lambda_1 + \lambda_3 m_s - a_s)]\} \\ + \sum_{a_s < \lambda_2} \beta(\lambda_2 - a_s) + \sum_{a_s < \lambda_2} \log \{1 + \exp[-\beta(\lambda_2 + \lambda_3 m_s - a_s)]\} \\ + \sum_{a_s > \lambda_2} \log \{1 + \exp[+\beta(\lambda_2 + \lambda_3 m_s - a_s)]\}.$$

In (A15) as in (A3) the sums over  $s$  include sums over degenerate levels.

Now we can easily interpret (A4).

$$N = -\frac{\partial \Phi}{\partial \lambda_1} = \sum_{a_s < \lambda_1} 1 - \sum_{a_s < \lambda_1} \{1 + \exp[\beta(\lambda_1 + \lambda_3 m_s - a_s)]\}^{-1} \\ + \sum_{a_s > \lambda_1} \{1 + \exp[-\beta(\lambda_1 + \lambda_3 m_s - a_s)]\}^{-1} \\ \approx \sum_{a_s < \lambda_1} 1 - \sum_m \int_0^{\lambda_1} d\epsilon g_1(\epsilon m) \{1 + \exp[\beta(\lambda_1 + \lambda_3 m_s - \epsilon)]\}^{-1} \\ + \sum_m \int_{\lambda_1}^{\infty} d\epsilon g_1(\epsilon m) \{1 + \exp[-\beta(\lambda_1 + \lambda_3 m_s - \epsilon)]\}^{-1}.$$

The function  $g_1(\epsilon m)$  is the number of single-neutron levels per unit energy range at  $\epsilon$  having magnetic quantum number  $m$ . The integrands have sharp maxima near  $\epsilon = \lambda_1$ , so we approximate them by

$$N = \sum_{a_s < \lambda_1} 1 - \sum_m g_1(\lambda_1 m) \int_0^{\lambda_1} d\epsilon \{1 + \exp[\beta(\lambda_1 + \lambda_3 m_s - \epsilon)]\}^{-1} \\ + \sum_m g_1(\lambda_1 m) \int_{\lambda_1}^{\infty} d\epsilon \{1 + \exp[-\beta(\lambda_1 + \lambda_3 m_s - \epsilon)]\}^{-1} \\ = \sum_{a_s < \lambda_1} 1 + \sum_m \lambda_3 m g(\lambda_1 m).$$

So

$$(A16) \quad N = \sum_{a_s < \lambda_1} 1$$

since the levels at  $\lambda_1$  will include for each  $m$  also  $-m$ . But (A16) states that, within the accuracy of its development,  $\lambda_1$  is the Fermi energy of the neutron gas, i.e. the highest occupied level in the ground state.

We now evaluate  $f_1$  from (A5). Since  $N$  is a constant of the motion, it is independent of the parameter  $\lambda_1$ , and so

$$\begin{aligned} f_1 &= -\beta^{-1} \frac{\partial^2 \Phi}{\partial \lambda_1^2} \\ &= \sum_{a_s} \{1 + \exp[\beta(\lambda_1 + \lambda_3 m_s - a_s)]\}^{-1} \{1 + \exp[-\beta(\lambda_1 + \lambda_3 m_s - a_s)]\}^{-1} \\ &\approx \sum_m \int_0^\infty d\epsilon g(\epsilon m) \{1 + \exp[\beta(\lambda_1 + \lambda_3 m - \epsilon)]\}^{-1} \\ &\quad \times \{1 + \exp[-\beta(\lambda_1 + \lambda_3 m - \epsilon)]\}^{-1} \\ (A17) \quad &\approx \beta^{-1} \sum_m g_1(\lambda_1 m) = \beta^{-1} G_1. \end{aligned}$$

Here  $G_1$  represents the total number of neutron levels per unit energy range at the neutron Fermi energy, summed over the values of  $m$ .

In the same way we find to the same order of accuracy from (A8) and (A10) that

$$(A18) \quad Z = \sum_{a_s < \lambda_2} 1,$$

$$(A19) \quad f_2 = \beta^{-1} G_2.$$

Thus  $\lambda_2$  is the proton Fermi energy.  $G_2$  is the total number of single-proton levels per unit energy range at the proton Fermi energy, summed over the values of  $\mu$ .

Applying the same methods to (A9) and (A11) we obtain

$$\begin{aligned} M &= -\frac{\partial \Phi}{\partial \lambda_3} = -\sum_{a_s < \lambda_1} m_s \{1 + \exp[\beta(\lambda_1 + \lambda_3 m_s - a_s)]\}^{-1} \\ &\quad + \sum_{a_s > \lambda_1} m_s \{1 + \exp[-\beta(\lambda_1 + \lambda_3 m_s - a_s)]\}^{-1} \\ &\quad - \sum_{a_s < \lambda_2} \mu_s \{1 + \exp[\beta(\lambda_2 + \lambda_3 \mu_s - a_s)]\}^{-1} \\ &\quad + \sum_{a_s > \lambda_2} \mu_s \{1 + \exp[-\beta(\lambda_2 + \lambda_3 \mu_s - a_s)]\}^{-1}; \\ (A20) \quad &M = \lambda_3 \bar{m}^2 G, \end{aligned}$$

where

$$(A21) \quad G = G_1 + G_2 = \sum_m g_1(\lambda_1 m) + \sum_\mu g_2(\lambda_2 \mu)$$

and

$$(A22) \quad \bar{m}^2 = G^{-1} \left[ \sum_m m^2 g_1(\lambda_1 m) + \sum_\mu \mu^2 g_2(\lambda_2 \mu) \right];$$

also

$$(A23) \quad f_3 = \beta^{-1} \bar{m}^2 G.$$

We now turn to (A13) which defines the excitation energy  $U$ . Making use of the values we have so far obtained,

$$\begin{aligned} U = \frac{\partial}{\partial \beta} & \left[ - \sum_{a_s < \lambda_1} \log \{1 + \exp[-\beta(\lambda_1 + \lambda_3 m_s - a_s)]\} \right. \\ & - \sum_{a_s > \lambda_1} \log \{1 + \exp[\beta(\lambda_1 + \lambda_3 m_s - a_s)]\} \\ & - \sum_{a_s < \lambda_2} \log \{1 + \exp[-\beta(\lambda_2 + \lambda_3 \mu_s - \alpha_s)]\} \\ & - \sum_{a_s > \lambda_2} \log \{1 + \exp[\beta(\lambda_2 + \lambda_3 \mu_s - \alpha_s)]\} \\ & \left. - \frac{3}{2} \log \beta + \frac{1}{2} \log \{\bar{m}^2 G G_1 G_2\} \right], \end{aligned}$$

$$(A24) \quad \begin{aligned} U = \beta^{-1} & \sum_{a_s < \lambda_1} \log \{1 + \exp[-\beta(\lambda_1 + \lambda_3 m_s - a_s)]\} \\ & + \beta^{-1} \sum_{a_s > \lambda_1} \log \{1 + \exp[\beta(\lambda_1 + \lambda_3 m_s - a_s)]\} \\ & + \beta^{-1} \sum_{a_s < \lambda_2} \log \{1 + \exp[-\beta(\lambda_2 + \lambda_3 \mu_s - \alpha_s)]\} \\ & + \beta^{-1} \sum_{a_s > \lambda_2} \log \{1 + \exp[\beta(\lambda_2 + \lambda_3 \mu_s - \alpha_s)]\} - \lambda_3 M - \frac{3}{2} \beta^{-1}. \end{aligned}$$

This result is obtained by evaluating the sums as integrals, but one set of integrals has been replaced again by the sums over logarithmic terms. It is easily seen from the form (A24) that the exponent of (A12) becomes

$$(A25) \quad -\beta(\Phi + \lambda_1 N + \lambda_2 Z + \lambda_3 M - E_0 - U) = 2U\beta + \frac{3}{2}.$$

We now complete the simplification of (A24), again evaluating the sums as integrals,

$$(A26) \quad U = \frac{1}{6} \pi^2 G \beta^{-2} - \frac{1}{2} \lambda_3 M - \frac{3}{2} \beta^{-1}.$$

This can be called (interpreting  $\beta$  as an inverse temperature) the equation of state for the nucleon gas. Apart from the term in  $M$  and the addition of another term  $-\frac{1}{2}\beta^{-1}$  due also to the inclusion of  $M$  as a constant of the motion, this is the same as the equation of state derived by Lang and LeCouteur (1954). Then

$$2U\beta + \frac{3}{2} = 2\left(\frac{1}{6} \pi^2 G \beta^{-2} - \frac{3}{4}\right) - \beta \lambda_3 M.$$

But from (A26)

$$\frac{\pi^2}{6} GU = \left(\frac{\pi^2}{6} G \beta^{-1} - \frac{3}{4}\right)^2 - \frac{9}{16} - \frac{\pi^2}{12} G \lambda_3 M.$$

We observe from (A20) that  $\lambda_3 M = M^2 / \bar{m}^2 G$  is a number small compared to  $G^{-1}$ , whereas we must limit the application of this treatment to  $U > G^{-1}$  so that the integral representations of the sums shall have validity. Expanding the radical, and neglecting  $9/16$  in comparison with  $\frac{1}{6}\pi^2 GU$ , we find

$$\begin{aligned}
 2U\beta + \frac{3}{2} &= 2\left(\frac{\pi^2}{6}GU + \frac{9}{16} + \frac{\pi^2}{12}G\lambda_3M\right)^{1/2} - \beta\lambda_3M \\
 (A27) \quad &= 2\left(\frac{\pi^2}{6}GU\right)^{1/2} - \frac{1}{2}\beta\lambda_3M.
 \end{aligned}$$

We have used, in the small term, for the inverse temperature

$$(A28) \quad t^{-1} = \beta = (\frac{1}{6}\pi^2GU^{-1})^{1/2}.$$

Finally we must evaluate  $f_4$  from (A14), which yields

$$(A29) \quad f_4 = +\frac{1}{3}\pi^2G\beta^{-3} - \frac{3}{2}\beta^{-2}.$$

Collecting the values for  $f_1, f_2, f_3, f_4$  from (A17), (A19), (A23), (A29) and for the exponent from (A27) we have from (A12) the level density of the gas model of the nucleus expressed as

$$(A30) \quad P(UZN M) =$$

$$(2\pi)^{-2}\beta^3(G_1G_2\bar{m}^2G)^{-1/2}(\frac{1}{3}\pi^2G - \frac{3}{2}\beta)^{-1/2}\exp\{2(\frac{1}{6}\pi^2GU)^{1/2} - \frac{1}{2}\beta M^2(\bar{m}^2G)^{-1}\}.$$

If we evaluate the sum over all  $M$  of this expression as an integral, it is easily seen that

$$\begin{aligned}
 P(UZN) &= \sum_{M=-\infty}^{\infty} P(UZN M) \\
 (A31) \quad &= (2\pi)^{-3/2}\beta^{5/2}(G_1G_2)^{-1/2}(\frac{1}{3}\pi^2G - \frac{3}{2}\beta)^{-1/2}\exp\{2(\frac{1}{6}\pi^2GU)^{1/2}\},
 \end{aligned}$$

which, apart from the term  $(-\frac{3}{2}\beta)$  in the radical, is the value obtained by Lang and LeCouteur (1954, equation A9) by this type of calculation except that they did not treat  $M$  as a constant of the motion.

The substitution  $\beta = t^{-1}$  and the use of (A26) reduce the formula to

$$\begin{aligned}
 (A32) \quad P(UNZ M) &= \\
 \frac{1}{12}(G_1G_2\bar{m}^2)^{-1/2}G^{1/2}\{2U + (\bar{m}^2G)^{-1}M^2 + 3t\}^{-3/2}\exp\{2(\frac{1}{6}\pi^2GU)^{1/2} - M^2(2\bar{m}^2Gt)^{-1}\}.
 \end{aligned}$$

In (A31) we have written for simplicity and with small error

$$(2U + \lambda_3M + 3t)^{-1}(2U + \lambda_3M + \frac{3}{2}t)^{-1/2} \approx (2U + \lambda_3M + 3t)^{-5/2}.$$

(A31) gives the density of levels with specified  $M$ . If we require the density of levels of specified  $J$  (Bethe 1937),

$$(A33) \quad P(UNZJ) = P(UNZ, M = J) - P(UNZ, M = J+1).$$

#### REFERENCES

- BETHE, A. H. 1937. Revs. Mod. Phys. **9**: 69.
- BLATT, J. M. and WEISSKOPF, V. F. 1952. Theoretical nuclear physics. John Wiley & Sons, Inc., New York.
- DUCKWORTH, H. E., HOGG, B. J., and PENNINGTON, E. M. 1954. Revs. Mod. Phys. **26**: 463.
- ELLIOTT, J. P. and FLOWERS, B. H. 1955. Proc. Roy. Soc. A, **229**: 356.
- FERMI, E. 1950. Nuclear physics notes. The University of Chicago Press, Chicago.
- GRAVES, E. and ROSEN, L. 1953. Phys. Rev. **89**: 343.
- GREEN, A. E. S. and EDWARDS, D. F. 1953. Phys. Rev. **91**: 46.
- GREEN, A. E. S. and ENGLER, N. A. 1953. Phys. Rev. **91**: 40.
- HARVEY, J. A. 1955. Unpublished.

- HARVEY, J. A., HUGHES, D. J., CARTER, R. S., and PILCHER, V. E. 1955. Phys. Rev. **99**: 10.  
HUGHES, D. J. and HARVEY, J. A. 1955. Neutron Cross Sections, BNL 325. Brookhaven  
National Laboratories.
- HUIZENGA, J. R. 1955. Physica, **21**: 410.
- KING, R. W. 1954. Revs. Mod. Phys. **26**: 327.
- KLINKENBERG, P. F. A. 1952. Revs. Mod. Phys. **24**: 63.
- LANG, J. M. B. and LECOUTEUR, K. J. 1954. Proc. Phys. Soc. A, **67**: 586.
- LEVINSON, C. and FORD, K. W. 1955. Phys. Rev. **99**: 792.
- NILSSON, S. G. 1955. Kgl. Danske Videnskab. Selskab, Mat.-fys. Medd. **29**. No. 16.
- VAN PATTER, D. M. and WHALING, W. 1954. Revs. Mod. Phys. **26**: 402.
- ROSE, M. E. 1953. Phys. Rev. **91**: 610.
- SCHROEDINGER, E. 1948. Statistical thermodynamics. Cambridge University Press,  
London.
- WAPSTRA, A. H. 1955. Physica, **21**: 367, 385.

# THE STRENGTHS, WIDTHS, AND SHAPES OF INFRARED LINES

## I. GENERAL CONSIDERATIONS<sup>1</sup>

By WILLIAM S. BENEDICT,<sup>2</sup> ROBERT HERMAN,<sup>3</sup> GORDON E. MOORE,<sup>4</sup>  
AND SHIRLEIGH SILVERMAN<sup>5</sup>

### ABSTRACT

A discussion is given of methods by which the strengths, widths, and shapes of spectral lines may be derived from measurements obtained with spectrometers whose resolving power is sufficient to separate individual spectral lines but is insufficient to portray accurately the true line contour. The Lorentz shape for collision broadened lines is taken as a first approximation to the true line shape for most of the discussion. Numerous corrections that should be taken into account in interpreting experimental data are included. These arise from instrumental effects, overlapping of the individual lines, and deviations from the Lorentz shape. The three types of measurements discussed in some detail are the measurements of the "equivalent width," of the apparent breadth of a line at high optical density, and of the apparent extinction of a line or group of lines at the troughs between lines and in the wings. It is shown how these various types of measurements can be combined to yield the line strength, width, and shape.

### I. INTRODUCTION

A detailed knowledge of the strength, shape, and width of individual lines in molecular band spectra has become increasingly important in recent years in subjects such as chemical kinetics, meteorology, and astrophysics, and has yielded information concerning molecular structure and intermolecular forces. Among the many applications of interest one might mention the use of spectroscopic intensities to study population distributions in gases and therefore the temperature if the system is in equilibrium, deviations from equilibrium, concentrations in reacting systems, abundances in terrestrial, planetary, and stellar atmospheres, and the problems of radiant energy transfer between the layers of such atmospheres. In all these applications it is essential to know the line strength, a quantity related to the quantum-mechanical transition probability, and in addition to know the line shape and width, which depend upon intermolecular forces and hence upon the environmental conditions of temperature and pressure.

Since in the experimental detection of radiation by a spectrometer of finite resolving power the apparent spectral distribution over a line may be considerably distorted from the true one, it is not a simple matter to determine

<sup>1</sup>Manuscript received May 9, 1956.

Contribution from the Laboratory of Astrophysics and Physical Meteorology, The Johns Hopkins University, Baltimore, Maryland, the Applied Physics Laboratory, The Johns Hopkins University, Silver Spring, Maryland, and the University of Maryland, College Park, Maryland.

The work reported herein was supported in part by the Bureau of Ordnance under contract NOrd-7386 and Office of Naval Research, Department of the Navy, and by the Air Force, Cambridge Research Center.

<sup>2</sup>Laboratory of Astrophysics and Physical Meteorology, The Johns Hopkins University.

<sup>3</sup>Department of Physics, University of Maryland, College Park, Maryland. Visiting Professor on leave from Applied Physics Laboratory, The Johns Hopkins University. Present address: Research Staff, General Motors Corporation, Detroit, Michigan.

<sup>4</sup>Applied Physics Laboratory, The Johns Hopkins University.

<sup>5</sup>Office of Naval Research, Washington, D.C. On leave from Applied Physics Laboratory, The Johns Hopkins University.

the three interrelated parameters of strength, shape, and width even for systems in equilibrium. It has therefore been customary to make assumptions concerning some of these properties in order to determine the others.

For example, it has often been assumed that all the lines in a vibration-rotation band have the classical Lorentz shape and equal widths independent of rotational quantum number (for example, Elsasser 1942; Penner and Weber 1951; Goody and Wormell 1951). Under such assumptions it is possible in some cases to deduce the width and strength parameters from the apparent absorption as a function of pressure and path length observed with a low-resolution spectrometer. A method often employed to determine the strengths of the lines has been to broaden the lines at high pressures in order to reduce the instrumental modification of the true spectrum so that the strength of the entire band might be measured (for example, see Penner and Weber 1953). The individual line strengths can then be computed from quantum-theoretical formulas relating their strengths to the total band strength (Herzberg 1945, 1950). While recourse to such methods has sometimes been used because of the lack of better data, the reliability of the results obtained on the basis of these assumptions is open to question. It seems probable both from theoretical considerations and from the few experimental measurements available that deviations from the Lorentz shape occur, especially in the distant wings of a line, where the shape is governed by the specific intermolecular forces operative during collision. The intermolecular forces also give rise to different widths for lines involving different rotational states, as has been demonstrated for a few highly polar molecules in the infrared (Lindholm 1938; Foley 1946) and by numerous measurements in the microwave region of the spectrum (Bleaney and Penrose 1948; Johnson and Slager 1952), where very high resolving power is available. This effect, which has been at least partially explained by some theories of line broadening (Anderson 1949; Smith and Howard 1950), can be quite large as will be seen in the following paper (Benedict, Herman, Moore, and Silverman 1956), which deals with the specific example of the hydrogen chloride molecule. In attempting to calculate line strengths from theory and a knowledge of the total band strength, the approximate nature of the best available theories introduces an uncertainty. In addition, in order to measure the band strength by the pressure broadening technique the assumption is usually made that the band strength is independent of pressure. While this latter seems to be a fair approximation in non-polar molecules, there is evidence that for polar molecules the molecular interactions at high pressures can grossly perturb the band strength (Coulon *et al.* 1954).

For all these reasons it is, therefore, highly desirable to measure absorption intensities at low densities in such a manner that it is possible to determine independently the strength, shape, and width of each individual line and the variation of these quantities with rotational quantum number, temperature, and pressure.

The ideal method of making independent determinations of the strength, shape, and width of a line would be to employ a spectrometer of sufficiently high resolving power that the true shape of the line could be observed directly.

Such resolving power is available in the microwave region and has yielded valuable information concerning the shapes and widths of the few lines which lie in the range accessible to microwave techniques (Bleaney and Penrose 1948; Johnson and Slager 1952). It is desirable to make similar measurements in other spectral regions. The infrared offers two advantages over the visible and ultraviolet regions: the spectrum in the infrared consists of vibration-rotation bands involving a single electronic state for which the theoretical interpretation of line strength and collision widths is simpler than for electronic transitions; and there are wider ranges of pressure and temperature over which the line contour is determined predominantly by broadening due to binary collisions rather than from the Doppler effect. Since sufficient resolving power to observe the true line shape at low gas densities is not available in the infrared,<sup>6</sup> it will be necessary to adopt methods which are as nearly independent of instrumental effects as possible.

The purpose of the present paper is to outline in detail methods which may be used to measure independently the strength, width, and shape of individual spectral lines in such a manner that the difficulties introduced by the finite resolving power of the spectrometer employed are largely eliminated. For most of the discussion it is assumed that the Lorentz line shape is a first approximation to the true shape. Methods are given for checking the validity of this assumption and for correcting the measurements for deviations from the Lorentz shape.

While some of the basic methods discussed in this paper have been used by other investigators (Nielsen, Thornton, and Dale 1944; Goldberg 1951; Vincent-Geisse 1954), more correction terms of various types are included here than have been employed previously. Inasmuch as by careful experimental work an accuracy of about 5% or better may be achieved in the measurement of transmission and related quantities, it has been our aim to include enough correction terms to ensure that no error larger than about 1% is introduced in the reduction of the data. When, however, the accuracy of the experiments is lower, many of the correction terms will be unnecessary and more approximate formulas will suffice.

The methods discussed in this paper have been applied in detail to several of the vibration-rotation bands of HCl and DCl to illustrate their applicability. The results are given in the following paper (Benedict, Herman, Moore, and Silverman 1956) for the 1-0 band of HCl and will be given in later papers for other vibrational transitions and for the 1-0 band at elevated temperatures. In addition we hope to report in later papers on the results of the application of the methods described in this paper to several molecules of interest in the atmosphere and in flames, notably CO, CO<sub>2</sub>, and H<sub>2</sub>O.<sup>7</sup>

<sup>6</sup>The highest resolving power yet obtained in the infrared corresponds to an effective slit width of about 0.03 cm<sup>-1</sup> at 3000 cm<sup>-1</sup>. While this compares favorably with the half-width of lines at atmospheric pressure, which are of the order of ~0.05–0.5 cm<sup>-1</sup>, the effect of the finite resolving power still introduces a considerable modification to the true line shape, especially near the line center.

<sup>7</sup>For preliminary accounts of some of this work see Benedict and Silverman (1954); Herman, Moore, Silverman, and Wallis (1955); Benedict, Moore, and Silverman (1955).

## II. GENERAL THEORETICAL RELATIONS

The purpose of the present section is to collect several definitions and relations, which are for the most part well known, in such a form that they are conveniently available when needed for our subsequent developments.

The strength of a line can be measured in absorption by determining the integrated absorption  $S$  of a line, defined by the relation

$$(1) \quad S = \int_0^{\infty} k_s d\nu,$$

where  $k_s$  is the extinction coefficient in  $\text{cm}^{-1}$ . The extinction coefficient  $k_s$  is given in terms of the transmission  $\tau = I_s/I_s^0$  of a gas at a path length  $l$ , where  $I_s^0$  is the incident light intensity at frequency  $\nu$  and  $I_s$  is the intensity of the light transmitted by the sample, according to Lambert's law, namely,

$$(1a) \quad -\ln \tau = \epsilon_s = k_s l,$$

where  $\epsilon_s$  is the extinction. Since the width of an absorption line in a gas depends upon the pressure, in general Beer's law does not hold, i.e.,  $k_s$  is not proportional to concentration. However, for a gas at densities sufficiently low that the mechanism of absorption is not altered, e.g., by induced dipole transitions during collisions, then the integrated absorption  $S$  is directly proportional to the number of molecules of the absorber in the optical path. Thus

$$(2) \quad S = S' \rho \cong S^0 P$$

yields the line strength,  $S^0$  (or  $S'$  in appropriately different units), where  $P$  is the pressure and  $\rho$  the density of the absorber. The line strength so defined is directly related to the quantum-mechanical transition probability. In the pressure region with which we shall be concerned, the perfect gas approximation that density is proportional to pressure will introduce only a trivial error.<sup>8</sup>

There are two principal aims of our study of line strength; first, to measure  $S^0$  for as many lines as possible in a given vibration-rotation band so that the relative line strengths in the band may be compared with theory; and second, to evaluate the strengths of various vibrational bands of a particular molecule, i.e., the sum of the strengths of the individual lines in each band, and to relate these to the electric dipole moment function of the molecule. In order to distinguish the line strengths from the band strength we write for the line strength the expression  $S_{v,J}^0$ , where  $v$  and  $J$  are understood to signify all the vibrational and rotational quantum numbers necessary to specify the transition. The band strength  $S_v^0$  is then given by the expression

$$(3) \quad S_v^0 = \sum_J S_{v,J}^0,$$

where the sum is taken over all the lines of the band. If the absorption in the region of interest arises from a group of overlapping bands, including bands

<sup>8</sup>We shall use frequency in  $\text{cm}^{-1}$  so that  $S$  is given in  $\text{cm}^{-2}$ ,  $S^0$  in  $\text{cm}^{-2} \text{ atm}^{-1}$ , and  $S'$  in  $\text{cm}^{-2} (\text{Amagat})^{-1}$ . The unit Amagat is the density of the gas at S.T.P. For an ideal gas 1 Amagat is  $n_0 m_0$ , where  $n_0$  is Loschmidt's number and  $m_0$  is the mass of one molecule.

arising from different isotopic species or from excited vibrational states, then the absorption strength  $\bar{S}^0$  is given by

$$(3a) \quad \bar{S}^0 = \sum_i S_{v,i}^0.$$

This absorption strength is the quantity needed when comparing our results on resolved lines with strengths determined by the technique of broadening the fine structure at high pressure.

The shape of the absorption line and its width depend upon the mechanisms responsible for broadening the line. These are the natural width, the Doppler effect, and collision broadening. In the infrared region the natural width  $\sim (2\pi c\Delta t)^{-1}$  is very small since the lifetime  $\Delta t \sim 10^{-4}$  sec., so that we need consider only Doppler and collision broadening. The extinction coefficient for a Doppler broadened line is given by

$$(4) \quad k_{v,D} = (\ln 2/\pi)^{\frac{1}{2}} (S/\gamma_D) \exp\left\{(-\ln 2)[(\nu - \nu_0)/\gamma_D]^2\right\},$$

and the Doppler half-width,  $\gamma_D$ , is

$$(5) \quad \gamma_D = [2 \ln 2/(mc^2/kT)]^{\frac{1}{2}} \nu \cong 3.58 \times 10^{-7} (T/M)^{\frac{1}{2}} \nu,$$

$T$  being the absolute temperature and  $M$  the molecular weight. At room temperature the Doppler half-widths for the molecules with which we will be concerned (HCl, DCl, CO, CO<sub>2</sub>, and H<sub>2</sub>O) are  $\sim 0.002$ – $0.008$  cm<sup>-1</sup> in the spectral region under consideration, namely  $\sim 1800$ – $6000$  cm<sup>-1</sup>. The Doppler effect becomes important only at the lowest pressures we have employed. In our experiments the principal processes responsible for determining the line shape are binary collisions.

While the exact shape of collision broadened lines is a matter of some theoretical uncertainty, there appears to be general agreement that close to the resonant frequency,  $\nu_0$ , the extinction coefficient is well represented by the Lorentz line shape formula, which in the infrared region where  $\nu \sim \nu_0 \gg \gamma_L$  is

$$(6) \quad k_{v,L} = \frac{S}{\pi} \frac{\gamma_L}{(\nu - \nu_0)^2 + \gamma_L^2},$$

where  $\gamma_L$  is the Lorentz half-width. The half-width is proportional to the frequency of collisions interrupting the process of radiation absorption, and is hence to a good approximation proportional to the total pressure or density of a pure gas, so

$$(7) \quad \gamma_L \cong \gamma^0 P \cong \gamma' \rho,$$

or for gas mixtures

$$(7a) \quad \gamma_L \cong \sum_i \gamma_i^0 P_i \cong \sum_i \gamma'_i \rho_i$$

where  $\gamma_i^0$  and  $\gamma'_i$  are the pressure broadening constants of the  $i$ th component of the mixture on the spectral line in question in cm<sup>-1</sup> atm<sup>-1</sup> or cm<sup>-1</sup> Amagat<sup>-1</sup>, respectively.

The "frequency of collisions interrupting the radiating process" is a concept of some ambiguity for which numerous theories have been presented.<sup>9</sup> The

<sup>9</sup>For a review of the theories see Breene (1955).

more useful of these theories will be compared with our experimental results in a later paper. It is sufficient at this time to point out that the collision frequency, and hence  $\gamma^0$ , is dependent upon the specific intermolecular forces and therefore upon the relative orientation of the radiating and colliding molecules. When the forces are of long range and are angle-dependent as in the case of polar molecules,  $\gamma^0$  may vary widely with the rotational quantum numbers of the radiating molecule. For molecules with short-range forces only or for collisions between nearly spherical molecules less dependence of  $\gamma^0$  on rotational quantum number is to be expected.

Spitzer (1940) has shown on the basis of general theoretical arguments that the Lorentz shape should begin to fail at frequencies of the order of  $1 \text{ cm}^{-1}$  from the line center. In the more distant wings of the line the shape is governed to an increasing extent by the specific perturbations of the energy levels during collision, rather than merely by the frequency of collisions. Theoretical expressions for the absorption coefficient in these wings have been given by several investigators (Nielsen, Thornton, and Dale 1944; Goldberg 1951; Vincent-Geisse 1954) and in especial detail by Lindholm (1946). These theories consider statistically the perturbation during collision and relate the average perturbation to the absorbed frequency. In general, if the upper and lower energy levels of a line are perturbed differently, an asymmetric line shape results. This phenomenon has been demonstrated for atomic radiation (Marganau and Watson 1936) where the enhanced polarizability of the atom in the excited state causes the violet wing to fall off in intensity more rapidly than  $(\nu - \nu_0)^{-2}$ , while the red wing falls off less rapidly. However, it seems unlikely that such pronounced asymmetry will appear in vibration-rotation spectra, where the polarizabilities of the molecule in the upper and lower states are nearly identical. As with the Lorentz half-widths, however, the shape of the wings may be expected to depend on the rotational states involved.

The shape of lines for which both Doppler and collision broadening are important has been discussed by a number of investigators, and is given (Plass and Fivel 1953) for the case where  $|\nu - \nu_0| \gg \gamma_D$  or  $\gamma_L$  by

$$(8) \quad k_{v,D,L} = \frac{S\gamma_L}{\pi(\nu - \nu_0)^2} \left[ 1 + \left( \frac{3}{2a^2} - 1 \right) \left( \frac{\gamma_L}{\nu - \nu_0} \right)^2 + \left( \frac{15}{4a^4} - \frac{5}{a^2} + 1 \right) \left( \frac{\gamma_L}{\nu - \nu_0} \right)^4 + \dots \right],$$

where

$$(8a) \quad a = (\ln 2)^{\frac{1}{2}} (\gamma_L / \gamma_D).$$

It can readily be seen from Eq. (8) that the Lorentz formula is approached sufficiently far from the line center.

So far we have considered only an isolated spectral line. In molecular spectra there are a large number of lines that often overlap. In this case the extinction coefficient is given by

$$(9) \quad k_v = \sum_i k_{v,i},$$

where the sum is taken over all the individual lines contributing to the blend. In the evaluation of line strengths under conditions of overlapping it is necessary to correct for the effects of blending. Methods of applying such corrections are included in the following sections.

The above considerations are true in general, but cannot often be applied directly since they are dependent upon having available the true contour of the line. This implies observing the spectrum with a spectrometer of effectively infinite resolving power, a condition seldom attainable in the infrared and optical regions of the spectrum. If the spectrometer employed has a finite effective slit  $d$  ( $\text{cm}^{-1}$ ), then the true line shape is not observed and the absorption is modified to an extent which depends on the effective slit width. The exact relationship between the observed transmittance,  $\tau'$ , and the true transmittance,  $\tau$ , depends upon the slit function, i.e., the functional dependence of the intensity on the frequency at the detector when the spectrometer is set at a given frequency.

Detailed calculations of the effects of various slit functions have been published by several investigators (Amat 1952; Kostkowski and Bass 1955). For our purposes, since we shall describe measurements for which the slit corrections are minor, it is adequate to use the simplest realistic slit function, namely, a triangular one. For this slit function it can be shown that<sup>10</sup>

$$(10) \quad \tau_{\nu'}' = \tau_{\nu'} + \frac{d^2}{12} \left| \frac{d^2 \tau_{\nu}}{d\nu^2} \right|_{\nu=\nu'} + \frac{d^4}{360} \left| \frac{d^4 \tau_{\nu}}{d\nu^4} \right|_{\nu=\nu'} + \dots$$

The three types of measurements we employ which are essentially independent of slit correction are discussed in the following three sections.

### III. LINE STRENGTHS AND WIDTHS FROM EQUIVALENT WIDTH MEASUREMENTS

The equivalent width,<sup>11</sup>  $W$ , is defined by the relation

$$(11) \quad W = \int_0^\infty (1 - \tau') d\nu,$$

which is the integral of the fractional energy removed from the incident radiation, or in other words the area above the transmission curve. The range in  $\nu$  should be large enough to include all frequencies at which  $(1 - \tau')$  is different from zero. If this range covers a single line and no others, then we may meaningfully speak of the equivalent width of that particular line. In practice in molecular spectra there is often overlapping of the individual lines, so that it is difficult to decompose the total equivalent width of a group of lines into the  $W$ 's for the individual components. In all cases, however, the experimentally measured value of the equivalent width should be independent of the slit

<sup>10</sup>This result depends on the assumption that the incident intensity is a linear function of  $\nu$ . This is nearly always the case for a spectrometer of fairly high resolution unless the slit width includes a feature such as an interfering atmospheric absorption line.

<sup>11</sup>The name "equivalent width" for the important quantity  $W$ , although established in the literature, appears unfortunate, since it is related to an area rather than to any measure of width. It must not be confused with the half-width  $\gamma$ , a property of the true extinction curve of a line, nor with the actual width of the absorption measured at a particular extinction, a quantity for which we use the term "breadth" and the symbol  $b$ .

function of the spectrometer as long as the spectrum is scanned sufficiently slowly so that the recorder deflection follows the intensity of the radiation falling upon the detector.

Although the equivalent width is independent of the effective slit-width, it is of great practical advantage to employ the narrowest slits consistent with a good signal-to-noise ratio. Such high resolving power is necessary to measure lines of small  $W$ . As will be seen shortly, these lines are of particular importance in establishing the line strengths. With wider slits the value of the apparent transmittance over such lines does not differ sufficiently from unity to allow precision in its measurement. High resolving power is also useful in reducing the apparent overlapping of individual lines caused by finite resolving power as well as in revealing the presence of satellite lines which might otherwise be obscured. Such satellite lines are very often present, arising from less abundant isotopes or from absorption by vibrationally excited molecules. Corrections can usually be made to account for the contribution of these weaker lines to equivalent width measurements once their presence has been ascertained.

If the shape and strength of a line is known, its equivalent width may be calculated from Eq. (11). For lines with the Lorentz shape the equivalent width is given by the well-known Ladenburg-Reiche equation (Ladenburg and Reiche 1911), namely

$$(12) \quad W = 2\pi\gamma_L f(x),$$

$$(12a) \quad f(x) = xe^{-x}[J_0(ix) - iJ_1(ix)],$$

where

$$(12b) \quad x = Sl/(2\pi\gamma_L) = S^0l/(2\pi\gamma^0),$$

and  $J_0(ix)$  and  $J_1(ix)$  are the Bessel functions of order 0 and 1, respectively.<sup>12</sup> For a pure gas, since both  $S$  and  $\gamma_L$  are proportional to the pressure (at constant temperature), the quantity  $x$  is independent of pressure and may be varied only by varying the path length. For a gas mixture  $x$  can be varied for a particular line at constant path length by varying the partial pressure of the absorbing component relative to that of the other components of the mixture. This is possible since  $S$  depends only upon the amount of absorber present while  $\gamma_L$  depends upon the partial pressures of all the components (see Eq. (7a)). One sees from Eq. (12) that for a pure gas or for a gas mixture of constant fractional composition the equivalent width of a line is proportional to the pressure as long as the line is isolated and has the Lorentz shape.

The pressure limit below which  $W$  is no longer proportional to  $P$  is reached when the contribution of the Doppler width can no longer be neglected. For lines where the Doppler contribution is important Plass and Fivel (1953) have obtained a result for lines of large  $x$  which can be rearranged to give for the ratio of the observed equivalent width to that expected for a truly Lorentzian line the expression

<sup>12</sup>A useful table of  $f(x)$  has been prepared by L. H. Stover. It is to be published as part of a paper by L. D. Kaplan and D. F. Eggers entitled "Intensity and Line-width of the 15 Micron CO<sub>2</sub> Band Determined by a Curve-of-growth Method".

$$(13) \quad \frac{W}{W_L} = 1 + \frac{3}{16} a^{-2} x^{-1} + \frac{45}{512} a^{-4} x^{-2} - \frac{3}{32} a^{-2} x^{-2} + \dots,$$

where  $a$ , as given by Eq. (8a), is proportional to the pressure.

The smallest value of  $W$  that we have been able to measure accurately is  $\sim 0.04 \text{ cm}^{-1}$ . If  $\gamma_D$  is  $\sim 3 \times 10^{-3} \text{ cm}^{-1}$  (a typical value in our experiments), then in order for the Doppler contribution to affect the equivalent width of such a line by as much as a few per cent it is necessary for the ratio  $\gamma_D/\gamma_L$  to be greater than  $\sim 2$ . For lines of greater  $W$  and  $x$  a larger ratio is necessary to introduce the same percentage deviation. Since  $\gamma^0$  is usually of the order of  $\sim 0.1 \text{ cm}^{-1} \text{ atm}^{-1}$ , the effect of Doppler broadening becomes appreciable at pressures of the order of  $10^{-2} \text{ atm}$ . Once a value of  $\gamma^0$  has been obtained from measurements at higher pressure, low-pressure results can be corrected readily for Doppler broadening by Eq. (13).

The highest pressure at which the equivalent width of Lorentz lines is proportional to pressure will be reached when overlapping by neighboring lines becomes significant. A good rule of thumb is that when the extinction at the bottom of the trough between a pair of lines is less than 0.1, the measured value of the equivalent widths of the lines is affected to no more than a few per cent.

If it can be assumed that the relative values of the ratio  $S^0/\gamma^0$  are known for a group of lines, it is possible to evaluate the line strengths and widths from measurements at a single path length. For example, if one assumes that all the lines in a band have the same width and that the relative line intensities are calculable from theory, e.g., from the rigid rotor intensity formula, it is possible to evaluate the quantities  $S^0$  and  $\gamma^0$ . If a plot of the data obtained under such assumptions agrees with the Ladenburg-Reiche curve, the assumptions are probably good. However, the correctness of the assumptions is best checked by the determination of  $S^0$  and  $\gamma^0$  for each line individually.

Often there are cases where the ratio  $S^0/\gamma^0$  for a pair of lines is known with considerable precision. For example, the lines corresponding to the same transition in molecules differing only by isotopic substitution resulting in relatively small differences in the reduced mass should have very nearly equal widths and an intensity ratio close to the isotopic abundance ratio. The major portion of the other factors affecting the intensity, e.g., population distribution, line frequency, can be calculated. In HCl the isotopic molecules  $\text{HCl}^{35}$  and  $\text{HCl}^{37}$  form such a pair. However, in going from  $\text{HCl}^{35}$  to  $\text{DCl}^{35}$  the large change in the reduced mass on isotopic substitution introduces an appreciable change in  $\gamma^0$ , and the ratio of the  $S^0$ 's is no longer as precisely known. The abundance ratio of  $\sim 3/1$  for  $\text{HCl}^{35}/\text{HCl}^{37}$  is quite favorable to work with as will be seen in the following paper. By measuring the ratio of the equivalent widths of a pair of isotopic lines one can estimate in what region of the Ladenburg-Reiche curve they fall. If the ratio is near the value 3, the lines are in the linear region, while a ratio near the value 1.75 indicates they are in the square-root region. Intermediate ratios correspond to the transition region between the linear and the square-root relationships.

Another case might be mentioned in which the intensity ratio of a pair of lines can be expected to be known theoretically with some certainty. This is the case where the lines come from molecules with different resultant nuclear spins. In the spectrum of  $H_2O^{18}$ , for example, there are numerous close pairs of lines where the intensity ratio is very nearly 3/1 resulting from such differences. These lines would also be expected to have very nearly the same widths.

In order to determine both  $S^0$  and  $\gamma^0$  for a particular line of a pure gas from the measurement of equivalent width, it is necessary to determine  $W$  at more than one value of  $x$ , i.e., at more than one path length. In practice it is best if the values of  $x$  cover a wide range and include some points with  $x < 0.5$ . For small values of  $x$  the so-called "linear region" is approached where

$$(14) \quad f(x) \cong x(1-x/2+\dots),$$

whence

$$(14a) \quad W^0 = W/P \cong S^0/[1 - W^0/(4\pi\gamma^0) + \dots].$$

Accordingly, measurements of equivalent widths at values of  $x$  sufficiently small so that the second term in Eq. (14) may be neglected yield the line strength directly. In practice it is difficult to measure accurately such weak lines. However, for somewhat stronger lines an approximate value of  $\gamma^0$  will yield a sufficiently good correction so that  $S^0$  may be determined.

At large values of  $x$  the so-called "square-root region" is approached where

$$(15) \quad f(x) \cong (2x/\pi)^{\frac{1}{2}}[1 - 1/(8x) + \dots],$$

whence

$$(15a) \quad W^0 \cong 2(S^0\gamma^0 l)^{\frac{1}{2}}[1 - \pi(\gamma^0/W^0)^2 + \dots].$$

It is usually relatively easy to measure lines with sufficiently large equivalent widths so that the correction term in Eq. (15) can be neglected or estimated with adequate precision. Thus one obtains directly the product  $S^0\gamma^0$ .

The quantities  $S^0$  and  $\gamma^0$  can be obtained by the following graphical procedure. The experimental data are plotted as  $\log W^0$  versus  $\log l$ . The Ladenburg-Reiche curve shown in Fig. 1 obtained from Eq. (12) is then superimposed to give the best fit of the experimental points. When this is done the intersection of the "linear region" asymptote with the line  $\log l = 0$  yields  $\log S^0$ . Furthermore, the asymptotes of the "linear region" and the "square-root region", with slopes 1 and  $\frac{1}{2}$ , respectively, intersect at the point  $W^0 = 4\gamma^0$ . Hence both  $S^0$  and  $\gamma^0$  can be obtained once the Ladenburg-Reiche curve has been located on a plot of  $\log W^0$  versus  $\log l$ .

In the experimental determination of equivalent width the absorption is measurably above the noise over only a relatively small frequency range, while the wings of the lines actually extend to much larger distances from the line center. The area under these wings, which can amount to as much as several per cent of the total area, but which cannot be measured directly, should be included in the value of  $W$  for a line. The magnitude of the "wing contribution" to be added to the measured area can be calculated once the

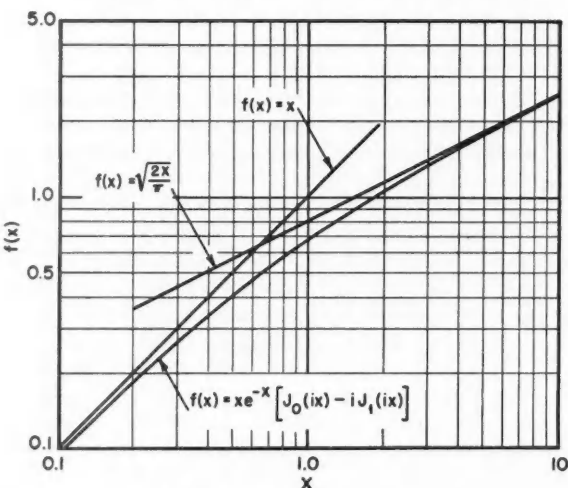


FIG. 1. Plot of the Ladenburg-Reiche function showing also the limiting small  $x$  ("linear") and large  $x$  ("square-root") asymptotes.

shape of the lines in the wings is known. If the assumption is made that the line in question has the Lorentz shape at all frequencies, it is simple to evaluate the "wing contribution."

If the measurement of the area under a line is carried out to a distance  $g$  ( $\text{cm}^{-1}$ ) on each side of the line, at which points the extinction is small and changing slowly across the slit width, it can be shown by direct integration that for a Lorentz line the contribution to the equivalent width from both wings beyond points  $g$  is

$$(16) \quad W_w = \frac{2S^0\gamma^0P^2l}{\pi g} \left( 1 - \frac{\gamma_L^2}{3g^2} + \dots \right).$$

Since any good measurement of equivalent width extends over several half widths,  $\gamma_L \ll g$ , only the first term in Eq. (16) need be retained. Therefore, for lines in the linear region of the Ladenburg-Reiche curve, Eq. (12), the true value of  $W$  is related to the measured value,  $W'$ , to first order by

$$(17a) \quad W \cong W' + 2W\gamma_L/(\pi g) \cong W'[1 + 2\gamma_L/(\pi g)],$$

and in the square-root region

$$(17b) \quad W \cong W' + W^2/(2\pi g) \cong W'[1 + W'/(2\pi g)].$$

An iteration method can be used to apply the corrections to the measured equivalent widths. The line strength  $S^0$  can be estimated from  $W'$  for a line in the linear region neglecting the correction. This value can then be used to estimate from a value of  $W'$  for the same line measured at sufficiently long path lengths that it is in the square-root region and can in turn be used to calculate corrected values of  $W$  for the line. This process converges very rapidly to yield consistent values of the line strength and half-width.

Both theory and experiment indicate that the line shape far from the resonant frequency of an absorption line is probably not given by the Lorentz law. It is therefore possible that  $W^0$  will exhibit a pressure dependence even in the pressure range where both the Doppler contribution and overlap by neighboring lines are unimportant. The magnitude of the effect for any particular line shape can be estimated by numerical integration. As an example, one case for which an analytical expression may be obtained for a non-Lorentz shape which appears to be a fair approximation to the true shape as observed in HCl<sup>2</sup>, and possibly in other polar molecules, has been worked out in Appendix A. It leads to the result that there would be an excess equivalent width,  $\Delta W$ , over that resulting from the Lorentz shape,  $W_L$ , given by

$$(18) \quad \frac{\Delta W}{W_L} = \frac{1}{2\pi} \left( \frac{2-\eta}{\eta-1} \right) \left( \frac{W_L^0 - 2\gamma^0}{\nu_m} \right) P - \frac{1}{\pi^2} \left( \frac{2-\eta}{\eta-1} \right)^2 \left( \frac{W_L^0 - 2\gamma^0}{\nu_m^2} \right) \gamma^0 P^2 + \dots,$$

where  $\eta$  and  $\nu_m$  are additional shape parameters as defined in Appendix A.

This result indicates that the non-Lorentz shape may have a small but noticeable effect on the determination of  $\gamma_L$  from the observed equivalent width. For example, if  $\nu_m \sim 1 \text{ cm}^{-1}$  as is predicted by Spitzer's theory (Spitzer 1940) and if  $\eta \sim 1.8$ , as the results on HCl at high optical densities indicate, then at  $\sim 0.1 \text{ atm}$ . pressure and 20 cm. path length the equivalent width of a strong line like  $R(2)$  of HCl<sup>35</sup> would be affected to about 6%. At higher pressures the effect would be somewhat larger, but in this case isotopic overlap becomes important. However, if  $\nu_m \gtrsim g$ , the practical limit of measurement, as will generally be the case, an appreciable fraction of the  $\Delta W$  required theoretically by Eq. (18) will not have been included in the wing contribution by Eq. (17b).

#### IV. STRENGTH-WIDTH PRODUCTS AND SHAPES FROM BREADTHS OF STRONG LINES

A second type of measurement that is relatively free from instrumental error can be made on isolated lines at optical densities such that there is very high absorption at the line center and measurable absorption over a frequency region of several slit widths. The apparent breadth,  $b_\epsilon'$ , of such a line at any particular value of the extinction,  $\epsilon$ , can be measured directly from the recorder tracing and is related to the product of the line strength and half-width.

For a Lorentz line the extinction is given by the expression

$$(19) \quad \epsilon_r = \frac{S^0 \gamma^0 l P^2}{\pi[(\nu - \nu_0)^2 + (\gamma^0 P)^2]} = \frac{2x(\gamma^0)^2 P^2}{(\nu - \nu_0)^2 + (\gamma^0 P)^2}.$$

The true breadth of the line at a particular value of the extinction,  $b_\epsilon = 2(\nu_\epsilon - \nu_0)$ , is then related to the strength-width product by

$$(20) \quad S^0 \gamma^0 = \frac{\pi b_\epsilon^2}{4P^2 l} \left[ 1 + \left( \frac{2\gamma^0 P}{b_\epsilon} \right)^2 \right].$$

For breadths  $b_\epsilon \gg \gamma^0 P$  the second term in the bracket in Eq. (20) can be neg-

lected; for smaller values of  $b_*$  an approximate value of  $\gamma^0$  can often be estimated which yields a sufficiently accurate correction term.

In any accurate application of Eq. (20) two additional corrections should be considered. The first of these is the slit-width correction which depends upon the slit function of the spectrometer. The measured breadth must to first order be reduced by the amount

$$(21) \quad \Delta b_* \cong 2\Delta\tau / \left( \frac{d\tau'}{d\nu} \right),$$

where  $d\tau'/d\nu$  is the slope of the experimental transmission curve at  $\epsilon$  and where  $\Delta\tau = \tau' - \tau$  is the difference between the observed and true transmission at the points where the measurements of breadth are made. Taking  $\Delta\tau$  from Eq. (10) for a triangular slit function and assuming that  $d\tau'/d\nu$  may be taken as  $d\tau/d\nu$  from Eq. (1), then the correction becomes

$$(22) \quad \Delta b_* \cong \frac{2\epsilon - 3}{3} \frac{d^2}{b_*},$$

where as before  $d$  is the slit width. Hence to this order the fractional slit-width correction is zero at  $\epsilon = 3/2$  and is small when  $b_*^2 \gg d^2$ .

The second additional correction which should be included is the correction for overlapping lines. As was pointed out earlier it is practically impossible to observe a strong line in molecular spectra without adjacent lines making some contribution to the absorption. Breadth measurements of the type considered here may be considered useful if other lines contribute less than  $\sim 10\%$  to  $\epsilon_*$  at both  $\nu_0 + b_*/2$  and  $\nu_0 - b_*/2$ . The total extinction may be written as

$$(23) \quad \epsilon_* = \sum_i \epsilon_{i*} \cong \frac{lP^2}{\pi} \left[ \frac{S_1^0 \gamma_1^0}{(\nu_1 - \nu)^2} + \sum_j \frac{S_j^0 \gamma_j^0}{(\nu_j - \nu)^2} \right] = \epsilon_1 + \epsilon_j,$$

where  $S_1^0$  and  $\gamma_1^0$  are the parameters of the strong local line and the sum is taken over all other lines contributing to the absorption. In a regular band of the type considered by Elsasser (1942) made up of lines of equal strength  $S^0$  and width  $\gamma^0 P$  and constant spacing  $\delta$ , the quantity  $\epsilon_j$  in Eq. (23) becomes

$$(24) \quad \epsilon_j = \frac{S^0 \gamma^0 P^2 l}{\pi} \sum_{j=1}^{\infty} [(j\delta - \frac{1}{2}b)^{-2} + (j\delta + \frac{1}{2}b)^{-2}],$$

and the ratio  $\epsilon_j/\epsilon_1$  is given in terms of  $z = b/\delta$  by

$$(25) \quad \epsilon_j/\epsilon_1 = \sum_{j=1}^{\infty} \frac{z^2}{2j^2} \sum_{i=0}^{\infty} \frac{(2i+1)z^{2i}}{(2j)^{2i}}$$

$$(26) \quad \cong 0.822z^2 + 0.406z^4 + 0.159z^6 + 0.055z^8 + \dots$$

Thus the correction due to overlapping lines is relatively small even at frequencies  $\sim \delta/3$  from the line center. Since  $d\epsilon_j/d\nu \ll d\epsilon_1/d\nu$  over the frequency range where breadth measurements can be made on a particular line, Eq. (20) can be corrected for the effect of distant lines by multiplying by  $(1 - 0.822z^2 + \dots)$ . For an Elsasser-type band when all the above corrections are included to first order, Eq. (20) becomes

$$(27) \quad S^0 \gamma^0 \cong \frac{\pi e b_*^2}{4P^2 l} \left[ 1 + 4 \left( \frac{\gamma^0 P}{b_*} \right)^2 + \frac{4\epsilon - 6}{3} \left( \frac{d}{b_*} \right)^2 - 0.822 \left( \frac{b_*}{\delta} \right)^2 \right].$$

Since the Elsasser model is rarely a good approximation, the overlapping-line correction must in many cases be evaluated by direct summation. This task is not difficult if the frequency, strength, and width for each line is known, since only a few of the nearest and strongest lines usually need to be included in the sum.

An explicit formula corresponding to Eq. (20) including the various correction terms can be given for one other case of interest, namely that where a pair of lines of equal width are close together but distant from other lines. Such a situation occurs, for example, in the HCl spectrum, where each line of  $\text{HCl}^{35}$  is accompanied by a weaker satellite due to  $\text{HCl}^{37}$ . In the 1-0 band the  $\text{HCl}^{35}-\text{HCl}^{37}$  spacing is  $\sim 2 \text{ cm}^{-1}$ , while the separation between lines of the same isotopic species is  $\sim 20 \text{ cm}^{-1}$ . If the line whose breadth is to be measured has a strength  $S^0$  and that of the other line is  $rS^0$ , then from Eq. (23) one can calculate the value of  $\epsilon$  corresponding to a measured  $b_\epsilon$ . By this procedure one finds that the right side of Eq. (20) must be divided by the expression

$$(28) \quad \left[ 1 + \frac{r}{4} \left( \frac{b_\epsilon}{\delta} \right)^2 + \frac{3r}{16} \left( \frac{b_\epsilon}{\delta} \right)^4 + \dots \right],$$

where  $\delta$  is the separation between the lines. Accordingly, the stronger line can be measured over a somewhat wider range of  $b_\epsilon/\delta$  than can the weaker. In the case of  $\text{HCl}^{35}$ , where  $r \sim 1/3$ , width measurements can be made out to  $b_\epsilon \sim \delta$ . For the less abundant isotopic species the correction becomes of the order of 10% at  $b_\epsilon \sim \delta/3$ .

If at high optical densities a pair of close lines of equal half-width and known intensity ratio coalesce so that there is practically no transmission between them, but they are distant from other lines, then the measured total breadth of the combined lines can be used to determine the product  $S^0\gamma^0$ . For this case no explicit formula relating the measured breadth to  $S^0\gamma^0$  has been derived. It is, however, relatively easy to relate the measured breadth to the strength-width product if  $\delta$  and  $r$  are known. The measured combined breadth of such a pair of lines at extinction  $\epsilon$  is given by

$$(29) \quad b_\epsilon = q + \delta + s$$

where  $q$  is the distance ( $\nu - \nu_{0,1}$ ) from the stronger component to the nearest point of the blended line where the extinction is  $\epsilon$ , and  $s$  is the distance ( $\nu - \nu_{0,2}$ ) from the weaker component of the pair to the other side of the blend. Then the extinction is given by

$$(30a) \quad \epsilon_{q,s} = S^0\gamma^0/P^2\pi^{-1}[q^{-2} + r(q+\delta)^{-2}]$$

$$(30b) \quad = S^0\gamma^0/P^2\pi^{-1}[rs^{-2} + (s+\delta)^{-2}].$$

Eqs. (29) and (30) can be solved by successive approximations for  $q$ ,  $s$ , and  $S^0\gamma^0$ , all the other quantities being known experimentally.

If the exact position of the line center for the stronger component can be located, e.g., by observing the spectrum at low pressure, the distance  $q$  can be measured directly and used in Eq. (30a) to evaluate the product  $S^0\gamma^0$ .

## V. STRENGTH-WIDTH PRODUCTS FROM THE TROUGHS BETWEEN LINES

A third type of measurement that depends very little upon resolving power is that of the extinction in a region where the correction terms in Eq. (10) are small, i.e., far from the line center. Therefore this type of measurement is also useful primarily at relatively high optical densities, since only in this case is there measurable extinction sufficiently far from the line center.

The extinction due to a band consisting of lines all having the Lorentz shape is given by Eq. (23) for a frequency range where  $(\nu - \nu_0)^2 \gg \gamma_L^2$ . Accordingly, the extinction at any frequency where this condition holds should be proportional to  $lP^2$ . This proportionality should hold even if the lines have non-Lorentzian shapes of the type given by Eq. (A1). In all our experimental results on several different molecules it was found to hold within experimental error at pressures up to one atmosphere.

At the high optical densities permitting measurements with  $(\nu - \nu_0)^2 \gg \gamma_L^2$ , it is sometimes experimentally difficult to locate the frequency precisely with reference to the black line centers. It is, however, easy and convenient to make measurements of extinction at the minima between neighboring lines, for which the frequency may be calculated from a knowledge of the line positions and strengths. We term these minima "troughs" and characterize further two especially useful situations, the "internal troughs" which occur between close pairs of similar lines of known intensity ratio, such as isotopic pairs of equal  $J$  in  $\text{HCl}^{35}-\text{HCl}^{37}$  or  $K$ -doublets in  $\text{H}_2\text{O}$ , and the "external troughs" between lines of successive  $m$ -numbering in monoisotopic bands of diatomic or linear polyatomic molecules. In this section we derive the relations between the trough extinction and the strength-width product of the neighboring lines.

If there is an isolated pair of Lorentz lines of equal width separated by a frequency difference  $\delta \gg \gamma_L$  and with strengths  $S^0$  and  $rS^0$ , it can be shown that at the minimum between the lines the extinction is given by

$$(31) \quad \epsilon_{i.t.} = \frac{S^0 \gamma^0 l P^2}{\pi \delta^2} (1+r^{\frac{1}{2}})^3,$$

and the minimum occurs at a frequency difference  $|\nu - \nu_0|$  from the center of one line given by

$$(32) \quad |\nu - \nu_0| = \delta(1+r^{\frac{1}{2}})^{-1}.$$

In accurate applications of Eq. (31) corrections similar to those discussed in the previous section should be included for finite resolving power, the line width, and other lines in the band. The corrected expression for the product of the line strength and half-width of a Lorentz line from the measured extinction  $\epsilon_{i.t.}$  at an internal trough between the line in question and another of the same width and strength  $rS^0$  is then

$$(33) \quad S^0 \gamma^0 \cong \frac{\pi \delta^2 \epsilon_{i.t.}}{l P^2} (1+r^{\frac{1}{2}})^{-3} \left[ 1 - \frac{1}{2}(1+r^{-\frac{1}{2}})(1+r^{\frac{1}{2}}) \frac{d^2}{\delta^2} + r^{-\frac{1}{2}}(1+r^{\frac{1}{2}})^2 \left( \frac{\gamma^0 P}{\delta} \right)^2 - \frac{\sum_i S_i^0 \gamma_i^0 (\nu - \nu_{0,i})^{-2}}{S^0 \gamma^0 (1+r^{\frac{1}{2}}) \delta^{-2}} \right].$$

The corrections for slit width and line width have opposite signs and for many conditions all corrections may be neglected. Hence internal trough measurements yield quite directly the product  $S^0\gamma^0$ .

A particularly simple expression can be given for the extinction in the "external trough," when the band is of the idealized Elsasser type, having a large number,  $2n$ , of lines of equal spacing  $\delta$ , strength  $S^0$ , and width  $\gamma^0$ . This expression may be corrected approximately for more realistic conditions in any "near-Elsasser" portion of a band where isotopic and upper-state lines are negligibly weak and where the spacings, strengths, and widths of up to  $n \sim 5$  successive lines on each side are changing sufficiently slowly that they may be approximated by expressions quadratic in  $n$ . For spectra not meeting these conditions, and for work of the highest accuracy in any situation, the detailed summation, Eq. (23), will be required.

In the ideal Elsasser band, the summation in Eq. (33) becomes

$$(34) \quad \epsilon_{e.t.} = 2\pi^{-1} S^0 \gamma^0 / P^2 \delta^{-2} \sum_{n=0}^{\infty} (n + \frac{1}{2})^{-2} = \pi S^0 \gamma^0 / P^2 \delta^{-2}.$$

Rearranging, and including the line width and slit width corrections as before, one obtains

$$(35) \quad S^0 \gamma^0 = \frac{\epsilon_{e.t.} \delta^2}{\pi / P^2} \left( 1 + \frac{4(\gamma^0)^2 P^2}{\delta^2} - \frac{2d^2}{\delta^2} + \dots \right).$$

For the "near-Elsasser" case we have, since

$$\nu_m \cong \nu_0 + (B'' + B')m - (B'' - B')m^2,$$

$$\delta_m = \nu_{m+1} - \nu_m = 2B' - 2(B'' - B')m,$$

and

$$(36a) \quad \begin{aligned} \nu &\cong \frac{1}{2}(\nu_{m+1} + \nu_m), \\ \nu_i - \nu &= \pm(n + \frac{1}{2})\delta_m \left[ 1 \mp \frac{2n(n+1)}{2n+1} \frac{B'' - B'}{\delta_m} \right], \quad (n = 0, 1, 2, \dots). \end{aligned}$$

If it is assumed that

$$(36b) \quad \begin{aligned} S_i^0 &= \bar{S}_m^0 [1 \pm (n + \frac{1}{2})h_m + (n + \frac{1}{2})^2 t_m], \\ \gamma_i^0 &= \bar{\gamma}_m^0 [1 \pm (n + \frac{1}{2})p_m + (n + \frac{1}{2})^2 u_m], \end{aligned}$$

where  $\bar{S}_m^0$  and  $\bar{\gamma}_m^0$  are the average line strength and width parameters of the neighboring lines with  $n = \pm \frac{1}{2}$ , then in the summation of the products  $S_i^0 \gamma_i^0 (\nu - \nu_{0,i})^{-2}$  the first-order terms in  $(B'' - B')$ ,  $h_m$ , and  $p_m$  vanish. To second order the extinction in the external trough,  $\epsilon_{e.t.}$ , becomes

$$(37) \quad \epsilon_{e.t.} \cong \frac{\pi \bar{S}_m^0 \bar{\gamma}_m^0 / P^2}{\delta_m^2} \left\{ 1 + \frac{2n}{\pi^2} \left[ t_m + h_m p_m + u_m + \frac{2(B'' - B')}{\delta_m} (h_m + p_m) \right. \right. \\ \left. \left. + 3 \left( \frac{B'' - B'}{\delta_m} \right)^2 \right] \right\}.$$

The correction terms in Eq. (37) are written in the usual order of descending importance, and for many cases they will all be small. The quantity  $h_m$  vanishes

at the branch maximum, and  $t_m$  will likewise vanish at somewhat higher  $|m|$ . The quantity  $(B'' - B')/\delta_m$  is of the order of 0.01 or less for most vibration-rotation bands. Pronounced variations in line width with  $m$  leading to high values of  $p_m$  and  $u_m$  are not encountered except for light, polar molecules, such as HF, where the direct summation is practical since there are few important lines. Hence, the numerical value of the terms in the square brackets in Eq. (37) will often not exceed 0.1, and the fact that mathematically the bracketed term is non-convergent if  $n \rightarrow \infty$  is of no practical importance. Comparison of Eq. (37) with the results of direct summation for a number of cases in such molecules as CO and CO<sub>2</sub> has shown that it is sufficiently accurate to take  $n \sim 5$ , i.e.,  $2n/\pi^2 \cong 1$ , in applying Eq. (37) for any case where the correction is  $< 0.1$ . Direct summation must be used for larger corrections. With this proviso, the completely corrected expression for  $\bar{S}^0 \gamma^0$  is

$$(38) \quad \bar{S}^0 \gamma^0 \cong \frac{\epsilon_{e.t.} \delta_m^2}{\pi l P^2} \left[ 1 + \frac{4(\gamma^0)^2 P^2}{\delta_m^2} - \frac{2d^2}{\delta^2} - t_m - h_m p_m - u_m - \frac{2(B'' - B')}{\delta_m} (h_m + p_m) \right].$$

## VI. LINE SHAPES

The preceding sections have described three methods of obtaining the product  $S^0 \gamma^0$  for a given line. The equivalent width gives this product as integrated over a relatively narrow range of  $(\nu - \nu_0)$ ; the breadth gives it at an arbitrary number of values of  $(\nu - \nu_0)$ ; and the troughs give the mean  $S^0 \gamma^0$  for a pair of lines at specific values of  $(\nu - \nu_0)$  imposed by the nature of the spectrum. If all these methods yield the same value of  $\gamma^0$ , this is direct evidence for the validity of the Lorentz shape for that line over the range of  $(\nu - \nu_0)$  included. The equivalent width measurement is to be thought of as most directly yielding the Lorentz  $\gamma^0$ , inasmuch as it most heavily weights the regions at low  $(\nu - \nu_0)$  which are most certain to be governed by the impact shape.

The ratio of the product  $S^0 \gamma^0$  at some specific  $|\nu - \nu_0|$  as determined from the breadth or trough measurement to the equivalent-width value may be defined as the "shape factor",  $\chi(\nu - \nu_0)$ . It is also possible to obtain a value for  $\chi$  given by the ratio of the observed extinction to that calculated by Eq. (23) for any observable value of  $\nu$ , even when many lines at different  $\nu - \nu_{0,i}$  contribute importantly to the sum. In this case  $\chi$  does not correspond to a single value of  $(\nu - \nu_0)$ . If  $\chi > 1$ , we refer to positive deviations from the Lorentz shape; if  $\chi < 1$ , to negative deviations. Measurements of the shape factor in the wings of a single line will be useful if  $\chi \neq 1$  at the external troughs. Provided that the center of the line can be accurately located, and that the corrections for slit widths, line widths, and overlapping are small, one may derive the expression for this case similarly to Eq. (38), namely,

$$(39) \quad S^0 \gamma^0 = \frac{\pi \epsilon (\nu - \nu_0)^2}{l P^2} \left[ 1 + \left( \frac{\gamma^0 P}{\nu - \nu_0} \right)^2 + \left( \frac{1}{2} - \frac{1}{3} \epsilon \right) \left( \frac{d}{\nu - \nu_0} \right)^2 - \frac{\sum_i S_i^0 \gamma_i^0 (\nu - \nu_{0,i})^{-2}}{S^0 \gamma^0 (\nu - \nu_0)^{-2}} \right].$$

The functional form of  $\chi(\nu - \nu_0)$  may thus be obtained for  $(\nu - \nu_0) \ll \delta/2$ .

Even if no significant deviations from  $\chi = 1$  have been demonstrated at distances from the resonant frequency out to half the spacing between lines, there are exceptional cases in molecular spectra where it is possible to measure  $\chi$  at still higher values of  $\nu - \nu_0$ , and thus to check the Lorentz shape in the extreme wings. One such case is at the band origin of a  $\Sigma-\Sigma$  band of a linear molecule where there is a "missing" line at  $m = 0$ . Another possibility at extremely high optical densities is in the extreme wings of the band where the summed tails of strong lines contribute most of the absorption. This type of measurement is particularly useful in favorable cases where the absorption can be measured beyond the frequency at which the lines of the band converge to form a head. In all the cases suggested in this paragraph a large number of distant strong lines at different frequencies contribute to the extinction. Hence it is difficult from such data to deduce precisely the shape of a single line. Should  $\chi$  deviate widely from unity, one may assume various functional forms of  $\chi(\nu - \nu_0)$ , and carry out a detailed summation until agreement with experiment is obtained.

It may be pointed out again that the determinations leading to tests of the line shape can be made to a good approximation without a knowledge of  $S_i^0$  and  $\gamma_i^0$ , since only the products  $S_i^0\gamma_i^0$  are involved. To obtain  $\gamma_i^0$ , however, it is necessary to carry out some measurements at low optical density whereby  $S_i^0$  is measured.

#### APPENDIX A

Consider a line whose shape is given by the Lorentz equation out to some limiting frequency from the line center  $\nu_m = |\nu(\text{cutoff}) - \nu_0|$  where  $\nu_m \gg \gamma_L$ , and beyond  $\nu_m$  by a modified equation which is symmetrical in  $(\nu - \nu_0)$ . Specifically, near the line center (region *a*) the absorption coefficient is given by

$$(A1a) \quad k_a = CS^0\gamma^0 P^2 \pi^{-1} [(\nu - \nu_0)^2 + (\gamma^0 P)^2]^{-1}, \quad 0 \leq |\nu - \nu_0| \leq \nu_m,$$

where  $S^0$  is the true strength of the line and  $C$  is a normalizing factor which may differ from unity if the line deviates from the Lorentz shape in any frequency range. The absorption coefficient in region *b* where  $|\nu - \nu_0| > |\nu_m|$  is assumed to be given by a modified Lorentz equation where the exponent of  $(\nu - \nu_0)$  is  $\eta$  rather than 2, namely,

$$(A1b) \quad k_b = \frac{CS^0\gamma^0 P^2}{\pi\nu_m^2} \left[ \left( \frac{\nu - \nu_0}{\nu_m} \right)^\eta + \left( \frac{\gamma^0 P}{\nu_m} \right)^\eta \right]^{-1}.$$

On expanding in terms of  $\gamma_L/(\nu - \nu_0)$  one obtains

$$(A2) \quad k_b \cong \frac{CS^0\gamma^0 P^2}{\pi} \left[ 1 - \frac{\eta}{2} \left( \frac{\gamma^0 P}{\nu - \nu_0} \right)^2 \right] \nu_m^{\eta-2} (\nu - \nu_0)^{-\eta}.$$

In order to evaluate  $C$  we note that

$$(A3) \quad S = 2 \int_0^{\nu_m} k_a d(\nu - \nu_0) + 2 \int_{\nu_m}^{\infty} k_b d(\nu - \nu_0) \\ = \frac{2CS^0P}{\pi} \left\{ \tan^{-1} y^{-1} - \frac{y}{\eta-1} \left[ 1 - \frac{\eta(\eta-1)}{2(\mu+1)} y \right] \right\},$$

where  $y = \gamma^0 P / \nu_m$ . Hence, by expanding in  $y \ll 1$ , the normalizing factor  $C$  is given by

$$(A4) \quad C = 1 + \frac{2}{\pi} \left( \frac{\eta-2}{\eta-1} \right) y + \frac{4}{\pi^2} \left( \frac{\eta-2}{\eta-1} \right)^2 y^2 + \frac{2}{\pi} \left[ \frac{4}{\pi^2} \left( \frac{\eta-2}{\eta-1} \right)^3 + \frac{\eta-2}{6(\eta-1)} \right] y^3 + \dots$$

The equivalent width of the line defined by Eq. (14) is given by

$$(A5) \quad W = W_a + W_b$$

where

$$(A5a) \quad W_a = \int_{-\nu_m}^{\nu_m} (1 - e^{-k_a l}) d(\nu - \nu_0)$$

and

$$(A5b) \quad W_b = 2 \int_{\nu_m}^{\infty} (1 - e^{-k_b l}) d(\nu - \nu_0).$$

If the line in question is sufficiently strong so that it is in the square-root region of the Ladenburg-Reiche curve, Eq. (18a), then

$$(A6) \quad W_a = 2(CS^0 \gamma^0 l P^2)^{\frac{1}{2}} - 2 \int_{\nu_m}^{\infty} (1 - e^{-k_a l}) d(\nu - \nu_0).$$

Assuming that  $k_a l$  is sufficiently small at  $(\nu - \nu_0) = \nu_m$  that the exponentials in Eqs. (A5b) and (A6) may be expanded, one finds upon integration that the equivalent width of the line is

$$(A7) \quad W = C^{\frac{1}{2}} W_L(S^0 l P) + \frac{2CS^0 l P}{\pi} \left( \frac{2-\eta}{\eta-1} \right) y + \frac{CS^0 l P}{\pi} \left[ \frac{2}{3} + \frac{CS^0 l}{\pi \gamma^0} \left( \frac{1}{3} - \frac{1}{2\eta-1} \right) - \frac{\eta}{\eta+1} \right] y^3 + \dots$$

where  $W_L(S^0 l P)$  is the equivalent width expected at  $l$  and  $P$  for a Lorentz line of strength  $S^0$ . Defining  $\Delta W$  by the relation

$$(A8) \quad \Delta W = W_a + W_b - W_L(S^0 l P)$$

one finds upon combining Eqs. (A4), (A7), and (A8) that

$$(A9) \quad \frac{\Delta W}{W_L} = \frac{1}{2\pi} \left( \frac{2-\eta}{\eta-1} \right) \left( \frac{W_L^0 - 2\gamma^0}{\nu_m} \right) P - \frac{\gamma^0}{\pi^2} \left( \frac{2-\eta}{\eta-1} \right) \left( \frac{W_L^0 - 2\gamma^0}{\nu_m^2} \right) P^2 + \dots$$

#### REFERENCES

- AMAT, G. 1952. Publs. sci. et tech. ministère air (France), No. 276.
- ANDERSON, P. W. 1949. Phys. Rev. **76**: 647.
- BENEDICT, W. S., HERMAN, R., MOORE, G. E., and SILVERMAN, S. 1956. Can. J. Phys. **34**: 850.
- BENEDICT, W. S., MOORE, G. E., and SILVERMAN, S. 1955. Bull. Am. Phys. Soc. **30** (No. 2): 28.
- BENEDICT, W. S. and SILVERMAN, S. 1954. Bull. Am. Phys. Soc. **29** (No. 1): 15.
- BLEANEY, B. and PENROSE, R. P. 1948. Proc. Phys. Soc. (London), **60**: 548.
- BREENE, R. G. 1955. The shift and shape of spectral lines. Geophysical Research Papers No. 41, Air Research and Development Command. Sept.

- COULON, R., GALATRY, L., OKSENGORN, B., ROBIN, S., and VODAR. 1954. *J. phys. radium*, **15**: 641.
- ELSASSER, W. M. 1942. Heat transfer by infrared radiation in the atmosphere. *Harvard Meteorological Series No. 6*.
- FOLEY, H. M. 1946. *Phys. Rev.* **69**: 616.
- GOLDBERG, L. 1951. *Astrophys. J.* **113**: 567.
- GOODY, R. M. and WORMELL, T. W. 1951. *Proc. Roy. Soc. A*, **209**: 178.
- HERMAN, R., MOORE, G. E., SILVERMAN, S., and WALLIS, R. F. 1955. *Bull. Am. Phys. Soc.* **30** (No. 2): 27.
- HERZBERG, G. 1945. Molecular spectra and molecular structure. Vol. II. D. van Nostrand Company, Inc., New York.
- 1950. Molecular spectra and molecular structure. Vol. I. Second edition. D. van Nostrand Company, Inc., New York.
- JOHNSON, C. M. and SLAGER, D. M. 1952. *Phys. Rev.* **87**: 677.
- KOSTKOWSKI, H. J. and BASS, A. M. 1955. *J. Opt. Soc. Amer.* **45**: 900.
- LADENBURG, R. and REICHE, F. 1911. *Ann. Physik*, **42**: 181.
- LINDHOLM, E. 1938. *Z. Physik*, **109**: 223.
- LINDHOLM, E. 1946. *Arkiv Mat. Astron. Fysik*, A, **32**: No. 17.
- MARGANAU, H. and WATSON, W. W. 1936. *Revs. Mod. Phys.* **8**: 22.
- NIELSEN, J. R., THORNTON, V., and DALE, E. B. 1944. *Revs. Mod. Phys.* **16**: 307.
- PENNER, S. S. and WEBER, D. 1951. *J. Chem. Phys.* **19**: 807, 1351.
- PENNER, S. S. and WEBER, D. 1953. *J. Chem. Phys.* **21**: 149.
- PLASS, G. N. and FITEL, D. J. 1953. *Astrophys. J.* **117**: 225.
- SMITH, W. V. and HOWARD, R. 1950. *Phys. Rev.* **79**: 132.
- SPITZER, L. 1940. *Phys. Rev.* **58**: 348.
- VINCENT-GEISSE, J. 1954. *J. phys. radium*, **15**: 539.

# THE STRENGTHS, WIDTHS, AND SHAPES OF INFRARED LINES

## II. THE HCl FUNDAMENTAL<sup>1</sup>

BY WILLIAM S. BENEDICT,<sup>2</sup> ROBERT HERMAN,<sup>3</sup> GORDON E. MOORE,<sup>4</sup>  
AND SHIRLEIGH SILVERMAN<sup>5</sup>

### ABSTRACT

The methods described in Part I are applied in detail to the determination of strengths, widths, and shapes of the vibration-rotation lines of the 1-0 bands of HCl<sup>16</sup> and HCl<sup>37</sup> observed at 300°K. The variation of the line strengths with rotational quantum numbers is compared with theory to yield a value of the ratio of the permanent electric dipole moment to the product of the effective charge and the equilibrium internuclear distance of  $+0.988 \pm 0.022$ . The band strength was found to be  $130 \text{ cm}^{-2} \text{ atm}^{-1}$  which should be good to  $\sim 5\%$ . A marked variation of line width with rotational quantum number has been found which follows approximately the Boltzmann population distribution. This result is compared with a theory that considers resonant dipole-dipole and billiard ball interactions. The line widths were found to vary from  $\sim 0.25 \text{ cm}^{-1} \text{ atm}^{-1}$  for  $J = 3$  to  $\sim 0.07 \text{ cm}^{-1} \text{ atm}^{-1}$  for  $J = 13$ . Evidence is obtained that at distances greater than  $\sim 1.5 \text{ cm}^{-1}$  from the line centers the absorption is greater than is given by the Lorentz line shape. In the wings of the lines the absorption is better represented by a line shape varying as  $(\nu - \nu_0)^{-\eta}$  where  $\eta \sim 1.8$ .

### I. INTRODUCTION

In this paper the methods described in the previous paper (Benedict, Herman, Moore, and Silverman 1956), referred to as Part I, are applied in detail to the spectral lines in the fundamental vibration-rotation band of HCl observed in absorption at room temperature.

This particular molecule was chosen as a first example for a number of reasons. The vibration-rotation bands of HCl lie in regions of the spectrum which are relatively free from overlapping atmospheric absorption bands and where sensitive photoconducting detectors facilitate the use of high resolving power. Since the individual lines are widely spaced, there is a minimum of overlapping, and measurements can be made at relatively great distances from the line centers. Other reasons for choosing this particular molecule are that the individual lines are relatively wide, since the collision diameter associated with a highly polar molecule is large, and because there is a marked dependence

<sup>1</sup>Manuscript received May 9, 1956.

Contribution from the Laboratory of Astrophysics and Physical Meteorology, The Johns Hopkins University, Baltimore, Maryland, the Applied Physics Laboratory, The Johns Hopkins University, Silver Spring, Maryland, and the University of Maryland, College Park, Maryland.

The work reported herein was supported in part by the Bureau of Ordnance under contract NOrd-7386 and Office of Naval Research, Department of the Navy, and by the Air Force, Cambridge Research Center.

<sup>2</sup>Laboratory of Astrophysics and Physical Meteorology, The Johns Hopkins University.

<sup>3</sup>Department of Physics, University of Maryland, College Park, Maryland. Visiting Professor on leave from Applied Physics Laboratory, The Johns Hopkins University. Present address: Research Staff, General Motors Corporation, Detroit, Michigan.

<sup>4</sup>Applied Physics Laboratory, The Johns Hopkins University. Present address: Shockley Semiconductor Laboratory, Mountain View, California.

<sup>5</sup>Office of Naval Research, Washington, D.C. On leave from Applied Physics Laboratory, The Johns Hopkins University.

of line width on rotational quantum number. The latter effect occurs because most of the colliding molecules are in the first several rotation states at room temperature, making the effect of resonance interaction relatively important. Furthermore, the separation of the isotopic doublets arising from  $\text{HCl}^{35}$  and  $\text{HCl}^{37}$ ,  $\sim 2 \text{ cm}^{-1}$ , is sufficiently large so that strength and width measurements can be made on individual isotopic lines. Since the relative intensity in isotopic line pairs is governed by the chlorine isotopic abundance ratio, i.e.  $\text{Cl}^{35}/\text{Cl}^{37} \cong 75.4/24.6 \cong 3.07$  (Nier and Hanson 1936), one has a "built-in" intensity calibration. The possibility of deuterium substitution provides a second pair of molecules with nearly identical potential functions and electronic structure, which permits additional checks to be made since the properties of one of the molecules should be calculable from those of the other. For example, if the electric moment function were determined from observations of the intensities of HCl bands, then one should be able to calculate the intensities of DCl bands to within the accuracy of the theory employed. Another advantage in studying a diatomic molecule is that theoretical interpretation is considerably simpler than for the simplest polyatomic molecules.

The 1-0 or fundamental band of HCl has been studied extensively in the past (Herzberg 1950). It was among the first infrared bands in which vibration-rotation lines were resolved (Imes 1919). Intensity measurements for this band have been made by Bourgin (1928), by Penner and Weber (1953), and by Coulon, Galatry, Oksengorn, Robin, and Vodar (1954). The band strength has also been derived from dispersion measurements by Rollefson and Rollefson (1935) and by Hammer (1948). In recent high resolution work the line positions and molecular constants have been accurately determined (Mills, Thompson, and Williams 1953). "Line" strengths for the unresolved isotopic doublets have been measured by Bourgin (1927) and Dennison (1928) and compared by the latter with the intensity distribution predicted by Oppenheimer (1926) for a rotating-vibrating molecule.

Attempts to evaluate the line widths from low dispersion data have not been particularly successful (Weber and Penner 1953) since the assumption of equal line widths was employed. The only previous line width measurements that have been made on individual lines of HCl are those of Lindholm (1939), who studied the 4-0 band in the photographic infrared. At pressures of 3.5 atm. the widths of the strongest lines could be measured directly. He found a marked variation of line width with rotational quantum number  $J$  for which various theories have been offered (Anderson 1949, 1950; for further references see Breene 1955). It might be mentioned that the widest lines studied by Lindholm were found to have total widths,  $\sim 2 \text{ cm}^{-1}$  at 3.5 atm., which are considerably greater than one might expect from kinetic theory collision diameters.

In the present paper we present the experimental results regarding line strengths, line widths, and line shapes obtained for the 1-0 band of HCl observed at room temperature. In addition the relative line strengths are compared with theory. An experimental determination of the integrated band strength is also presented.

## II. THEORY

In addition to the theoretical discussion given in Part I of this paper we give very briefly a few results that are required here concerning line strengths. Using the work of Herman and Wallis (1955) for a diatomic molecule in a  $^1\Sigma$ -state the line strength  $S_m^0$  can be related to the total band strength  $\mathbf{S}_v^0$  approximately as follows:

$$(1) \quad \frac{S_m^0}{\mathbf{S}_v^0} = \frac{\exp[-E(J'')/kT]}{Q_J(v'', T)} \frac{\nu_m}{\bar{\nu}_{v'', v'}} |m| F_{v'', v'}(m),$$

where  $E(J'')$  is the rotational energy of the absorbing state;  $Q_J(v'', T)$  is the rotational partition sum for the absorbing vibrational state  $v''$ ;  $\nu_m$  is the resonant frequency of the line;

$$(1a) \quad m = \begin{cases} -J & \text{for the } P\text{-branch,} \\ J+1 & \text{for the } R\text{-branch;} \end{cases}$$

$\bar{\nu}_{v'', v'}$ , the "effective vibrational frequency", is defined by the condition

$$(1b) \quad \sum_m \frac{\exp[-E(J'')/kT]}{Q_J(v'', T)} \frac{\nu_m}{\bar{\nu}_{v'', v'}} |m| F_{v'', v'}(m) = 1;$$

and the quantity  $F_{v'', v'}(m)$  is a correction which arises from the interaction of vibration and rotation. For the 1-0 band  $F_{0,1}(m)$  is given to first order in  $B_e/\omega_e$ , where  $B_e$  and  $\omega_e$  are the usual spectroscopic constants (Herzberg 1950), by

$$(2) \quad F_{0,1}(m) \cong 1 - (8\theta B_e/\omega_e)m + \dots,$$

where

$$(2a) \quad \theta = M_0/(M_1 r_e).$$

The quantities  $M_0$  and  $M_1$  are the permanent electric moment and effective charge on the vibrating atoms, respectively, and  $r_e$  is the equilibrium internuclear separation, which appear in the expansion for the electric moment  $\mathbf{M}$  given by

$$(2b) \quad \mathbf{M} = \sum_i M_i (\mathbf{r} - \mathbf{r}_e)^i.$$

In practice we use the complete expression for  $F_{0,1}$  given in Herman and Wallis (1955).

Since in general  $\theta$  is not known, the  $F$ -factor cannot be calculated from Eq. (2). However, the  $F$ -factors for the individual lines when measured experimentally yield both the magnitude and sign of  $\theta$ . From Eq. (1) it follows that the ratio of the  $F$ -factors for  $P$ -branch and  $R$ -branch lines originating from the same  $J$ -state is given by

$$(3) \quad \frac{F_{v'', v'}(P)}{F_{v'', v'}(R)} = \frac{S_J^0(P)}{S_J^0(R)} \left( \frac{J+1}{J} \right) \frac{\nu_J(R)}{\nu_J(P)},$$

where the notation  $P$  and  $R$  indicates the respective branches. For lines whose measured equivalent widths lie in the linear region of the Ladenburg and Reiche curve (see Eq. (14a), Part I) the ratio of the equivalent widths,  $W(P)/W(R)$ , can be substituted for the ratio of the line strengths. In order to determine  $\theta$  from the ratio of the  $F$ -factors by means of Eq. (3), pairs of lines of the highest  $J$  values available should be used, since for these the ratio of

the line strengths deviates the most from unity. If no measurements are available in the linear region of the Ladenburg-Reiche curve of growth, it is possible to employ lines in the square-root region provided that an assumption is made concerning the line widths. For lines in the *P* and *R* branches having the same value of  $|m|$  it may be reasonable to assume that the line widths are equal. This assumption is justified on the basis of theory (Anderson 1949, 1950; Breene 1955) as well as by the results reported in this paper. In this case the ratio of the *F*-factors is given by the relation

$$(4) \quad \frac{F_{r'',r'}(P)}{F_{r'',r'}(R)} = \frac{S^0(P)}{S^0(R)} \frac{\nu(R)}{\nu(P)} e^{-\Delta E/(kT)},$$

where  $\Delta E = E(|m|-1) - E(|m|)$ . For square-root lines one can substitute for  $S^0(P)/S^0(R)$  in Eq. (4) the expression  $[W^0(P)/W^0(R)]^2$ .

### III. EXPERIMENTAL

The spectrometer used in this work consists of a grating monochromator of the Pfund-type equipped with a fore-prism to separate overlapping orders. For the HCl fundamental band a The Johns Hopkins University grating with 7500 lines per inch was used in the first order. Either a Nernst glower or zirconium arc lamp with a rock salt window served as a radiation source. In either case the source was operated from a voltage stabilizing device. The signal from the detector, a cooled PbTe cell, was fed to a phase-sensitive, 990-cycle amplifier, and the output of the amplifier was recorded automatically by a Brown Recording Potentiometer. The recorder deflection varied linearly with the incident light intensity to within the limits to which the linearity was determined, namely, about 1%. In order to maintain a signal-to-noise ratio of at least 50 it was necessary to use an effective spectral slit width of about 0.3–0.4 cm<sup>-1</sup> for the HCl fundamental, although the slit width varied somewhat from run to run.

Absorption measurements were made in cells of various lengths ranging from  $\sim 0.028$  cm. to  $\sim 140$  cm. Accurately spaced microcells (Hochheimer and Moore 1955) were used for short path lengths; conventional cells were used for path lengths in the range  $\sim 3$  to  $\sim 20$  cm.; and a Pfund, perforated mirror, triple-pass cell was used to obtain a path length of  $\sim 140$  cm. The mirrors in the 140 cm. cell were gold-coated by evaporation to resist attack by HCl.

Commercial HCl stated by the manufacturer to be 99.0% pure was freed of condensable materials, notably water vapor, by passing it slowly through a glass wool packed trap cooled to dry-ice temperatures. While this was all the purification usually employed, for a few runs the gas was fractionally distilled twice under vacuum, the central 50% being retained each time. The spectrum of this purified sample did not differ measurably from that of the undistilled material.

Filling of the absorption cells was accomplished by first pumping them to a pressure  $< 10^{-4}$  mm. of Hg and then admitting the HCl. The pressure of HCl was measured with a manometer read with a cathetometer. The mercury in the manometer was protected from HCl attack by a layer of silicone oil. The pressure in the cell was checked both before and after each run. Only if the pressure was constant to better than 1% was the run considered acceptable.

#### IV. EVALUATION OF EQUIVALENT WIDTHS

The evaluation of the equivalent width  $W$  for a particular line involves measuring the geometric area under that line (Eq. (11), Part I). Two practical difficulties arise when one attempts to make such measurements. First, it is often difficult to locate precisely the base-line and the zero-line, i.e., the positions corresponding to zero absorption and to complete absorption, respectively. Second, the correction for the absorption under the wings of the line, which cannot be measured directly, must be included in the value of  $W$  according to the method discussed in Part I.

In this investigation the base-line was determined by connecting regions of negligible absorption with a smooth curve whose shape was established from a blank run. For HCl at low optical densities there is a considerable region between each pair of lines where the absorption is extremely small. In such cases the location of the base-line is well determined by connecting the regions of low absorption by a straight line segment. At the highest optical densities employed ( $\sim 140$  cm. atm.) there is considerable absorption in the troughs between strong lines. In the latter case it was necessary to establish the base-line at the ends of the band and to interpolate over a large frequency range. Accordingly, at these high optical densities the base-line is less precisely determined. The zero-line was located either by imposing an opaque shutter in the optical path or by observing the recorder deflection at the center of a strong line at high optical density. The near-coincidence of these two methods proved that the stray light level was less than 2%.

The area under each line was measured directly on the recorder tracing. The area of the line was divided into a number of trapezoidal strips of equal height. The height of the strips was so chosen that there were always at least 10 trapezoidal strips and usually as many as 20. The average widths of the strips for a particular line were measured, summed, and then multiplied by the strip height. This area, divided by the height between the zero- and base-lines, and divided by the dispersion, is the basic value of equivalent width, in  $\text{cm}^{-1}$ . These basic values were corrected by Eqs. (17a) and (17b) of Part I for the wing absorption.

#### V. RESULTS AND DISCUSSION

In this section we present the experimental data on the 1-0 band of HCl and apply the methods discussed in Part I and in this paper to determine line strengths, widths, and shapes as well as the total band strength and the effective charge on the vibrating atoms.

##### *Equivalent Widths*

An example of the spectrum from which equivalent width measurements were made is shown in Fig. 1. The two curves in Fig. 1 show the same lines observed at two different path lengths and pressures so chosen that the equivalent widths of the lines in the two tracings are roughly equal, but the upper trace, taken at long path and low pressure, shows lines near the square-root limit of the Ladenburg-Reiche curve, while the lower trace, taken at short path and higher pressure, illustrates the same lines in the nearly linear

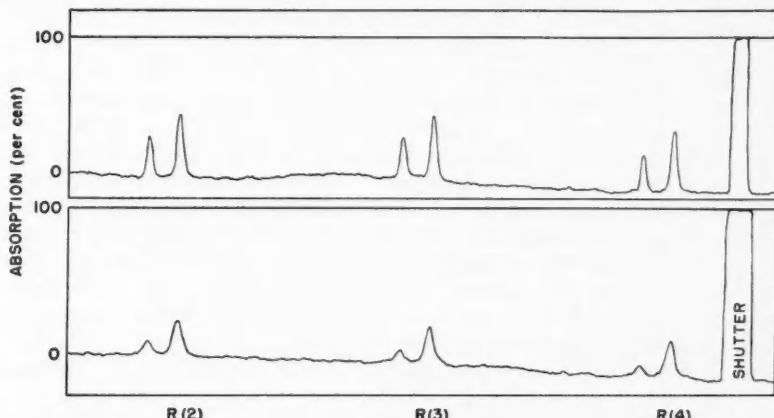


FIG. 1. Examples of the type of absorption spectra of HCl from which equivalent width measurements were made illustrating typical signal-to-noise ratios and resolution employed. The lower tracing taken at  $l = 0.028$  cm. and  $P = 1$  atm. shows  $R$ -branch lines in the linear region of the curve of growth. The upper tracing taken at  $l = 20$  cm. and  $P = \sim 0.01$  atm. shows the same lines in the square-root region.

region. One notices that the ratios of both the peak heights and the areas of a given isotopic pair are considerably larger in the near-linear trace than in the near-square-root example. In fact the ratio of the areas for the linear lines is  $\sim 3 : 1$  and for the square-root lines  $\sim 1.75 : 1$ . These examples illustrate typical signal-to-noise levels and spectral resolution employed in the HCl 1-0 band.

Before one can apply with confidence the relations concerning equivalent widths given in Part I, it is necessary to show that the equivalent width behaves as predicted, in that the measured values are independent of the resolving power employed and that the equivalent width is proportional to pressure over a considerable pressure range. Measurements were carried out to check both of these points.

TABLE I  
EXAMPLES TO INDICATE THE INDEPENDENCE OF  
EQUIVALENT WIDTH UPON SPECTRAL SLIT WIDTH

Slit ( $\text{cm}^{-1}$ )	$R(5)-\text{HCl}^{35}$ $W (\text{cm}^{-1})$	$R(5)-\text{HCl}^{37}$ $W (\text{cm}^{-1})$
0.24	0.525	0.322
0.29	0.546	0.306
0.34	0.564	0.327
0.41	0.560	0.319
0.47	0.566	0.322
0.71	0.538	0.314
1.02	0.536	0.308
1.78	0.522 <sup>a</sup>	0.297 <sup>a</sup>

<sup>a</sup>These values were obtained by measuring the sum of the  $\text{HCl}^{35}$  and  $\text{HCl}^{37}$  lines and decomposing this area in the theoretically expected ratio for these lines,  $\text{HCl}^{35}/\text{HCl}^{37} = (3.07)^{\frac{1}{2}}$ .

Table I gives the equivalent width of an isotopic pair of HCl lines at a variety of slit widths ranging from the smallest that could be employed consistent with a good signal-to-noise ratio to a slit so wide that the pair of isotopic lines coalesced into a blend with a single absorption maximum. In the latter case it is necessary to measure the sum of the equivalent widths for the pair and to apportion values to the individual lines in the theoretical ratio. As can be seen from Table I, there is no obvious trend in the measured value of  $W^0$  with slit width, confirming that the equivalent width is independent of the resolving power employed. The scatter of a few per cent in the sets of measurements gives an indication of the precision with which the individual measurements are made. It should be pointed out that all equivalent widths employed in this paper include a correction for the area in the wings of the line where the absorption is too small to be measured directly. As an illustration of the magnitude of this correction in a typical case Table II is included

TABLE II  
EXAMPLES OF TYPICAL WING CORRECTIONS IN EQUIVALENT WIDTH MEASUREMENTS, LINES  $R(0)$  OF HCl, PATH LENGTH 0.109 CM.;  $W^0$  VALUES ARE IN  $\text{CM}^{-1} \text{ATM}^{-1}$

Run	$W^0, \text{HCl}^{35}$		$W^0, \text{HCl}^{37}$	
	Uncorrected	Corrected	Uncorrected	Corrected
1	0.3922	0.4205	0.1401	0.1574
2	0.4258	0.4473	0.1523	0.1694
3	0.3714	0.4056	0.1309	0.1502
4	0.4117	0.4415	0.1530	0.1676
5	0.4291	0.4536	0.1425	0.1670
Average	0.4060	0.4337 $\text{cm}^{-1}$	0.1438	0.1623 $\text{cm}^{-1}$
Std. dev.	0.0217	0.0180	0.0082	0.0072

which gives the uncorrected and corrected values of  $W^0$  for five independent runs of line  $R(0)$  for both  $\text{HCl}^{35}$  and  $\text{HCl}^{37}$  in a cell 0.109 cm. long. One sees that the correction in these cases is  $\sim 5\text{--}10\%$ . These lines are in the nearly linear region. For square-root lines the corrections usually are somewhat smaller. It is gratifying to note that the inclusion of the wing correction actually tends to reduce the spread of the individual measurements as demonstrated by the standard deviations of the sets of values given in Table II.

The dependence of equivalent width on pressure for the isotopic pair of lines  $R(2)$  is shown in Fig. 2. The points represent the experimental data, while the solid curves are calculated theoretically for a pair of lines both having Lorentz shape for pressure broadening and taking into account the Doppler contribution. The Lorentz line width was adjusted to fit the data of  $\text{HCl}^{35}$  in the pressure region  $\sim 5\text{--}60$  mm. of Hg. The curve through the  $\text{HCl}^{37}$  points was obtained using Eq. (12) in Part I and assuming that this line has the same Lorentz width as that of  $\text{HCl}^{35}$ . The good fit to the experimental points for  $\text{HCl}^{37}$  shows that the lines of the isotopic pair do indeed have very nearly identical widths. The increase in  $W^0$  at the low pressure end of the

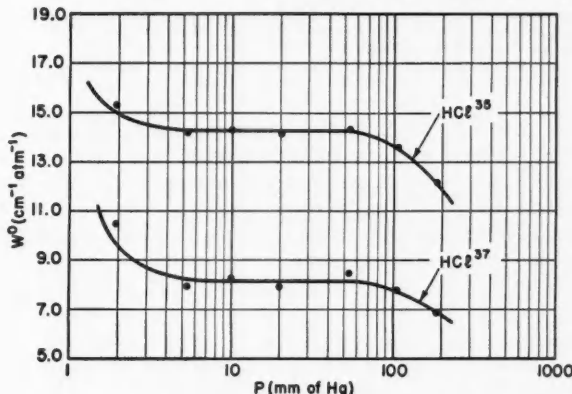


FIG. 2. Plot of  $W^0$  versus pressure for lines  $R(2)$  of  $\text{HCl}^{35}$  and  $\text{HCl}^{37}$  showing experimental points and theoretical curves calculated for Lorentz collision broadening and including the effects of both Doppler broadening and overlapping of isotopic lines.

curves results from the Doppler contribution, which is included in the theoretical curves by employing Eq. (13) of Part I. The decrease in  $W^0$  at the high pressure end of the curves results from the overlapping of the isotopic lines. The theoretical curve in this region was calculated by direct graphical integration under plots of the absorption expected for a pair of overlapping Lorentz lines. The experimental points on Fig. 2 each represent the average of several runs, ranging from two at the highest pressure, where the large areas are easily measured, to six at the low pressure end, where the small values of the equivalent width are relatively difficult to measure precisely. There is also somewhat more uncertainty in the points at low pressures because of difficulties in measuring the pressure accurately with our apparatus, so that the apparent deviations between the points and the calculated curve in the low pressure region are not considered to be beyond experimental error. One sees from Fig. 2 that an intermediate pressure region exists over which  $W^0$  is independent of pressure. In this particular example a range of pressures of about a factor of 10 seems to be usable without correction for Doppler broadening or overlapping lines.

Now that it has been established that the measured values of the equivalent widths have the predicted dependences on pressure and resolving power, we will proceed to use the equivalent width data to evaluate line strengths and widths.

Table III lists the values of  $W^0$  for all the lines measured at each path length. Where necessary these values have been corrected for any Doppler contribution. For the most part each entry in Table III is the average of measurements made upon 3 to 10 recorder tracings at a variety of pressures. The number of independent measurements for each entry is included with the tabulated values of  $W^0$ .

TABLE III

MEASURED EQUIVALENT WIDTHS PER ATMOSPHERE,  $W^0$ , AT VARIOUS PATH LENGTHS. DOPPLER AND WING CORRECTIONS HAVE BEEN INCLUDED. NUMBERS IN ITALICS ARE FOR HCl<sup>17</sup>. THE SMALL, RAISED NUMBERS INDICATE THE NUMBER OF INDEPENDENT MEASUREMENTS AVERAGED

Line	$\nu$ , cm <sup>-1</sup>	$W^0$				
		$l = 0.028$	$l = 0.109$	$l = 10.0$	$l = 20.0$	$l = 140$ cm.
<i>R(15)</i>	3129.38 <i>26.98</i>					0.0437 <sup>7</sup>
<i>R(14)</i>	19.62 <i>17.22</i>					0.1629 <sup>10</sup> <i>0.0645<sup>10</sup></i>
<i>R(13)</i>	09.08 <i>06.70</i>					0.1054 <sup>3</sup> <i>0.0410<sup>3</sup></i> 0.205 <sup>5</sup>
<i>R(12)</i>	3097.78 <i>95.40</i>					0.295 <sup>3</sup> <i>0.124<sup>3</sup></i> 0.819 <sup>8</sup>
<i>R(11)</i>	85.72 <i>83.36</i>					0.621 <sup>3</sup> <i>0.324<sup>3</sup></i>
<i>R(10)</i>	72.92 <i>70.56</i>			0.697 <sup>3</sup> <i>0.364<sup>3</sup></i>		1.115 <sup>8</sup> <i>0.588<sup>8</sup></i>
<i>R(9)</i>	59.38 <i>57.04</i>	0.0502 <sup>2</sup>		1.23 <sup>3</sup> <i>0.783</i>		1.852 <sup>5</sup>
<i>R(8)</i>	45.12 <i>42.80</i>	0.1072 <sup>5</sup> <i>0.0441<sup>2</sup></i>		2.16 <sup>3</sup> <i>0.973</i>		2.90 <sup>8</sup> <i>1.55<sup>8</sup></i>
<i>R(7)</i>	30.14 <i>27.87</i>	0.0534 <sup>3</sup>	0.2074 <sup>8</sup> <i>0.0689<sup>4</sup></i>	3.13 <sup>3</sup> <i>1.71<sup>3</sup></i>		4.44 <sup>8</sup> <i>2.42<sup>8</sup></i>
<i>R(6)</i>	14.47 <i>12.18</i>	0.0977 <sup>3</sup>	0.330 <sup>6</sup> <i>0.141<sup>6</sup></i>	4.67 <sup>3</sup>		6.54 <sup>8</sup>
<i>R(5)</i>	2998.10 <i>95.83</i>	0.1545 <sup>3</sup> <i>0.0546<sup>2</sup></i>	0.506 <sup>6</sup> <i>0.203<sup>6</sup></i>	6.73 <sup>3</sup> <i>3.93<sup>3</sup></i>		8.81 <sup>5</sup> <i>5.02<sup>5</sup></i>
<i>R(4)</i>	81.05 <i>78.80</i>	0.1924 <sup>3</sup> <i>0.0594<sup>1</sup></i>	0.694 <sup>1</sup> <i>0.272<sup>1</sup></i>	8.13 <sup>3</sup> <i>5.37<sup>3</sup></i>		11.66 <sup>5</sup> <i>6.73<sup>5</sup></i>
<i>R(3)</i>	63.33 <i>61.11</i>	0.2420 <sup>2</sup>	0.782 <sup>1</sup>	9.67 <sup>3</sup>		13.55 <sup>8</sup>
<i>R(2)</i>	44.96 <i>42.76</i>	0.2439 <sup>3</sup> <i>0.0816<sup>2</sup></i>	0.811 <sup>1</sup> <i>0.331<sup>1</sup></i>	9.96 <sup>3</sup> <i>6.08<sup>3</sup></i>		14.19 <sup>11</sup> <i>8.09<sup>11</sup></i>
<i>R(1)</i>	25.94 <i>23.76</i>	0.2165 <sup>3</sup> <i>0.0762<sup>3</sup></i>	0.705 <sup>4</sup> <i>0.299<sup>4</sup></i>	8.58 <sup>3</sup> <i>5.05<sup>3</sup></i>		12.01 <sup>5</sup> <i>7.21<sup>5</sup></i>
<i>R(0)</i>	06.28 <i>04.14</i>	0.1253 <sup>3</sup> <i>0.0464<sup>2</sup></i>	0.434 <sup>5</sup> <i>0.162<sup>5</sup></i>	6.60 <sup>3</sup> <i>3.75<sup>3</sup></i>		9.05 <sup>8</sup> <i>5.24<sup>8</sup></i>
<i>P(1)</i>	2865.13 <i>63.04</i>	0.1272 <sup>3</sup> <i>0.0395<sup>1</sup></i>	0.413 <sup>6</sup> <i>0.159<sup>6</sup></i>	6.28 <sup>3</sup> <i>3.55<sup>3</sup></i>		8.76 <sup>8</sup> <i>5.10<sup>8</sup></i>
<i>P(2)</i>	43.65 <i>41.60</i>	0.1962 <sup>3</sup> <i>0.0694<sup>3</sup></i>	0.627 <sup>4</sup> <i>0.251<sup>4</sup></i>	8.49 <sup>3</sup> <i>4.64<sup>3</sup></i>		11.35 <sup>8</sup> <i>6.63<sup>8</sup></i>
<i>P(3)</i>	21.59 <i>19.57</i>	0.2203 <sup>3</sup> <i>0.0855<sup>1</sup></i>	0.715 <sup>1</sup> <i>0.301<sup>1</sup></i>	9.63 <sup>3</sup> <i>5.44<sup>3</sup></i>		12.84 <sup>8</sup> <i>7.22<sup>8</sup></i>
<i>P(4)</i>	2798.96 <i>96.97</i>	0.1959 <sup>3</sup> <i>0.0655<sup>3</sup></i>	0.676 <sup>1</sup> <i>0.272<sup>1</sup></i>	8.69 <sup>3</sup> <i>5.09<sup>3</sup></i>		12.26 <sup>8</sup> <i>7.20<sup>8</sup></i>
<i>P(5)</i>	75.77 <i>73.82</i>	0.1445 <sup>3</sup> <i>0.0454<sup>2</sup></i>	0.527 <sup>6</sup> <i>0.204<sup>6</sup></i>	7.59 <sup>3</sup> <i>4.29<sup>3</sup></i>		10.42 <sup>8</sup> <i>6.11<sup>8</sup></i>
<i>P(6)</i>	52.04 <i>50.13</i>	0.1116 <sup>3</sup>	0.375 <sup>6</sup> <i>0.146<sup>6</sup></i>	5.97 <sup>3</sup> <i>3.30<sup>3</sup></i>		7.67 <sup>8</sup> <i>4.33<sup>8</sup></i>
<i>P(7)</i>	27.78 <i>25.91</i>	0.0599 <sup>2</sup>	0.2414 <sup>6</sup> <i>0.0949<sup>6</sup></i>	3.88 <sup>3</sup> <i>2.34<sup>3</sup></i>		5.31 <sup>8</sup> <i>3.00<sup>8</sup></i>
<i>P(8)</i>	03.00 <i>01.17</i>	0.1302 <sup>6</sup> <i>0.0452<sup>2</sup></i>	2.56 <sup>3</sup> <i>1.62<sup>3</sup></i>	2.56 <sup>3</sup> <i>1.62<sup>3</sup></i>		3.59 <sup>8</sup> <i>2.02<sup>8</sup></i>
<i>P(9)</i>	2677.72 <i>75.93</i>	0.0671 <sup>2</sup>	0.0671 <sup>2</sup>	1.36 <sup>3</sup> <i>0.95<sup>3</sup></i>		2.21 <sup>5</sup> <i>1.32<sup>5</sup></i>
<i>P(10)</i>	51.96 <i>50.20</i>			0.873 <sup>3</sup> <i>0.484<sup>3</sup></i>		1.323 <sup>5</sup> <i>0.701<sup>5</sup></i>
<i>P(11)</i>	25.72 <i>24.01</i>			0.486 <sup>3</sup> <i>0.220<sup>3</sup></i>		0.757 <sup>8</sup> <i>0.408<sup>8</sup></i>
<i>P(12)</i>	2599.02 <i>97.36</i>			0.235 <sup>3</sup> <i>0.097<sup>3</sup></i>		0.376 <sup>8</sup> <i>0.182<sup>8</sup></i>
<i>P(13)</i>	71.88 <i>70.26</i>			0.095 <sup>3</sup> <i>0.034<sup>3</sup></i>		0.1491 <sup>3</sup> <i>0.0562<sup>3</sup></i> 0.270 <sup>8</sup>
<i>P(14)</i>	44.31 <i>42.74</i>				0.0417 <sup>3</sup>	0.524 <sup>3</sup> <i>0.1030<sup>8</sup></i>
<i>P(15)</i>	16.32 <i>14.79</i>					0.0809 <sup>8</sup> <i>0.0304<sup>8</sup></i>

### Line and Band Strengths and Line Widths for Self-broadening

The data in Table III were treated by the analytical method described in Part I. Line strengths were estimated from the data at relatively short path lengths where the lines are nearly in the linear region of the Ladenburg-Reiche curve. These approximate line strengths were employed to estimate the band strength  $S_v^0$  and the parameter  $\theta$  which were needed to calculate smoothed values of the individual line strengths by means of Eq. (1). These smoothed line strengths were then combined with the data in Table III taken at relatively long path length to obtain values of the line-width parameter  $\gamma^0$ , which in turn were used to correct the short path measurements for deviations from the linear law. This entire process was repeated until self-consistency was obtained.

Since one of the objects of this work was to verify Eq. (1) experimentally, it was necessary to demonstrate its validity before the smoothing process for the line strengths could be employed. This theoretical relationship can be checked and a value of  $\theta$  estimated by examining  $F_{0,1}(P)/F_{0,1}(R)$  given by Eq. (3) or Eq. (4) as a function of  $|m|$ . Fig. 3 is a plot of  $F_{0,1}(P)/F_{0,1}(R)$  vs.

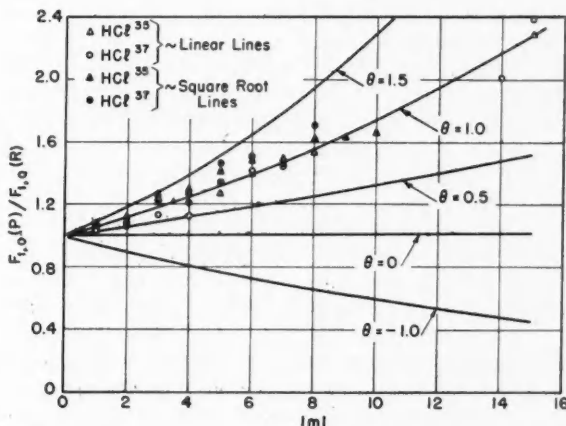


FIG. 3. Experimentally determined ratios of  $F$ -factors for the fundamental band of  $\text{HCl}$  and theoretical curves plotted versus  $|m|$  for various values of  $\theta = M_0/(M_1 r_e)$ .

$|m|$  as obtained from Eq. (4) and the data for both linear and square-root lines from Table III. One notices that the points scatter about the theoretical curve for  $\theta = 1.0$ , confirming the theoretical dependence upon  $\theta$  and suggesting that  $\theta \sim +1.0$ . If the vibration-rotation interaction term were omitted from the theoretical expression, the ratio would in all cases be unity. The interaction term becomes very important at high values of  $|m|$ . For example, at  $J = 15$  the observed ratio  $F_{0,1}(P)/F_{0,1}(R) \cong 2.3$  showing that line  $P(15)$  is more than twice as strong relative to  $R(15)$  as would be expected from the rigid rotor intensity formula. Because of the strong  $J$ -dependence of the  $F$ -factor, measurements at high rotational quantum numbers are particularly valuable in evaluating  $\theta$ . In order to make use of this fact several runs were made of the weak,

near-linear lines at high values of  $J$  in the  $P$  and  $R$  branches of the band in the 140 cm. cell at about atmospheric pressure. To obtain even higher values of  $J$  similar runs were made in a 20.3 cm. cell heated to  $\sim 600^\circ$  K. These data were employed with Eq. (3) to yield values of  $\theta$  which are given in Table IV. The average value of  $\theta$  obtained in this manner is  $\theta = 0.988$  with a probable error of 0.02, estimated from the scatter of the individual values. This value for  $\theta$  is very close to the value of unity implicit in Oppenheimer's theory

TABLE IV  
VALUES OF  $\theta = M_0/(M_{1s})$  FROM VARIOUS PAIRS OF HCl LINES  
IN THE NEAR-LINEAR REGION

Cl isotope	$J''$	$T(\text{°K.})$	$\theta$
35	19	600	0.885
37	18	600	0.999
37	17	600	1.055
35	15	300	1.103
35	14	300	1.035
37	14	300	0.995
37	13	300	0.842

Average =  $0.988 \pm 0.022$  (prob. error).

(Oppenheimer 1926). Thus the application of Oppenheimer's result to fundamental bands of HCl by Dennison (1928) is valid. From a study of the polarization of HCl and DCI, Bell and Coop (1938) have concluded that  $\theta$  should be negative. It might be pointed out that their method rests upon assigning a significance to a very small difference in the measured dipole moments of HCl and DCI.

Now that a value of  $\theta$  has been obtained it is possible to calculate a value of the band strength  $\bar{S}_{1,0}^0$  from each experimentally determined line strength. An average of these individual values of  $\bar{S}_{1,0}^0$  weighted as the number of independent measurements for each line yields  $\bar{S}_{1,0}^0 = 133.6 \text{ cm}^{-2}$  (atm. at  $300^\circ$ ) $^{-1}$  with a probable error calculated from the statistical scatter of  $\sim 0.4 \text{ cm}^{-2} \text{ atm}^{-1}$ . This procedure, however, suffers from the weakness that equal weight is given to all lines regardless of line strength. Since the equivalent widths of the weaker lines are quite difficult to measure precisely, an alternative procedure which weights lines in proportion to their strengths yields an average value of the total band strength as follows:

$$(5) \quad \bar{S}_v^0 = \left[ \sum_m (S_m^0)_{\text{meas}} \right] / \left[ \sum_m (S_m^0 / S_v^0)_{\text{cale}} \right],$$

where both sums are taken only over the experimentally measured lines of a given isotopic species. Thus the average total band strengths can be determined for the individual 1-0 bands of  $\text{HCl}^{35}$  and  $\text{HCl}^{37}$ . In order to obtain the strength of the 1-0 band averaged over the two isotopic species one employs Eq. (3a) of Part I. In the case of the fundamental vibration of HCl one expects theoretically that the ratio of band strengths for the two isotopic species is nearly inversely proportional to the ratio of the reduced masses. Thus the strengths of the fundamentals of  $\text{HCl}^{35}$  and  $\text{HCl}^{37}$  should be in the ratio 1/0.9985. This

difference is considerably less than could be detected experimentally. By employing Eq. (5) and weighting each line according to the number of measurements made on it, we obtain for the 1-0 band of HCl using the lines of both isotopes

$$\bar{S}_{1,0}^0 = 130 \text{ cm}^{-2}(\text{atm. at } 300^\circ \text{ K.})^{-1}$$

or

$$\bar{S}'_{1,0} = 143 \text{ cm}^{-2}(\text{amagat})^{-1}.$$

If the data on  $\text{HCl}^{35}$  and  $\text{HCl}^{37}$  are analyzed independently by this procedure the following values are obtained:

$$\text{HCl}^{35}: \bar{S}_{1,0}^0 = 129 \text{ cm}^{-2}(\text{atm. at } 300^\circ \text{ K.})^{-1},$$

and

$$\text{HCl}^{37}: \bar{S}_{1,0}^0 = 135 \text{ cm}^{-2}(\text{atm. at } 300^\circ \text{ K.})^{-1}.$$

The disagreement between these two values is far beyond that expected statistically from the scatter of the individual values. The authors feel that the discrepancy in the  $\text{HCl}^{35}$  and  $\text{HCl}^{37}$  band strengths is an indication of the existence of some unrecognized systematic error in the measurements.<sup>6</sup> Accordingly, the band strengths given above should be considered uncertain to perhaps as much as 5%. This value is in general somewhat lower than those of most other workers as summarized in Penner and Weber (1953). It is, however, in good agreement with values of 116 and 132  $\text{cm}^{-2}$   $\text{atm}^{-1}$  that can be obtained from recent published data on argon and nitrogen broadening of HCl, respectively (Coulon, Galatry, Oksengorn, Robin, and Vodar 1954).

In order to calculate the "effective charge" of the vibrating dipole moment from the band strength, various procedures and approximations may be used. These will be discussed in detail elsewhere. It may be pointed out here that according to the simplest approximation, that of a dipole-moment function  $M = M_0 + M_1(r - r_e)$ ,  $\bar{S}_v^0 = 130$  corresponds to  $|M_1| = 0.877$  debye  $\text{\AA}^{-1}$ , which with  $M_0 = 1.085$  debye requires that  $|\theta| = 0.980$ . Thus our independently determined values of  $S_v$  and  $\theta$  are quite consistent.

Table V compares the individual experimental line strengths with values calculated from Eq. (1) with  $\theta = 0.988$  and  $\bar{S}_v^0 = 130 \text{ cm}^{-2}$  (atm. at  $300^\circ \text{ K.}$ )<sup>-1</sup>. The calculated values in Table V were used with the data at  $l = 10 \text{ cm.}$ ,  $20 \text{ cm.}$ , and  $140 \text{ cm.}$  in Table III to obtain values for the half-width parameter  $\gamma^0$ . These are given in Table VI and plotted vs.  $|m|$  in Fig. 4.

An alternative method for obtaining line strengths and half widths from the equivalent width is to plot the "curve of growth" for the lines, i.e., to plot  $\log W^0$  vs.  $\log l$  as outlined in Part I, and to use the experimental points to locate the Ladenburg-Reiche curve. We preferred the analytical method since it does not rely on estimating visually when a curve best fits the points, and it is more convenient when a large amount of data must be processed. As an example of how well the Ladenburg-Reiche curve located analytically fits the experimental points, Fig. 5 shows the curve of growth for a few lines. The

<sup>6</sup>In order to bring these values into agreement it would be necessary that the  $\text{Cl}^{37}$  isotopic abundance in our sample be 25.5% rather than the usually accepted value of 24.6%.

TABLE V

EXPERIMENTAL LINE STRENGTHS AND STRENGTHS CALCULATED ON THE BASIS OF  $S_0^0 = 130 \text{ cm}^{-2}$   
(ATM. AT  $300^\circ\text{K.}$ ) $^{-1}$  AND  $\theta = 0.988$  FOR THE HCl 1-0 BAND AT  $300^\circ\text{K.}$

Line	$S_0^0$ <sub>exp</sub>	$S_0^0$ <sub>calc</sub>	Line	$S_0^0$ <sub>exp</sub>	$S_0^0$ <sub>calc</sub>
$P(1)$ 35	4.56	4.547	$R(0)$ 35	4.71	4.820
37	1.54	1.478	37	1.61	1.568
$P(2)$ 35	7.46	7.596	$R(1)$ 35	8.52	8.538
37	2.54	2.470	37	2.95	2.776
$P(3)$ 35	8.49	8.611	$R(2)$ 35	9.61	10.248
37	3.10	2.802	37	3.13	3.333
$P(4)$ 35	7.58	7.843	$R(3)$ 35	9.43	9.896
37	2.48	2.554	37	3.46	3.220
$P(5)$ 35	5.79	6.064	$R(4)$ 35	7.65	8.103
37	1.93	1.976	37	2.47	2.639
$P(6)$ 35	4.16	4.078	$R(5)$ 35	5.98	5.766
37	1.44	1.327	37	2.03	1.878
$P(7)$ 35	2.46	2.408	$R(6)$ 35	3.69	3.611
37	0.918	0.7864	37	1.40	1.177
$P(8)$ 35	1.30	1.263	$R(7)$ 35	2.11	2.006
37	0.427	0.4126	37	0.661	0.6547
$P(9)$ 35	0.647	0.5916	$R(8)$ 35	1.07	0.9935
37		0.1933	37	0.418	0.3245
$P(10)$ 35		0.2479	$R(9)$ 35	0.481	0.4408
37		$8.119 \times 10^{-2}$	37		$0.1440$
$P(11)$ 35		$9.326 \times 10^{-2}$	$R(10)$ 35		0.1754
37		$3.058 \times 10^{-2}$	37		$5.741 \times 10^{-2}$
$P(12)$ 35		$3.163 \times 10^{-2}$	$R(11)$ 35		$6.280 \times 10^{-2}$
37		$1.038 \times 10^{-2}$	37		$2.059 \times 10^{-2}$
$P(13)$ 35		$9.668 \times 10^{-3}$	$R(12)$ 35		$2.028 \times 10^{-2}$
37		$3.180 \times 10^{-3}$	37		$6.659 \times 10^{-3}$
$P(14)$ 35		$2.668 \times 10^{-3}$	$R(13)$ 35		$5.924 \times 10^{-3}$
37		$8.804 \times 10^{-4}$	37		$1.949 \times 10^{-3}$
$P(15)$ 35		$6.690 \times 10^{-4}$	$R(14)$ 35		$1.564 \times 10^{-3}$
37		$2.207 \times 10^{-4}$	37		$5.149 \times 10^{-4}$
			$R(15)$ 35		$3.745 \times 10^{-4}$
			37		$1.237 \times 10^{-4}$

abscissa in this case is  $\log(S^0 l)$  where the individual  $S^0$ 's are taken as  $S_0^0$ <sub>calc</sub> from Table V. This abscissa was chosen so that the curves of growth of all the lines should coincide in the linear region and any deviations in the square-root region would be evidence of different line widths. As can be seen from Fig. 5 the points for the four lines  $R(0)$  and  $P(1)$  of  $\text{HCl}^{35}$  and  $\text{HCl}^{37}$  fall closely on the same curve of growth over the whole range. The Ladenburg-Reiche curve located analytically for these points is shown as the solid curve in the figure. In addition the linear and square-root asymptotes are included as solid lines. The intersection of the two asymptotes is at  $W^0 = 4\gamma^0 \cong 0.87 \text{ cm}^{-1} \text{ atm}^{-1}$  or

TABLE VI

EXPERIMENTAL LINE HALF-WIDTH PARAMETERS IN  $\text{cm}^{-1} \text{ atm}^{-1}$  FOR SELF-BROADENING IN THE 1-0 BAND OF HCl AT 300°K.

$ m $	R-Branch		P-Branch		Average
	HCl <sup>35</sup>	HCl <sup>37</sup>	HCl <sup>35</sup>	HCl <sup>37</sup>	
1	0.217	0.222	0.214	0.220	0.218
2	0.213	0.234	0.221	0.222	0.223
3	0.245	0.256	0.250	0.244	0.249
4	0.233	0.255	0.240	0.255	0.246
5	0.208	0.235	0.229	0.238	0.227
6	0.178	0.182	0.194	0.189	0.186
7	0.150	—	0.150	0.158	0.153
8	0.124	0.114	0.130	0.138	0.127
9	0.111	0.093	0.096	0.124	0.106
10	0.0955	—	0.0882	0.0850	0.0896
11	0.0860	0.0843	0.0822	—	0.0842
12	0.0834	—	—	—	(0.0834)
13	0.063	0.061	0.067	0.073	0.066

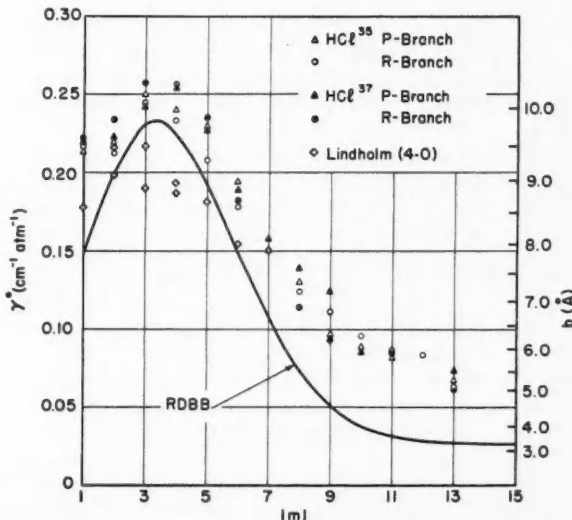


FIG. 4. Experimental values of line widths per atm.,  $\gamma^0$ , versus  $|m|$  for the HCl 1-0 band. The theoretical curve is that calculated for the resonant-dipole-billiard-ball approximation. The corresponding collision diameters  $b$  are given. Line widths measured by Lindholm in the 4-0 band are shown for comparison.

$\gamma^0 \cong 0.218 \text{ cm}^{-1} \text{ atm}^{-1}$ . For comparison the data for  $|m| = 7$  are included. In this case the data scatter about the same linear asymptote, but definitely drop to a lower line at the square-root end, demonstrating that the lines with  $|m| = 7$  are narrower than those with  $|m| = 1$ .

A detailed theoretical discussion of the variation of  $\gamma^0$  with  $m$ , which as shown by the experimental results of Table III and Fig. 4 is quite large, will

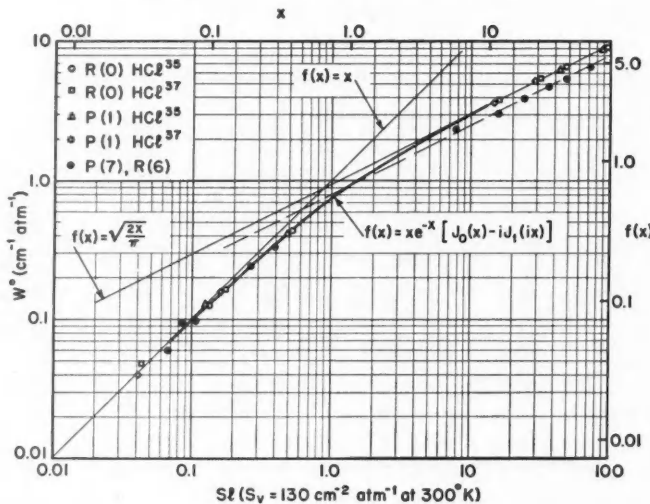


FIG. 5. Examples of curves of growth for the lines  $|m| = 1$  and  $7$ . The solid curve and asymptotes for the case  $|m| = 1$  are calculated from the Ladenburg-Reiche equation.

be deferred for a later paper, in which the corresponding data for temperatures up to  $1200^\circ\text{K}$ . and for the isotopes  $\text{DCl}^{35}$  and  $\text{DCl}^{37}$  will also be considered. It may be sufficient here to point out a few of the more salient points. The width of a given line  $m$  is the average of the widths resulting from encounters with molecules in different rotational states  $J_2$  weighted according to population. There will be a different "collision diameter"  $b_{m,J_2}$  for each rotational state so that the expression for line width becomes

$$(6) \quad \gamma_m^0 = \frac{\bar{v}}{2c} \sum_{J_2} N_{J_2} b_{m,J_2}^2,$$

where  $\bar{v}$ , the most probable velocity of encounter, is given by

$$\bar{v} = (2kT\mu)^{\frac{1}{2}}$$

where  $\mu$  is the reduced mass of the system. For  $\text{HCl}-\text{HCl}$  collisions  $\bar{v} = 5.90 \times 10^4 \text{ cm. sec}^{-1}$  at  $300^\circ\text{K}$ . The partial collision diameters  $b_{m,J_2}$  depend upon the specific intermolecular forces, the most important for  $\text{HCl}$  self-broadening being dipole-dipole forces. These vary as  $r^{-3}$ , where  $r$  is the intermolecular distance, when resonance occurs, i.e., when  $J_2 = J' \pm 1$  or  $J'' \pm 1$ , but are of shorter range leading to lower collision diameters for other values of  $J_2$ . When  $(J_2 - J)$  is very large, there will be some lower limit to  $b_{m,J_2}$  corresponding to the kinetic theory or "billiard-ball" collision diameter  $b_0$ . Hence a simple expression for  $\gamma_m^0$  including resonant dipole and billiard-ball terms or RDBB approximation is obtained by setting

$$(7a) \quad b_{\text{RDB}}^2 = \frac{2}{3} \frac{M_0^2}{\hbar\bar{v}} [1 - \frac{1}{4}(J_2 + 1)^{-2}]^{\frac{1}{2}}$$

for  $|m| - 2 \leq J_2 \leq |m| + 1$  and

$$(7b) \quad b_{BB}^2 = b_0^2$$

for other values of  $J_2$ . If  $f$  is the fraction of molecules in the resonating rotational states,

$$(7c) \quad f = \frac{\sum_{J_2=|m|-2}^{|m|+1} (2J_2+1) e^{-E(J_2)/kT}}{\sum_{J_2} (2J_2+1) e^{-E(J_2)/kT}},$$

then, neglecting the second term in the brackets in Eq. (7a) and using  $M_0 = 1.085$  debye and  $b_0 = 3.31 \text{ \AA}$ ,<sup>7</sup> we have, for  $300^\circ \text{ K.}$  (in  $\text{cm}^{-1}\text{atm}^{-1}$ ),

$$(8) \quad \gamma_m^0 \cong 0.301f + 0.0264(1-f).$$

The solid curve in Fig. 4 results from Eq. (8) and the appropriate fractional populations. It will be noted that the observed points fall above the solid RDBB curve for all  $m$ . The calculated curve, however, closely parallels the experimental points, suggesting that the above mechanisms yield the major contributions to the broadening. The additional broadening is presumably due to the non-resonant dipole-dipole forces and other shorter-range forces including dipole-quadrupole, quadrupole-quadrupole, and dipole-induced-dipole forces. The effects of these forces may be calculated according to the general theory of Anderson (1949, 1950) as amplified by Tsao and Curnutte (1954) and Smith, Lackner, and Volkov (1955), but the computation is laborious. It is believed that the dipole-quadrupole forces are the most important of the added terms, and a conspectus of all the data for HCl and its isotopes will permit a fair fit with one additional adjustable parameter, namely the quadrupole moment. In this connection the particularly large positive deviation of the measured line width for  $|m| = 1$  from the RDBB curve is to be noted inasmuch as lines of low  $|m|$  have the largest contribution from quadrupole forces.

The results of Lindholm (1939) for the 4-0 band are included in Fig. 4. Our results on the 1-0 band are from 10 to 30% higher. Theoretically one would expect slightly lower widths in the 4-0 than in the 1-0 band, perhaps of the order of 2-3%, because the resonance between the rotational levels of the colliding molecules, most of which are in the ground vibrational state, is less close with those in  $v = 4$  than  $v = 1$ . Inasmuch as Lindholm's measurements were made at a pressure of 3.5 atm. by an entirely different technique, the disagreement is not extreme.

#### *Line Width from Nitrogen-broadening*

The preceding results refer to the self-broadening of HCl. Mention should also be made of a few experiments—however, not of comparable accuracy—in which spectra were obtained of a small amount of HCl (9-25 mm.) pressurized to 1 atm. with N<sub>2</sub>. The original objective of these experiments was to measure the line strengths in a relatively long cell by bringing the lines into the linear region of the curve of growth by means of foreign gas broadening. The results, however, were very inconsistent, although carefully measured

<sup>7</sup>This parameter is quite poorly defined. The value chosen was derived by Hirschfelder, Bird, and Curtiss (1954) from measurements of viscosity.

amounts of HCl were mixed in a large evacuated bulb with N<sub>2</sub> before admission to the 10 cm. cell. Presumably this inconsistency was due to poor mixing of the gases or adsorption on the walls of the mixing chamber. While it was possible to obtain with fair accuracy the equivalent widths of the stronger lines falling in the near-square-root region of the curve of growth, the uncertainty in the amount of HCl present precluded an absolute determination of their half-widths. However, it was possible to obtain relative half-widths assuming that the composition of a given mixture remained constant during a run.

In order to obtain numerical values for the line width parameter for nitrogen-broadening,  $\gamma^0(N_2)$ , it was assumed that this constant was known for one value of  $m$ . This, together with the observed  $W$ , yielded a value of the concentration of HCl in the cell, which was then used to obtain values of  $\gamma^0(N_2)$  for the other lines. Inasmuch as the ratio of the widths for HCl-HCl and HCl-N<sub>2</sub> broadening has been measured for line  $R(2)$ , we took for  $m = 3$ ,  $\gamma^0(N_2) = 0.089 \text{ cm}^{-1}$ , corresponding to our  $\gamma^0$  for HCl-HCl and the published ratio of 0.355 (Benesch and Elder 1953). Our resulting values of  $\gamma^0(N_2)$  at each  $|m|$ , given in Table VII, agreed for the isotopic pairs and the  $P$  and  $R$  branches, so that it is felt that our values cannot be far wrong. A marked  $m$ -dependence roughly paralleling the self-broadening results is apparent.

TABLE VII  
HALF-WIDTH PARAMETERS FOR HCl BROADENED BY NITROGEN

$ m $	$\gamma^0 (\text{cm}^{-1} \text{ atm}^{-1})$	Ratio (HCl-N <sub>2</sub> )/(HCl-HCl)	$b (\text{\AA})$
1	0.092	0.426	6.0
2	0.088	0.394	5.8
3	(0.089)	(0.355)*	5.9
4	0.069	0.28	5.2
5	0.062	0.27	4.9
6	0.054	0.29	4.6
7	0.040	0.26	3.9
8	0.031	0.25	3.5

\*This value was obtained from Benesch and Elder (1953).

For the highest value of  $m$  included in Table VII  $\gamma^0(N_2)$  corresponds to a collision diameter of 3.5 Å, which, being intermediate between the kinetic theory values of 3.31 Å for HCl-HCl and 3.75 Å for N<sub>2</sub>-N<sub>2</sub> (Hirschfelder, Bird, and Curtiss 1954), is probably close to the lower limit to be expected at high  $m$ . The increased diameters at lower  $m$ , reaching 6.0 Å at  $m = 1$ , reflect the influence of angle-dependent, long-range forces. The most important such force is probably the interaction between the HCl dipole moment and the N<sub>2</sub> quadrupole moment. For encounters with such forces operative the selection rules are  $\Delta J(N_2) = 0, \pm 2$ ;  $\Delta J(HCl) = \mp 1$ . Resonance is never exact, but can become nearly so for each HCl line at some value of  $J(N_2)$ . For the most heavily populated N<sub>2</sub> levels, the closest resonance and hence the greatest collision diameter will occur for  $J(HCl) < 4$ . The variation of  $\gamma^0$  with  $m$  is thus qualitatively understandable. The quantitative calculation by

Anderson's theory (Anderson 1949, 1950) is laborious. Inasmuch as our data are not of extreme precision, the quadrupole moment of  $N_2$  is uncertain, and other forces such as dipole-induced-dipole must also contribute; such a calculation has not been attempted.

#### *Line Shapes*

The methods described in Sections IV, V, and VI of Part I were applied to test the validity of the Lorentz shape and to determine the shape factor at values of  $|\nu - \nu_0|$  greater than those used in the equivalent-width measurements, which were of the order of  $1\text{ cm}^{-1}$  and less. In the remainder of this section we will present various values of  $\chi$ , defined as the ratio of the observed extinction to that calculated using the Lorentz shape with the Lorentz parameters  $S^0$  and  $\gamma^0$  being the calculated values in Table V and the average values in Table VI, respectively.

One such set of measurements was made at the "internal trough" between the  $HCl^{35}$  and  $HCl^{37}$  lines, a convenient location. In the  $HCl$  fundamental the separation  $\delta$  ranges from  $1.62\text{ cm}^{-1}$  at  $P(13)$  to  $2.38\text{ cm}^{-1}$  at  $R(12)$ . The strength ratio of an isotopic pair of lines varies only slightly with  $m$  and as can be seen from Table V is  $0.327 \pm 0.002$ . Hence the position of the trough is at  $(\nu - \nu_0^{35})$  from  $-0.96$  to  $-1.41$ , and at  $(\nu - \nu_0^{37})$  from  $+0.66$  to  $+0.97$ . With the average slit used,  $d \cong 0.35\text{ cm}^{-1}$ , the slit-correction term in Eq. (33), Part I, amounts to  $\sim -6\%$ . The line-width correction term is greatest for  $P(4)$ , being  $(5.1 P^2)\%$  where  $P$  is in atmospheres. The overlapping line correction is less than  $1\%$  for all lines. Hence all the correction terms in Eq. (33), Part I, are of minor importance under our experimental conditions.

Measurements of extinction,  $\epsilon_{l.t.}$ , at the internal trough were made on all suitable runs, when the transmission was  $10\text{--}80\%$ , in which range the accuracy of measurement is least dependent upon noisy signal or uncertainties in location of the  $100\%$ -transmission base-line. The accuracy of an individual measurement appears good to  $\pm 20\%$  for low  $\epsilon$ , and considerably better for higher  $\epsilon$ . Runs providing suitable data were principally those with  $l = 10\text{ cm.}$ ,  $P = 100, 500$ , and  $700\text{ mm.}$ , and  $l = 20\text{ cm.}$ ,  $P = 80$  to  $200\text{ mm. of Hg}$ . The observed  $\epsilon$  was proportional to  $lP^2$  within the accuracy of measurement. For each line values of  $\chi_{l.t.}$  were calculated employing Eq. (33), Part I. These were averaged, and the results are presented in Table VIII. Some of the entries come from only one or two determinations and are correspondingly uncertain. Others are based on as many as 10 runs. The weighted average of  $\chi_{l.t.}$  for all the  $P$ -branch lines is  $1.093 \pm 0.022$ ; for the  $R$  branch lines it is  $1.119 \pm 0.024$ , where the quoted uncertainties are the standard deviations divided by the square root of the number of items included in the averaging.

Other checks on the line shape were made by measuring the total breadth of the  $HCl^{35}\text{--}HCl^{37}$  doublets at optical densities such that the internal-trough extinction was nearly complete but the external-trough extinction was low so that the base-line was still well defined. The runs with  $l = 10\text{ cm.}$ ,  $P = 500$  and  $700\text{ mm.}$ , were suitable for this purpose for the stronger lines. Extinction was measured at the levels at which the total breadth was  $\delta + 2.0\text{ cm}^{-1}$  and  $\delta + 4.0\text{ cm}^{-1}$ . At the former value, the measurements yield  $\chi_2$ , which corre-

TABLE VIII  
EXPERIMENTAL SHAPE FACTORS FOR LINES IN THE HCl 1-0 BAND AT 300°K.

Line	$\chi_{1.t.}$	$\chi_2$	$\chi_4$	$\chi_{e.t.}$
$R(9)$	1.37			1.17
$R(8)$	1.23			1.21
$R(7)$	1.10			1.31
$R(6)$	1.24	1.08	1.29	1.29
$R(5)$	1.20	0.98	1.10	1.30
$R(4)$	1.02	0.92	1.06	1.40
$R(3)$	1.12	0.94	1.13	1.44
$R(2)$	1.04	0.97	1.09	1.68
$R(1)$	1.07	0.97	1.18	1.87
$R(0)$	1.06	0.99	1.16	3.80
$P(1)$	1.10	1.01	1.21	2.31
$P(2)$	1.05	1.09	1.21	1.96
$P(3)$	1.10	1.17	1.12	1.58
$P(4)$	1.10	0.96	1.13	1.64
$P(5)$	0.95	1.11	1.10	1.71
$P(6)$	1.03	1.18	1.21	1.98
$P(7)$	1.20			1.56
$P(8)$	1.13			
$P(9)$	1.17			
$P(10)$	1.19			
$P(11)$	1.47			
$P(13)$	0.91			

sponds in Eq. (29), Part I, to  $q = 1.23 \text{ cm}^{-1}$  and  $s = 0.77 \text{ cm}^{-1}$ ; and at the latter value,  $\chi_4$  corresponds to  $q = 2.35 \text{ cm}^{-1}$  and  $s = 1.65 \text{ cm}^{-1}$ . Equation (30), Part I, then leads to the values of  $\chi$  listed in Table VIII. There appears to be no significant variation with  $m$ , the average values for the 13 lines  $R(6)-P(6)$  being  $\chi_2 = 1.029 \pm 0.023$ ,  $\chi_4 = 1.153 \pm 0.015$ . It may be noted that the  $|v - v_0|$  in  $\chi_2$  roughly corresponds with those for  $\chi_{1.t.}$  of the  $R$  branch. It is not certain whether the averaged differences in  $\chi$ , 1.03 for the former and 1.12 for the latter, are significant. If real, they indicate a very slight asymmetry of the shape, the "red" wing (negative values of  $v - v_0$ ) being stronger than the "blue" wing. The values for  $\chi_4$  are significantly greater than unity. While we may conclude that the Lorentz shape is correct to within  $\sim 10\%$  when  $|v - v_0|$

<1.5  $\text{cm}^{-1}$  it seems definite that positive deviations are commencing in both wings as  $|\nu - \nu_0|$  becomes larger than  $\sim 1.5 \text{ cm}^{-1}$ .

In order to measure the effective  $\chi$  when  $|\nu - \nu_0| > 2 \text{ cm}^{-1}$  it becomes necessary to use still higher optical densities so that the strong lines are completely opaque between both isotopic lines and that absorption high enough to measure takes place in the external troughs. These conditions were achieved at  $l = 140 \text{ cm.}$ ,  $P = 200, 300, 450, 600$ , and  $750 \text{ mm.}$  The measurements of  $\epsilon$  in the troughs at the several pressures were, however, not very consistent because of the difficulty in locating the base-line when absorption is high over a considerable region of the spectrum. The uncertainty in the derived values of  $\chi_{\text{e.t.}}$  for  $|m| > 3$  is as high as  $\pm 20\%$ . In order to calculate  $\chi_{\text{e.t.}}$  the expected Lorentz extinction was computed for several values of  $\nu$  near the observed minima, the theoretical  $k_{\text{min}}$  and  $\nu_{\text{min}}$  being then determined by interpolation. The frequencies of the minima agreed in all cases with the calculated values to within  $\pm 1 \text{ cm}^{-1}$ , which implies that the shape factor is nearly symmetrical in  $(\nu - \nu_0)$ . The values of  $\chi_{\text{e.t.}}$  also given in Table VIII are, however, all well above unity and also above  $\chi_4$  showing that the greater-than-Lorentz trend increases with  $|\nu - \nu_0|$ . The greater values of  $\chi_{\text{e.t.}}$  in the  $P$  branch are probably due mostly to the greater separations in that branch.

The most accurate values of  $\chi$  at high  $|\nu - \nu_0|$  and an approximate determination of the functional relation of  $\chi(\nu - \nu_0)$  may best be obtained near the band center between the lines  $R(0)$  and  $P(1)$ . To ensure good precision in these measurements several scans between  $m = +4$  and  $m = -3$  were made with  $l = 140 \text{ cm.}$  and pressures 200 to 600 mm. with intervening scans at  $P = 0$  so that drifts in the base-line level were followed and largely compensated. A superposition of the spectral tracings is presented in Fig. 6. From these the extinction was measured at a large number of frequency intervals and the  $\epsilon_{\text{Lor}}$  was likewise calculated at close frequency intervals.

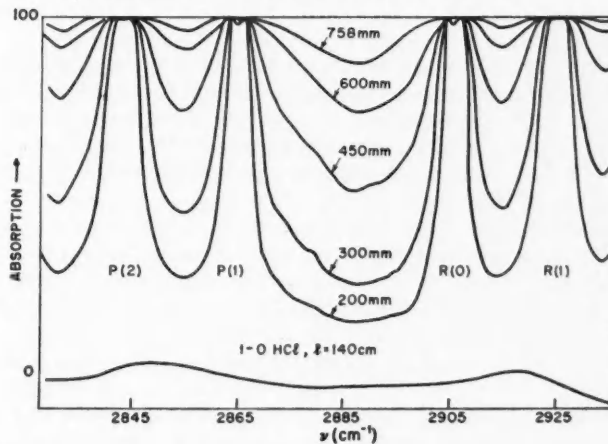


FIG. 6. Tracings of the absorption curves for various pressures taken near the 1-0 band center at  $l = 140 \text{ cm.}$

Results for frequencies near the  $R(0)$  line are shown in Fig. 7. Frequencies are plotted at the bottom, and frequency differences,  $\Delta\nu = \nu - \nu_0$ , from the resonant frequencies of both  $\text{HCl}^{35}$  and  $\text{HCl}^{37}$  are given at the top. The plotted points are  $\epsilon/P^2$ . Results for four pressures define a single curve showing that

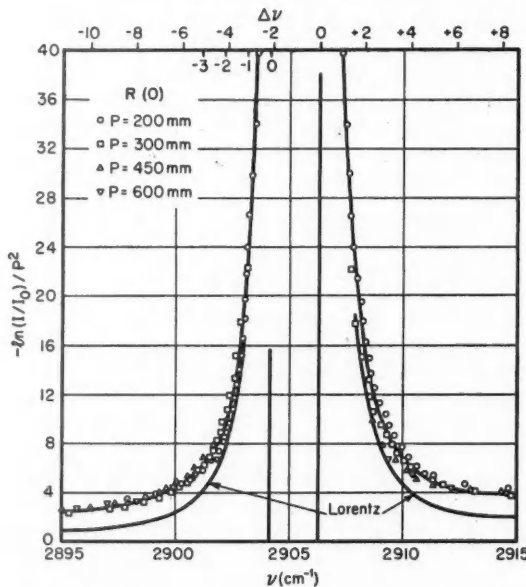


FIG. 7. Plot of  $\epsilon/P^2$  versus  $\nu$  near the lines  $R(0)$  for  $\text{HCl}^{35}$  and  $\text{HCl}^{37}$  at high optical density obtained from the absorption curves shown in Fig. 6. The absorption expected from Lorentz lines is also shown.

$\epsilon$  is proportional to  $P^2$  as would be the case for a Lorentz line. The frequency dependence is, however, increasingly above Lorentzian as  $|\nu - \nu_0|$  becomes larger than  $1.5 \text{ cm}^{-1}$ . The deviations are very nearly symmetrical in the two wings. The unsymmetrical gross appearance of the doublet line arises from the two unequal isotopic components and from the contributions of the stronger, wider  $R(1)$  lines at higher frequency.

Further results of the shape determination for the four central lines are shown in Fig. 8, where the frequency scale has been contracted and the  $-\ln(I/I_0)/P^2$  scale expanded to emphasize the shape near the band origin ( $2886.0 \text{ cm}^{-1}$  for  $\text{HCl}^{35}$ ). The "observed" points given by the solid circles were taken from the composite experimental curve of the four pressures. The increase above the Lorentz curve, already large in Fig. 7, continues to increase as one goes from  $R(0)$  to the center with  $\chi$  reaching 3.80 at  $2886 \text{ cm}^{-1}$ . Between  $2886 \text{ cm}^{-1}$  and line  $P(1)$  there is a further, rather abrupt rise in  $\chi$ , which may also be noted as a small hump in the experimental curves shown in Fig. 6. In order to emphasize this feature, Fig. 8 also plots as open circles the dif-

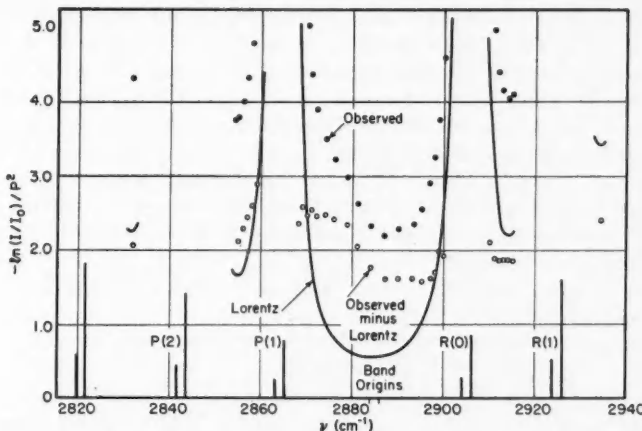


FIG. 8. Plot of  $\epsilon/P^2$  versus  $\nu$  for several lines near the origins of the 1-0 bands of  $\text{HCl}^{35}$  and  $\text{HCl}^{37}$ . The observed points represent averages taken from the various curves in Fig. 6. The solid curves give the result to be expected for Lorentz lines. The open circles show the deviations of the observed absorption from that obtained for Lorentz lines.

ferences between the observed and Lorentz values of  $\epsilon/P^2$  for various values of  $\nu$ . The difference is nearly constant between  $R(0)$  and the band origin, but rises rather abruptly between  $2886$  and  $2878 \text{ cm}^{-1}$  to another level some 40% greater which remains fairly constant near  $P(1)$ . Corresponding to this rise the  $\chi$  values on both the red and blue wings of  $P(1)$  are 25–40% greater than at comparable  $|\nu - \nu_0|$  from  $R(0)$ . The maximum observed value of  $\chi$  is 4.47 at  $\nu \cong 2881 \text{ cm}^{-1}$ .

It is believed significant that this additional, unsymmetrical excess of non-Lorentzian absorption occurs near frequencies where  $\text{HCl}$  lines with  $\Delta J = 0$  would fall. For example, the calculated frequencies for a  $Q$ -branch of  $\text{HCl}^{35}$  are  $Q(1) = 2885.4$ ,  $Q(3) = 2882.3$ ,  $Q(4) = 2879.9$ , and  $Q(8) = 2864.1$ , all in  $\text{cm}^{-1}$ .  $Q$ -Branch lines are, of course, forbidden for dipole radiation in unperturbed linear  ${}^1\Sigma$  molecules, but as was predicted by Condon (1932) and subsequently observed for many homopolar molecules as well as for  $\text{HCl}$  broadened by  $\text{N}_2$  (Coulon, Galatry, Oksengorn, Robin, and Vodar 1954), a  $Q$ -branch can appear at pressures high enough so that the fields of the colliding molecules induce the otherwise forbidden radiation. The resulting absorption should be proportional to the square of the density as it is in our observations. Although at our pressures of less than 1 atm.  $\text{HCl}$  lines of the expected spacing could have been resolved if they were of normal width, i.e. about the same width as  $P$  and  $R$  branch lines, we observe only a broad hump, showing that if the observed hump corresponds to Stark-induced "lines" they are quite smeared-out.

Since both the "hump" absorption and the rest of the absorption in the wings of the lines varies as  $P^2$ , we are unable to make a definite distinction between these two effects in increasing  $\chi$ . We feel, however, that little of the

absorption at  $\nu > 2886 \text{ cm}^{-1}$  and perhaps 40% of the absorption excess between 2869 and 2886  $\text{cm}^{-1}$  is due to the induced-absorption mechanism, so that the greater apparent  $x$  on the wings of  $P(1)$  is not significant in the discussion of HCl line shape in general.

Some of the data pertaining to line shape, particularly those for the wings of  $R(0)$ , are plotted in Fig. 9. On a log-log scale we present values of  $x$  as a function of  $|\nu - \nu_0|$ . It must again be emphasized that at a given  $\nu$ , the quantity  $|\nu - \nu_0|$  is not always uniquely determined since a number of lines may be making sizable contributions to the  $S\gamma/(\nu - \nu_0)^2$  sum. For Fig. 9 we chose the  $|\nu - \nu_0|$  that makes the largest single contribution. When plotted in this manner, the points for the blue wing of  $R(0)$  fall fairly well on a straight

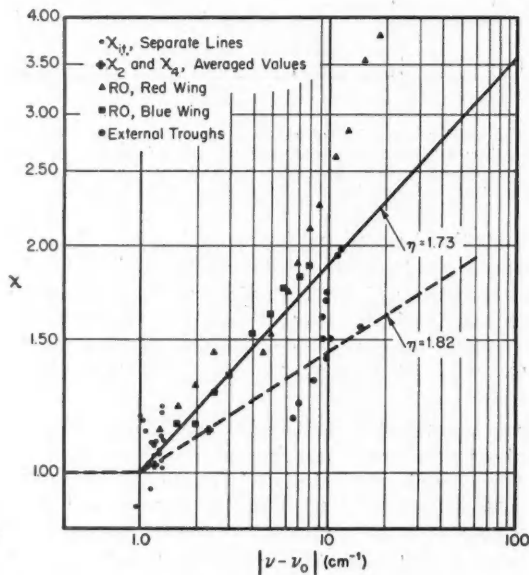


FIG. 9. The shape factor  $x = \epsilon(\text{obs})/\epsilon(\text{Lorentz})$  plotted versus the distance from the line center.

line while those for the red wing of the  $R(0)$  line curve upward above this line. Since each experimental point includes contributions from lines of  $|\nu - \nu_0|$  greater than the plotted major distance, the true line shape curve should fall below both sets of points, but closer to the blue set since the other important contributions in the latter case come from lines of smaller  $|\nu - \nu_0|$  where there is less deviation from Lorentzian. The solid line, which corresponds to the shape discussed in the Appendix to Part I, Eq. (Alb), with  $\nu_m = 1.00 \text{ cm}^{-1}$ ,  $\eta = 1.73$ , appears to give a fairly good representation of the shape of  $R(0)$ . Using this line shape for all lines the calculated extinction at all frequencies between 2888 and  $2915 \text{ cm}^{-1}$  fits observation to within  $\sim 20\%$ .

The other points in Fig. 9, for the  $\chi_{1.t.}$ , the average  $\chi_2$ , the average  $\chi_4$ , and  $\chi_{e.t.}$ , scatter and fall in general somewhat below the solid line. The dashed line, which represents them fairly well, corresponds to  $\nu_m = 1.00$ ,  $\eta = 1.82$ . Because of the nature of the spectrum and the difficulty in making sufficiently accurate measurements it is impossible to derive a separate shape for each line. The body of the data suggests that some shape of the form of Eq. (A1) of Part I with  $\eta$  between 1.7 and 1.85 is a much better approximation for the lines of HCl than is the Lorentz shape at least in the range of  $|\nu - \nu_0|$  between 1.5 and  $40 \text{ cm}^{-1}$ . It also appears that the shape is nearly symmetrical in  $\nu - \nu_0$ , the possible maximum difference in the exponent  $\eta$  for the red and violet wings being  $\sim 0.1$ . It is improbable that the shape factor would continue to increase indefinitely at still higher  $|\nu - \nu_0|$  since the second moment of the absorption coefficient must be finite. However, our experiments do not extend to high enough optical densities to bear on this point. With another increase of 100 or so in optical density, it might be possible to obtain values of  $\chi$  at frequencies above  $3100 \text{ cm}^{-1}$  and below  $2600 \text{ cm}^{-1}$  where  $|\nu - \nu_0| > 100 \text{ cm}^{-1}$ .

The empirical shape factor suggested for HCl appears reasonable in view of the result (Lindholm 1946) concerning the shape of lines subject to a statistical perturbation by intermolecular potentials varying with intermolecular distance as  $\pm cr^{-n}$ . The shape, at frequencies far from  $\nu_0$ , is then given by  $k \propto (\nu - \nu_0)^{-(n+3)/n}$ . Since for resonant dipole-dipole forces  $n = 3$ ,  $\eta = (n+3)/n = 2.0$ , and the statistical shape remains Lorentzian. For dipole-quadrupole forces,  $n = 4$ , we have  $\eta = 1.75$  and for non-resonant dipole-dipole forces,  $n = 6$ , we have  $\eta = 1.50$ . Inasmuch as the line widths (cf. Fig. 4 and the associated discussion) include contributions from all these and possibly other causes but with  $n = 3$  predominating, values of  $\eta$  intermediate between 1.7 and 2.0 are to be expected. The lower-than-average exponent for  $R(0)$  reflects the larger-than-average contribution of the short-range forces for that line.

It should be pointed out again that the rather large deviations from the Lorentz shape observed when  $|\nu - \nu_0|$  exceeds  $\sim 2 \text{ cm}^{-1}$  do not invalidate the use of the Lorentz shape and its consequence, the Ladenburg-Reiche curve-of-growth, in the determination of  $S^0$  and  $\gamma^0$ . The deviations from the Lorentz shape contribute very little to the band strength at low pressure. Integrated over the HCl 1-0 band the ratio of the contribution of the above-Lorentzian absorption to the total integrated intensity is only  $\sim 0.025 P$ . Thus at 1 atm., the highest pressure at which we worked, the contribution is only about 2.5% and is smaller at lower pressures. The values of  $\gamma^0$  were derived principally from measurements of equivalent width in which only very small contributions from  $|\nu - \nu_0| > 1 \text{ cm}^{-1}$  were included, and as demonstrated in Fig. 3,  $W/P$  showed no upward deviation at the higher pressures such as would result from the modified-Lorentz shape.

#### CONCLUSION

The results reported in this paper constitute a rather exhaustive study of the experimental factors involved in the quantitative absorption of radiation,

in the region of the 1-0 vibration-rotation transition, of the HCl<sup>35</sup> and HCl<sup>37</sup> molecules at room temperature and at pressures of 1 atm. and lower, where binary collisions constitute by far the largest number of the intermolecular encounters. Quantitative results of good accuracy have been obtained for the total band strength, and the intensity distribution among the lines has been used to evaluate the effects of the vibration-rotation interaction upon the intensities. The variation with rotational quantum number of the Lorentz collision diameter for HCl self-broadening has been established and an indication of its magnitude obtained for HCl-N<sub>2</sub> collisions. The Lorentz shape has been found to be accurate on both the high-frequency and low-frequency sides of the resonant frequency out to  $|\nu - \nu_0| = 1.0 \text{ cm}^{-1}$ ; at higher frequency shifts the observed absorption is greater than Lorentzian and an approximate law for the variation has been found.

In theory, it should be possible to correlate the empirical facts concerning the line and band strengths with the variation of electric charge with inter-nuclear distance, and the facts concerning line width and shape with the inter-molecular force fields. Because of the many variables in both these problems, it is desirable to obtain further data before attempting these correlations. Such data for the first problem can be obtained by measuring the strengths of additional vibration-rotation transitions, in the overtone and difference bands of both HCl and DCI. We have obtained results on the absorption of HCl and DCI out to the 3-0 band, and at temperatures up to 1200° K. These results will be reported in a subsequent paper. The variation of line widths with temperature and isotopic substitution has also been derived from these measurements and will be the subject of another article.

We wish to acknowledge with gratitude the assistance of Mr. Bernard F. Hochheimer with the experimental measurements and of Mrs. Josephine P. Hochheimer and Mrs. Jacquelyn S. Kimrey with the reduction of data and computations. Finally we wish to express our appreciation to Dr. Richard F. Wallis, Naval Research Laboratory, for many stimulating discussions.

#### REFERENCES

- ANDERSON, P. W. 1949. *Phys. Rev.* **76**: 647.  
——— 1950. *Phys. Rev.* **80**: 511.  
BELL, R. P. and COOP, I. E. 1938. *Trans. Faraday Soc.* **34**: 1209.  
BENEDICT, W. S., HERMAN, R., MOORE, G. E., and SILVERMAN, S. 1956. *Can. J. Phys.* **34**: 830.  
BENESCH, W. and ELDER, T. 1953. *Phys. Rev.* **91**: 308.  
BOURGIN, D. G. 1927. *Phys. Rev.* **29**: 794.  
——— 1928. *Phys. Rev.* **32**: 237.  
BREENE, R. G. JR. 1955. The shift and shape of spectral lines. Geophysical Research Papers No. 41, Geophysical Research Directorate, Air Force Cambridge Research Center, Air Research and Development Command.  
CONDON, E. U. 1932. *Phys. Rev.* **41**: 759.  
COULON, R., GALATRY, L., OKSENGORN, B., ROBIN, S., and VODAR. 1954. *J. phys. radium*, **15**: 641.  
DENNISON, D. M. 1928. *Phys. Rev.* **31**: 503.  
HAMMER, C. F., JR. 1948. Dissertation, University of Wisconsin, Madison, Wis. (Quoted in Penner and Weber (1953).)  
HERMAN, R. and WALLIS, R. F. 1955. *J. Chem. Phys.* **23**: 637.  
HERZBERG, G. 1950. Molecular spectra and molecular structure. Vol. I. Spectra of diatomic molecules. D. van Nostrand Company, Inc., New York.  
HIRSCHFELDER, J. O., BIRD, R. B., and CURTISS, C. F. 1954. Molecular theory of gases and liquids. John Wiley and Sons, Inc., New York. p. 1111.

- HOCHHEIMER, B. F. and MOORE, G. E. 1955. J. Opt. Soc. Amer. **45**: 891.  
IMES, E. S. 1919. Astrophys. J. **50**: 251.  
LINDHOLM, E. 1939. Z. Physik, **113**: 596.  
\_\_\_\_\_. 1946. Arkiv. Mat. Astron. Fysik, A, **32**: No. 17.  
MILLS, I. M., THOMPSON, H. W., and WILLIAMS, R. L. 1953. Proc. Roy. Soc. A, **218**: 29.  
NIER, A. O. and HANSON, E. E. 1936. Phys. Rev. **50**: 722.  
OPPENHEIMER, J. R. 1926. Proc. Cambridge Phil. Soc. **23**: 327.  
PENNER, S. S. and WEBER, D. 1953. J. Chem. Phys. **21**: 649.  
ROLLEFSON, R. and ROLLEFSON, A. 1935. Phys. Rev. **48**: 779.  
SMITH, W. V., LACKNER, H. A., and VOLKOV, A. B. 1955. J. Chem. Phys. **23**: 389.  
TSAO, C. J. and CURNUTTE, B. 1954. Line widths of pressure broadened spectral lines. Scientific Report IA-8, Cambridge Air Force Research Center Contract No. AF19 (122)65, Ohio State University, June 28.  
WEBER, D. and PENNER, S. S. 1953. J. Chem. Phys. **21**: 1503.

# THE DIURNAL BEHAVIOR OF SUDDEN COMMENCEMENTS OF MAGNETIC STORMS AT AGINCOURT<sup>1</sup>

BY J. A. JACOBS AND T. OBAYASHI

## ABSTRACT

The diurnal variations in the frequencies of sudden commencements of magnetic storms are examined, using the magnetograms from Agincourt for the period from 1946 to 1953 inclusive. The occurrence frequencies of sudden commencements exhibit an apparent diurnal tendency which has its minimum in the morning hours and maximum in the afternoon. The frequency distributions for several groups classified by their amplitudes, however, show different diurnal variations from one another. In order to confirm such local-time effects, a statistical analysis of the shape of sudden commencements has been made, and each sudden commencement classified according to its shape. Results show the following diurnal characteristics. A pronounced augmentation of the sudden commencement impulse occurs in the afternoon hours. In the morning the initial rise of sudden commencements is usually slight and they are frequently inverted in the *H*-trace, although some of them are quite clear in the *D*-trace. The local-time variation of the horizontal magnetic vectors at several stages of the initial phase is also estimated statistically. These results suggest that the diurnal control of the magnetic variation must be due to some additional field produced in the earth's upper atmosphere at the time of sudden commencement, tending to modify the primary cause.

## 1. INTRODUCTION

A detailed study of magnetic storms has recently been undertaken at the University of Toronto. An explanation of the physical mechanism of magnetic storms is one of the oldest problems in geophysics, and, as with many other fundamental problems, a complete solution has not yet been given. Most storms however follow a fairly well defined pattern, although there are considerable local variations. They are characterized by a world-wide sudden commencement which consists of a rise in the magnetic field within quite a short time interval (of the order of a few minutes). Newton (1944) showed that there was a time lag of 22 hr. (for great magnetic storms), and 34 hr. (for storms of smaller intensity) between the passage across the central meridian of active sunspots and the commencement of a great storm. Sudden commencements show considerable variation from place to place—Forbush and Vestine (1955) have shown, for example, that sudden commencements are enhanced during daylight hours at Huancayo, thereby indicating an atmospheric source for sudden commencements. Evidence has also been given that the size of sudden commencements is larger in the auroral zone. Newton (1948) has called attention to a reverse impulse in the horizontal force component which sometimes precedes the sudden commencement increase by about a minute or so, whilst Fukushima (1951) has noticed a pre-sudden-commencement bay-like disturbance at high latitudes, preceding the onset of the magnetic storm by about one hour. Heppner (1954) has related these high latitude bay disturbances to changes in the appearance of aurora.

<sup>1</sup>Manuscript received March 23, 1956.

Contribution from the Geophysics Laboratory, Department of Physics, University of Toronto, Toronto, Ontario.

There have been many theories of magnetic storms and aurorae. Certainly, as Ferraro has said, "the history of magnetic storms and aurorae is strewn with the wrecks of discarded theories". In particular, the Chapman-Ferraro theory (see Ferraro 1952) attempts to explain the initial phase of magnetic storms as due to a neutral ionized corpuscular stream moving in a magnetic field which has an inverse cube distribution in the direction of the beam. Although Ferraro (1952) calculated the build-up of the compressed magnetic field as the beam is retarded and identified it with the sudden commencement, their theory cannot account simply for the observed phenomena given above. It was thus decided in the first place to carry out a detailed analysis of the sudden commencement of magnetic storms, first analyzing all available data and secondly trying to formulate a theory consistent with these observed facts. It is obvious that data should be collected from a large number of stations well distributed in different latitudes. To this end 53 storms were selected covering the five-year period 1949-1953, and all known magnetic observatories were asked to loan the original or photostated copies of the relevant magnetograms. So far the response has been very encouraging and a considerable amount of data has been analyzed and a comprehensive world-wide atmospheric electric current system for the sudden commencement of magnetic storms has been obtained (Jacobs and Obayashi 1956). In the first place, however, an investigation was carried out on the diurnal behavior of sudden commencements at Agincourt, the results of which are discussed in this paper. Also a more detailed and comprehensive classification of sudden commencements has been attempted, the results of which are given in the Appendix. This is the first time that such a detailed classification has been given and its value has become apparent in later work. In the rest of the paper, the notation sc will be used to denote any *sudden change* except a crotchet (a solar flare effect) which may be either a sudden commencement SC or a sudden impulse SI.

## 2. PREVIOUS INVESTIGATIONS

The first suggestion of a possible local-time effect of sc's was made by Moos (1910). Following several earlier investigations by Rhodes (1932) and McNish (1934), Newton (1947, 1948) pointed out the diurnal behavior in the occurrence frequency of sc's. His results stimulated the statistical investigation of this problem, and many interesting results have since been reported by various authors. In particular Ferraro and co-workers (Ferraro and Parkinson 1950; Ferraro, Parkinson, and Unthank 1951; Ferraro and Unthank 1951; Ferraro 1954), McIntosh (1951), McIntosh and Watson (1950), and Ishikawa and Kaduna (1951) have made comprehensive analyses of the diurnal variation of amplitude as well as the occurrence frequency of sc's using data from many observatories throughout the world. Although they did not obtain any significant diurnal variation in the occurrence frequency of sc's (at least in the low latitude zone), appreciable diurnal change in amplitude was found in middle and high latitudes. Recently, the anomalous behavior of sc's at Huancayo has been studied by Ferraro and Unthank (1951), Sugiura (1953), Yumura (1954), and Forbush and Vestine (1955). Other important results concerning the preliminary reverse impulse of sc's have been given by

Nagata (1952). All these results demonstrate very clearly the dependence of sc's on local-solar-time.

In order to gain a better insight into the complex nature of sc's similar analyses will be necessary, making use of data from other observatories, especially those in high latitudes. As a first step, attempts are made in this paper to analyze the statistical nature of sc's (including the initial phase of magnetic storms) with the aid of magnetograms from Agincourt. The main topics dealt with are the occurrence frequency of sc's, the qualitative classification of the shape of sc's, and the diurnal variation of amplitude of sc's.

### 3. FREQUENCY DISTRIBUTION OF SC'S AT AGINCOURT

The data have been obtained from the magnetograms of  $H$ ,  $D$ , and  $Z$  at Agincourt ( $\phi = 43.8^\circ$  N.,  $\lambda = 79.3^\circ$  W.) during the period from 1946 to 1953.

Abrupt changes of the magnetic field are picked out and classified into two groups of SC's and SI's according to Ferraro's classification (1951). SC's comprise sc's (including inverted SC's) which are followed by magnetic storms. A magnetic storm as defined here has a geomagnetic activity  $K_p > 5_0$  and a duration longer than twelve hours.\* As may be expected, there are many borderline cases of sc's for which the decision whether to include them or reject them is difficult. Such cases are decided by comparing them with the data from other stations.

The total number of SC's (or SI's) of all types and the total number of SC\*'s (or SI\*'s) in this period are given in Table I. The local-time frequencies

TABLE I

SC's	SC*'s	SI's	SI*'s
106	28	114	32

of them are plotted in Fig. 1. The frequency distributions of SC's and SI's, classified into four groups according to the amplitudes of their horizontal component, are illustrated in Fig. 2.

Generally speaking, the local-time change in the frequency distribution of sc's seems to have a broad minimum around the morning and a maximum in

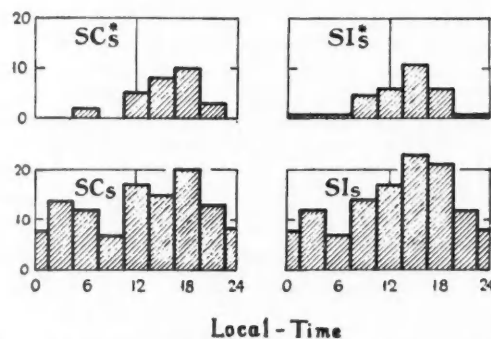


FIG. 1. The occurrence frequencies of SC's (and SI's) and SC\*'s (and SI\*'s) at Agincourt for the period 1946 to 1953.

\* $K_p$  are the planetary three-hour range indices which are reported regularly by J. Bartels and J. Veldkamp in the Journal of Geophysical Research.

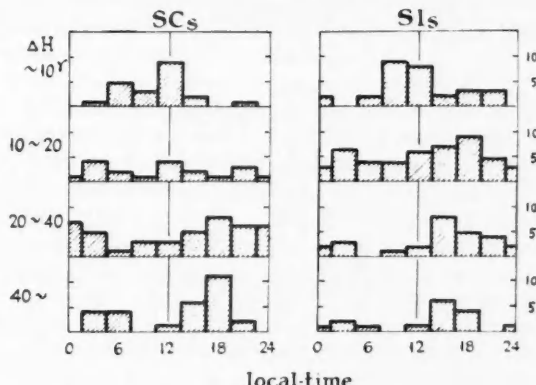


FIG. 2. The local-time frequency distribution of the occurrence of SC's and SI's for four different groups depending on the size of the  $H$ -component. The scale on the right-hand side gives the frequencies.

the afternoon. However, as can be seen in Fig. 2, the sc group of small amplitude (including inverted sc's) exhibits a morning maximum of occurrence. It should be noted that in this case of small amplitude most of the records which were classified as sc's were decided by the magnetograms of the  $D$ -trace. On the contrary large amplitude sc's appear to be most frequent in the afternoon.

Some minor results were also obtained. SC\*'s occur more frequently in the afternoon hours and inverted SC's appear only during the morning hours. These results agree well with results obtained by other investigators. These characteristics of sc's will be discussed again in a later paragraph.

#### 4. QUALITATIVE CLASSIFICATION OF THE SHAPE OF SC'S

As has already been shown, local-time is a determining factor both for the amplitude of sc's as well as for their frequency distribution. In order to investigate these points more clearly, it is desirable to examine the statistical characteristics of the shapes of sc's including also the developing process of the initial phase of a magnetic storm. A classification of the different types of sc's has already been given by Newton (1947). Hence in this section, a somewhat qualitative classification of the shapes of sc's is made.

Nine groups describing the shape of sc's are defined and the idealized shapes are shown in Fig. 3. Here the numbers 9 to 5 indicate a positive change (north-

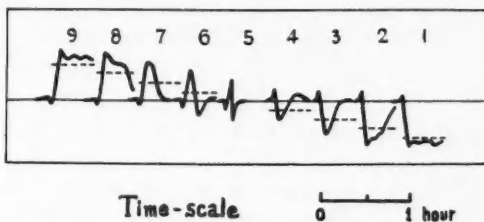


FIG. 3. Idealized shapes of sudden commencements.

wards, eastwards, and downwards in the  $H$ ,  $D$ , and  $Z$  traces respectively) and the numbers 5 to 1 indicate a negative change. All sc's in the three elements ( $H$ ,  $D$ , and  $Z$ ) are classified according to their shapes into these categories (1 to 9). Plotting these values against local-time, the frequency distribution of the different shapes can be obtained. These curves are shown in Fig. 4. Ordinates of this diagram represent the different shape numbers.

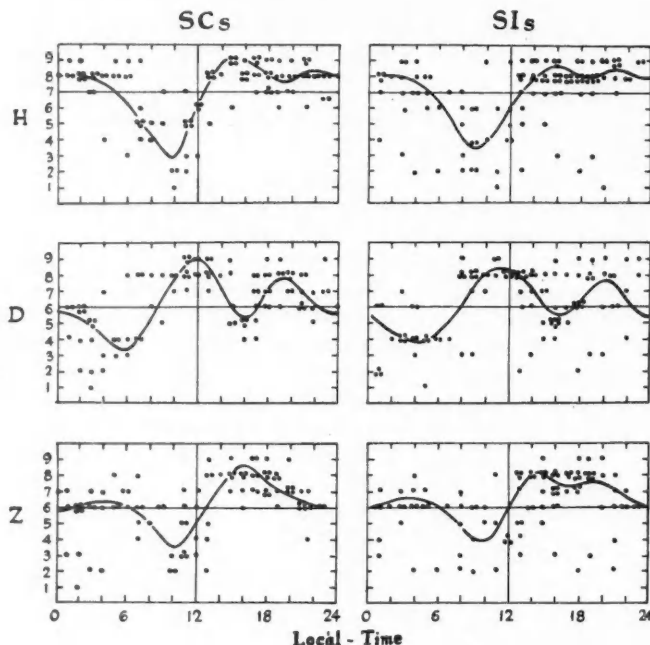


FIG. 4. Local-time change of different shapes of sc's for  $H$ ,  $D$ , and  $Z$  components.

As can be seen from the curves of the  $H$ -component, well-developed shapes (8-9) appear during the afternoon hours. In contrast with this tendency the variation is slight or inverted during the forenoon. From the variation of the  $D$ -component it appears that the deviation is towards the east (7-9) around noon hours, turning to west (3-1) after midnight. Although the shapes taken by the sc movements are variable, they are found to be related to the time of day and these curves do provide some qualitative aspects of the local-time modification of sc's.

##### 5. DIURNAL VARIATIONS OF AMPLITUDE OF SC'S

In the previous analysis, the general aspects of sc's have been revealed qualitatively. However, to estimate the detailed changes of the magnetic field, more quantitative methods, using actual numerical values from the

magnetograms, are necessary. For this reason the following method is adopted to estimate the average diurnal variation of the magnetic field representing sc's.

Values of  $\Delta X_m$ ,  $\Delta Y_m$ , and  $\Delta Z_m$ , i.e. deviations from the normal values (in geomagnetic coordinates), were calculated from the magnetograms during the main impulse (defined as the average of the *first five minutes* after the sc) and during the initial phase of the magnetic storm (at 15-min. intervals during the first storm hour). As individual magnetic storms have widely different magnitudes, the following procedure of normalization was introduced. To generalize the magnitude of the sc of a magnetic storm, the average value of  $\Delta H$  during the main impulse—denoted by  $\bar{\Delta H}$ —is defined from five low latitude stations, San Juan, Honolulu (or Apia), Zose, Alibag, and Elisabethville (or Hermanus). These stations are suitably located at different longitudes so that the effect of local-solar-time on sc's may be eliminated by averaging  $\Delta H$  at these stations. Thus  $\bar{\Delta H}$  can be regarded as the representative magnitude of a particular magnetic storm. In this way the normalized values of an individual sc denoted by  $X_m'$ ,  $Y_m'$ , and  $Z_m'$  are obtained as ratios of the individual values of  $\Delta X_m$ ,  $\Delta Y_m$ , and  $\Delta Z_m$  to  $\bar{\Delta H}$ .

From the data of typical world-wide sc's of 53 storms during the period from

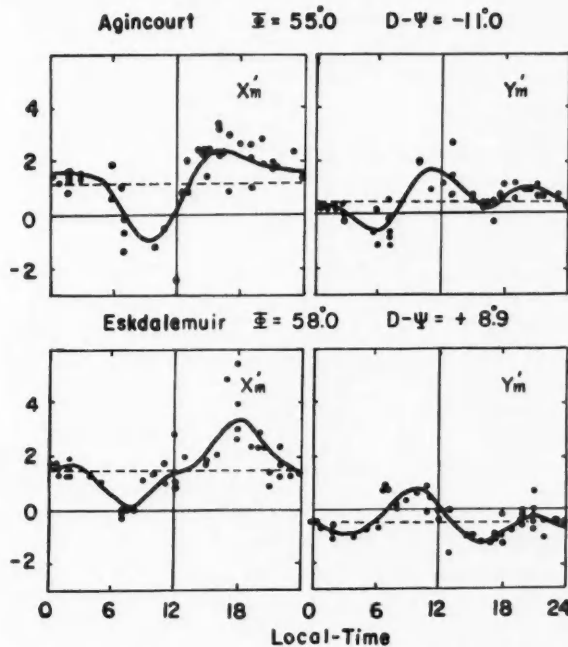


FIG. 5. Diurnal variations of the amplitude (normalized) of sc's at Agincourt and Eskdalemuir. ( $\Phi$  is the geomagnetic latitude and  $D-\Psi$  the declination measured from the geomagnetic meridian.)

1949 to 1953 the diurnal curves of  $X_m'$ ,  $Y_m'$ , and  $Z_m'$  for various stages of the initial phase were obtained. A similar analysis was carried out from the data at Eskdalemuir, Scotland ( $\phi = 55.3^\circ$  N.,  $\lambda = 3.2^\circ$  W.) for the sake of comparison. The results for  $X_m'$  and  $Y_m'$  are shown in Fig. 5, which indicates a diurnal behavior at both observatories. Superposed on the constant term in the  $X$ -component, the diurnal wave can be seen quite clearly, decreasing in the forenoon and increasing in the afternoon hours. A semidiurnal wave is predominant in the  $Y$ -component which has its major (eastwards) maximum around noon and a minor one about 21 hr. The diurnal variation seems to be reinforced during the daylight hours. Such a mode of variation of the magnetic field coincides neither with the ordinary  $Sq$  nor the  $Ds$ -field, appropriate to the latitude of Agincourt. As shown in Fig. 6, in the initial phase of magnetic

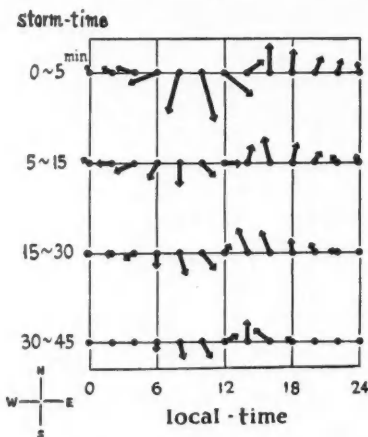


FIG. 6. Diurnal variations of the horizontal magnetic vector for several stages during the initial phase of magnetic storms.

storms, following a sudden rise, the general tendency of the diurnal variation vector is similar. The amplitude of the diurnal variation, however, becomes smaller in the later stages.

#### 6. CONCLUSIONS

The frequency occurrence and the diurnal variations of the normalized amplitude  $X_m'$ ,  $Y_m'$ , and  $Z_m'$  of sc's at Agincourt have been analyzed. The general aspects of these results agree well with those from other stations such as Eskdalemuir, Abinger, Lerwick, and Cheltenham. The behavior of sc's at these observatories must be due to some additional magnetic field produced in the earth's atmosphere, tending to impress or suppress the primary cause of the sc. This may explain the diurnal variation of the occurrence frequency of sc's.

A far wider and more detailed analysis is necessary, however, in order to obtain the complete physical picture of sc's. The world-wide atmospheric

electric current-systems corresponding to SC's have been derived and the physical mechanism of the diurnal behavior of SC's discussed in some detail in another paper (Jacobs and Obayashi 1956).

#### ACKNOWLEDGMENTS

This work was supported by the Geophysical Research Division of the Air Force Cambridge Research Centre, under contract AF 19(604)-761.

#### APPENDIX I. CLASSIFICATION OF SUDDEN COMMENCEMENTS OF MAGNETIC STORMS

I. SC Sudden commencement followed by a magnetic storm.

1. SC<sup>0</sup> Ordinary sudden commencement type 1 to 9.
2. rSC SC with reverse impulse,<sup>†</sup> type  $\bar{1}$  to  $\bar{9}$ .
3. SC\* SC with reverse impulse,<sup>‡</sup> type 1\* to 9\*.

For pictorial description of types 1 to 9, see Fig. 3.

II. aSC Polar (arctic) sudden commencement.

Abrupt large changes occur immediately (say, within a few minutes) after the SC—sometimes SC followed by an abrupt “bay”-type change near the auroral zone.

pSC Pulsational commencement.

Small rapid pulsation occurs at the outset of a magnetic storm (especially in polar regions).

SI Sudden impulse.

SI is not followed by a magnetic disturbance.

Note: Values of sc in *H*, *D*, and *Z* are taken algebraically as positive if towards north, east, and vertically downwards.

In Fig. 3, types 6 to 9 are positive, and types 4 to 1 are negative.

#### REFERENCES

- FERRARO, V. C. A. 1952. J. Geophys. Research, **57**: 15 and references therein.  
 ——— 1954. J. Geophys. Research, **59**: 309.
- FERRARO, V. C. A. and PARKINSON, W. C. 1950. Nature, **165**: 243.
- FERRARO, V. C. A., PARKINSON, W. C., and UNTHANK, H. W. 1951. J. Geophys. Research, **56**: 177.
- FERRARO, V. C. A. and UNTHANK, H. W. 1951. Geofis. pura e appl. **20**: 3.
- FORBUSH, S. E. and VESTINE, E. H. 1955. J. Geophys. Research, **60**: 299.
- FUKUSHIMA, N. 1951. Rept. Ionos. Research, Japan, **5**: 85.
- HEPPNER, J. P. 1954. J. Geophys. Research, **59**: 329.
- ISHIKAWA, G. and KADENA, M. 1951. Rept. Ionos. Research, Japan, **5**: 144.
- JACOBS, J. A. and OBAYASHI, T. 1956. Geofis. pura e appl. In press.
- MCINTOSH, D. H. 1951. J. Atm. and Terrest. Phys. **1**: 223.
- MCINTOSH, D. H. and WATSON, R. A. 1950. Nature, **165**: 1018.
- MCNISH, A. G. 1934. Assembly Lisbonne IUGG A.T.M.E. No. 9. 234.
- MOOS, N. A. F. 1910. Colaba Magnetic Data 1846-1905, Bombay.
- NAGATA, T. 1952. Rept. Ionos. Research, Japan, **6**: 13.
- NEWTON, H. W. 1944. Monthly Notices Roy. Astron. Soc. **103**: 4.  
 ——— 1947. J. Geophys. Research, **52**: 441.  
 ——— 1948. Monthly Notices Roy. Astron. Soc., Geophys. Suppl. **5**: 159.
- RHODES, L. 1932. Terrestrial Magnetism and Atm. Elec. **37**: 273.
- SUGIURA, M. 1953. J. Geophys. Research, **58**: 558.
- YUMURA, T. 1954. Mem. Kakioka Mag. Obs. **7**: 27.

<sup>†</sup>Preliminary reverse impulse with a duration of *a few minutes*.

<sup>‡</sup>Rapid reverse impulse with a duration of *less than a minute*.

---

## NOTES

---

### THE SUDDEN INCREASE IN COSMIC RAY INTENSITY OF FEBRUARY 23, 1956<sup>1</sup>

By D. C. ROSE AND J. KATZMAN

The sudden increase in cosmic ray intensity which has recently been widely reported was observed at Ottawa both with neutron monitors and with counter telescopes and at Resolute with a counter telescope. The coordinates of the stations are as follows:

Ottawa—lat. 45.5° N., long. 75.6° W., geomagnetic lat. 56.8° N., altitude of station 325 ft. above sea level;

Resolute—lat. 74.7° N., long. 94.9° W., geomagnetic lat. 83.0° N., altitude of station 56 ft. above sea level.

The equipment at Ottawa included two neutron monitors, a large cubical counter telescope, a side of the cube being 65 cm., and a number of other counter telescope arrangements involved in experiments being carried out in the laboratory. The method of recording is such that every time a scaler completes a cycle of operation, a "pip" is put on an Esterline Angus operations recorder chart. The chart operates at 1 ft./hr. and the scaling factor in the various recording circuits is normally adjusted so that between one and two pips per minute are recorded. Two pens on the recorder mark minutes and the time is kept to an accuracy of  $\pm 20$  sec. and may be checked with standard time to greater accuracy at any time. Considerable detail can be obtained from the record in that intervals can be measured with an accuracy of better than 0.1 min.; therefore, short averaging times can be used.

Fortunately, two neutron monitors were in operation. The old monitor, which has been operating for about two years, has two recording channels which when added together give a mean counting rate of about 110 counts per minute. The new monitor uses larger and thinner-walled counters and is mounted in a position with less roof shielding. It has three recording channels and a normal counting rate of about 300 per minute. At the peak of the increase, the recording circuits of the new monitor were swamped, indicating that a larger scaling factor should be used.

The results from the neutron monitors are shown in Fig. 1. The upper curve shows the measurements from the old monitor during February 23 and 24. The lower curve shows the daily means of the new monitor for all of February and part of March. These data have been corrected for barometric pressure using a coefficient of 0.73% per mb.

Fig. 2 shows the results of the counter telescope measurements at Ottawa and at Resolute. The upper curve is for Resolute. Unfortunately, the telescope there, which has a normal counting rate of about 230 counts per minute, was out of adjustment because of some component failures which had not been

<sup>1</sup>Issued as N.R.C. No. 4008.

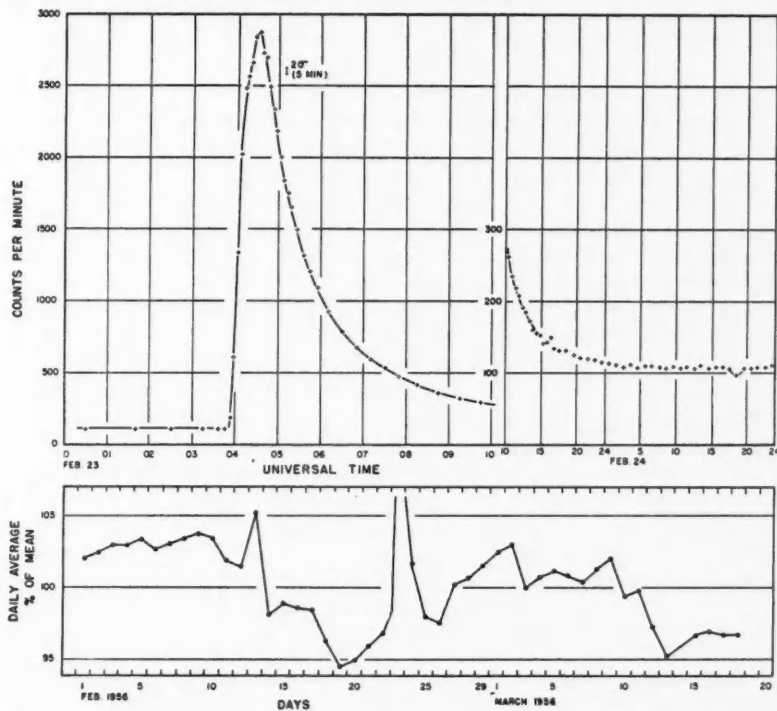


FIG. 1. Nucleon component as measured by neutron monitors. Upper curve shows the sudden increase at 0350 U.T., February 23, 1956, lower curve the daily average for February and part of March, 1956.

detected and which resulted in the count being low. However, two recording channels, both on the triple coincidence circuit, gave the same result, which is that shown and which is believed to be a correct representation of the change in intensity. The Resolute telescope has 12.5 cm. of lead between the second and third tray and the roof and aluminum parts of the trays make a total of about 14.1 cm. of lead equivalent.

The lower curves show the results at Ottawa, the center curve being for the triple coincidence channel with a total of 14.4 cm. lead equivalent, and the lower curve showing the double coincidence counting rate using the two top trays of the same telescope with a total of 2.4 cm. of lead equivalent in the roof and trays.

The curves in Fig. 2 have not been corrected for barometer. During February 23, the barometer at Ottawa rose not quite steadily from 998.0 mb. at zero hours to 1005.8 mb. at 2400 hours. The change from 0300 until 1200 was only 3 mb. Corrections for barometer would make a negligible change in the shape of the increase though the small decrease starting at 22 hours, Febru-

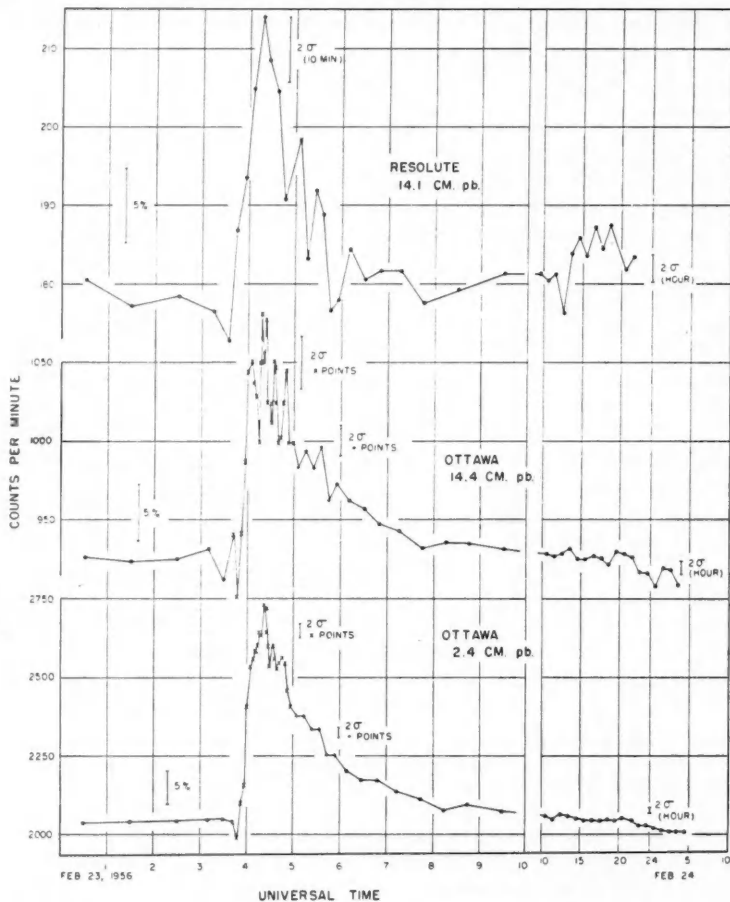


FIG. 2. The meson component measured by counter telescopes. Upper curve—Resolute at geomagnetic latitude  $83.0^\circ$  N.; center and lower curves—Ottawa at geomagnetic latitude  $56.8^\circ$  N.

ary 23, was probably mostly barometric. The barometer records for Resolute are not yet available. All times quoted here are universal or zero meridian time.

The following features are those most notable from these results:

1. The nucleon component increase is many times the normal rate (a factor of 28) while the meson component increases by only a fraction of the normal rate.
2. The percentage increase in the intensity as measured by coincidence in counter trays varies quite appreciably with the amount of absorber. The

hard component, through 14.4 cm. of lead, increased by only 12% while that through 2.4 cm. of lead increased by nearly 30%.

3. The time of onset of the increase appears to be earlier in the case of the nucleon component than in the meson component. This is not necessarily real since the magnitude of the increase was so much greater in the former case. Unless the rate of rise was very high indeed, the increase of greater magnitude would appear to start first. A careful examination of the records shows that the nucleon component started to increase at  $0350 \pm 1$  U.T. and the component measured by counter telescopes at  $0358 \pm 1$ . At Resolute the time could not be assessed quite as accurately. The curve shows a high point between 0340 and 0350 but an examination of the record suggests that this may be fortuitous and though there is an apparent increase in this period, the real rise is estimated to start at  $0358^{+2}_{-8}$  which would make it not significantly different from that at Ottawa.
4. The shape of the curve at Resolute is of the same general form as that at Ottawa. This is unlike the November 19, 1949, increase. For that event (Rose 1951) the shape of the curve at Resolute was completely different from that at Ottawa, the time of maximum being considerably later.
5. The increase occurred during considerable activity in intensity variations of the type usually associated with solar activity. This is shown by the lower curve in Fig. 1. A similar decrease in intensity of much smaller magnitude was apparent in the meson component.

The above are features of these measurements from a preliminary examination of the records. The only conclusions to be presented at this stage are that the magnitude of the increase was very large, since Ottawa was not in a favored impact zone and preliminary reports from the European area\* indicate a much larger increase there. The magnitude of the increase is very sensitive to energy as the difference between the nucleon and hard components shows. The increase occurred with appreciable magnitude at Resolute, which is at a geomagnetic latitude which should not be reached by particles coming directly from the sun. The increase was obviously associated with the solar flare seen in Japan which started at 0334 and ended at 0414 (Preliminary Report on Solar Activity 1956).

ROSE, D. C. 1951. Can. J. Phys. **29**: 227.

High Altitude Observatory and National Bureau of Standards. Preliminary Report on Solar Activity, March 2, 1956.

RECEIVED APRIL 20, 1956.  
DIVISION OF PURE PHYSICS,  
NATIONAL RESEARCH COUNCIL,  
OTTAWA, CANADA.

\*The authors have already received several reports on this sudden increase from other laboratories and wish to thank all those who have made such an early distribution of their data.

**A SIMPLE FORMULA FOR EVALUATING THE MADELUNG CONSTANT  
OF A NaCl-TYPE CRYSTAL\***

BY G. C. BENSON

The electrostatic potential  $\phi_+$  at a positive ion site due to the other ions of charge  $\pm e$  in an ideal infinite NaCl-type crystal with nearest neighbor distance  $a$  is given by

$$(1) \quad \phi_+ = -\alpha_M^{(e/a)}.$$

This equation defines the Madelung constant  $\alpha_M$  which can also be written as

$$(2) \quad \alpha_M = \sum_{l_1=-\infty}^{\infty} \sum_{l_2=-\infty}^{\infty} \sum_{l_3=-\infty}^{\infty} (-1)^{l_1+l_2+l_3+1} (l_1^2 + l_2^2 + l_3^2)^{-\frac{1}{2}}.$$

The sum in equation (2) is only conditionally convergent. Direct evaluation of  $\alpha_M$  by use of this sum is laborious and requires care in the way the terms are grouped.

Madelung (1918) obtained a more rapidly convergent expression for  $\alpha_M$  by considering the potential  $\phi_+$  as arising from the superposition of the potentials due to a series of plane and linear distributions of charge. This leads to the formula

$$(3) \quad \alpha_M = 2 \ln 2 + 16 \sum_{l_1 \text{ odd}}^{\infty} \sum_{l_2 \text{ odd}}^{\infty} \frac{\exp[-\pi(l_1^2 + l_2^2)^{\frac{1}{2}}]}{(l_1^2 + l_2^2)^{\frac{1}{2}} \{1 + \exp[-\pi(l_1^2 + l_2^2)^{\frac{1}{2}}]\}} \\ + 8 \sum_{k=1}^{\infty} \sum_{l_1 \text{ odd}}^{\infty} (-1)^{k+1} K_0(\pi \nu k),$$

where  $K_0(x)$  is the modified Bessel function of the second kind. Since Madelung's original work a number of other methods (Ewald 1921; Evjen 1932; Frank 1950; Bertaut 1952) have been used for the evaluation of  $\alpha_M$ .

Recently in the course of a study of the deformation at the surface of a crystal (Benson, Schreiber, and Patterson 1956), another formula for the Madelung constant was found:

$$(4) \quad \alpha_M = 48\pi \sum_{l_1 \text{ odd}}^{\infty} \sum_{l_2 \text{ odd}}^{\infty} \frac{\exp[-\pi(l_1^2 + l_2^2)^{\frac{1}{2}}]}{\{1 + \exp[-\pi(l_1^2 + l_2^2)^{\frac{1}{2}}]\}^2}.$$

This can also be written as

$$(5) \quad \alpha_M = 12\pi \sum_{l_1 \text{ odd}}^{\infty} \sum_{l_2 \text{ odd}}^{\infty} \operatorname{sech}^2[\frac{1}{2}\pi(l_1^2 + l_2^2)^{\frac{1}{2}}],$$

but equation (4) is more suitable for numerical calculation. This simple formula, which does not seem to have been described previously, was obtained by the following argument.

When an infinite NaCl-type crystal is separated into two semi-infinite hemi-crystals with {100} faces by a translation of one half a distance  $(\eta - 1)a$  in a direction normal to these faces, the energy of interaction of the two hemi-crystals (stated per ion pair in the surface) can be expressed in the form

$$(6) \quad U_s(\eta) = -(e^2/a)B(\eta) + R(\eta).$$

\*Issued as N.R.C. No. 4015.

The first term of this equation represents the electrostatic interactions and

$$(7) \quad B(\eta) = 8 \sum_{l_1=1}^{\infty} \sum_{l_2=1}^{\infty} \frac{\exp[-\pi(l_1^2+l_2^2)^{\frac{1}{2}}]}{(l_1^2+l_2^2)^{\frac{1}{2}} \{1+\exp[-\pi(l_1^2+l_2^2)^{\frac{1}{2}}]\}^2}.$$

When  $\eta = 1$ ,  $B(1) = 0.06524647$  is the usual electrostatic contribution to the surface energy (van der Hoff and Benson 1954).  $R(\eta)$  represents the repulsive interactions and if for simplicity only contributions from nearest neighbors are considered, then  $R(\eta)$  is the repulsive interaction energy between a positive and a negative ion separated by a distance  $\eta a$ . The condition for a minimum of  $U_s(\eta)$  at  $\eta = 1$  is

$$(8) \quad -(e/a)B'(1)+R'(1) = 0$$

where the prime indicates differentiation with respect to  $\eta$ .

On the basis of the same type of model, the cohesive energy per ion pair in an ideal infinite crystal with nearest neighbor distance  $\eta a$  can be written as

$$(9) \quad U_c(\eta) = -\alpha_M(e^2/\eta a) + 6R(\eta)$$

and for equilibrium at  $\eta = 1$

$$(10) \quad \alpha_M(e^2/a) + 6R'(1) = 0.$$

Thus from equations (8) and (10)

$$(11) \quad \alpha_M = -6B'(1),$$

which leads at once to formula (4).

The derivation given above is of some interest since it illustrates the relationship between the electrostatic contributions to the cohesive and surface energy of the crystal. However it is rather unsatisfactory from a mathematical point of view since it involves the introduction of a model with repulsive forces which cancel out at a later stage. Attempts to find a more direct route to equation (4) have been unsuccessful.

In Table I the first few terms of the series in equation (4) are given to 10 places of decimals. The convergence of the sum is good and taking terms up

TABLE I

$l_1^2 + l_2^2$	$\frac{48\pi\exp[-\pi(l_1^2+l_2^2)^{\frac{1}{2}}]}{\{1+\exp[-\pi(l_1^2+l_2^2)^{\frac{1}{2}}]\}^2}$	Number of terms	Total
2	1.7326660054	1	1.7326660054
10	0.0073082290	2	1.7472824634
18	0.0002453754	1	1.7475278388
26	0.0000166498	2	1.7475611388
34	0.0000016702	2	1.7475644788
50	0.0000000339	3	1.7475645805
58	0.0000000061	2	1.7475645928
74	0.0000000003	2	1.7475645934

to  $l_1^2 + l_2^2 = 58$  yields a value of  $\alpha_M$  correct to nine significant figures. The most accurate value of the Madelung constant given in the literature is  $\alpha_M = 1.7475645946331821_{\pm 9}$  (Sakamoto 1953) calculated by Ewald's method.

Equation (4) would be quite suitable for working out a value of  $\alpha_M$  to a

larger number of decimal places. However as far as the physical significance of this constant is concerned it is rather pointless to attempt to refine Sakamoto's value. Emersleben (1955) has discussed this question quite recently.

In conclusion the author wishes to thank Dr. F. van Zeggeren for helpful discussions of this problem.

- BENSON, G. C., SCHREIBER, H. P., and PATTERSON, D. 1956. Can. J. Phys. **34**: 265.  
 BERTAUT, F. 1952. J. phys. radium, **13**: 499.  
 EMERSLEBEN, O. 1955. Z. physik. Chem. **204**: 43.  
 EVJEN, H. M. 1932. Phys. Rev. **39**: 675.  
 EWALD, P. P. 1921. Ann. Physik, **64**: 253.  
 FRANK, F. C. 1950. Phil. Mag. **41**: 1287.  
 VAN DER HOFF, B. M. E. and BENSON, G. C. 1954. J. Chem. Phys. **22**: 475.  
 MADELUNG, E. 1918. Physik. Z. **19**: 524.  
 SAKAMOTO, Y. 1953. J. Sci. Hiroshima Univ. A, **16**: 569.

RECEIVED MAY 4, 1956.  
 DIVISION OF PURE CHEMISTRY,  
 NATIONAL RESEARCH COUNCIL,  
 OTTAWA, CANADA.

#### SHIELDING OF A TRANSIENT ELECTROMAGNETIC DIPOLE FIELD BY A CONDUCTIVE SHEET

BY JAMES R. WAIT

It is of interest to know the way in which a sheet of conductive material can effectively shield an observer from a transient electromagnetic source. It is the purpose of this note to show that a previous derivation (Wait 1951, 1953) for an arbitrarily oriented magnetic dipole with a harmonically time-varying moment can be readily extended to the transient case. In fact, the resulting expressions for the transient field components on either side of the sheet are seen to be much simpler in form than in the steady state case.

As discussed earlier, it is convenient to regard the arbitrarily oriented magnetic dipole source as the superposition of a vertical and horizontal dipole with respect to the horizontal sheet. Therefore, it is sufficient to consider the two problems separately.

The source is a small current-carrying loop of area  $dA$  carrying a total current  $I$  and is located at the origin of a cylindrical coordinate system  $(\rho, \phi, z)$ . The axis of the loop and the equivalent magnetic dipole is oriented in the  $z$  direction. The thin sheet of conductivity  $\sigma$  and thickness  $d$  is located in the plane  $z = -h$ , being a distance  $h$  below the source dipole. Subject to the approximation that the significant distances (i.e.,  $h$ ,  $\rho$ , and  $z$ ) are small compared to the free space wavelength, the magnetic fields can be written

$$(1) \quad \mathbf{H}(i\omega) = -\text{grad } \Psi(i\omega) = [H_r(i\omega), 0, H_z(i\omega)]$$

for a source which varies as  $e^{+i\omega t}$ . The magnetic potential is given by:

$$(2) \quad \Psi(i\omega) = \frac{dA}{4\pi} \left[ \frac{I(i\omega)z}{(\rho^2 + z^2)^{3/2}} + I(i\omega) i\omega \frac{\partial}{\partial z} \int_0^\infty \frac{e^{-\lambda\theta} J_0(\lambda\rho)}{(\lambda/\alpha) + i\omega} d\lambda \right],$$

where

$$\begin{aligned}\beta &= 2h+z \text{ for } z > -h, \\ &= -z \quad \text{for } z < -h,\end{aligned}$$

and

$$\alpha = \sigma \mu d / 2 \text{ with } \mu = 4\pi \times 10^{-7}.$$

The electric field can be expressed in similar form where again the functional dependence on  $i\omega$  is emphasized:

$$\mathbf{E}(i\omega) = [0, E_\phi(i\omega), 0],$$

$$(3) \quad E_\phi(i\omega) = \frac{-\mu I(i\omega) i\omega dA}{4\pi} \left[ \frac{\rho}{(\rho^2 + z^2)^{3/2}} + i\omega \frac{\partial}{\partial \rho} \int_0^\infty \frac{e^{-\lambda\beta}}{\lambda/\alpha + i\omega} J_0(\lambda\rho) d\lambda \right]$$

where  $J_0$  is the Bessel function of order zero and of the first type. The source current  $j(t)$  is now considered to be a step function, that is

$$(4) \quad j(t) = I_0 u(t)$$

where  $u(t) = 1$  for  $t > 0$ ,  $= 0$  for  $t < 0$ . The frequency spectrum  $I(i\omega)$  can then be regarded as the Laplace transform of the current, so that

$$(5) \quad I(i\omega) = \int_0^\infty j(t) e^{-i\omega t} dt = I_0/i\omega.$$

The corresponding potential  $\psi(t)$  is then given formally by an inverse Laplace integral as follows:

$$(6) \quad \psi(t) = \frac{1}{2\pi i} \int_{c-i\infty}^{c+i\infty} \Psi(i\omega) e^{i\omega t} d(i\omega)$$

where  $c$  is some small positive constant. In the case of the step function source, the integration with respect to  $i\omega$  can be readily carried out to yield

$$(7) \quad \psi(t) = \frac{I_0 dA}{4\pi} \left[ \frac{z}{r^3} + \frac{\partial}{\partial z} \int_0^\infty e^{-\lambda\beta} e^{-\lambda t/\alpha} J_0(\lambda\rho) d\lambda \right] u(t)$$

where  $r = (\rho^2 + z^2)^{\frac{1}{2}}$ . The integration with respect to  $\lambda$  can now be carried out giving an expression for the magnetic potential in simple closed form:

$$(8) \quad \psi(t) = \frac{I_0 dA}{4\pi} \left[ \frac{z}{r^3} \mp \frac{\beta + t/\alpha}{r_a^3} \right] u(t)$$

where

$$r_a = [(\beta + t/\alpha)^2 + \rho^2]^{\frac{1}{2}}$$

and where the upper sign is to be used for  $z > -h$  and the lower sign for  $z < -h$ . The magnetic field components are then given by

$$(9) \quad h_\rho(t) = \frac{I_0 dA}{4\pi} \left[ \frac{3\rho z}{r^5} \mp \frac{3(\beta + t/\alpha)\rho}{r_a^5} \right] u(t)$$

and

$$(10) \quad h_z(t) = \frac{I_0 dA}{4\pi} \left[ \frac{3z^2}{r^5} - \frac{1}{r^3} - \frac{3(\beta + t/\alpha)^2}{r_a^5} + \frac{1}{r_a^3} \right] u(t).$$

The single component of the electric field is obtained from equation (3) after

performing the integrations with respect to  $i\omega$  and  $\lambda$ . It is expressible in closed form as follows:

$$(11) \quad e_\phi(t) = -\frac{\mu I_0 dA}{4\pi} \left\{ \left[ \frac{\rho}{(\rho^2 + z^2)^{3/2}} - \frac{\rho}{(\rho^2 + \beta^2)^{3/2}} \right] \delta(t) + \frac{3\rho(\beta + t/\alpha)}{\alpha r_a^5} u(t) \right\}$$

where  $\delta(t)$  is the unit impulse function at  $t = 0$ . It should be noted that below the sheet ( $z < -h$ ), the first term in the above expression, multiplying  $\delta(t)$ , vanishes.

The validity of these transient fields can now be confirmed directly by noting that they satisfy the boundary conditions:

$$(12) \quad e_\phi(t)]_{z=-h+d/2} - e_\phi(t)]_{z=-h-d/2} = 0,$$

$$(13) \quad h_\rho(t)]_{z=-h+d/2} - h_\rho(t)]_{z=-h-d/2} = \sigma d e_\phi(t)]_{z=-h}.$$

These conditions state, subject to the smallness of  $d$ , that the tangential electric field is continuous through the sheet and the magnetic field is discontinuous by the amount of transverse current in the sheet.

The small current-carrying loop or magnetic dipole is now considered to be oriented in the  $y$  direction of an  $(x, y, z)$  cartesian coordinate system with the sheet located at  $z = -h$ . The magnetic potential for the case of harmonic time excitation is

$$(14) \quad \Psi' = \frac{I(i\omega)dA}{4\pi} \left[ \frac{y}{r^3} \mp i\omega \frac{\partial}{\partial y} \int_0^\infty \frac{e^{-\beta\lambda}}{\lambda/\alpha + i\omega} J_0(\lambda\rho) d\lambda \right]$$

where again the upper sign is to be used for  $z > -h$  and the lower sign for  $z < -h$ . If the current is now of step-function form,  $j(t) = I_0 u(t)$ , then the transient magnetic potential  $\psi'(t)$  is again expressible in simple form:

$$(15) \quad \psi'(t) = \frac{I_0 dA}{4\pi} \left[ \frac{y}{r^3} \mp \frac{\partial}{\partial y} \int_0^\infty e^{-(\beta + t/\alpha)\lambda} J_0(\lambda\rho) d\lambda \right] = \frac{I_0 dA}{4\pi} \left[ \frac{y}{r^3} \pm \frac{y}{r_a^3} \right] u(t).$$

The magnetic field components of the horizontal transient magnetic dipole are then given by:

$$(16) \quad \begin{aligned} h_r'(t) &= \frac{I_0 dA}{4\pi} \left[ \frac{3xy}{r^5} \pm \frac{3xy}{r_a^5} \right], \\ h_y'(t) &= \frac{I_0 dA}{4\pi} \left[ \left( \frac{3y^2}{r^5} - \frac{1}{r^3} \right) \pm \left( \frac{3y^2}{r_a^5} - \frac{1}{r_a^3} \right) \right], \text{ and} \\ h_z'(t) &= \frac{I_0 dA}{4\pi} \left[ \frac{3yz}{r^5} - \frac{3y(\beta + t/\alpha)}{r_a^5} \right]. \end{aligned}$$

The transient electric field components can be found from the spectrum functions  $E_x(i\omega)$ ,  $E_y(i\omega)$ , and  $E_z(i\omega)$  given in a previous paper (Wait 1953). The results are only of secondary interest and they do not need to be written out here. They can be employed, however, to verify the boundary conditions relating the tangential electric and magnetic fields at the conducting sheet.

The most significant feature of the results is that the magnetic field components of a small wire loop with a step-function excitation of current can be expressed in very simple closed form. In fact, the secondary magnetic field in

the upper region can be derived directly from an image located a distance  $h+t/\alpha$  below the plane of the sheet. For very small times ( $t \ll \alpha$ ), the sheet is acting as a perfect conductor, and the image is located a distance  $h$  below the sheet. At very large times ( $t \gg \alpha$ ) the image recedes to an infinite distance below the sheet, leaving only the contribution of the primary field. The magnetic field in the lower region also has a very simple interpretation. The source of the secondary field is derivable from a virtual source dipole a height  $h+t/\alpha$  above the sheet whose moment is always equal and opposite to the source dipole. For small times, the virtual and the actual source are effectively coincident, which corresponds to perfect shielding by the conductive sheet. At larger times, the virtual source recedes from the sheet, giving rise to a measurable field below the sheet. This corresponds to incomplete shielding of the transient source. In the limiting case of very large times ( $t \gg \alpha$ ), the virtual source has receded to infinity leaving only the primary field.

In the foregoing analysis the propagational effects of the field in the air have been neglected. In the frequency domain, this requires that the significant distances such as  $h$  and  $r$  are much less than a free space wavelength (Wait 1951). In the transient domain, the corresponding restriction is that the expressions for these quasi-static fields are only strictly valid for times  $t \gg r/c$  or  $h/c$  where  $c = 3 \times 10^8$  meters per sec.

While the results in this note refer specifically to a wire loop with a step-function current excitation, the results can be extended to other source current waveforms by the principle of superposition.

WAIT, J. R. 1951. Can. J. Phys. **29**: 577.  
\_\_\_\_\_. 1953. Appl. Sci. Research, B, **3**: 230.

RECEIVED APRIL 3, 1956.  
NATIONAL BUREAU OF STANDARDS,  
BOULDER, COLORADO.

#### ELECTROMAGNETIC FIELD SOLUTIONS FOR ROTATIONAL COORDINATE SYSTEMS

BY ROBERT C. HANSEN

Morse and Feshbach (1953) show, by using vector potentials, that Maxwell's equations can in general be solved in only six coordinate systems: cartesian; circular, elliptic, and parabolic cylinder; spherical; and conical. Problems with rotational symmetry have also been treated by Spencer (1951), using direct separation of one component of field. This note, which is a summary of Hughes Technical Memorandum 398 (Hansen 1955), demonstrates the vector potential approach for rotational systems, a process that is believed to be simpler and more open to physical interpretation than the direct separation technique.

In the five rotational coordinate systems: circular cylinder, spherical, prolate and oblate spheroidal, and rotational parabolic, fields with rotational symmetry can easily be expressed. Assume homogeneous isotropic media and

a harmonic time dependence. Let the coordinate system have variables  $u_1, u_2, \phi$ , and scale factors  $h_1, h_2, h_3$ . The fields of interest will be independent of the angle of rotation  $\phi$ . The object is to solve the vector Helmholtz equation

$$\text{curl curl } \mathbf{E} = k^2 \mathbf{E},$$

which is equivalent to solving Maxwell's equations in this case. Assume a form of solution:

$$\mathbf{E} = \text{curl } \mathbf{a}_3 f$$

where  $\mathbf{a}_3$  is a unit vector in the  $\phi$  direction and  $f$  is a scalar. Now insert this into the Helmholtz equation, giving an equation for  $f$ :

$$\text{curl curl curl } \mathbf{a}_3 f = \text{curl } \mathbf{a}_3 k^2 f$$

which is the same as

$$\text{curl curl } \mathbf{a}_3 f = \mathbf{a}_3 k^2 f + \nabla V;$$

$V$  is a scalar which can be shown to be zero (Hansen 1955). Expanding the left-hand side gives

$$\begin{aligned} \text{L.H.S.} = & \mathbf{a}_1 \frac{1}{h_2 h_3} \frac{\partial}{\partial \phi} \left[ \frac{h_2}{h_1 h_3} \frac{\partial}{\partial u_1} (h_3 f) \right] + \mathbf{a}_2 \frac{1}{h_1 h_3} \frac{\partial}{\partial \phi} \left[ \frac{h_1}{h_2 h_3} \frac{\partial}{\partial u_2} (h_3 f) \right] \\ & - \mathbf{a}_3 \frac{1}{h_1 h_2} \left\{ \frac{\partial}{\partial u_1} \left[ \frac{h_2}{h_1 h_3} \frac{\partial}{\partial u_1} (h_3 f) \right] + \frac{\partial}{\partial u_2} \left[ \frac{h_1}{h_2 h_3} \frac{\partial}{\partial u_2} (h_3 f) \right] \right\}. \end{aligned}$$

If  $h_1$  and  $h_2$  are independent of  $\phi$ , which is valid for the five rotational systems,  $\phi$  independence of the field makes the  $\mathbf{a}_1$  and  $\mathbf{a}_2$  terms of the left-hand side expansion vanish. The equation for  $f$  is now reduced to a scalar equation

$$\frac{\partial}{\partial u_1} \left[ \frac{h_2}{h_1 h_3} \frac{\partial}{\partial u_1} (h_3 f) \right] + \frac{\partial}{\partial u_2} \left[ \frac{h_1}{h_2 h_3} \frac{\partial}{\partial u_2} (h_3 f) \right] + k^2 h_1 h_2 f = 0.$$

It is noted that this equation is *not* the scalar Helmholtz equation, since  $h_3$  is not independent of  $u_1, u_2$  for the rotational systems. Similarity to the scalar Helmholtz equation is enhanced by expanding the terms of the equation to get  $f$  (rather than  $h_3 f$ ) as the dependent variable. The result is

$$\begin{aligned} & \frac{\partial}{\partial u_1} \left[ \frac{h_2 h_3}{h_1} \frac{\partial f}{\partial u_1} \right] + \frac{\partial}{\partial u_2} \left[ \frac{h_1 h_3}{h_2} \frac{\partial f}{\partial u_2} \right] + k^2 h_1 h_2 h_3 f \\ & + h_3 \left\{ \frac{\partial}{\partial u_1} \left[ \frac{h_2}{h_1 h_3} \frac{\partial h_3}{\partial u_1} \right] + \frac{\partial}{\partial u_2} \left[ \frac{h_1}{h_2 h_3} \frac{\partial h_3}{\partial u_2} \right] \right\} = 0, \end{aligned}$$

which is just the scalar Helmholtz equation plus two additional terms. For the five coordinate systems, the term in curly braces is exactly  $-h_1 h_2 / h_3^2$  so the scalar equation is now

$$\frac{\partial}{\partial u_1} \left[ \frac{h_2 h_3}{h_1} \frac{\partial f}{\partial u_1} \right] + \frac{\partial}{\partial u_2} \left[ \frac{h_1 h_3}{h_2} \frac{\partial f}{\partial u_2} \right] + f \left[ k^2 h_1 h_2 h_3 - \frac{h_1 h_2}{h_3} \right] = 0.$$

If now the *scalar Helmholtz equation* is separated (Stratton 1941) into a  $\phi$  equation and one involving  $u_1, u_2$ , it is seen that the  $u_1, u_2$  equation for  $m = 1$  is just the scalar equation above, where  $m$  is the  $\phi$  eigenvalue. This then gives the vector solution in rotational coordinate systems:

$$\mathbf{E}_1 = \text{curl } \mathbf{a}_\phi f_{m=1},$$

where  $f$  is the  $u_1, u_2$  part of the scalar Helmholtz or wave solutions which are well known. A second independent solution will be

$$\mathbf{E}_2 = \operatorname{curl} \operatorname{curl} \mathbf{a}_\phi g_{m=1},$$

where  $g$  is a scalar similar to  $f$ . Orthogonality of the solutions is shown in Hansen (1955).

The physical interpretation of the use of the  $m = 1$  scalar wave functions is augmented by considering a rotationally symmetric field in spherical coordinates, where a general solution is also possible. The general solution is

$$\mathbf{E}_1 = \operatorname{curl} \mathbf{a}_r r\psi, \quad \mathbf{E}_2 = \operatorname{curl} \operatorname{curl} \mathbf{a}_r r\psi.$$

Two components of interest are

$$E_{1\phi} = -\frac{\partial \psi}{\partial \theta}, \quad E_{2\theta} = \frac{1}{r} \frac{\partial^2 (r\psi)}{\partial r \partial \theta}.$$

The corresponding components from the  $\phi$  vector (rotational) solutions do not display  $\theta$  derivatives, and are

$$E_{2\phi} = f, \quad E_{1\theta} = -\frac{1}{r} \frac{\partial (rf)}{\partial r}.$$

These must be identical to the general solutions above, and are identical because of the special relationship

$$f_{m=1}(u_2) = -\frac{\partial}{\partial u_2} f_{m=0}(u_2).$$

Hence, the  $m = 1$  scalar wave function is necessary to produce the  $\theta$  differentiation. In spherical coordinates, the relation is

$$P_n^1(\cos \theta) = -\frac{\partial}{\partial \theta} P_n(\cos \theta),$$

whereas in cylindrical coordinates it is

$$J_1(\rho) = -\frac{\partial}{\partial \rho} J_0(\rho).$$

In conclusion, the vector potential method of separation permits a clear understanding of how the rotationally symmetric solutions are obtained, and why the  $m = 1$  scalar wave function is needed. These solutions are readily written as curls of the scalar wave function times a  $\phi$  unit vector, for the five rotational coordinate systems: circular cylinder, spherical, prolate and oblate spheroidal, and rotational parabolic.

HANSEN, R. C. 1955. Vector wave solutions and separable coordinates. Tech. Mem. 398. July. Hughes Aircraft Company, Culver City, California.

MORSE, P. M. and FESHBACH, H. 1953. Methods of theoretical physics. Vol. II. McGraw-Hill Book Company, Inc., New York and London. Section 13.1.

SPENCER, D. E. 1951. J. Appl. Phys. 22: 386.

STRATTON, J. A. 1941. Electromagnetic theory. McGraw-Hill Book Company, Inc., New York and London. Chap. I.

RECEIVED APRIL 11, 1956.

RESEARCH LABORATORIES,  
HUGHES AIRCRAFT COMPANY,  
CULVER CITY, CALIFORNIA.

---

## LETTERS TO THE EDITOR

---

*Under this heading brief reports of important discoveries in physics may be published. These reports should not exceed 600 words and, for any issue, should be submitted not later than six weeks previous to the first day of the month of issue. No proof will be sent to the authors.*

### The Luminescent Response of Silver Activated Zinc Sulphide to Lithium Ions of Different Energies\*

The fluorescence of glass under the impact of positive rays led to their discovery by Goldstein (1886). Other materials were found to give a brighter fluorescence than glass, in particular, willemite, a natural silicate of zinc. J. J. Thomson (1913) found that the brightness of the fluorescence of a willemite screen diminished with continued exposure to positive rays, and eventually disappeared, necessitating occasional renewal of the screen. Also, some materials deteriorated more quickly than others; for example, willemite provided a longer, though less spectacular, source than zinc blende, a naturally occurring zinc sulphide. About 1910 the fluorescent screen was largely supplanted as a positive ion detector by the photographic plate. With the advent of sensitive photomultiplier tubes, there has been a recent revival of interest in fluorescent materials in connection with scintillation counters.

Some measurements of the light output of inorganic phosphors under positive ion excitation and the decline of the light output with prolonged ion bombardment have been made by Hanle and Rau (1952) using  $H_2^+$ ,  $He^+$ ,  $Ne^+$ ,  $A^+$ , and  $Xe^+$  ions with energies from 15 to 35 kev. A further study of the deterioration of silver activated zinc sulphide ( $ZnS-Ag$ ) under  $H_2^+$  ion bombardment at energies up to 10 kev. has been reported by Berthold (1955). Young (1955) has measured the reduction of luminescent efficiency of  $ZnS-Ag$  for electron excitation caused by prolonged bombardment of the phosphor with  $H^+$ ,  $H_2^+$ ,  $He^+$ ,  $Ne^+$ ,  $N_2^+$ , and  $A^+$  ions with energies from 1 to 25 kev.

The object of the present experiment has been to extend the work of Hanle and Rau to higher ion energies and to include other types of ions, with a view to the possible use of a scintillation detector of 50–100 kev. positive ions in a high resolution mass spectrometer. Such a detector was introduced by Richards and Hayes (1949) in their time-of-flight mass spectrometer, using potassium and rubidium ions with energies up to 30 kev., and some general observations were made concerning the light output as a function of ion energy. However, in subsequent work with this instrument, this detector was replaced by an electron multiplier. With the exception of the work just mentioned, most of the previous investigations have involved ions of the rare gases, so it was felt that a study of the effects of ions of less inert elements would be instructive, especially in view of the strong dependence of luminescent efficiency on the chemical composition of the phosphor. As a first step in this investigation, measurements have been made of the relative light output of  $ZnS-Ag$  (Sylvania Phosphor CR 20) under bombardment with  $Li^+$  ions with energies from 15 to 40 kev. This letter reports the results of these measurements.

Several samples of the above phosphor were deposited in differing amounts on microscope cover glasses. These glasses were mounted on a disk within a vacuum system. By steady rotation of the disk, each phosphor sample in turn was made to move across the path of a collimated beam of lithium ions. The ions were produced from a heated filament coated with spodumene. The homogeneity of the ion beam had previously been checked by deflecting the beam in the field of a permanent magnet. With the magnet in place, a visual inspection of the phosphor made with high ion currents showed that only a negligible proportion of the light emitted was due to impurity ions other than lithium. The subsequent measurements on the phosphor samples were made without any magnetic analysis of the beam.

The light output from the phosphor samples, after transmission through the phosphor and the glass substrate, was focused onto the photocathode of a 1P21 photomultiplier, the d-c. output of which was displayed on a Brown Electronik recorder. A peak was produced on the recorder chart corresponding to each phosphor sample "scanned" by the ion beam. This technique of continuous scanning reduced any deterioration of the phosphor to negligible proportions and also enabled rapid comparison of the different samples to be made. A number of scans were made using different ion energies. Ion currents from 1 to  $3 \times 10^{-13}$  amp. were employed, the ion current during any one scan being constant to within 3 or 4%. Previous measurements had confirmed that the light output from a given sample at a given ion energy was directly proportional to the total ion current in the range  $10^{-13}$  to  $10^{-12}$  amp. For each phosphor sample, the photomultiplier output, corrected to a standard ion current of  $10^{-13}$  amp., was

\*This work was supported by the Office of Scientific Research, Air Research and Development Command, U.S. Air Force, the Ontario Research Foundation, and the National Research Council of Canada.

plotted as a function of ion energy. In Fig. 1 is shown the curve obtained for a sample of thickness 2.5 mgm. per cm.<sup>2</sup>, which is very close to the optimum thickness. On a double-logarithmic scale the curve is linear within the range of energies shown, with a gradient of 2.46. Similar

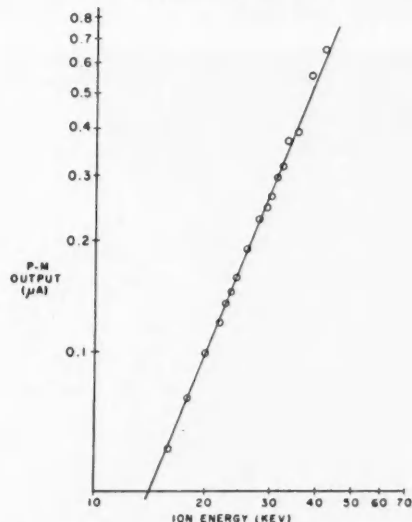


FIG. 1. Double-logarithmic plot of the photomultiplier output as a function of ion energy, for a sample of 2.5 mgm. per cm.<sup>2</sup> of ZnS-Ag under bombardment with lithium ions.

curves were obtained for the 10 other samples, all with gradients between 2.45 and 2.55. The mean gradient for the 11 samples was 2.49. These results indicate a variation of light output  $I$  with ion energy  $E$  of the form

$$I \propto E^{2.5},$$

the exponent of  $E$  being determined to within a few per cent.

Hanle and Rau (1952) found that, under bombardment with ions of the rare gases, the light output from ZnS-Ag was directly proportional to the ion energy to an accuracy of 5 or 6% for energies in the range 15 to 30 kev. Their experiment differed from that reported here in two respects. In the first place, their photomultiplier was located on the same side of the phosphor layer as that bombarded by the ions so that the light measured suffered virtually no optical absorption in the phosphor, whereas in the present experiment the light was measured after transmission through the phosphor layer to the other surface. The second difference lies in the different ions used in the two experiments. Further investigations are planned in an attempt to determine which of these two factors is responsible for the difference between the results of the two experiments. A study of the deterioration of the phosphor as a function of the ion energy and the type of ion is also contemplated. It is hoped that these experiments will be the subject of a future publication.

- BERTHOLD, W. 1955. Naturwissenschaften, **42**: 436.  
 GOLDSTEIN, E. 1886. Berl. Ber. Ledet, **39**: 691.  
 HANLE, W. and RAU, K. H. 1952. Z. Physik, **133**: 297.  
 RICHARDS, P. I. and HAYES, E. E. 1949. Rev. Sci. Instr. **21**: 99.  
 THOMSON, J. J. 1913. Rays of positive electricity. Longmans, Green & Co., London.  
 YOUNG, J. R. 1955. J. Appl. Phys. **26**: 1302.

RECEIVED MAY 28, 1956.  
 DEPARTMENT OF PHYSICS,  
 HAMILTON COLLEGE,  
 McMMASTER UNIVERSITY,  
 HAMILTON, ONTARIO.

CLIFFORD F. EVE\*  
 HENRY E. DUCKWORTH

\*Holder of a Research Council of Ontario Scholarship 1954-55, and currently holder of a Shell Oil Fellowship.

### The Index of Refraction of Liquid Helium

Changes in the index of refraction,  $n$ , have been measured from  $1.5^\circ\text{K}$ . to the boiling point ( $4.2^\circ\text{K}$ .) for liquid helium at its saturated vapor pressure. A specially designed metal cryostat (see Fig. 1), placed on a Jamin refractometer (Bellingham and Stanley), contains a 9.68 cm.

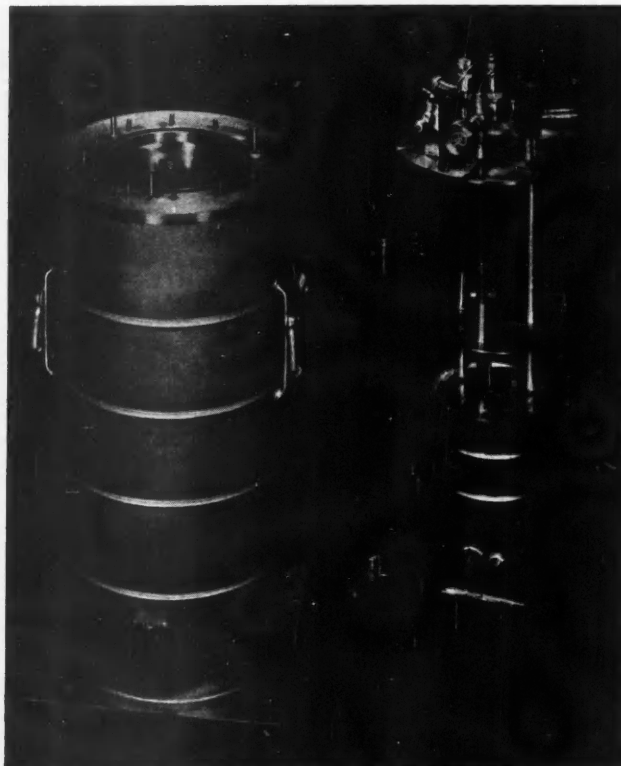


FIG. 1. The cryostat, shown disassembled.

long copper cell. This cell is separate from the helium bath and is filled with liquid helium by condensation of helium gas purified by a liquid air cooled charcoal trap. Two optically flat fused silica windows, sealed by compression of indium O-rings against the copper, form the ends of the cell. The comparison light beam passes through an evacuated tube parallel to the helium cell and within the cryostat. The four windows on the outer wall of the cryostat were cut from selected microscope slides and sealed with rubber O-rings.

As the temperature of the liquid helium was varied the index of refraction changed, and fringes were counted visually as they moved past the cross-hairs of the refractometer telescope. Between  $4.2^\circ\text{K}$ . and the  $\lambda$ -point ( $2.17^\circ\text{K}$ .), about 720 fringes were counted; between the  $\lambda$ -point and  $1.5^\circ\text{K}$ . about 30 fringes were counted, moving in the opposite sense. The mercury green line ( $\lambda = 5461 \text{ \AA}$ ) was used, one fringe corresponding to a change in index of about  $6 \times 10^{-6}$ . The bath temperatures were read on a Wheatstone Bridge using a carbon resistance thermometer which had been calibrated against the 1955 vapor pressure tables (Clement *et al.* 1955).

The absolute value of  $n$  may be obtained as follows. The Lorenz-Lorentz equation

$$(1) \quad \frac{n^2 - 1}{n^2 + 2} = \frac{4\pi}{3} \frac{N\alpha}{M} \rho$$

relates

$$n = \text{index of refraction} = n(P, T, \lambda),$$

$N$  = Avogadro's number,

$M$  = molecular weight,

$\alpha$  = polarizability per molecule =  $\alpha(\lambda)$ ,

$\rho$  = density =  $\rho(P, T)$ .

and

The use of a more complicated expression than (1), say, for example, equation (27) of Kirkwood (1936), alters  $n$  by only about  $2 \times 10^{-6}$ . If  $\alpha$  does not depend on temperature, then for any particular wavelength, (1) may be written as

$$(2) \quad \rho = k \frac{n^2 - 1}{n^2 + 2},$$

where  $k$  is a constant. The coefficient of thermal expansion of liquid helium, along the saturated vapor pressure curve, may be expressed as

$$(3) \quad \beta_s = -\frac{1}{\rho} \frac{d\rho}{dT}.$$

The author has measured  $\beta_s$  for helium II (Atkins and Edwards 1955). (Note  $\beta_s$  was called  $\alpha_s$  in this reference.) From (2) we may write

$$(4) \quad \beta_n = -6n(n^2 - 1)^{-1}(n^2 + 2)^{-1}dn/dT$$

where  $\beta_n$  means the coefficient of expansion as determined from the measurements of refractive index. A value of  $n$  to give a  $\beta_n$  equal to the measured value of  $\beta_s$  at one temperature was selected. All other values of  $n$  at different temperatures were then obtained from the measurements of differences in index. The results are shown in Fig. 2. They indicate that  $n$  increases

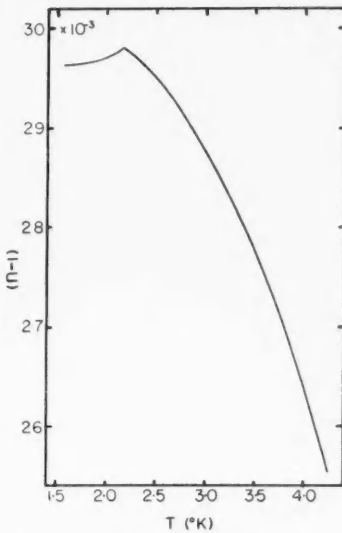


Fig. 2. The index of refraction of liquid helium, as a function of temperature.

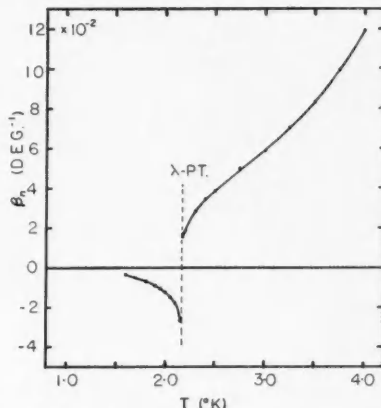


Fig. 3. The coefficient of expansion of liquid helium, as a function of temperature.

from about 1.0296 at 1.6° K. to 1.0298 at the  $\lambda$ -point, and decreases to 1.0257 at 4.2° K. As 220 experimental points were taken, they have been omitted from Fig. 2 for clarity. Few of the points deviated from the curve by more than  $10^{-3}$ . Differences in index are thus very precisely determined. The actual values of  $n$  as determined by this fitting procedure, however, are probably uncertain by about  $\pm 0.0007$ .

These values should be compared with the measurements of Wilhelm and Cove (Satterly 1936), who obtained  $1.028 \pm 0.008$  as the index of liquid helium II (against gaseous helium) at a temperature just below 2.1° K.; and of Johns and Wilh-lm (1938), who obtained  $1.0206 \pm 0.0012$  at 4.22° K. and  $1.0269 \pm 0.0004$  at 2.253° K. and 2.139° K. for  $\lambda = 5461 \text{ \AA}$ . In both cases

Wollaston cells were used to determine critical angles, which were of the order of  $80^\circ$ . The uncertainties stated do not include the effects of possible distortion of the plates of the cells near the edges.

Using equation (4) and taking values of  $d\eta/dT$  at various temperatures from Fig. 2, values were obtained for  $\beta_n$  for both helium II and helium I. For helium II  $\beta_n$  agrees with  $\beta_s$  to within about 2%. This confirms that the molecular polarizability  $\alpha$  is constant over this temperature range. Assuming that  $\alpha$  remains constant for helium I also, the values of  $\beta_n$  shown in Fig. 3 were obtained. It is interesting to note that the coefficient of expansion for helium I begins to fall rapidly as the  $\lambda$ -point is approached from above.

- ATKINS, K. R. and EDWARDS, M. H. 1955. Phys. Rev. **97**: 1429.  
CLEMENT, J. R., LOGAN, J. K., and GAFFNEY, J. 1955. Proc. Conférence de Physique des Basses Températures, Paris. p. 601.  
JOHNS, H. E. and WILHELM, J. O. 1938. Can. J. Research, A, **16**: 131.  
KIRKWOOD, J. G. 1936. J. Chem. Phys. **4**: 592.  
SATTERLY, J. 1936. Revs. Mod. Phys. **8**: 347.

RECEIVED JUNE 15, 1956.  
ROYAL MILITARY COLLEGE,  
KINGSTON, ONTARIO.

M. H. EDWARDS

## THE PHYSICAL SOCIETY

MEMBERSHIP of the Society is open to all who are interested in Physics.

FELLOWS pay an Entrance fee of £1 1s. (\$3.00) and an Annual Subscription of £2 2s. (\$6.00).

STUDENTS: A candidate for Studentship must be between the ages of 18 and 26, and pays an Annual Subscription of 5s. (\$0.75).

MEETINGS: Fellows and Students may attend all Meetings of the Society including the annual Exhibition of Scientific Instruments and Apparatus.

PUBLICATIONS include the *Proceedings of the Physical Society*, published monthly in two sections, and *Reports on Progress in Physics*, published annually. Volume XVIII, 1955, is now available (price 50s. (\$7.15)). Members are entitled to receive many of the Publications at a reduced rate.

Further information can be obtained from:

THE PHYSICAL SOCIETY  
1, LOWTHER GARDENS, PRINCE CONSORT ROAD  
LONDON, S.W.7, ENGLAND



# CANADIAN JOURNAL OF PHYSICS

## Notes to Contributors

### Manuscripts

(i) **General.** Manuscripts, in English or French, should be typewritten, double spaced, on paper  $8\frac{1}{2} \times 11$  in. **The original and one copy are to be submitted.** Tables and captions for the figures should be placed at the end of the manuscript. Every sheet of the manuscript should be numbered.

Style, arrangement, spelling, and abbreviations should conform to the usage of this journal. Names of all simple compounds, rather than their formulas, should be used in the text. Greek letters or unusual signs should be written plainly or explained by marginal notes. Superscripts and subscripts must be legible and carefully placed.

Manuscripts and illustrations should be carefully checked before they are submitted. Authors will be charged for unnecessary deviations from the usual format and for changes made in the proof that are considered excessive or unnecessary.

(ii) **Abstract.** An abstract of not more than about 200 words, indicating the scope of the work and the principal findings, is required, except in Notes.

(iii) **References.** References should be listed **alphabetically by authors' names**, unnumbered, and typed after the text. The form of the citations should be that used in issues of this journal published in 1956; in references to papers in periodicals, titles should not be given and only initial page numbers are required. The names of periodicals should be abbreviated in the form given in the most recent *List of Periodicals Abstracted by Chemical Abstracts*. All citations should be checked with the original articles and each one referred to in the text by the authors' names and the year.

(iv) **Tables.** Tables should be numbered in roman numerals and each table referred to in the text. Titles should always be given but should be brief; column headings should be brief and descriptive matter in the tables confined to a minimum. Vertical rules should be used only when they are essential. Numerous small tables should be avoided.

### Illustrations

(i) **General.** All figures (including each figure of the plates) should be numbered consecutively from 1 up, in arabic numerals, and each figure referred to in the text. The author's name, title of the paper, and figure number should be written in the lower left corner of the sheets on which the illustrations appear. Captions should not be written on the illustrations (see Manuscripts (ii)).

(ii) **Line Drawings.** Drawings should be carefully made with India ink on white drawing paper, blue tracing linen, or co-ordinate paper ruled in blue only; any co-ordinate lines that are to appear in the reproduction should be ruled in black ink. Paper ruled in green, yellow, or red should not be used unless it is desired to have all the co-ordinate lines show. All lines should be of sufficient thickness to reproduce well. Decimal points, periods, and stippled dots should be solid black circles large enough to be reduced if necessary. Letters and numerals should be neatly made, preferably with a stencil (**do NOT use typewriting**) and be of such size that the smallest lettering will be not less than 1 mm. high when reproduced in a cut 3 in. wide.

Many drawings are made too large; originals should not be more than 2 or 3 times the size of the desired reproduction. In large drawings or groups of drawings the ratio of height to width should conform to that of a journal page but the height should be adjusted to make allowance for the caption.

**The original drawings and one set of clear copies (e.g. small photographs) are to be submitted.**

(iii) **Photographs.** Prints should be made on glossy paper, with strong contrasts. They should be trimmed so that essential features only are shown and mounted carefully, with rubber cement, on white cardboard with no space or only a **very small** space (less than 1 mm.) between them. In mounting, full use of the space available should be made (to reduce the number of cuts required) and the ratio of height to width should correspond to that of a journal page ( $4\frac{1}{2} \times 7\frac{1}{2}$  in.); however, allowance must be made for the captions. Photographs or groups of photographs should not be more than 2 or 3 times the size of the desired reproduction.

**Photographs are to be submitted in duplicate;** if they are to be reproduced in groups one set should be mounted, the duplicate set unmounted.

### Reprints

A total of 50 reprints of each paper, without covers, are supplied free. Additional reprints, with or without covers, may be purchased.

Charges for reprints are based on the number of printed pages, which may be calculated approximately by multiplying by 0.6 the number of manuscript pages (double-spaced typewritten sheets,  $8\frac{1}{2} \times 11$  in.) and including the space occupied by illustrations. An additional charge is made for illustrations that appear as coated inserts. The cost per page is given on the reprint requisition which accompanies the galley.

Any reprints required in addition to those requested on the author's reprint requisition form must be ordered officially as soon as the paper has been accepted for publication.

## Contents

	Page
The Effect of Incident Atomic Velocity on the Structure of Evaporated Silver Films— <i>R. A. Aziz and G. D. Scott</i>	731
The Raman Spectrum of Ethylene— <i>T. Feldman, J. Romanko, and H. L. Welsh</i>	737
Cross Sections of ( $p, sn$ ) in the Isotopes of Lead and Bismuth— <i>R. E. Bell and H. M. Skarsgard</i>	745
A Schematic Model for ( $p, sn$ ) Cross Sections in Heavy Elements— <i>J. D. Jackson</i>	767
Emission Band Spectra of Nitrogen. The Lyman-Birge-Hopfield System— <i>Alf Lofthus</i>	780
A Homogeneous Dielectric Sphere as a Microwave Lens— <i>G. Bekefi and G. W. Farnell</i>	790
Shell Effects on the Spacing of Nuclear Levels— <i>T. D. Newton</i>	804
The Strengths, Widths, and Shapes of Infrared Lines. I. General Considerations— <i>William S. Benedict, Robert Herman, Gordon E. Moore, and Shirleigh Silverman</i>	830
The Strengths, Widths, and Shapes of Infrared Lines. II. The HCl Fundamental— <i>William S. Benedict, Robert Herman, Gordon E. Moore, and Shirleigh Silverman</i>	850
The Diurnal Behavior of Sudden Commencements of Magnetic Storms at Agincourt— <i>J. A. Jacobs and T. Obayashi</i>	876
<b>Notes:</b>	
The Sudden Increase in Cosmic Ray Intensity of February 23, 1956— <i>D. C. Rose and J. Katzman</i>	884
A Simple Formula for Evaluating the Madelung Constant of a NaCl-type Crystal— <i>G. C. Benson</i>	888
Shielding of a Transient Electromagnetic Dipole Field by a Conductive Sheet— <i>James R. Wait</i>	890
Electromagnetic Field Solutions for Rotational Coordinate Systems— <i>Robert C. Hansen</i>	893
<b>Letters to the Editor:</b>	
The Luminescent Response of Silver Activated Zinc Sulphide to Lithium Ions of Different Energies— <i>Clifford F. Eve and Henry E. Duckworth</i>	896
The Index of Refraction of Liquid Helium— <i>M. H. Edwards</i>	898

